Bond Graph Modeling of Hydraulic Circuits on a Sweet Sorghum Harvester

by

Glen Christopher Rains

Dissertation submitted to the Faculty of the

Virginia Polytechnic Institute and State University

in partial fulfillment of the requirements for the degree of

Doctor of Philosophy

in

Agricultural Engineering

APPROVED:

Dr. John S. Cundiff, Chairman

Dr. David H. Vaughan

Dr. Harry H. Robertshaw

Dr. Hal L. Moses

Dr. John V. Perumpral

April 1992

Blacksburg, Virginia

Bond Graph Modeling of Hydraulic Circuits on a Sweet Sorghum Harvester

by

Glen Christopher Rains

Dr. John S. Cundiff, Chairman

Agricultural Engineering

(ABSTRACT)

A whole-stalk harvester was developed as part of a sweet sorghum-for-ethanol production system. Gathering chains grasped the stalks as they were cut at the base with a disk-cutter. These stalks were flipped onto a cross conveyor and deposited into an accumulator. Periodically the machine stopped and the accumulator was dumped. All the components on the harvester are powered hydraulically. Five pumps on the harvester supply flow to seven actuator circuits. Power is delivered to the pumps from the tractor PTO via a universal joint driveline. Each of the six existing circuits and one proposed circuit were modeled with bond graphs and implemented for computer analysis using TUTSIM. Model validation was done by comparing simulated and measured driveline torque, line pressure, and return line flow rate in each of the six existing circuits.

Data collected on the gathering chains circuit was used to analyze the effect of driveline joint angles on transmitted torque and pump output. Torque measurements at three driveline angles showed a torsional vibration with a primary harmonic at driveline rpm and a secondary at twice driveline rpm. A combination of Cardan joint characteristics, mass unbalance, the secondary couple, and non-linear driveline and V-belt stiffness was used to model the driveline. Resulting simulated torque emulated the experimental very well. Measured pressure in the gathering chains circuit showed relatively low fluctuations at the highest amplitude torsional vibration (highest driveline joint angles). It was concluded that driveline vibration would not significantly affect the gathering chains circuit performance.

The cross-conveyor motor circuit simulation showed close agreement to experimental results. Mean predicted flow, pressure, and torque were within 8.9, 7.3, and 7.7 percent of mean measured values. A simulation with a stalk load on the conveyor showed that power requirement increased only 8.0 percent.

The accumulator dump circuit was analyzed to determine if the load on the motor would become over-running and cavitate the pump or motor as the stalks were being dumped. Simulation showed that a bundle up to 300 kg could be dumped without over-running the motor, and since this was a larger bundle than the bin could hold, a design modification was not necessary.

The disk-cutter circuit was designed based on simulation results for several combinations of motor, pump, and sheave ratio. A 7.3 cm^3/rad motor, 2.53 cm^3/rad pump , and 2:1 sheave ratio produced the correct disk-cutter speed, and low torsional vibration when cutting the stalks, consequently this combination was selected for the design.

Acknowledgements

I would like to thank those people who have offered encouragement and help during my work on this dissertation. Dr. Cundiff has served as advisor and friend, for which I am very grateful. I would like to thank my committee members Dr. David Vaughan, Dr. Hal Moses, Dr. John Perumpral, and Dr. Harry Robertshaw for their advise and involvement in the completion of this project. I would also like to acknowledge the help from the shop crew, Leon Alley, Donnie Wingo, Clyde Adkins, and Steve Spradlin, who were instrumental in the construction and modification of the harvester. Leon Alley spent many days in the shop and field in support of the sweet sorghum project. I am also very thankful for the patience, love, and understanding of my Fiancee, Nikki Edmondson. Last, but definitely not least I would like to thank my mother and brothers for giving encouragement and support in everything I have done.

Table of Contents

List of Illustrations

List of Tables

Chapter 1 Introduction

Fluid power systems are an integral part of efficient power transmission in many mobile agricultural machines. Hydraulic systems deliver high power to remote locations on a machine, and should be designed to transmit power as efficiently as possible. The procedure used to design a hydraulic system may determine its cost effectiveness; thus, the decision to build, test, and rebuild, or to use some form of complex analysis beforehand, may be a factor in saving time and money.

Before mathematical models were available, selection of components was based on ideal steady-state performances, and then the system was built and tested. As manufacturers began providing performance data, efficiencies were used to account for losses and design accuracy improved. However, many circuits were rebuilt because the system did not meet the performance criteria for which it was designed. In part, this was due to inaccuracies in the analysis because inherent non-linearities were not taken into account. Also, designers may have discarded or ignored characteristics which ultimately proved critical to the final design. This design-test-rebuild method has proven to be costly and time consuming.

Increases in speed and reduction in cost of computer hardware have reduced computing cost within reach of even the smallest industrial or educational institution (Gordon, 1989). Digital computers can quickly and efficiently analyze a problem given a well developed analysis program. Synthesizing

circuits becomes more efficient, and several alternatives can be analyzed before buying components and constructing circuits. Once desired performance is simulated, then a prototype system may be built for testing. If the simulation was well done, only minor adjustments will be needed. Consequently, computer modeling and simulation of fluid power systems is becoming increasingly prevalent in industry and academia.

A prototype whole-stalk sweet sorghum harvester is being developed as part of an on-going program in the Agricultural Engineering Department to promote sweet sorghum as a feedstock for an ethanol industry in the Piedmont. All the sub-systems on the harvester are hydraulically powered. Procedures were developed to experimentally determine model parameters for the various actuators on the harvester. Once models were constructed for the components, they were joined together to form a simulation model for the complete harvester hydraulic system. The system model was then used to study circuit performance and evaluate design improvements.

Chapter 2 Literature Review

2.1 Ethanol Production

As mentioned in the introduction, the sweet sorghum harvester was developed as part of a program to promote sweet sorghum as an ethanol feedstock for the Piedmont. The use of ethanol as an octane enhancer for gasoline is continually increasing. As of 1987, 3.2 billion liters of fuel ethanol were produced annually in the United States. Today, with production of almost 3.8 billion liters, eight percent of the gasoline supply in the U.S. is an ethanol blend. Ethanol has several benefits which suggest that it will continue to be a viable alternative of the national liquid fuel supply.

1. Ethanol is domestically produced, and when used to displace gasoline, reduces U.S. dependence on imported oil.

2. Volatile organic compound (VOC) emissions from automobiles, which adversely affect the environment, are reduced.

3. Ethanol is produced from renewable resources such as corn, sugar cane, and sweet sorghum, and production of these feedstocks will provide alternative markets for U.S. agriculture.

Corn is the feedstock for over 90% of the ethanol currently produced in the U.S.. Increased production of ethanol could raise corn prices and result in inflated food costs. The investigation of new ethanol feedstocks is one solution to the potential food vs. fuel issue.

Amendments to the 1990 clean air act require CO non-attainment areas (44 cities representing 64 billion liters of gasoline sales annually) to implement an oxygenated fuels program by 1992. All fuels sold in these areas must have an average minimum oxygen content of 2.7%. Ethanol and its chemical derivative, ethyl tertiary butyl ether (ETBE), are both important oxygenating agents. Some sources project that the current 3.8 billion liter per year fuel ethanol industry will expand to 10 billion liters per year. It appears evident that liquid fuels from renewable resources will be of accelerating importance in the US economy.

Sweet sorghum is a high tonnage sugar crop that produces readily fermentable carbohydrates. It is drought resistant, has lower requirements for soil fertility and water, and produces higher biomass yields than grain (Lipinsky and Kresovich, 1980). In the eastern Piedmont, a physio-graphic region covering parts of seven states from Alabama to Pennsylvania, these attributes make sweet sorghum a desirable fuel crop.

2.1.1 Concept for Sweet Sorghum Industry in the Piedmont

A concept for a sweet sorghum-for-ethanol production system in the Piedmont has been developed. A central mill will buy sorghum grown by farmers as it stands in the field, and contract to have the sorghum harvested and the juice expressed. Juice will be transported to the mill for direct fermentation, and the fiber residue will be ensiled for later use as a feedstock for fiber conversion, a process whereby the structural carbohydrate is broken down to sugar and fermented.

Two options are available to the grower. In the first option, the fiber residue (presscake) will be ensiled in bunk silos as cattle feed. A credit for the silage will be subtracted from the total payment due the farmer. Option two will have the mill rent silo space from the farmer, and the mill will later retrieve the ensiled material for fiber conversion.

The procedure used for juice expression determines the yield obtained from the stalk. When juice is expressed from chopped whole-stalk, the fibrous material (rind and leaves) absorbs some of the juice from the sugar-rich pith, reducing the yield. In one experiment, 10% of the stalk mass was eliminated by separating out the rind-leaf, and juice expression was increased from 0.35 Mg juice/ton chopped whole-stalk, to 0.45 Mg juice/ton pith fraction (Cundiff and Rains, 1991).

Chopped material must be processed immediately (juice expressed and fiber residue ensiled), as breakdown of sugars begins when the rind is ruptured. Consequently, juice must be expressed and taken to the mill the same day it is harvested. Fields will only be harvested when there is available time at the mill to accept the juice. Since the harvest season in Virginia is 30 days, there is a very narrow window of time to process all the sweet sorghum from a given production area. Yearly capacity of a unit of equipment, for example the press, is quite limited; consequently, fixed cost per Mg processed is high. The amount of juice expressed is limited by the short time frame to process a large quantity of material.

2.1.2 Potential Harvest Systems

Worley (1990) studied two harvest systems which chop the stalks at the time of harvest. The first system, identified as the forage chopper system, uses a conventional forage chopper to harvest the sorghum and blow the chopped material into a forage wagon. The wagon unloads the material into a screw press for juice expression, and the fiber residue (presscake) is directly conveyed into a silo. The juice must be taken directly (within hours) to a central mill for direct fermentation into ethanol.

The pith combine system uses a modified forage harvester, or pith combine, as the harvester unit. The pith combine separates the rind-leaf material from the pith as the stalks are harvested. The rind-leaf is left on the field and the pith is conveyed into a wagon. From this point forward, handling is like the forage chopper system. Juice is expressed from the pith alone; consequently, expression efficiency is higher and more juice per unit of press operating time is collected.

Cundiff and Parrish(1984) discovered that there are negligible losses of the stalk fermentables when 1-m diameter bundles were left in an open field. The rind provided adequate protection for fermentables stored in the stalk; consequently, whole-stalk storage was considered a method by which stalks could be harvested when sugar content was optimal and not only when juice expression equipment was available.

A third system, identified as the Piedmont system, stores whole-stalks in the field for up to 30 days before juice expression. The stalks are cut by a pull-type whole-stalk harvester which leaves stalks in a windrow in the field. These stalks are later hauled to the on-farm processing site (beside bunk silo) when the central mill is ready to receive the expressed juice. After the normal season is over, juice may still be expressed and taken to the mill. With proper scheduling, the screw press and mill will then be operating at full capacity for 60 days, instead of 30.

Implementation of the Piedmont System predicates the development of a whole-stalk sweet sorghum harvester. Two of the four subsystems on a prototype harvest were built and tested in 1988 (Rains, 1990) and the remaining two subsystems were tested in 1990 (Cundiff and Rains, 1991). Final testing was done in 1991.

2.2 Description of Whole-Stalk Harvester

The whole-stalk harvester consists of four sub-systems: 1) gathering chains, 2) stalk flipper, 3) conveyor, and 4) accumulator (Figure 1). The sorghum is harvested as follows. The 1.6 to 2.0 meter tall stalks are cut by the disk-cutter 10 cm above the ground and grasped simultaneously 1.2 m above the ground by the gathering chains. The stalks are carried upwards and rearwards in a vertical position. When the stalks reach the top of the gathering chains, they are released and grasped at the base by the stalk flipper. The stalk flipper rotates the stalks 90° and lays them onto the cross conveyor. The conveyor then carries the stalks into the accumulator. Once the accumulator has been filled, the operator stops the harvester and dumps the bundle of stalks into an aligned-stalk windrow.

All the subsystems are powered hydraulically. The PTO from the tractor transmits power through a universal joint (U-joint) driveline to a jackshaft (harvester input shaft) on the harvester. The harvester input shaft distributes power via V-belt drives, to two multiple pumps, a multiple-3 pump on the left of the input shaft, and a multiple-2 pump on the right (Figure 2). These five pumps supply flow to seven actuating circuits on the harvester. The load functions used in the computer simulation require certain parameters representing the load, losses, and inertia of the hydraulic and mechanical components.

2.3 Mathematical Models

Mathematical models are developed to represent the physical laws governing a system, or to describe the functioning of components within a system (Grogan, 1985). They may be based on theoretical concepts, empirical data, or a combination of the two. The complexity of the model is

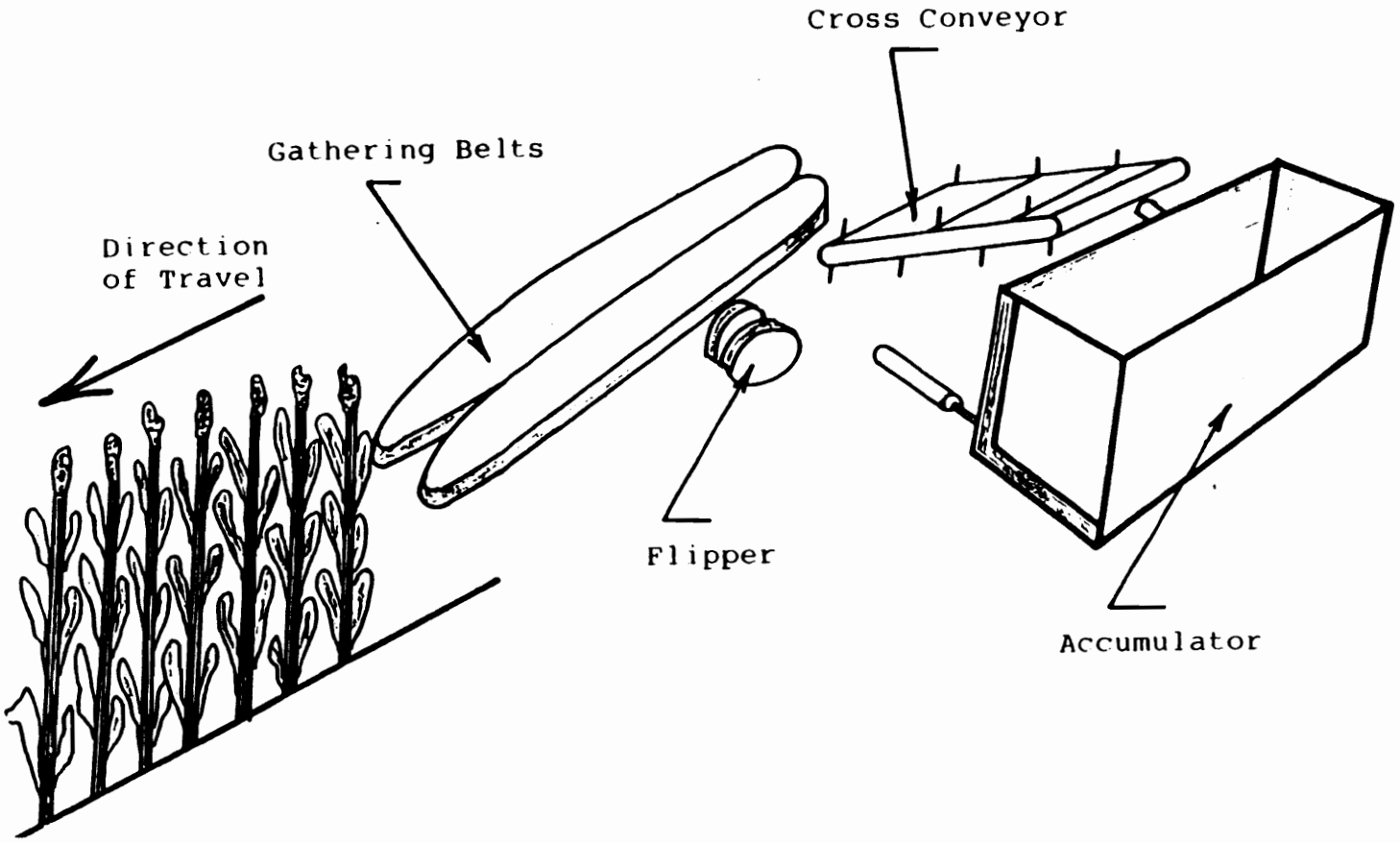

Figure 1. Components of sweet sorghum harvester aligned to harvest a row.

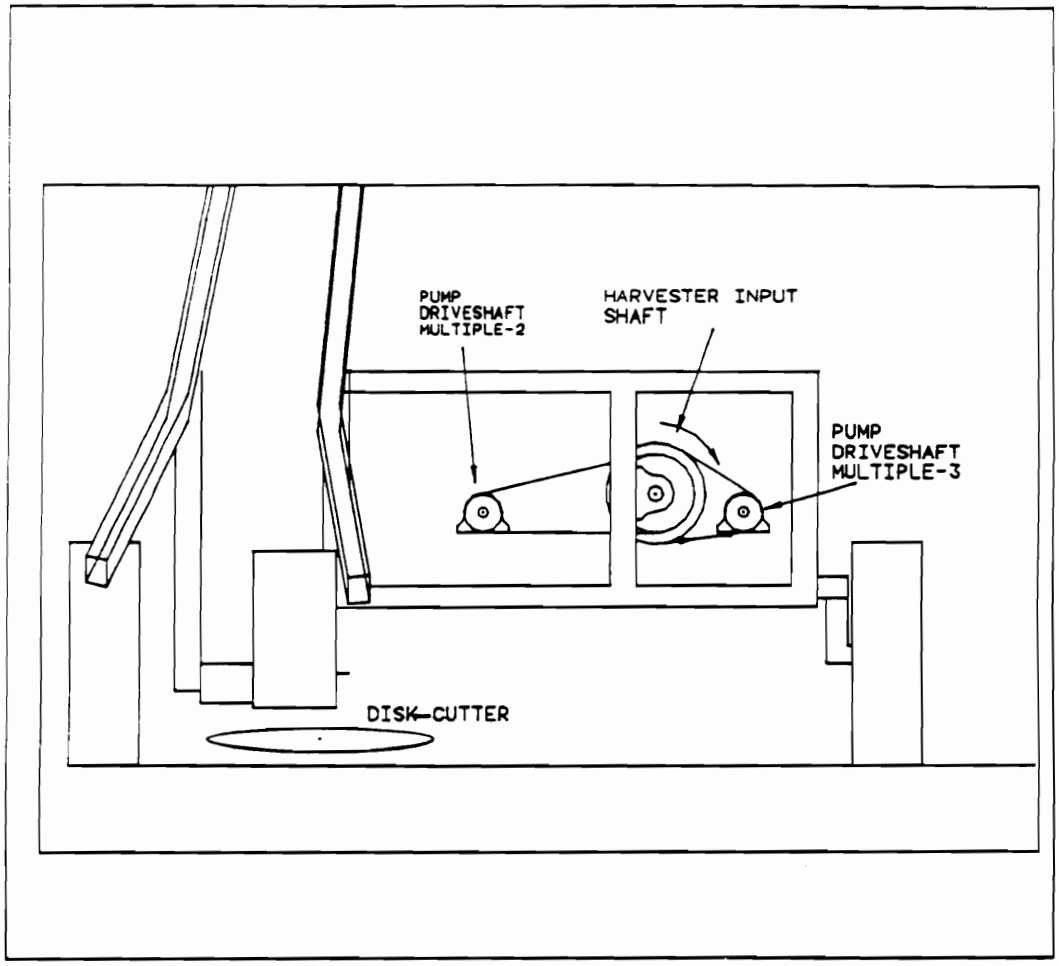

Figure 2. Front view of drive system for multipe-3 and multiple-2 pump.

determined by the type of results desired. The general rule-of-thumb is that a model should be made as simple as possible to give the desired results. Once the models have been constructed, computer implementation allows an engineer to quickly analyze and modify them.

The following is a review of mathematical models used for the simulation of hydraulic circuits. Several computer programs that have been used to analyze hydraulic circuits will be reviewed and critiqued. Finally, the use of bond graphs is evaluated as a modeling technique and simulation tool.

2.3.1 Steady-state Pump and Motor Performance

Wilson (1949) derived the first mathematical model for steady-state analysis of positive displacement pumps and motors. Wilson was the first to describe the performance of a hydrostatic transmission, and most of the subsequent studies have been based on modification of his equations. Consequently, an in-depth look at Wilson's equations is warranted. The pump characteristics will be examined with the knowledge that a pump and motor input and output are converse to each other; i.e., torque is input to turn the pump, while torque is output when a load is placed on the motor.

Wilson's equations were developed using non-dimensional constant coefficients to characterize the flow and torque losses. Flow losses were due to pump slip, and torque losses resulted from coulomb friction, viscous drag, and a constant torque term. Two separate equations were developed to represent volumetric and mechanical output.

Flow losses occur because of pump slip. Assuming laminar leakage flow through the pump clearances, actual flow is given by,

$$Q_p = D_p\omega_p - \frac{C_s\Delta P D_p}{\mu} \qquad [2.1]$$

where

Q_p = actual pump flow (m^3/s),

D_p = pump displacement (m^3/rad),

ω_p = pump speed (rad/s),

C_s = pump slip coefficient (dimensionless),

ΔP = pressure across ports (MPa), and

μ = viscosity ($N\text{-}s/m^2$).

The slip coefficient was experimentally determined, or derived from the volumetric efficiency curves provided by the manufacturer.

The torque losses define the mechanical efficiency of a pump. Actual torque input to the pump is

$$T_i = \Delta P D_p + C_f \Delta P D_p + C_{vd} \mu \omega_p D_p + T_c \qquad [2.2]$$

where

T_i = actual torque input (N-m),

C_f = coulomb friction coefficient (dimensionless),

C_{vd} = viscous drag coefficient (dimensionless),

T_c = constant torque term (N-m).

The first term is the ideal torque input; the second term is the torque to overcome coulomb friction; the third term is the torque to overcome viscous drag; and, the last term is a constant torque term. Coulomb friction is independent of pump speed and dependent on load pressure. The viscous drag is independent of load pressure and dependent on pump speed.

Merritt(1967) described the flow losses essentially the same as Wilson, except he divided the slip flow into external and internal losses. External losses were described as flow that leaked into the casing of the pump, and internal losses was flow which leaked or "slipped" from the high pressure

to low pressure side of the pump. Like Wilson, Merritt described torque losses by denoting viscous drag as a function of pump speed, and coulomb friction as a function of load pressure. The third torque component described by Merritt was the torque required to overcome seal friction, and he also denoted it as T_c.

Schlosser (1961) further refined Wilson's equations by replacing the constant torque term with a hydrodynamic torque loss which accounted for fluid acceleration. This term was a function of pump speed and fluid density. Schlosser also modified the flow loss by adding a term that accounted for turbulent leakage flow. This term is expressed as a function of the load pressure and fluid density. A non-dimensional coefficient, experimentally determined, was used to represent these losses.

Use of constant coefficients in these models failed to represent the performance of pumps and motors at different operating conditions because the coefficients were experimentally determined for a particular operating condition (McCandlish, 1981). Consequently, Wilson's equations are valid only at a given speed and pressure. In experiments with vane, piston, and gear pumps, the loss coefficients were found to vary with operating conditions.

Zarotti and Nervegna (1981) used the following procedure to improve the utility of constant coefficient models. The mathematical equations were created and coefficients determined based on statistical best-fit procedures. When the models proved to be unsatisfactory, a new model was tested based on observations from the experimental data. The new flow loss equation included coefficients that were a function of pressure and pump speed. A flow loss term attempted to describe the influence of pump speed. Similarly, a new torque loss equation included coefficients which were functions of pressure and speed. Close correlation between experimental and simulated values were found. Resulting equations were a mixed model based on physical losses and statistical procedures for determining a best fit. It was suggested that further testing be done to evaluate physical effects.

McCandlish and Dorey(1984) proposed a way to use Wilson's equations at different operating conditions. The loss coefficients used in the equations were made linear by interpolating between values determined at either end of the operating range. The linear equations took into account the dependence of slip flow and coulomb friction loss coefficients on speed, which was unexplored by Wilson. For even higher accuracy, the coefficients were described by quadratic functions, which were derived by selecting one more experimental data point between the operating range endpoints. These quadratic equations describe the slip flow and coulomb friction coefficients as functions of speed and pressure. Therefore, the physical effects were preserved in the equations, and their dependence on the operating conditions was incorporated. Results showed that the prediction of pump performance by the linear and quadratic coefficient equations was clearly better than the constant coefficient Wilson equations over a prescribed operating range.

2.3.2 Dynamic Pump and Motor Performance

Dynamic analyses have been performed to determine the transient response of a modeled component. Transients are usually observed by exciting the model with a step input, an impulse, a sine wave, or a random input (Blackburn et al., 1960). Most dynamic models are steady-state models with energy storage terms added to the equation. Merritt (1970) developed dynamic models for a pump and motor. Fluid compliance was added to the flow equation and inertial load was added to the steady-state torque equation. Merritt set the coulomb friction equal to zero in order to proceed with a linear analysis. Blackburn et al. (1960) allowed for simultaneous changes in both pressure and return lines while Merritt assumed the return pressure was always constant. Watton (1988) assumed that the fluid compliance would be included in the fluid volumes of the hydraulic lines when they were modeled.

Hibi and Ichikawa (1975) introduced a mathematical model to characterize the starting performance of motors. Their model included a friction term which increased with the rotational speed of the

motor. They found that friction torque increased with inlet pressure and decreased with rotational speed. Although the model successfully simulated the motors' performance over a full range from starting to full rotational speed, the equations did not offer physical insight to motor performance.

2.3.3 Valves and Conductors

This review of valves is focused on spool valve analysis as spool valves are almost universally used for directional control. For a critical centered valve, Merritt (1967) gives flow rate through a spool valve with the spool shifted a distance y as

$$Q_L = C_d w_o y \sqrt{1/\rho(P_s - P_L)} - C_d A_2 \sqrt{1/\rho(P_s + P_L)} \qquad [2.3]$$

where

Q_L = flow through valve orifice (m^3/s),

C_d = discharge coefficient (dimensionless),

ρ = fluid density (kg/m^3),

w_o = width of orifice (m),

y = displacement of spool (m),

P_s = supply pressure (MPa),

P_L = load pressure (MPa), and

A_2 = clearance area of spool landing for leakage flow (m^2).

Flow through the valve to the desired port is dependent on a loss term which quantifies fluid which slips past the spool landing to the low pressure side of the valve.

All models of pumps, motors, and valves, just presented, were developed based on lumped parameter analysis. These models may not accurately simulate flow through the hydraulic lines when the wavelength of pressure waves in the lines are comparable to line length (Thoma and Richter,

1987). If wavelength is comparable to line length, a distributed line model must be used and the characteristics of the fluid flow described by partial differential equations. Thoma and Richter compared a segmented line approach and a modal approach to the modeling of hydraulic lines. The segmented line approach connects several lumped parameters together to represent a length of line. The modal approach uses a Fourier solution to the partial differential equation. A combination mass, resistance, and compressibility was used to represent each mode modeled for the hydraulic line. The modal approach was found to give substantially better accuracy with the same computing resources. Lebrun (1985) also found good correlation between experimental data and analytical data with the modal approach. Blackburn et al. (1960) claimed that the lumped parameter model was adequate for relatively short lines and low frequency systems.

2.3.4 Cylinders

Cylinders are the simplest actuators in a hydraulic system. Interestingly, very little had been done to correctly model this component. Henke (1983) gave a typical mechanical efficiency curve for a cylinder which showed that efficiency varied from 90 to 65 percent as the pressure on the cylinder rose from zero to rated pressure. Although Henke mentioned that cylinders would possess their own volumetric efficiency curves, they were not presented. Watton (1989) developed equations for cylinder performance during extension and retraction. The developed equations were in conjunction with a servo-valve which controlled the cylinder. It was determined that the power transfer to the load (and efficiency) was dependent on the cap-to-rod end area ratio. Watton also developed dynamic models for cylinders by adding volume and capacitance of the fluid to the model. In addition, the load inertia and load force was also added to the steady-state force equation.

2.4 Computer Implementation

Although models have helped identify the physical parameters which determine the performance of a hydraulic component, the real use of these models has been their eventual implementation into simulation programs. There have been several programs developed over the years for the analysis of hydraulic systems.

2.4.1 Hydraulic Simulation Programs

Clark (1973) experimentally verified the output of a hydraulic simulation program called Power Hydraulic System Simulation (PHSSI). The PHSSI program was originally an electronic circuit analyzer written by IBM. In Clark's work, the experimental values agreed reasonably with the simulated; however, motor speed was about one-half of the actual speed. He postulated that this discrepancy may have been caused by the assumed fluid viscosity value. The program did not allow for temperature variations, except that fluid kinematic viscosity could be changed with each solution.

In 1977, Wright Patterson Air Force Base released a set of programs to aid in the design and analysis of hydraulic systems on aircraft. This set of programs included steady-state analysis (SSFAN), transient analysis (HYTRAN), transient thermal analysis (HYTTHA), and frequency response analysis (HSFR). Each program was written in FORTRAN and implemented on a mainframe computer. Components were modeled in subroutines that could be coupled together to simulate a complete circuit.

The SSFAN program (Lever and Young, 1977) considered non-linearities, corrected viscosity for pressure, and determined whether flow was laminar, transitive, or turbulent. Over the years, there

have been several researchers who have modified the SSFAN program to be more user friendly and/or useable for analysis of hydraulic circuits on agricultural equipment.

McKemie and Cundiff(1979) modified SSFAN to analyze the hydraulic circuit of a seedling harvester. The modifications included changing the pump subroutine from a pressure compensated variable displacement pump to a variable displacement pump, and adding two subroutines for hydraulic motors. The simulated motor input flows and pressures were within six percent of experimental values. If the simulation was verified at a given operating point, the authors suggested that SSFAN could be used to study circuit performance under different operating conditions; however, they advised that the program may not be used with confidence when optimizing a circuit design.

Kinoglu et al. (1982) did work on all the Air Force programs to make them more user friendly and more appropriate for analysis of industrial hydraulic circuits. Their complete software package contained a library of hydraulic components, an engineering data base with design data and characteristics of each component, and the Air Force simulation programs. Evaluation of the SSFAN program showed the simulation to be very close to calculated values (within two percent); however, the HYTRAN program was still under evaluation.

Kinoglu et al. (1982) also showed how a graphics pre-processor could be used to create a schematic of the hydraulic circuit. 2-D and 3-D schematics were developed, but were not yet integrated into the simulation programs at the time their results were published.

Kinoglu and Riley (1983) later reported integration of the SSFAN and HYTRAN programs with the graphics schematics. HYTRAN components were modified to better represent industrial hydraulics, and testing of the HYTRAN program revealed that simulation results were reasonably close to experimental.

Amann and Krutz (1982) developed a graphic pre-processor and a post-processor to output display for the SSFAN program. The goal was to reduce the time designers spend with data preparation,

and leave them more time to focus on the design of the circuit. Circuit components were picked from a menu and placed in the desired area with a joystick. A Megatek graphics device and VAX processor was utilized for display and computation. Comparison of experimental and simulation results, and modifications of SSFAN itself, were not mentioned.

SSFAN was reduced to a useable form on a microcomputer by Mailander and Leonyork (1987). A modified version of SSFAN for agricultural applications was used. Graphical Kernel System (GKS) was chosen as the graphics language for the pre-processor used to construct the circuit. An application processor was used as a central link between SSFAN and all other processors. The program was used as a teaching tool in an agricultural mechanization class. Students did have difficulty with operation of the computer, a problem which could be alleviated with better meshing of the processors. Laboratory results were predicted to within five percent by the modified SSFAN program.

A hydraulic circuit for a fertilizer applicator was designed and analyzed using the LSU-SSFAN CAD and simulation software (Kulkarni and Schueller, 1988) [The LSU-SSFAN version was the modified SSFAN program developed by Mailander and Leonyork, (1987)]. AutoCAD was customized for drawing the hydraulic circuits. The user remained in the AutoCAD environment during the entire circuit design, analysis, and display of results. Modifications were made in the AutoCAD environment and new models could be re-analyzed immediately. An object oriented database for components was conceptually designed but not physically implemented.

Bowns et al. (1981) developed the computing package General Hydraulic Simulation Language (GHSP). This package consisted of two main programs, the generation program and the simulation program. Data was input to the generator and then the component subroutines were called. The generator then produced a simulation program which included a centralized integration scheme. Component subroutines were represented by blocks and interconnected based on the power bond technique. Gear's method of integration was employed to accommodate the stiff systems inherent to hydraulics. Simulated values compared well to experimental results.

Bowns et al. (1983) described improvements and enhancements to GSHP. The library of component models was increased from approximately 100 to 200, and a provision was included to model components at varying levels of complexity, depending on the needs of the user.

Walters (1988) developed the Modular Optimized System Simulation (MOSS) package. This package was, however, primarily developed for electro-hydraulic controls. The output included bode plots, Nichol charts, and a stability boundary plot.

PERSIM (PERformance SIMulation) was developed in response for a need of a single program able to analyze the steady-state and dynamic response of hydraulic systems (Xu and Hong, 1984). The program used the performance rating concept to model hydraulic components. Instead of using the internal physical parameters, component characteristics were based on performance parameters which were readily available from the manufacturer. The simulation results presented were accurate to within two percent of experimental values.

A computer package, the Oil Hydraulic Circuit Simulator (OHCS), was developed to incorporate an expert system in the design and analysis of hydraulic circuits (Nakashima and Baba, 1989). OHCS linked together the circuit design, analysis, component selection, static and dynamic analysis, and inspection of completed drawings into one self-contained program. The system combined analytical techniques, based on theory, and heuristic knowledge, based on the experience of experts. OHCS ran in an ART environment on a symbolic LISP machine. 80 Mb of memory was required during runtime. It was reported that OHCS reduced work at the design level 50 percent.

2.4.2 Commercial Hydraulic Simulation Programs

There are several commercial packages dedicated to the analysis of hydraulic circuits. Fluid Engineering Simulation (FESIM) is an analysis program developed by FES, Inc. (Hong and Lee, 1989). It does static and dynamic analysis, as well as frequency, thermal, and contamination analyses. The

program consists of a comprehensive library of mathematical models that represent hydraulic components, and uses the modal approach to interconnect these components. Integration can be a fixed or variable step size to allow optimum speed and accuracy. Hong and Lee (1989) validated FESIM results by comparing predicted and experimental results from a servo-valve controlled fixed displacement motor, and found close agreement.

Hydraulic System Analysis (HYSAN) is an analysis system which may be run on an IBM compatible microcomputer. Included in the program is the hydraulic control theory and the mathematical model construction for conducting dynamic analyses. Morris (1984) presented the dynamic simulation of three hydraulic system models using HYSAN. Parameter changes were made to observe their affect on system responses, but he made no comparison to experimental data.

Flowmaster was developed over a 15-year period for fluid flow analysis (Miller, 1990). Analysis capabilities include, steady-state, transient, heat transfer, and component interaction. The graphical interface is written in C and the analytical modules are written in FORTRAN 77. Flowmaster is designed to be used for the analysis of any type of piping system, and is very versatile, but is also very expensive.

The before-mentioned computer programs were developed specifically for the design and analysis of hydraulic circuits. In addition, there are continuous simulation languages and packages which can be used to write programs for the analysis of hydraulic systems.

Advanced Continuous Simulation Language (ACSL) is software designed for modeling and evaluating the performance of continuous systems described by non-linear differential equations (Mitchell and Gauthier, 1981). ACSL includes variable time step integrators (used to simulate stiff systems), sorts equations so that no values are used before they are calculated, and is comparable with FORTRAN statements. The user can write his/her own FORTRAN subroutines within a simulation program.

TUTSIM (TUTSIM, 1990) is a simulation program which allows input either in block diagram, bond graph, or combined form. Continuous and discrete dynamic analysis can be performed. The package is written in Assembly and can be used on any IBM compatible computer. Some of its beneficial features include: the ability to be called from within another program, model files can be combined to create a larger model, and non-linear parameters can be used (Martin and Thoma, 1984). TUTSIM is used by manufacturers (Hydraulic & Pneumatic, 1989) for design, and educators (Ayers and Varma, 1986; Ge and Ayers, 1989) for engineering instruction.

2.5 Bond Graphs

The bond graph modeling technique was "discovered" by Paynter in 1959 (Karnopp and Rosenberg, 1968), and is a modeling tool which creates a graphical representation of the system being modeled. The system may be modeled from physical understanding, and mathematical equations extracted from the bond graph. Bond graphs use the same small number of symbols to represent all applicable types of systems (hydraulic, mechanical, electrical). First order differential equations can be systematically extracted from the model and solved with a computer. Since the equations are first order, they can be set-up in matrix form and solved directly.

There has been considerable amounts of fluid power research conducted with bond graphs as a modeling tool. League and Cundiff (1984) used the bond graph technique to model a hydrostatic drive test stand. The hydrostatic transmission was modeled based on Wilson's equations, and the rest of the mechanical and electrical components were modeled and directly connected to the bond graph of the transmission. The analytic model predicted the steady-state performance well, but had problems predicting the dynamic performance when the swashplate angle of the pump was varied. Bond and Martin (1980) modeled a general hydrostatic transmission and simplified the model to represent their particular problem. Parameters were taken from the component performance

curves. ENPORT IV, a program written solely for the analysis of bond graphs, was used to run the bond graph simulation. Most of the limitations in the results were caused by the programs inability to handle non-linear parameters. Thoma (1989) also presented a bond graph model of a hydrostatic transmission. TUTSIM was used to analyze the circuit, and flow, pressure, and motor speed were predicted. Results were not compared to experimental values.

Bond graph use can be enhanced by coupling with block diagrams. Thoma (1990) described bond graph models of several hydraulic components and gave simulation results. The models were combined bond graph and block diagram representations. Zalewski and Rosenberg (1986) illustrated the usefulness of combined bond graph and block diagram models. They conducted a simulation illustrating the inter-connectivity between the bond graph and block diagram. Martin and Thoma (1984) also gave an illustration of how bond graphs and block diagrams could be combined to analyze a pressure relief valve. TUTSIM was used for their analysis.

Bond graphs may also be used for general purpose analysis of any type hydraulic system. Thoma and Martin (1983) developed a bond graph model to simulate the noise generation in a pipe connecting a pump to a loading device. The noise resulted from power dissipation into the pipe wall and was graphed versus time. Linear models were used, but the authors did not feel they were a significant drawback due to the small amplitude of vibration. Barnard and Dransfield (1977) used bond graphs to develop a model of an open-loop system with valve controlled motor. Simulated results agreed with experimental data very closely.

Programs have been written to help assemble bond graphs more quickly for computer analysis. Granda (1985) built a pre-processor, called CAMP, to create bond graph representations of physical systems that could be converted to ACSL code. By systematically creating equations from the bond graphs input, the ACSL analysis procedure was enhanced.

ENPORT is a program written solely for the analysis of bond graphs. The latest version allows graphical input of the bond graph symbols on the computer screen for interactive use. ENPORT solves for the transient response and returns eigenvalues of the system.

Chapter 3 Objectives

Hydraulic simulation packages have been used for the design and analysis of hydraulic circuits. More general computer software (simulation packages) are also available to solve sets of mathematical equations derived by the analyst to describe the operation of a circuit. Hydraulic simulation packages generally do not contain models of mechanical or electrical components that are often coupled to the hydraulic system. By writing their own equations and solving with a general simulation package, the analyst has more power and flexibility; however, a disadvantage is the time commitment to write the dynamic equations governing a coupled hydraulic/mechanical/electrical system. The mathematical equations, once derived, must then be put into a computer program (e.g. FORTRAN, C, PASCAL, etc.) for simulation.

The convenience of a simulation program, and the flexibility of writing one's own mathematical equations, is combined with the application of the bond graph modeling technique and simulation with TUTSIM. Bond graph modeling of energy systems is based on power flow connections. A homogeneous set of symbols are used to represent any energy domain (hydraulic/mechanical/electrical), and thus create a coherent model. Once the system is modeled, the dynamic equations can be extracted and used in a computer simulation program.

The main objective of this project was to develop bond graph models that can be used for the analysis of hydro-mechanical systems on a whole-stalk sweet sorghum harvester. Specific objectives for this research are:

1. Develop analytical models of the hydraulic and mechanical components on the sweet sorghum harvester using bond graphs.

2. Experimentally and analytically determine model parameters of the hydraulic and mechanical components.

3. Simulate circuit performance and compare the predicted and experimental results.

4. Analyze effects of model modifications, and field conditions on performance.

Chapter 4 Component Models

4.1 Description of Hydraulic Circuits on Harvester

A universal joint driveline delivers power from the tractor PTO to the harvester input shaft. This shaft distributes power through V-belt drives to a multiple-3 pump on the right and a multiple-2 pump on the left (The "multiple-x" notation refers to an arrangement whereby several pumps are powered by a single input shaft. For example, a variable displacement pump with a double gear pump mounted on the auxiliary pump pad is described as a multiple-3 pump. A variable displacement pump with a single pump mounted on the auxiliary pump pad is a multiple-2 pump). These five pumps supply fluid power to seven actuating circuits, which include the following hydraulic components:

	Component	Number
1.	Fixed displacement gear pumps	3
2.	Variable displacement axial piston pumps	2
3.	Geroler motors with case drains	2
4.	Geroler motors without case drains	3
5.	Cross-over relief valves	2

6.	Relief valves	3
7.	Double-acting cylinders	4
8.	Directional control valve.	1

To familiarize the reader with the function of each circuit, a brief description of each is included here.

1. Gathering chains circuit- A variable displacement axial piston pump (Sundstrand Sauer Model 18) delivers flow to two gerolor-type motors (Charlynn Model 104-1066, 38.86 cm^3/rad) connected in series. One motor drives each side of the gathering chains. These chains have flexible loops of rubber bolted to tabs on each fifth link, and these rubber loops intermesh to grip the stalk. Intermeshing of the loops keeps the chains synchronized. The motors are mounted to the frame at the top of the gathering chains assembly.

2. Stalk flipper circuit - The flipper was constructed using two 50-cm diameter concave discs. An inner tube (size used for a motorbike) was placed between a rubber surface and the disc to create a deformable surface. The mounting bracket for each disc was designed such that the two discs could be forced together. The stalk is grasped by the stalk flipper 10-cm above the butt, just as the upper part is released by the gathering chains. A gear pump (Vickers G5-20-16) powered a geroler motor (Charlynn Model 101-1007 H-plus, 46.68 cm^3/rad), which drives one of the discs directly. The other disc is driven by frictional contact with the powered disc. The stalk flipper rotates the stalks 90° and lays them onto the cross conveyor.

3. Cross-conveyor circuit - A variable displacement axial piston pump (Cessna model 70442) delivers flow to a gerolor motor (Charlynn Model 101-1004 H-Plus, 25.30 cm^3/rad), which drives the cross conveyor. The conveyor has three chains spaced 100 cm apart. Each chain has 13 cm high spikes spaced 25 cm apart, which catch the stalks and carry them over into the accumulator.

4. Accumulator Circuit - A gear pump (Vickers model G5-10-20) delivers flow to a 3-section directional control valve (DCV). One circuit powers two cylinders connected in parallel which

move the accumulator in and out during filling, and collapse the accumulator all the way in for road travel. A second circuit delivers flow to two other parallel cylinders which change the angle of the conveyor. The conveyor is raised and lowered during harvest to fill the accumulator evenly. It is raised for road travel to allow the accumulator to be fully retracted. The third circuit activates a geroler motor (Charlynn Model 101-1008 H-Plus, 58.94 cm^3/rad) which dumps the accumulator. A chain drive connects this motor to the accumulator shaft, and rotation of this shaft dumps the accumulator.

5. Disk-cutter circuit - The disk-cutter is currently powered from the harvester input shaft using a chain drive and right angle gear box. It rotates at 500 rpm giving a blade tip velocity of 16 m/s, and cuts the stalk just above the ground. Currently there is no provision to move the disk-cutter up and down which creates a problem in uneven terrain. Plans are to use a gear pump to deliver flow to a geroler motor which will power the cutter via a V-belt drive. This entire assembly will be moved up and down with a cylinder controlled by the tractor operator. The gear pump has been installed and currently pumps flow back to the reservoir as the motor has not yet been installed.

One of the variable displacement piston pumps has a double gear pump mounted on the auxiliary pump mount to form the multiple-3 pump. The variable displacement pump supplies the gathering chain circuit, the first gear pump supplies the 3-section DCV and the second gear pump supplies the flipper (Figure 3). The other variable displacement pump supplies flow to the cross conveyor, and a gear pump mounted on the auxiliary pump mount supplies flow to the disk-cutter (Figure 4). Both circuit diagrams show the location of flow meters and pressure transducers used to obtain experimental data.

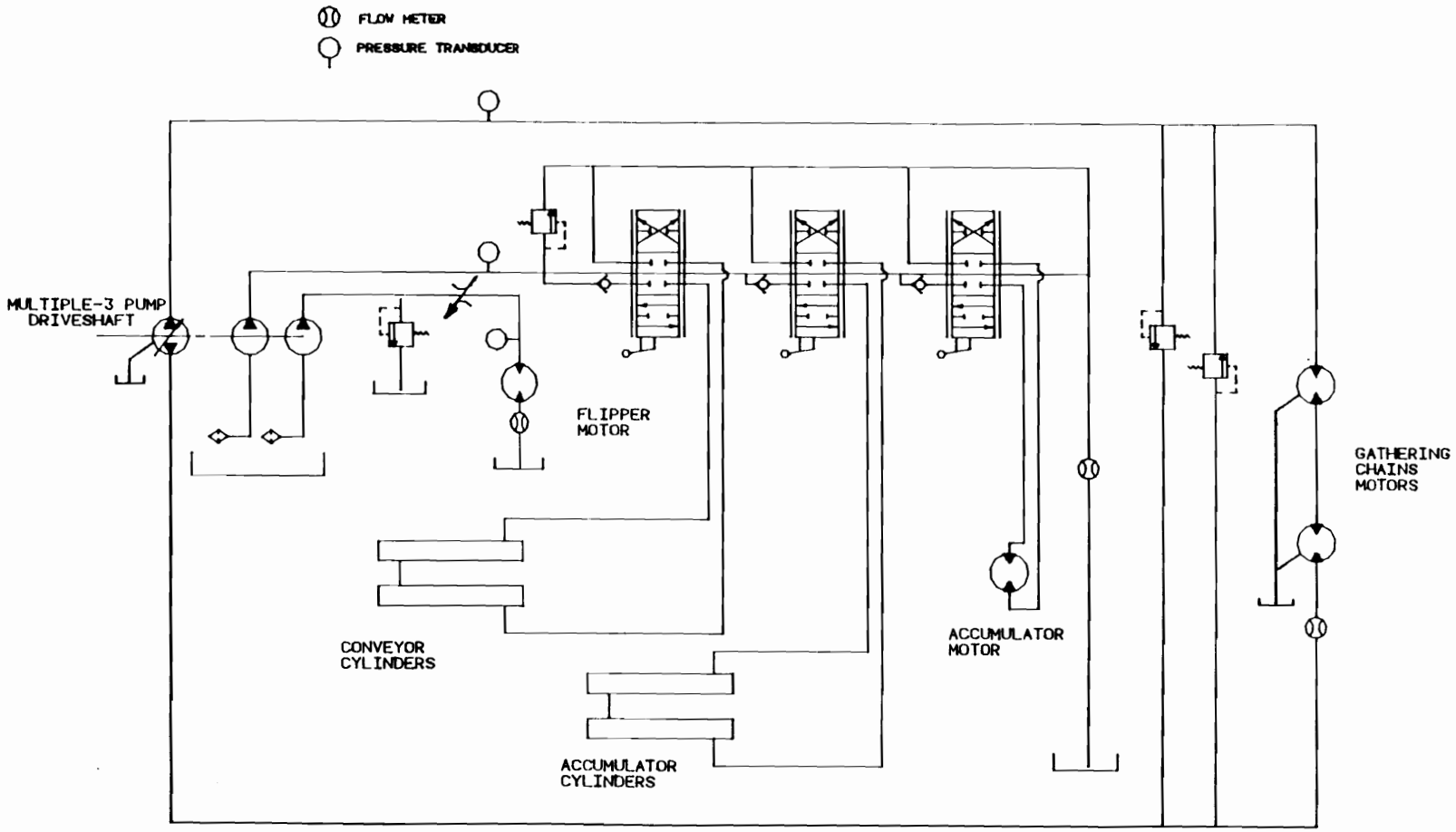

Figure 3. Hydraulic schematic for circuits supplied by multiple-3 pump (charge pump was not shown for simplification of drawing).

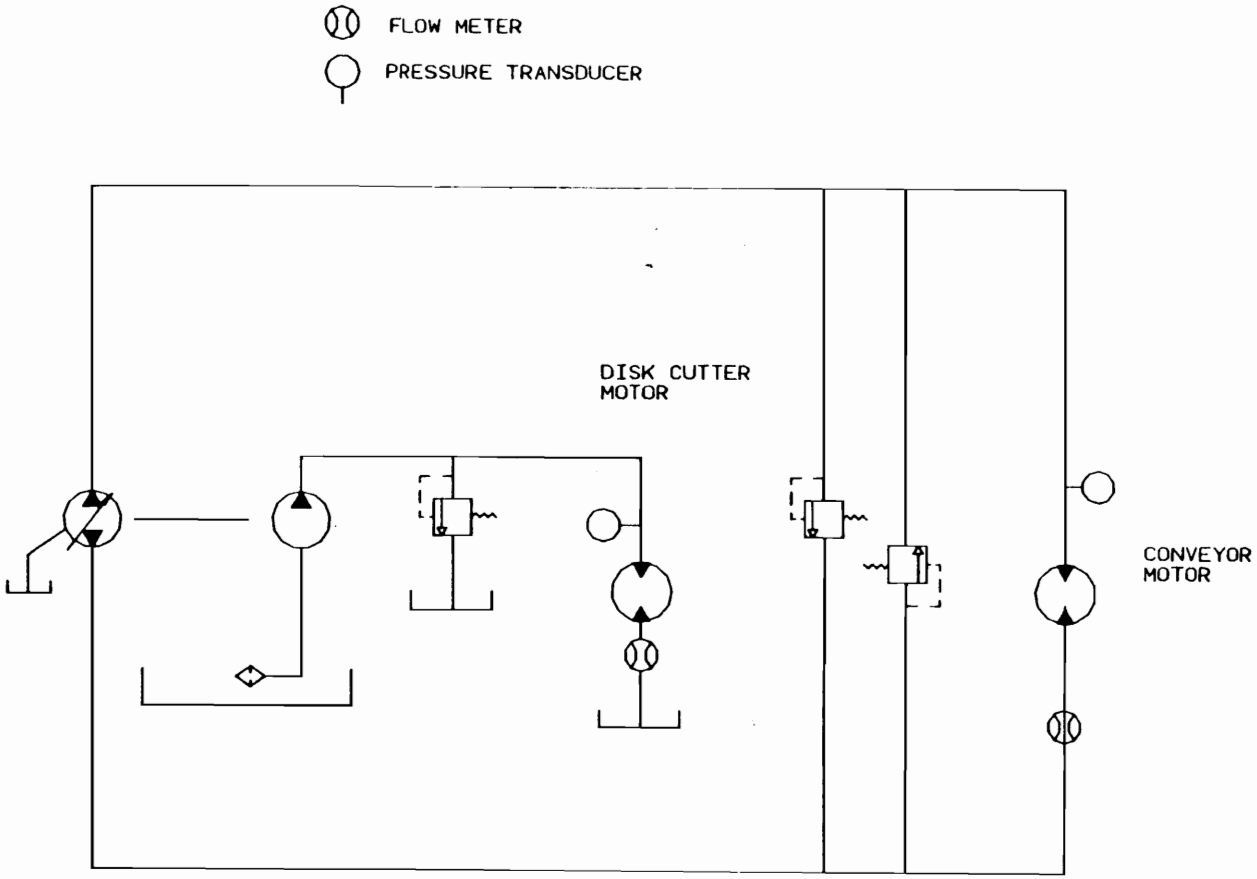

Figure 4. Hydraulic schematic for circuits supplied by multiple-2 pump (charge pump was not shown for simplification of drawing).

4.2 Component Models

Analytical models of the hydraulic and mechanical components were created using the bond graph modeling technique. Bond graphs have the following attractive features as a modeling tool.

1. Problems consisting of coupled energy systems(hydraulic, thermal, mechanical, electrical) can easily be represented by a single bond graph model. The same small number of symbols may represent any energy domain.

2. First order differential or integral equations, which are an ideal format for computer equation solving, can easily be extracted from the model.

3. State equations derived from bond graphs can be physically interpreted to give insight to interactions among system parameters. This understanding of the interactions is useful in determining what changes must be made to improve a system, or what factors are most important in the overall design.

4. Component models may easily be expanded or simplified without affecting the structure of the system model.

Fundamentals of bond graph modeling are presented in Appendix A. It is not the intent to teach the reader bond graphs; however, the short tutorial should give sufficient understanding to follow the concepts introduced.

The individual components (mechanical and hydraulic) were modeled separately, and later coupled together to form the complete actuating system. The following sections discuss the theory used to develop the models, and introduces the bond graph representation.

4.2.1 Input Drive Model

The input drive consists of the all the components from the tractor power take-off shaft to the pump driveshaft. The input drive model includes the engine output, driveline dynamics, and V-belt drive.

The tractor power take off (PTO) transmits power to the harvester input shaft via a 3-joint universal driveline (Figure 5). V-belts transmit power from the harvester input shaft to the multiple-3 pump mounted on the right, and multiple-2 pump mounted on the left. The sheave ratio for each pump drive is 2.5 to 1, meaning that at a maximum 1000 rpm PTO speed, pump speed will be 2500 rpm.

The 3-joint driveline consists of one constant velocity (CV) joint, and two Cardan joints. When an angle exists between the PTO shaft and the front shaft, the CV joint prevents output angular velocity fluctuation due to the angle. Cardan joints do not transmit uniform angular velocity between the input and output yokes when operated at an angle. Velocity fluctuations, and subsequent torsional vibrations, can cause disturbances in the driveline and affect the performance of the system.

When operated at an angle, output velocity from a Cardan joint leads then lags input velocity. Output velocity of the driven shaft is determined by

$$\omega_{out} = \frac{\omega_{in} \cos\theta}{1 - \sin^2\beta \sin^2\theta} \qquad [4.1]$$

where

ω_{out} = output velocity (rad/s),

θ = joint angle (rad),

β = rotational position of driven yoke from the plane perpendicular to joint angle

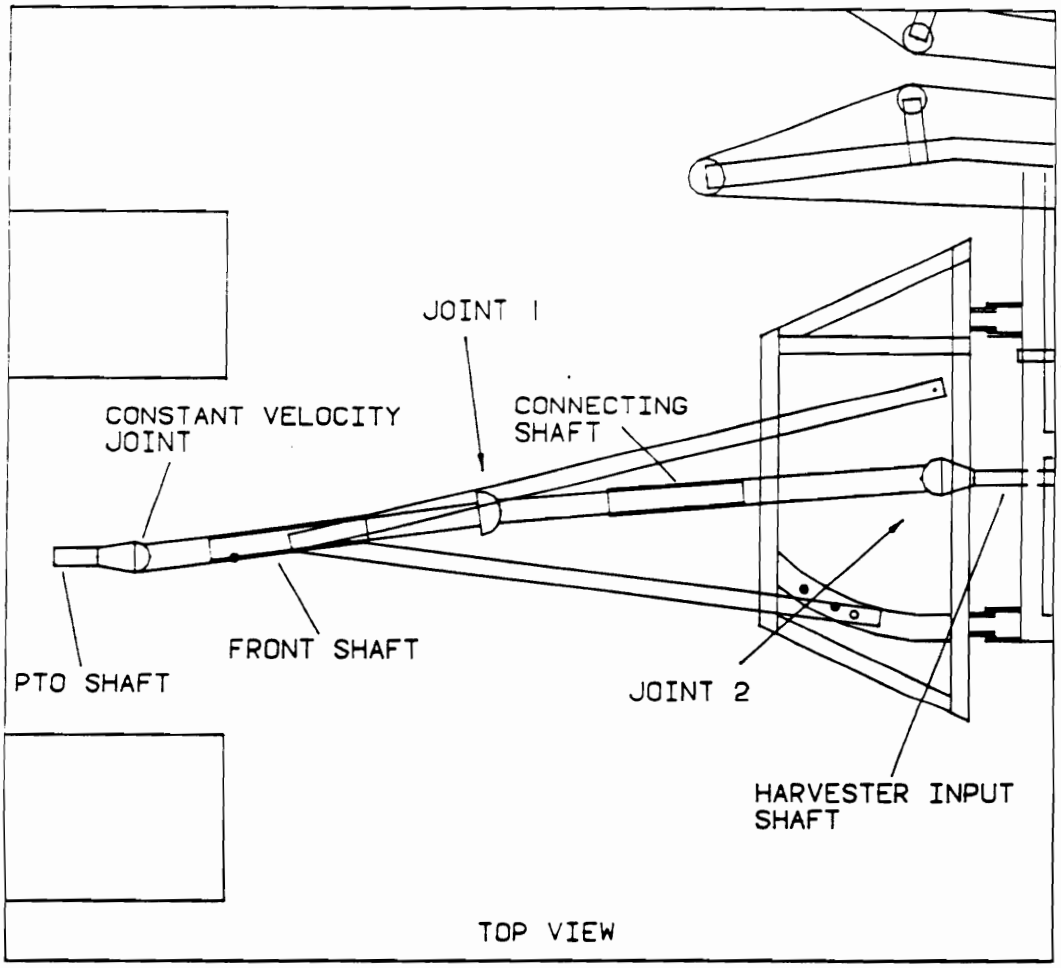

Figure 5. Top view of 3-joint universal driveline with each shaft defined

(rad), and

ω_{in} = input velocity of driving shaft (rad/s).

Angular velocity at the harvester input shaft can be determined by using Eqn. (4.1) for each joint and combining them; i.e. output velocity of joint 1 is the input velocity for joint 2. The angular velocity to the harvester input shaft becomes,

$$\omega_{his} = \frac{\cos\theta_1 \cos\theta_2 \omega_{in}}{(1 - \sin^2\beta_1 \sin^2\theta_1)(1 - \sin^2\beta_2 \sin^2\theta_2)} \qquad [4.2]$$

where

ω_{his} = harvester input shaft velocity (rad/s),

θ_1 = joint angle in joint 1 (rad),

θ_2 = joint angle in joint 2 (rad),

β_1 = rotational position of front shaft driving yoke measured from the plane perpendicular to joint angle (rad),

β_2 = rotational position of connecting shaft driving yoke measured from the plane perpendicular to joint angle (rad), and

ω_{in} = input velocity from tractor PTO (rad/s).

The driveline on the harvester is constructed such that β_2 is 30° ahead of β_1. The driveline is not in parallel phasing which is normal design procedure. Consequently, torsional vibrations in the driveline will be higher than would be expected if good design practice had been used. The manufacturers representative could not supply a reason why parallel phasing was not used.

Torsional vibration created by the kinematic relationship between the input and output yokes is usually the only behavior analyzed in a driveline. However, preliminary testing showed other phenomenon must be occurring, particularly at higher joint angles. After studying the literature,

and carefully analyzing the experimental data, two vibrational sources were added to the model of the driveline, shaft whirling and non-linear stiffness characteristics.

Shaft whirl (Figure 6) is the result of mass unbalance and secondary couples. Mass unbalance is caused by mass eccentricity and creates a centrifugal force that increases as the shaft angular velocity increases. The centrifugal force deflects the shaft, and deflection amplitude is a function of the shaft velocity, shaft length, mass eccentricity, and shaft stiffness. An additional shaft deflection is caused by a secondary couple. The secondary couple is a bending moment which results from a Cardan joint transmitting torque at an angle. The secondary couple acts on the shaft and causes shaft deflection like that produced by mass unbalance.

Shaft whirl may be responsible for changing the inertial load, and subsequently the torsional excitation in the driveline. The inertia of the shaft becomes larger when the shaft mass moves away from the axis of rotation. If the shaft end supports have unequal stiffness in the horizontal and vertical axis, then the shaft whirl follows an elliptical path (Figure 7). The inertia is then non-uniform and results in a varying torsional transmission through the shaft.

Non-linear stiffness was modeled as part of the driveline and V-belt effects. V-belts exhibit non-linear spring hardening characteristics which can change the natural frequency of the driveline response (Crolla, 1978). Backlash was associated with the splined couplings which join the connecting shaft, front shaft, and harvester input shaft, and gear reductions from the tractor transmission to the PTO shaft.

The input drive was modeled by implementing the shaft whirl, Cardan joint characteristics, and non-linear stiffness. The effects of the two Cardan joints were combined into one equation [Eqn. (4.2)]. This describes the output velocity of the driveline to the harvester input shaft as a function of the Cardan joint angles. Shaft whirl was calculated independently of the Cardan joint effects. The resulting variable inertia (J_o) was used as the inertia of the connecting shaft (whirling shaft). J_o was a function of the whirl amplitude and the whirl velocity. Cardan joint effects and shaft whirl

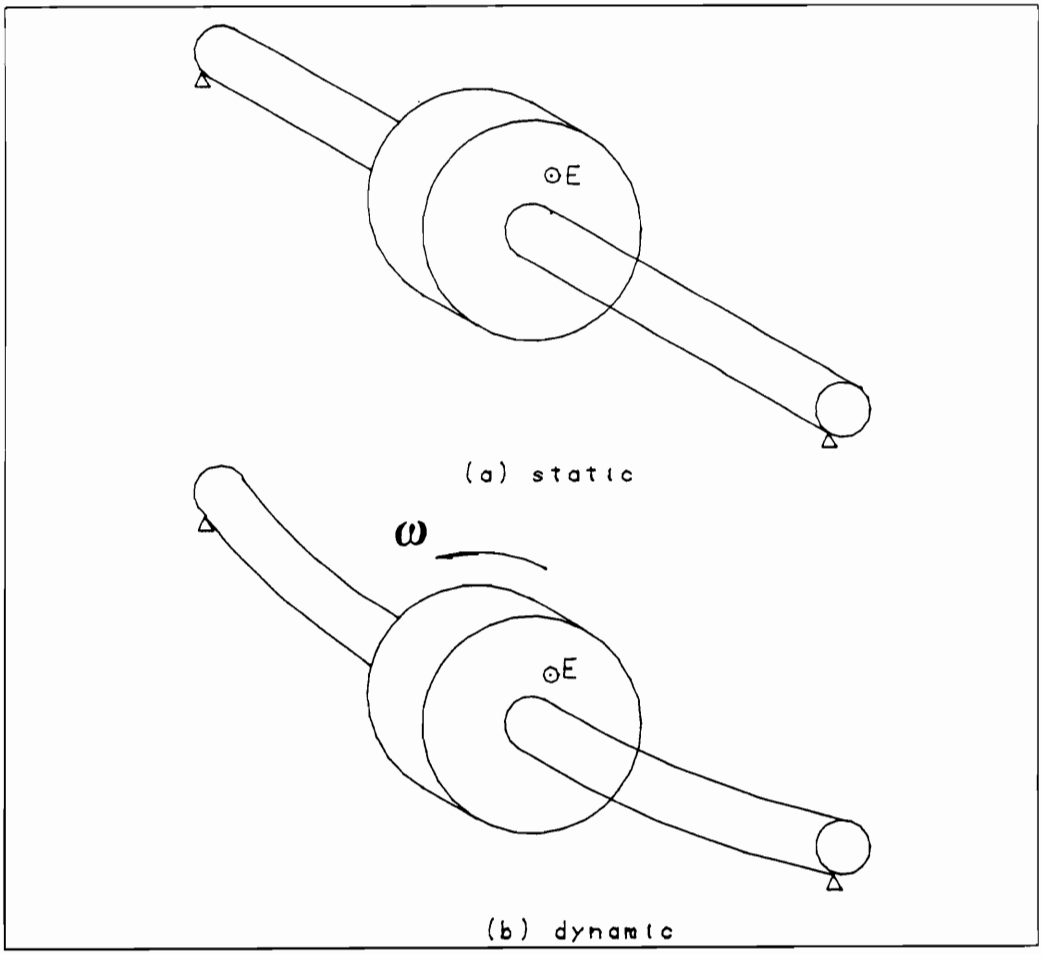

Figure 6. Diagram of shaft model in static (a) and dynamic (b) modes.

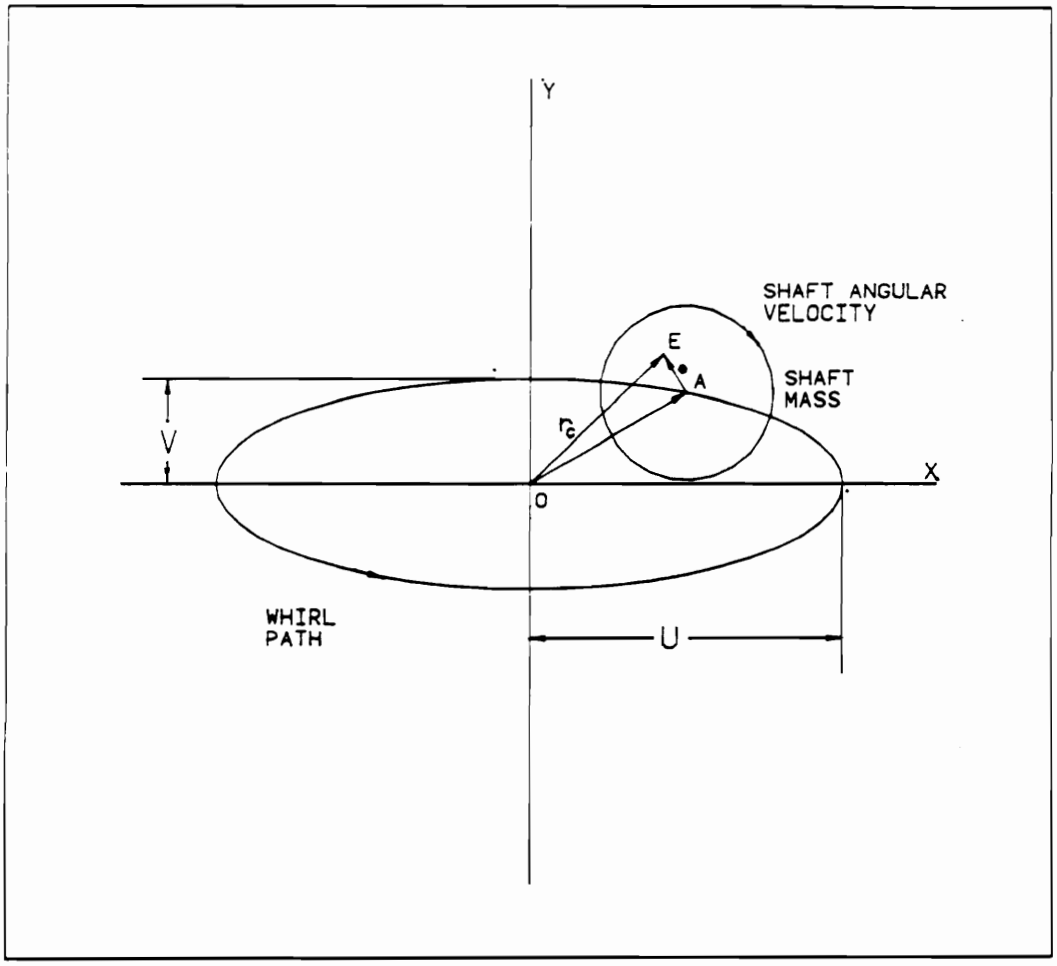

Figure 7. Elliptical path of shaft whirl from axial view.

were modeled in series (added together). In reality, the Cardan effects are coupled to the whirl to create a complex excitation. A more controlled set of experiments, with carefully measured parameters would be required to determine coupling between Cardan joints and shaft whirl. Consequently, the objective was to determine if experimental torsional excitation could be predicted from a combination of whirl, Cardan effects, and non-linear driveline stiffness.

The second order differential equation of the mass-spring-damper system for transmission of torque through a shaft is,

$$J_o\ddot{\beta}_o + R\dot{\beta}_o + \frac{1}{C_{dl}}\Delta\theta = T_L \qquad [4.3]$$

where

J_o = mass moment of inertia about point o (kg-m^2),

R = bearing resistor (N-s-m/rad),

T_L = the load torque (N-m),

$1/C_{dl}$ = non-linear stiffness (N-m/rad),

β = rotation of shaft (rad), and

$\Delta\theta$ = angular twist from tractor to harvester input shaft (includes backlash in tractor transmission and spline couplings) (rad).

The parallel axis theorem was used to determine the moment of inertia (J_o) as a function of whirl rotation (Figure 7). The mass moment of inertia about point O (geometric center of shaft) is then,

$$J_o = \bar{J} + m[r(t)]^2 \qquad [4.4]$$

where

J_o = mass moment of inertia (kg-m^2),

$\bar{J}$ = mass moment of inertia about point E (kg-m^2),

m = mass of shaft (kg), and

r(t) = distance between O and E (m).

Inserting J_o into Eqn. (4.3) gives a time varying value of the shaft moment of inertia. Derivation of the r(t) function is the critical component to determining the inertial term. r(t) is determined by an elliptical path with its center at the axis of rotation (Figure 7). The function of r(t) can be determined from vector addition of the distance from point O to A ($\vec{OA}$) and from point A to E ($\vec{AE}$).

$\vec{AE}$ is the distance e, which represents the eccentricity of the mass center to the geometric center of the shaft. $\vec{AE}$ is expressed in vector form as

$$\vec{AE} = (e\cos\omega t)\hat{i} + (e\sin\omega t)\hat{j} \qquad [4.5]$$

where

e = eccentricity of the shaft mass (m),

ω = shaft rotation velocity (rad/s),

i = x-direction unit vector, and

j = y-direction unit vector.

$\vec{OA}$ is the distance from the geometric center of the shaft mass at rest to the geometric center of the shaft as it is whirling. $\vec{OA}$ is calculated by,

$$\vec{OA} = (U\cos\dot{\gamma}t)\hat{i} + (V\sin\dot{\gamma}t)\hat{j} \qquad [4.6]$$

where

U = maximum shaft lateral deflection in the x direction (m),

V = maximum shaft lateral deflection in the y direction (m), and

$\dot{\gamma}$ = shaft whirl velocity (rad/s).

r(t) is then

$$r(t) = (u + e\cos\omega t)\hat{i} + (v + e\sin\omega t)\hat{j} \qquad [4.7]$$

where

u = U cos $\dot{\gamma}$t, and

v = V sin $\dot{\gamma}$t.

The unknown quantities to be determined, U,V and $\dot{\gamma}$, are functions of the support stiffness, secondary couple, and mass unbalance. Parameter determination will be discussed in Chapter 5.

The bond graph model of the mechanical drive (u-joint driveline and V-belt drives) from the tractor PTO to the pump driveshaft of the multiple-3 and multiple-2 pump is shown in Figure 8. The model does not allow the load from the harvester to affect the output from the tractor, making the tractor an ideal angular velocity source. The tractor engine had much more power output potential than the power requirement of the harvester, thus it is unlikely that harvester load fluctuation will significantly affect the rotational velocity of the PTO. The flow source (Sf) represents the angular velocity output at the tractor PTO.

The flow source (Sf) input is variable due to the fluctuating velocity of the tractor crankshaft, caused by acceleration of the crankshaft as each cylinder fires. For a six-cylinder, four stroke diesel engine, combustion occurs three times each crankshaft revolution. Since the PTO shaft rotates at one-half crankshaft speed, there are a total of six pulses each revolution of the PTO shaft. Torsional vibration of the PTO shaft has a frequency six times the rotational frequency.

A modulated transformer (MTF) models the relationship between input and output angular velocity and torque at a joint angle. Eqn. (4.2) is used as the transformer modulus (α) to calculate fluctuating velocity created by the u-joints. The modulus, is

$$\alpha = \frac{\omega_{his}}{\omega_{PTO}} = \frac{\cos\theta_1 \cos\theta_2}{(1 - \sin^2\beta_1 \sin^2\theta_1)(1 - \sin^2\beta_2 \sin^2\theta_2)} \qquad [4.8]$$

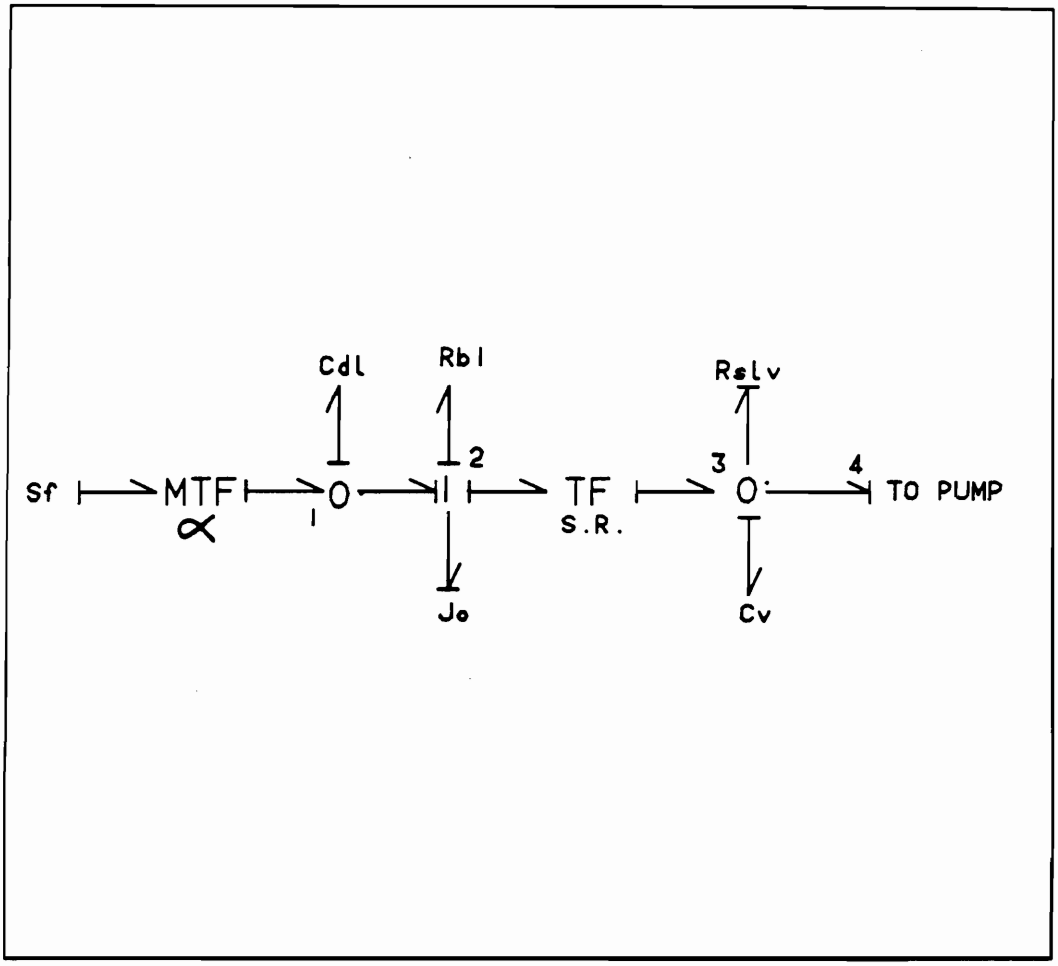

Figure 8. Bond graph model of the input drive sub-model.

0-junction (1) represents the torque input to the V-belts. The angular velocity input at 0-junction (1) is

$$\omega_{in} = \omega_{PTO}\alpha \qquad [4.9]$$

where

ω_{in} = angular velocity at harvester input shaft (rad/s),

ω_{PTO} = angular velocity at PTO (rad/s), and

α = modulus from Eqn. [4.3].

The capacitor, C_{dl} [Eqn. (4.2)], is the compliance and includes the shaft and V-belt effects. The resistor represents slippage of the V-belts on the sheaves which results in a reduction of rotational velocity. 1-junction (2) represents the angular velocity input to the V-belts. J_o is the inertia of the connecting shaft [Eqn. (4.4)]. The value for J_o is calculated from estimated parameters U,V, and $\dot{y}$. The resistor (R_{b1}) is a loss term based on bearing friction. TF has a modulus of 2.5, which represents the sheave ratio between the harvester input shaft and the pump driveshaft. Transformer output goes to 0-junction (3) which represents torque input to the pump. The capacitor (C_v) is the pump driveshaft compliance.

4.2.2 Motor/Pump models

A modified version of the Wilson equations was used to model pumps and motors. Wilson's equations were derived based on the following assumptions:

1. clearances between stationary and moving parts is constant,
2. leakage flow through clearances is laminar,
3. coefficient of friction between unlubricated surfaces is constant, and
4. steady-state operation.

4.2.2.1 Slippage Flow

Constant clearances between moving and stationary parts will be investigated first. The coefficient of slip (C_s) is very sensitive to the assumption of constant clearances. Leakage flow through the clearances in the pump or motor was assumed to be flow between a stationary plate (non-moving pump/motor housing) and moving plate (gears or pistons). Making the additional simplifying assumptions, one dimensional flow, zero fluid acceleration, and constant viscosity, results in reduction of the Navier-Stokes momentum equation to

$$\frac{dp}{dx} = \mu \frac{d^2u}{dy^2} \qquad [4.10]$$

where

p = pressure (MPa),

μ = viscosity (N-s/m^2),

u = fluid velocity (m/s),

x = space coordinate in the direction of fluid flow (m), and

y = distance from stationary plate (m).

The definition of shear stress is $\mu\frac{du}{dy}$. Integrating Eqn. (4.10) over the clearance width, h, and using the definition of shear stress produces

$$Q_{sl} = [-\frac{h^3}{12} \mu \frac{dp}{dx} + V\frac{h}{2}]w \qquad [4.11]$$

where

Q_{sl} = flow through passage (m^3/s),

V = velocity of moving plate (gear or piston) (m/s),

h = leakage clearance width (m), and

w = leakage clearance depth (m).

Eqn. (2.1) includes a term where leakage flow is a function of pressure differential and a dimensionless slip coefficient. Wilson (1949) proved that the second term on the right side of Eqn. (4.11) represents output flow which was carried by the moving part (piston or gear). The first term on the right side represents flow loss through the clearance. Equating the slip flow from Eqn. (2.1) to the first term on the right side of Eqn. (4.11) defines the slip flow coefficient.

$$C_s = \frac{K_1 h^3}{D_p} \qquad [4.12]$$

where

C_s = pump slip flow coefficient (dimensionless),

K_1 = constant, and

h = width of flow passage (m).

(Motor displacement may be substituted for pump displacement to discuss the motor slip flow coefficient.) The slip coefficient is proportional to the third power of the clearance; consequently, slight changes in h will cause a large change in C_s. Thus, a constant value of C_s may not be adequate to properly predict the performance of pumps and motors over a specified operating range. Although C_s varies with pressure and speed, as a first approximation, it can easily be made a linear function of speed. In addition, for motors with case drains, flow losses may be further differentiated as "external" and "internal" losses. Internal losses are the losses which occur when fluid passes from the high pressure to low pressure line without producing useful energy. External losses result from flow into the casing through clearances. Two loss coefficients were determined separately and included in the flow equation. To complete the flow analysis, an account of the flow loss due to compressibility must be added. By substituting separate flow loss coefficients for the constant flow loss coefficient in Eqn. (2.1) and changing subtraction to addition, the flow equation for a motor becomes

$$Q_m = D_m\omega_m + \frac{\Delta P D_m}{\mu}[C_{si}(\omega) + C_{se}(\omega)] + Q_c \qquad [4.13]$$

where

$C_{si}(\omega)$ = internal loss coefficient as a function of speed,

$C_{se}(\omega)$ = external loss coefficient as a function of speed,

D_m = motor displacement (m^3/rad),

ω_m = motor angular velocity (rad/s),

ΔP = pressure difference across ports (MPa),

Q_c = flow loss from fluid and conductor compliance (MPa), and

μ = fluid viscosity (N-s/m^2).

The motor equations are used to illustrate the loss coefficients. When there is significant back-pressure at the motor outlet port, a separate ΔP for each loss coefficient must be used in Eqn. (4.13). Flow from the motor inlet port to the outlet port, or to the casing, represents two separate pressure differentials for the leakage. Eqn. (4.13) becomes

$$Q_m = D_m\omega_m + \frac{\Delta P_i D_m}{\mu} C_{si}(\omega) + \frac{\Delta P_e D_m}{\mu} C_{se}(\omega) \qquad [4.14]$$

where

ΔP_i = inlet port pressure minus outlet port pressure (MPa), and

ΔP_e = inlet port pressure minus case pressure (MPa).

In the case where the pump or motor does not have an external drain, the external loss coefficient $[C_{se}(\omega)]$ is zero. For variable displacement pumps, flow losses are combined into a single loss coefficient, C_s. Since the charge pump relief flow dumps into the casing to provide a flow of cooling oil, it adds to the external leakage flow. There is no accurate method for quantifying the two flows separately, consequently the external leakage flow cannot be measured and a loss coefficient defined.

Eqn. (4.10) may be directly integrated over the slot clearance, h, by use of two sets of boundary conditions. These boundary conditions specify the velocity of the fluid to be u = 0 at the stationary plate, and u = rω at the moving plate representing the piston or gear. Wilson (1949) integrated Eqn. (4.10) to obtain the shear stress. The drag torque was equal to the shear stress times the area the drag force acted over (wdx) times the radius from the axis of rotation to the centroid of the clearance.

$$T_f = [- \frac{dp}{dx} \frac{h}{2} + \frac{\mu r \omega}{h}] w dx r \qquad [4.15]$$

where

T_f = viscous drag torque (N-m), and

r = distance from axis of rotation to centroid of clearance (m).

The second term on the right side of Eqn. (4.15) represents the torque derived from the flow carried around the gear tooth and does not represent a loss. The first term on the right side of Eqn. (4.10) represents the viscous drag torque from leakage flow. The viscous drag torque is defined in Eqn. (2.2). Equating the viscous drag torques in Eqns. (2.2) and (4.15), and solving for the viscous drag coefficient gives,

$$C_{vd} = \frac{K_2}{h D_p} \qquad [4.16]$$

where

C_{vd} = viscous drag torque coefficient,

K_2 = constant,

h = clearance width (m), and

D_p = pump displacement (D_m for motor) (m^3/rad).

The viscous drag coefficient is inversely proportional to the first power of the clearance, h. Unlike C_s, C_{vd} is not as sensitive to the clearance variation, and a constant value for it may be justified without significantly affecting accuracy.

The third approximation to Wilson's equations will now be examined. As seen from Eqn. (2.2), the torque required to overcome coulomb friction is dependent on the load pressure. Experiments conducted by McCandlish (1981) showed that torque loss was non-linearly dependent on speed and pressure. Assuming that the non-linear torque loss is basically a function of coulomb friction, a functional relationship for the coulomb friction coefficient is necessary. The coulomb friction coefficient is assumed to be a function of motor speed over the range from start-up to steady-state. Starting friction is high and reduces to running friction, which may vary with speed. In this study, it is assumed that the running friction coefficient changes with speed, and experimental studies were undertaken to define these functions.

Including inertial effects, torque output from a hydraulic motor is the sum five terms:

$$T_o = T_1 - T_2 - T_3 - T_4 - T_5 \qquad [4.17]$$

where

T_o = torque output from motor (N-m),

T_1 = torque produced hydraulically (N-m),

T_2 = torque loss caused by coulomb friction (N-m),

T_3 = torque loss caused by viscous drag (N-m),

T_4 = torque required by inertia (N-m), and

T_5 = motor torque constant (N-m).

4.2.2.2 Torque Terms

Torque output based on pressure difference and displacement is

$$T_1 = \Delta P D_m \qquad [4.18]$$

where

ΔP = outlet port pressure minus inlet port pressure (MPa), and

D_m = motor displacement (m^3/rad).

T_2 is the torque required to overcome friction between metal parts, and is defined by,

$$T_2 = \Delta P D_m C_f(\omega) \qquad [4.19]$$

where

$C_f(\omega)$ = running coulomb friction coefficient (dimensionless), and

ω = rotational speed of motor shaft (rad/s).

T_3 is the torque required to overcome viscous losses. The viscous loss coefficient is assumed to remain constant, and T_3 is defined as

$$T_3 = C_{vd}\mu\omega D_m \qquad [4.20]$$

where

C_{vd} = viscous drag coefficient (dimensionless), and

μ = viscosity (N-s/m^2).

T_4 represents the torque required to overcome the inertia of the motor. The total inertial load includes the moving parts in the motor, the fluid inertia, and the inertia of the load on the motor shaft. T_4 is defined as,

$$T_4 = J\frac{d\omega}{dt} \qquad [4.21]$$

where

J = total inertia (motor, fluid, and load) (kg-m^2), and

ω = rotational velocity (rad/s).

The sign of the inertial term is dependent on the characteristics of the inertial load. T_5 equals the constant torque term, T_c, which is the torque loss not accounted for by viscous drag, coulomb friction, and inertia. Schlosser (1961) attributed this loss to fluid flow dynamics, which is a function of fluid density.

4.2.2.3 Motor Models

Two motor bond graph models were developed to represent the hydraulic motors on the harvester. Open circuit hydraulic systems were modeled without including return line characteristics. Return lines should not significantly affect the torque output or flow through the motor, as they were sized to minimize back pressure. Return line characteristics were included in the model of closed circuit hydraulic systems. Pressure always exists in these return lines due to action of the charge pump and charge pump relief valve. When pressure in the return line drops below the charge relief setting (usually 1.0 Mpa) flow enters the return line to compensate for leakage; consequently, pressure is always slightly greater than the relief setting.

4.2.2.3.1 Open Circuit Motor Model

The bond graph model shown in Figure 9 was used for the motors in open circuit systems. Input to the motor model represents pressure and flow at the input port of the motor. 0-junction (12) represents the pressure at the motor input and 1-junction 13 represents the angular velocity of the

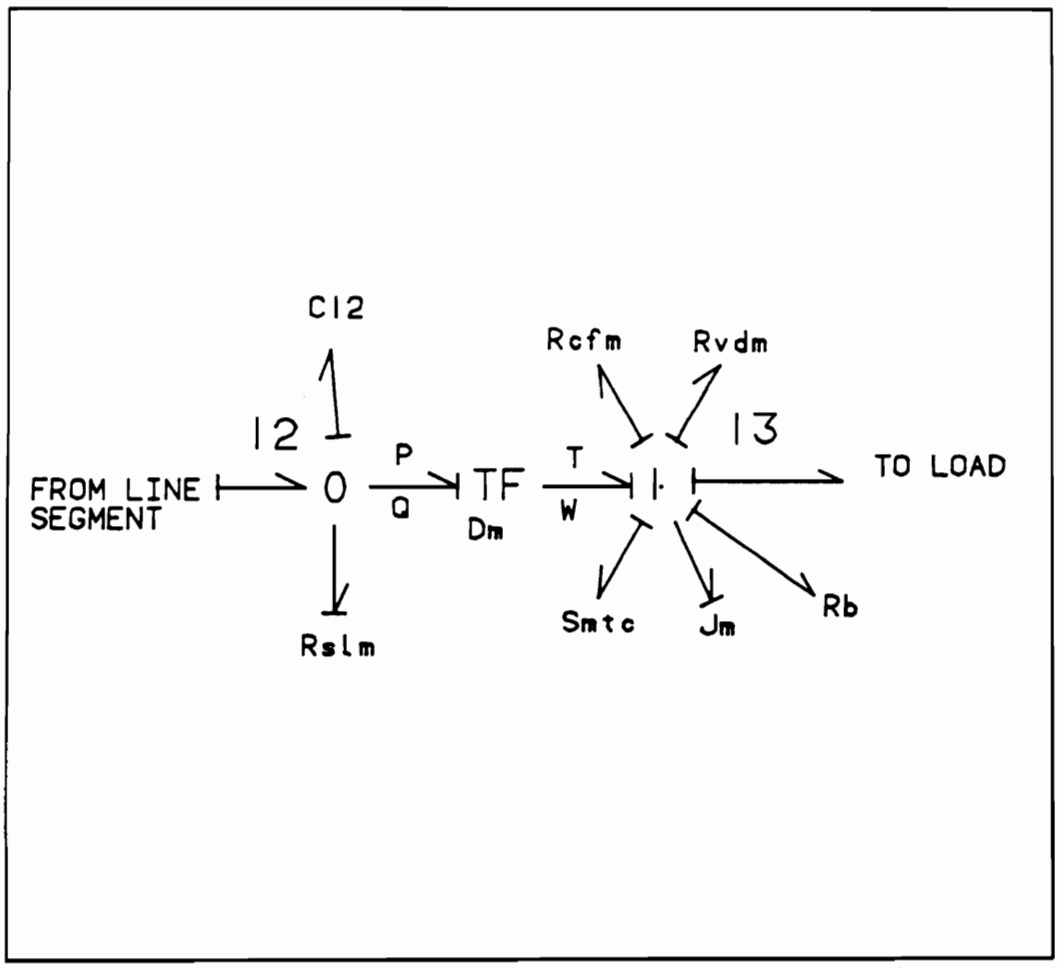

Figure 9. Bond graph model of a open circuit motor.

motor driveshaft. Motor flow losses are bonded to 0-junction (12), while motor torque losses are bonded to 1-junction (13). The two junctions are coupled together by an ideal power transformer with modulus equal to the motor displacement, which converts the hydraulic power to mechanical power.

The causality of the resistor representing flow loss (R_{slm}) at 0-junction (12) dictates that flow rate is output and pressure is input; consequently, slip flow is

$$Q_{slm} = \frac{1}{R_{slm}} \Delta P \qquad [4.22]$$

where

Q_{slm} = motor slip flow (cm^3/s),

R_{slm} = flow resistance (MPa s/cm^3), and

ΔP = pressure difference across motor (MPa).

R_{slm} represents the internal cross-port leakage due to flow slippage, and can be related to the slip coefficient

$$1/R_{slm} = C_s \frac{D_m}{\mu} \qquad [4.23]$$

where

C_s = motor slip flow coefficient (dimensionless),

μ = viscosity (N-s/m^2), and

D_m = motor displacement (m^3/rad).

The dynamic torque equation, Eqn. (4.17), is implemented at 1-junction (13). Torque output is equal to torque input minus losses and inertial effects. Because of the causality, angular velocity

was input to the linear resistor terms. Coulomb friction was represented by resistor R_{cfm}. Torque loss due to coulomb friction is

$$T_{cfm} = R_{cfm}\Delta PD_m \qquad [4.24]$$

where

R_{cfm} = motor coulomb friction resistance (dimensionless).

Torque developed by pressure (ΔPD_m) was input to the resistor to determine the coulomb friction coefficient. R_{vdm} is a resistor representing the viscous drag loss, and is related to the viscous drag loss coefficient by

$$R_{vdm} = C_{vd}\mu D_m \qquad [4.25]$$

where

C_{vd} = motor viscous drag coefficient (dimensionless).

Torque loss due to viscous friction is

$$T_{vdm} = R_{vdm}\omega \qquad [4.26]$$

where

ω = angular velocity of motor (rad/s).

The inertial term (J_m) bonded to 1-junction (13) represents the inertia of the internal rotating mass inside the motor, and inertia of the sprocket and load connected via a chain drive. The source element (S_{mtc}) represents the motor torque constant, T_c, defined in Eqn. (4.17). Torque output at this junction is the torque required to power the load coupled to the motor. R_b is the frictional losses from the motor bearings and bushings.

4.2.2.3.2 Closed Circuit Motor Model

The motor bond graph for a closed circuit system (Figure 10) was used for the gathering chains and conveyor motors. Pressure at the inlet and outlet ports of the motor are modeled by 0-junction ⑲ and 0-junction ㉑ , respectively. Bonds are connected to these junctions leading to and from the cross-over relief valve. Capacitance values (C_{19} and C_{21}) at each port model fluid compressibility and hose expansion characteristics.

Internal leakage (R_{inm}) is modeled by a flow path between 0-junctions ⑲ and ㉑ . 1-junction ⑳ connects this flow path, and flow at this junction is the leakage flow. The flow leakage is determined by the resistor, R_{inm}, defined by Eqn. (4.23). External leakage flow is determined by R_{exm} at 0-junction ⑲ . External leakage is included only for the gathering chains motors since they have a case drain line to release this flow back to the reservoir. Useful flow input to the motor is represented by 1-junction ㉒ .

Torque losses and inertial effects at 1-junction ㉓ are modeled identically for both open and closed circuit systems. Bonding of elements at 1-junction ㉓ is identical to the bonding previously discussed for 1-junction ⑬ in Figure 9.

4.2.2.4 Pump Models

There are two types of pumps used on the harvester hydraulic circuits, variable displacement axial piston pumps and external gear pumps. Variable displacement axial piston pumps supply flow to the gathering chains and cross conveyor circuits. Individual external gear pumps supply flow to the flipper, disk-cutter, and accumulator DCV, giving a total of five pumps on the harvester.

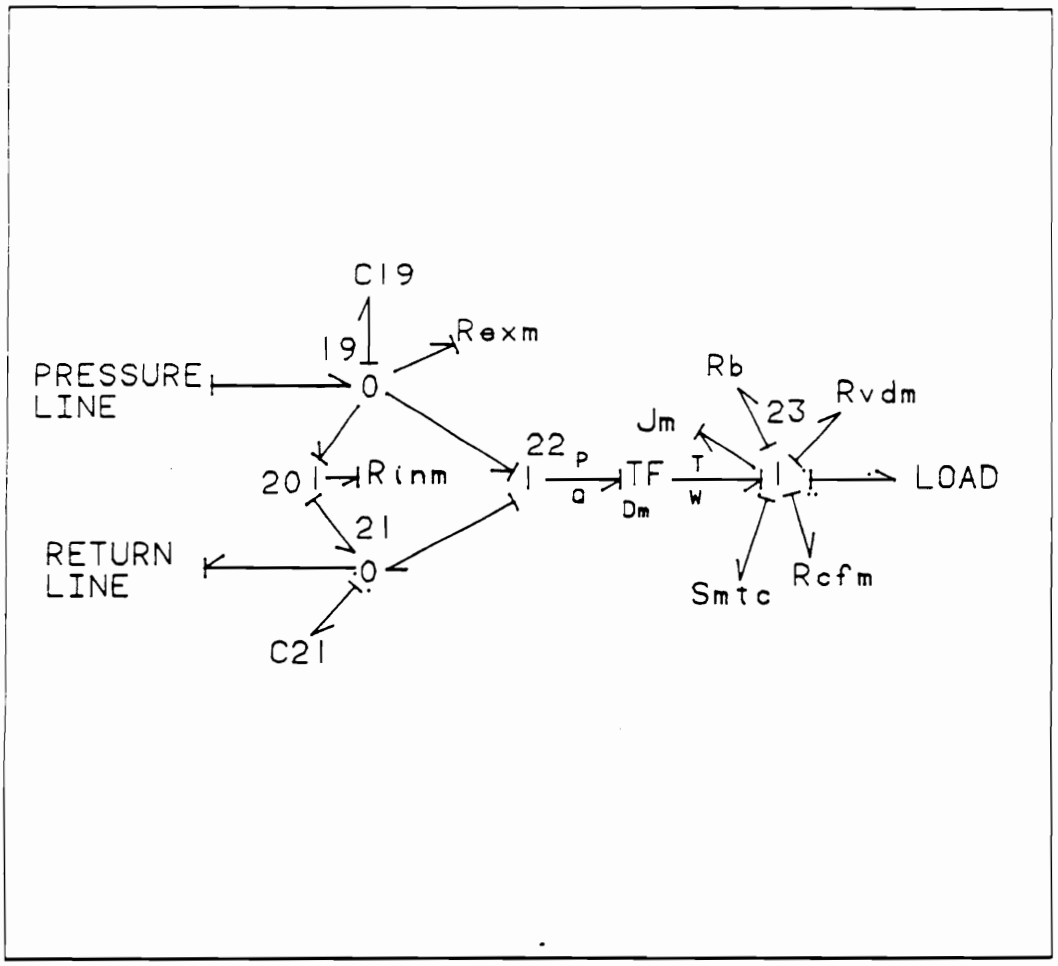

Figure 10. Bond graph model of a closed circuit motor.

4.2.2.4.1 Piston Pumps

The internal components of a piston pump are shown schematically in Figure 11. The pump has two pump units in the same housing, the main pump and charge pump.

The variable displacement unit consists of nine pistons which ride on a swashplate as the entire assembly revolves around the pump driveshaft. The pistons displace a volume of fluid proportional to the swashplate angle. The pump driveshaft also powers the charge pump. Charge pump flow is used to replenish fluid flow that leaks into the pump casing. Any flow not needed to replenish leakage is dumped across the charge pump relief valve into the pump casing and drains back to the reservoir, thus providing a flow of cooling fluid.

Figure 12 shows the bond graph model representation of a variable displacement pump. Input to the variable displacement model is coupled to the output from the drive input sub-model (Figure 8) discussed in Section 4.2.1. Output is coupled to line segment models which connect the pump to the cross-over relief valve.

1-junction (4) represents the angular velocity of the pump driveshaft. Pressure in the pressure and return lines of the pump are represented by 0-junction (6) and 0-junction (8), respectively. The forward and return line pressures are bonded to 1-junction (5), which models the ideal flow output from the pump without losses. Cross-port leakage flow due to slippage in the pump is modeled at 1-junction (7) which connects 0-junction (6) to (8).

A modulated transformer (MTF), representing the conversion from mechanical power to fluid power bonds 1-junction (4) to 1-junction (5). Modulus of the MTF is variable since the pump displacement is changed by increasing (more flow) or decreasing (less flow) pump swashplate angle.

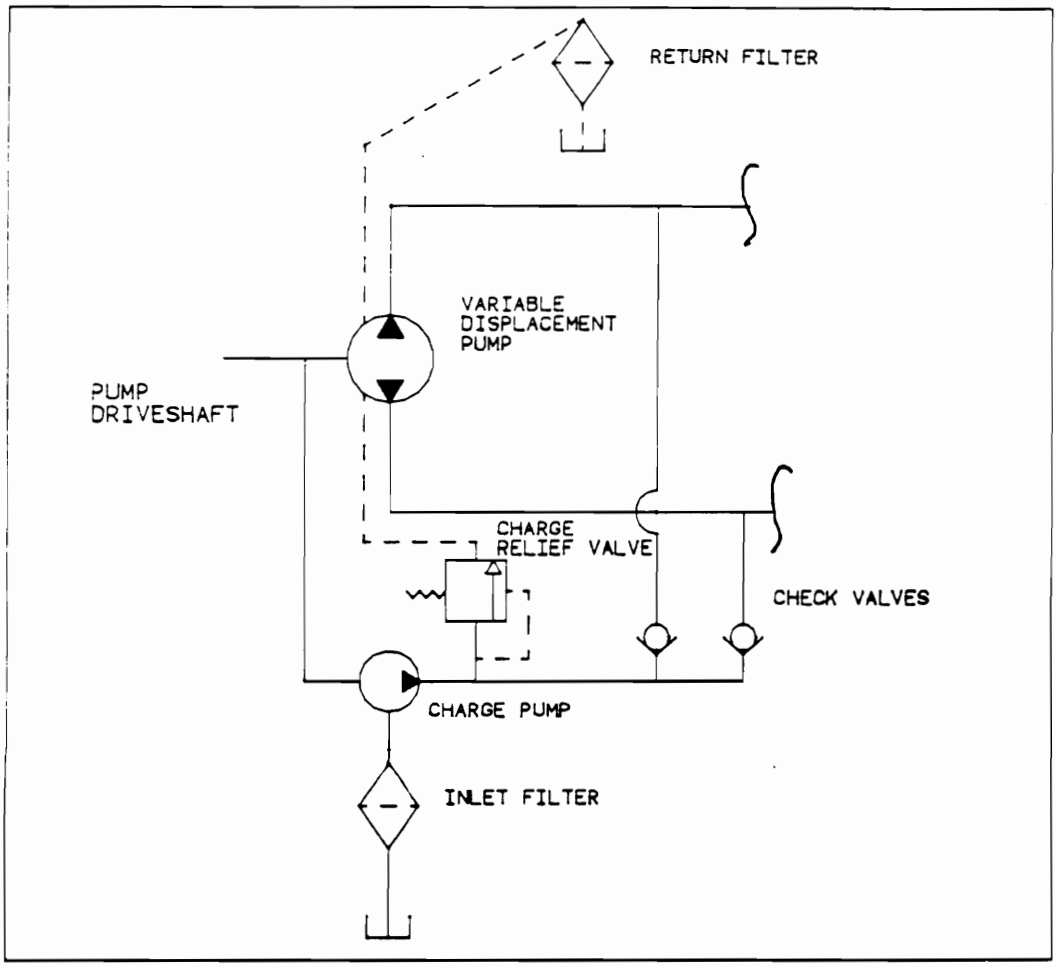

Figure 11. Hydraulic schematic of variable displacement axial piston pump.

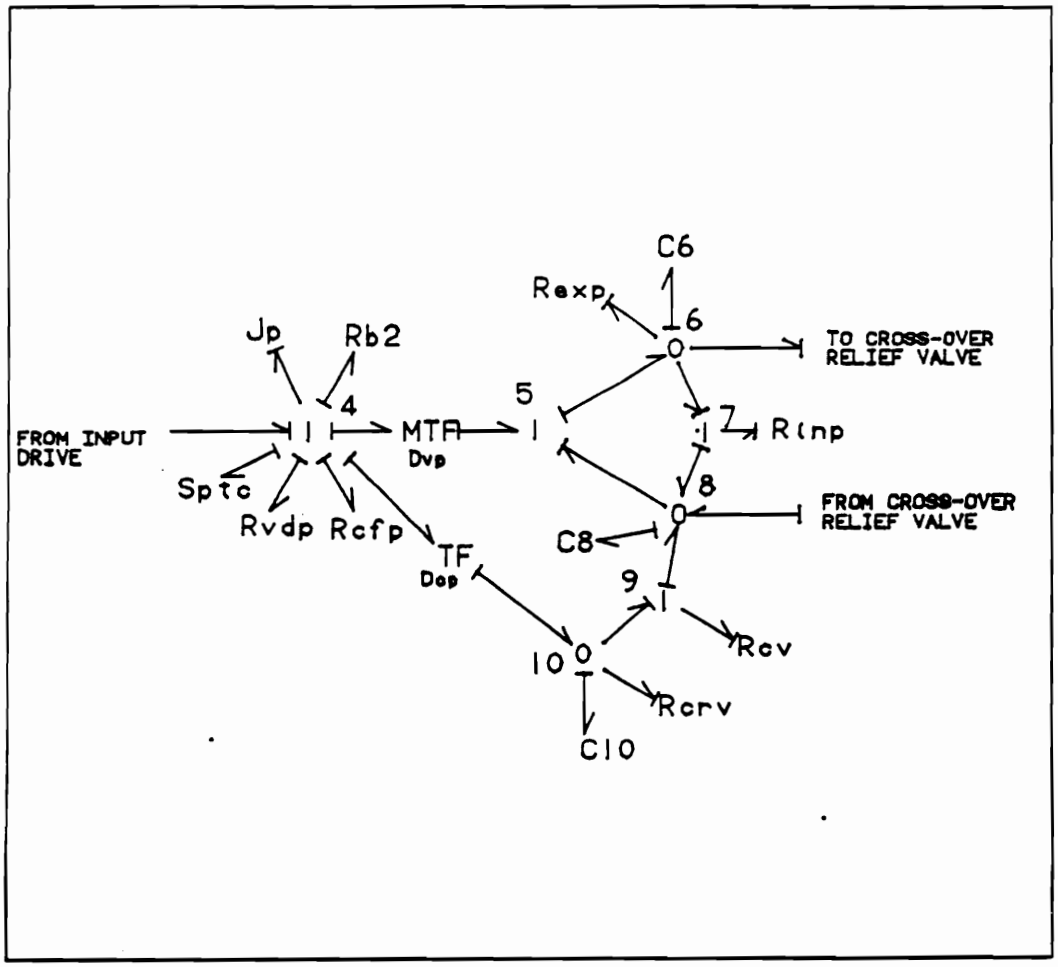

Figure 12. Bond graph model of a variable displacement axial piston pump.

1-junction ④ is also coupled through another transformer to 0-junction ⑩ . 0-junction ⑩ models pressure at the output of the charge pump. Flow from the charge circuit to the return line of the main hydraulic system is determined at 1-junction ⑨.

Torque losses at 1-junction ④, due to coulomb friction (R_{cfp}), viscous drag (R_{vdp}), inertia (J_p), and pump torque constant (S_{ptc}), are modeled. Both the piston pump and charge pump are driven by the pump driveshaft; consequently, total torque input to the variable displacement pump (from the source input) is the torque to power each pump, plus torque to overcome losses. The torque equation becomes

$$T_{in} = T_{cp} + T_{vp} + T_{cfp} + T_{vdp} + T_{Jp} + T_b + T_{ptc} \qquad [4.27]$$

where

T_{in} = torque input to 1-junction ④ (N-m),

$T_{vp} = P_{vp}D_{vp}$ = torque to rotate piston pump (N-m),

$T_{cp} = P_{cp}D_{cp}$ = torque to rotate charge pump (N-m),

$T_{vdp} = R_{vdp}\omega_{vp}$ = torque to overcome viscous drag (N-m),

$T_{cfp} = R_{cfp}P_{vp}D_{vp}$ = torque to overcome coulomb friction (N-m),

T_{Jp} = inertial torque = J $d\omega/dt$ (N-m),

T_b = bearing friction torque (N-m), and

T_{ptc} = pump torque constant (N-m).

Torque to overcome viscous drag, coulomb friction, and inertial effects are discussed in detail in Section 4.2.2.2. S_{ptc} includes the torque required to turn the gear pumps mounted on the auxiliary mounts of the piston pumps.

1-junction ⑤ is a constant flow port which models the flow output and pressure differential across the pump ports. The pressure in the main pump (P_{vp}) is the difference of the pressure at 0-junction ⑥ (pressure to move load) and 0-junction ⑧ (pressure in the return line),

$$P_{vp} = P_6 - P_8 \qquad [4.28]$$

where

P_6 = output port pressure at 0-junction (6) (MPa), and

P_8 = return port pressure at 0-junction (8) (MPa).

Torque from the transformer is then $D_{vp}\ P_{vp}$. Therefore, the bond leading from 1-junction (5) represents the hydraulic power leaving the pump, and the bond leading to 1-junction (5) represents the hydraulic power returning to the pump from the return line.

The pressure at 0-junction (6) is caused by the load on the hydraulic motor. C_6 represents the line compliance from the pump output to the cross-over relief valve. Pressure at 0-junction (8) is created by the charge circuit output. C_8 represents the line compliance in the return line from the cross-over relief valve to the pump inlet port. Flow leading from the bond is the ideal flow from the pump minus losses to external and internal leakage. The flow equation at 0-junction (6) is

$$Q_{out} = Q_5 - Q_{\exp} - Q_7 - Q_c \qquad [4.29]$$

where

Q_{out} = flow to the load (cm^3/s),

Q_5 = ideal flow developed by pump (cm^3/s),

Q_{exp} = external leakage to the casing (cm^3/s),

$Q_7 = Q_{inp}$, the internal cross-port leakage (cm^3/s), and

Q_c = flow loss due to combined fluid and line compliance (cm^3/s).

Internal leakage is modeled by a resistor (R_{inp}) bonded to 1-junction (7), and external leakage by a resistor, R_{exp}, bonded to 0-junction (6).

Pressure developed by the charge pump is the pressure at 0-junction (10). Pressure builds until the charge relief valve opens to dump flow to the casing. The relief valve is modeled as a non-linear resistor (R_{crv}), which is closed until the set pressure is reached. A capacitor (C_{10}) bonded to this junction models the fluid compressibility inside the charge pump.

Flow to replace leakage from the main circuit enters through 1-junction (9). R_{cv} is a non-linear resistor representing the flow characteristics of the check valve. The check valve opens when there is a pressure differential between the charge pump circuit and return. Flow can travel in only one direction which prevents return line flow from entering the charge pump circuit.

4.2.4.4.2 Gear Pumps

Gear pumps used on the harvester are external gear type with 11 teeth per gear. Two gears intermesh to pump the fluid. One gear is driven by the pump driveshaft and the other is an idler. Fluid enters the pump at the static pressure head from the reservoir, and is pumped by catching it in the space between the gear teeth and housing and carrying it around the housing to the outlet port. Figure 13 gives the bond graph model for a gear pump.

1-junction (4) is identical to the description given for the input to the piston pump (Figure 12) with the exception that torque is required only for a main pump, there is no charge pump. The transformer (using the pump displacement) determines the relationship between mechanical and hydraulic power.

Flow from the reservoir is assumed to enter the pump at atmospheric pressure. Static head in the reservoir is small compared to hydraulic system pressure. Therefore, the pressure at 0-junction (5) is the line pressure at the outlet port of the pump. Flow output from the pump modeled at 0-junction (5) is

$$Q_{out} = Q_{in} - Q_{slp} - Q_c \qquad [4.30]$$

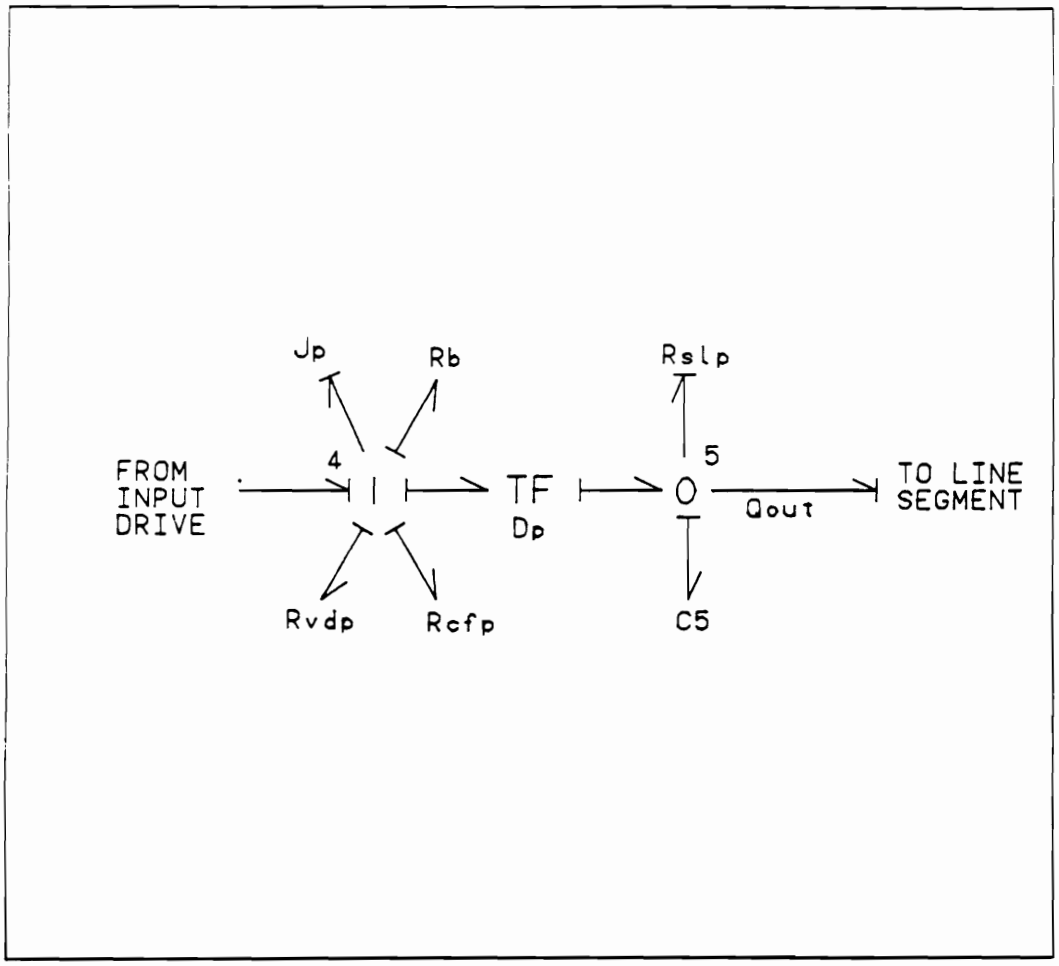

Figure 13. Bond graph model of an external gear pump.

where

Q_{out} = flow rate to the load (cm^3/s),

Q_{in} = $D_p\omega_4$, = ideal flow rate developed by pump (cm^3/s),

Q_{slp} = slip flow rate = $R_{slp}P_5$ (cm^3/s), and

Q_c = flow rate change due to compressibility (cm^3/s).

Ideal flow (Q_{in}) developed by the pump is determined by the transformer. Slip flow (Q_{slp}) is defined as cross-port leakage flow.

4.2.3 Cylinders

There are four hydraulic cylinders on the harvester. Each pair of cylinders is connected in parallel. The following discussion uses the symbols for flow, pressure, and loss coefficients shown in Figure 14. The cylinder is modeled for extension only.

Orifice flow is assumed through the passage around the cylinder head. Flow loss can be calculated as

$$Q_L = C_K\sqrt{(P_1 - P_2)} \qquad [4.31]$$

where

Q_L = leakage flow around cylinder head (cm^3/s),

C_k = orifice coefficient (dimensionless),

P_1 = cap end pressure (MPa), and

P_2 = rod end pressure (MPa).

Flow to produce cylinder extension will then be

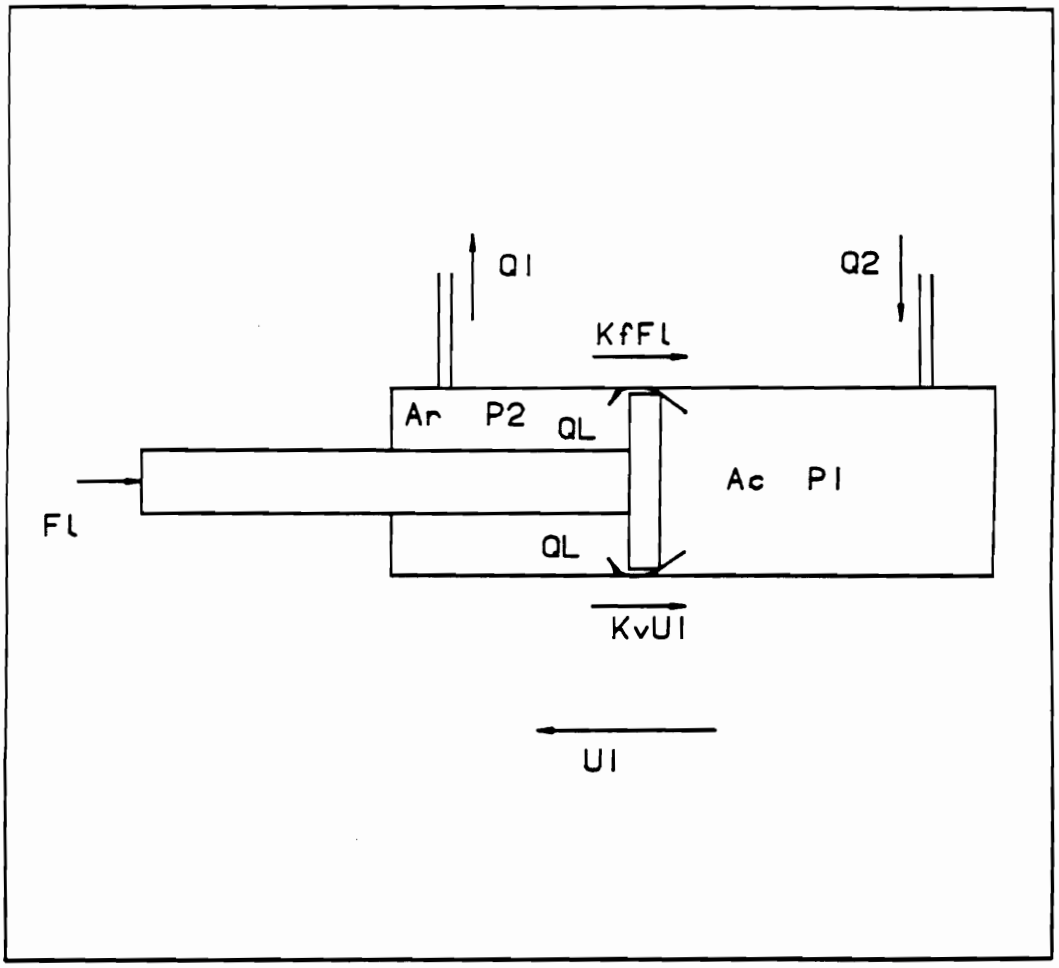

Figure 14. Cylinder with accompanying nomenclature and reacting forces.

$$U_1 A_c = Q_1 - Q_L \qquad [4.32]$$

where,

U_1 = velocity of cylinder rod (m/s),

A_c = cap end area (mm^2),

Q_1 = flow through cylinder (cm^3/s), and

Q_L = leakage flow around cylinder head (cm^3/s).

Flow and force losses are load dependent. From Figure 14, the force to extend a cylinder having back pressure is the sum of the load force (F_L), a frictional loss term ($K_{cfc}F_l$), a viscous loss term ($K_{vdc}U$), and the back pressure force (P_2A_r). In equation form,

$$P_1 A_c = F_L + K_{cfc}F_L + K_{vdc}U_1 + P_2 A_r \qquad [4.33]$$

where

P_1 = cap end pressure (MPa),

A_c = cap end area (mm^2)

F_L = load on the cylinder rod (N),

K_{vdc} = viscous drag coefficient for cylinder (N/s),

K_{cfc} = coulomb friction coefficient for cylinder (dimensionless),

U = cylinder rod linear velocity (m/s),

P_2 = back pressure (MPa), and

A_r = rod end area (mm^2).

The cylinder bond graph model representing the dynamic characteristics is shown in Figure 15. Fluid pressure is represented by 0-junctions, and rod velocity by a 1-junction.

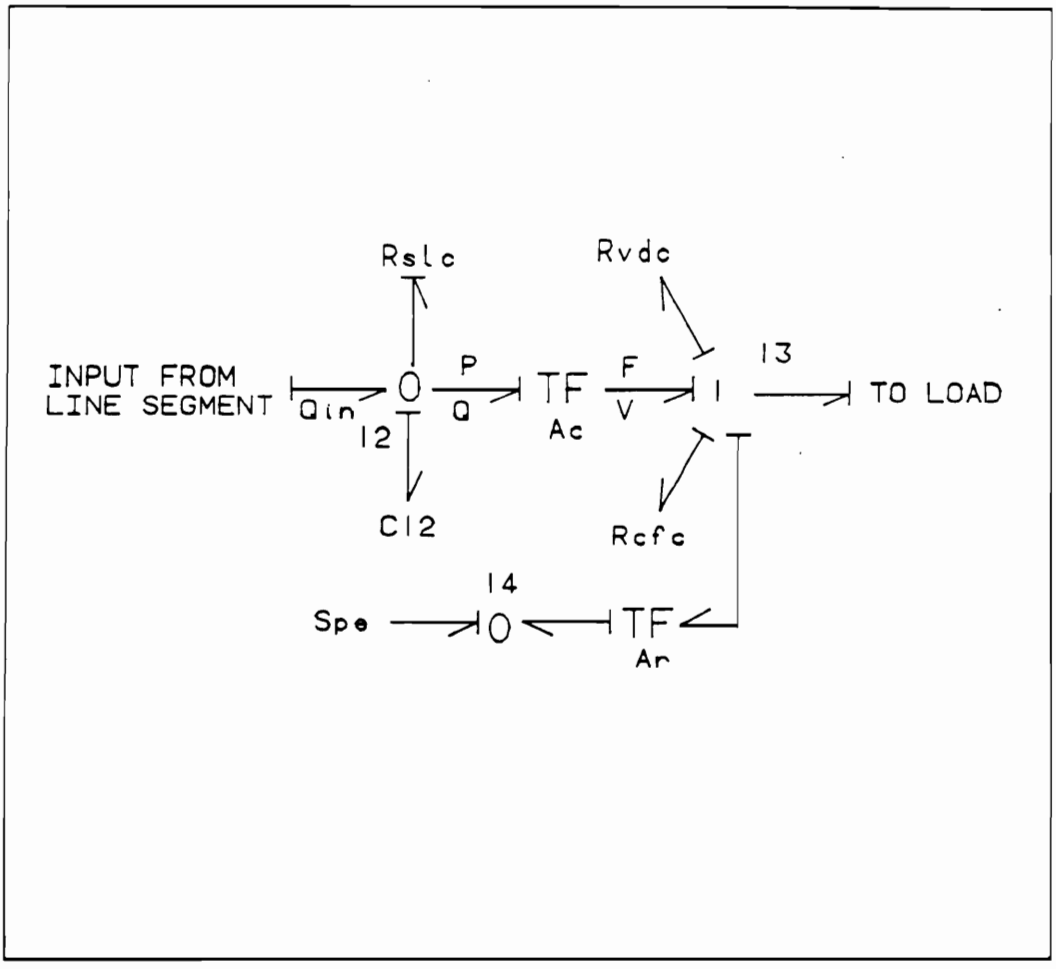

Figure 15. Bond graph model of the hydraulic cylinder.

Pressure entering the cap-end of the cylinder is determined at 0-junction (12) . This junction is coupled to 1-junction (13) through a transformer, with modulus equal to the cap end area (A_c). Linear velocity at 1-junction (13) is the rod speed during extension.

0-junction (14) is bonded to 1-junction (13) through another transformer. This transformer converts mechanical power back to hydraulic power to represent fluid exiting the return of the cylinder. Transformer modulus is the rod end area (A_r).

Slippage flow around the cylinder head and fluid compressibility are modeled at 0-junction (12) . Useful flow to move the load is

$$Q_{Load} = Q_{in} - Q_{slc} - Q_c \qquad [4.34]$$

where

Q_{Load} = useful flow rate (cm^3/s),

Q_{in} = flow rate input to cylinder (cm^3/s),

Q_{slc} = slip flow rate of cylinder (cm^3/s), and

Q_c = flow rate change due to compressibility (cm^3/s).

Flow loss due to compressibility is modeled by capacitor C_{12}, whose value is based on the fluid bulk modulus. Slip flow is determined by the resistor, R_{slc}, which is numerically equal to C_k from Eqn. (4.31), assuming flow loss is proportional to the square root of pressure.

Available force to move the load was defined by Eqn. (4.33). The bond graph models this equation at 1-junction (13) . As shown in Figure 15, the force equation at 1-junction (13) is

$$F_{in} = F_L + F_{cfc} + F_{vdc} + F \qquad [4.35]$$

where

F_{in} = $P_{12}A_c$ = force developed by fluid pressure (N),

F_L = force to move load (N),

$F_{cfc} = K_{cfc}F_L$ = force to overcome coulomb friction (N),

$F_{vdc} = K_{vdc}U$ = force to overcome viscous drag (N), and

$F_{\cdot} = (P_{14}A_r)$ = force resulting from back pressure (N).

Rod inertia is added to the load inertia and is modeled with the load sub-model.

4.2.4 Valve Models

There are two main valve types used in the harvester hydraulic system. A 3-section directional control valve (DCV) is used to control actuators which fill and dump the accumulator, and relief valves are used to protect the system from overload conditions that occur due to blockage of fluid flow or an actuator overload.

The DCV used to actuate the accumulator is a 3-position, 4-way, open center, 3 section valve. When the valve is in the neutral position, flow goes through the valve body to the return line and back to the reservoir. When the valve is shifted, the supply flow is diverted to the load and the actuator return is connected to the reservoir.

A 1-section DCV bond graph model is shown in Figure 16. Input to the DCV model comes from a line segment which connects the pump to the DCV, and output goes to a line segment which joins the DCV to an actuator.

Pressure drop through the valve was not considered; only control over flow direction was modeled. 0-junction (7) represents the pressure at the inlet to the DCV. 1-junction (8) is bonded to 0-junction (7), and models the flow rate when the valve is in its neutral position, i.e. flow is directed back to

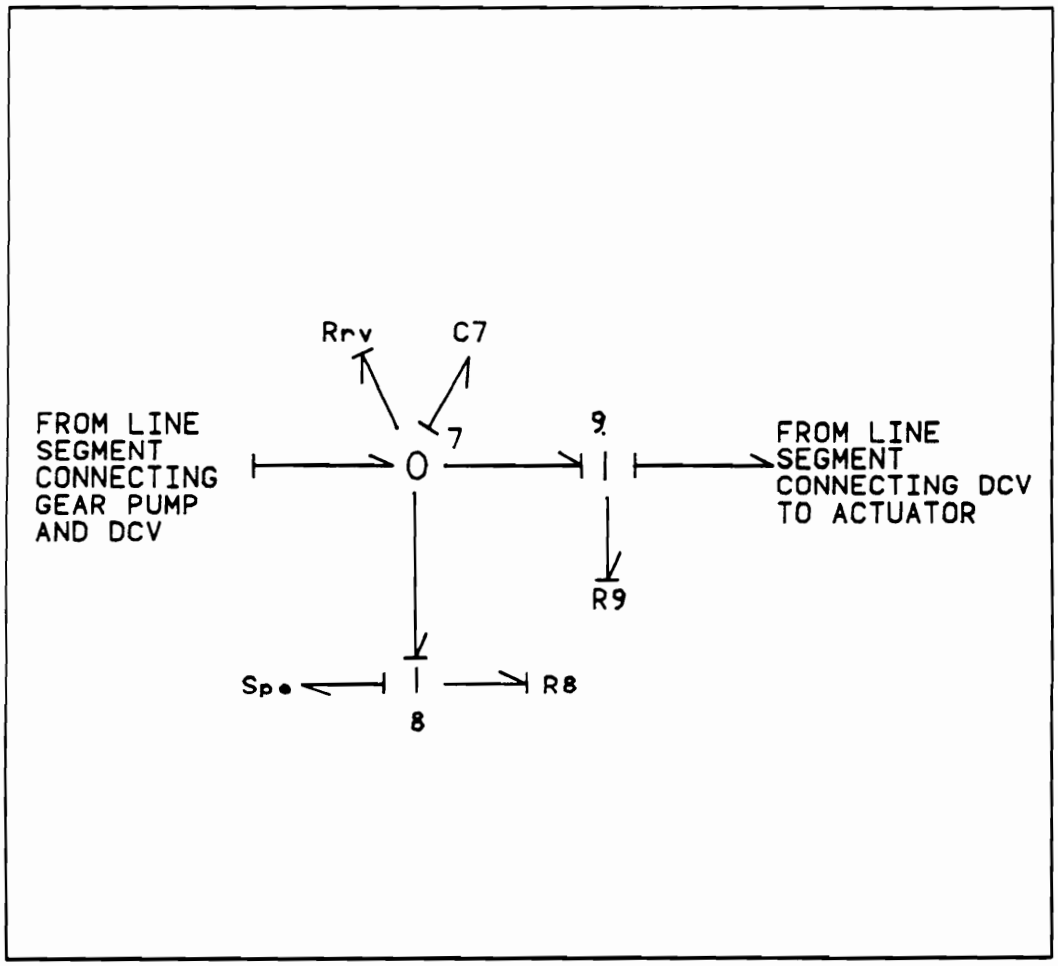

Figure 16. Bond graph model of 1-section DCV.

the return line. 1-junction (9), also bonded to 0-junction (7), models the flow which goes to the actuator when the valve is shifted.

The resistance at 1-junction (8), R_8, acts as an on/off switch. While the valve is in the neutral position, resistance is small, and flow can pass through the junction to the return. At the same time R_9 is very large, preventing flow from passing through to the load circuit. Once the valve is shifted, R_8 becomes large and R_9 becomes small, and flow is directed to the actuator.

The DCV has an integral relief valve, which is modeled at 0-junction (7) by a resistor, R_{rv}. The resistor is modeled such that flow output occurs when the pressure at the junction reaches the relief valve setting. The capacitor in the DCV bonded to 0-junction (7), C_7, represents the capacitance of the inlet and outlet line segment.

A cross-over relief valve is used in the gathering chains and cross-conveyor circuits. The cross-over relief valve has two relief valves which can dump fluid from the pressure line to the return line. Either side of the loop can be the pressure side, depending on the swashplate setting, thus two relief valves are needed.

The bond graph representation of a cross-over relief valve is shown in Figure 17. 0-junctions (13) and (16) are constant pressure ports which represent the pressure in the pressure and return line, respectively. Flow can pass through 1-junctions (14) and (15). Flow is determined by the resistors (R_{crv}) at these junctions. These resistors are non-linear 1-port elements, and are set to open once pressure reaches the relief setting. The capacitors, C_{13} and C_{16}, model fluid and line compliance.

4.2.5 Line Segments

Line segments are used to represent the conductor and fluid characteristics. Each segment of a fluid line contains a line resistance, fluid and line compliance, and fluid inductance. Hydraulic lines may

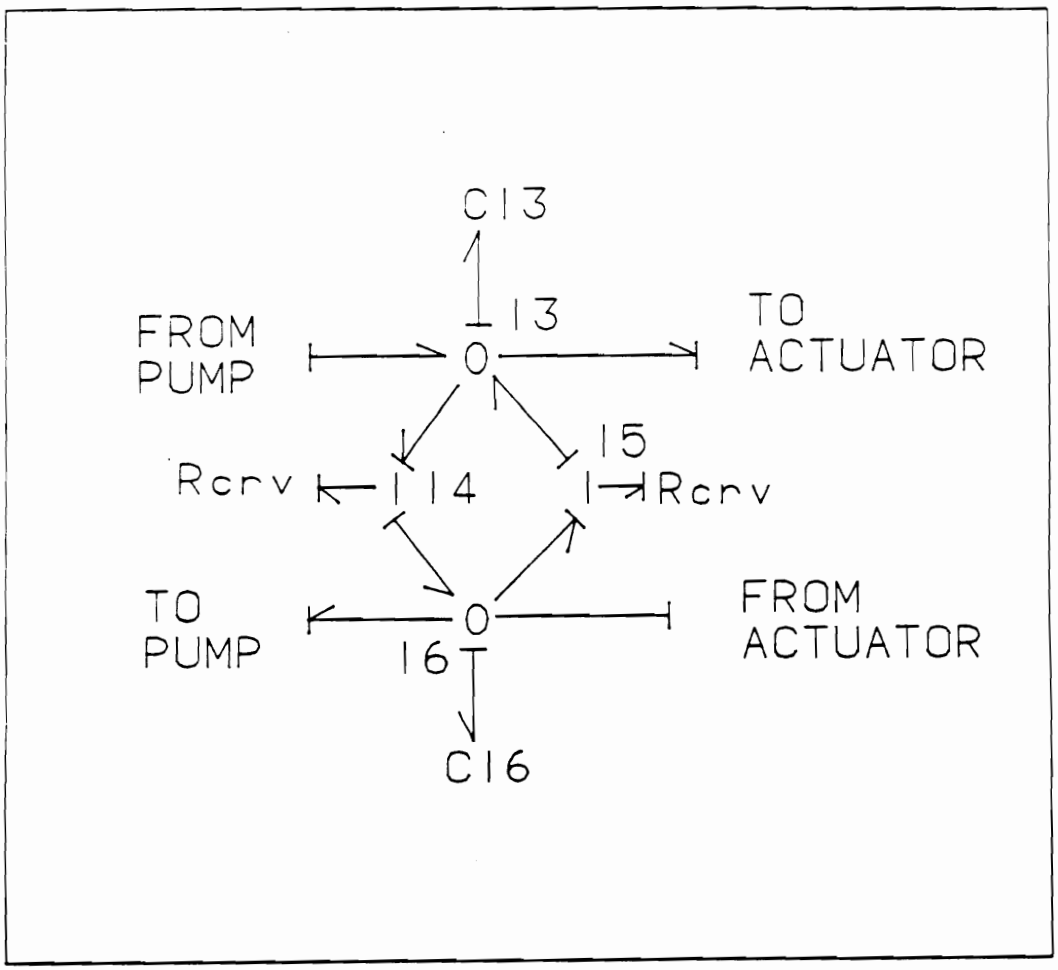

Figure 17. Bond graph model of cross-over relief valve.

be modeled as distributed parameter systems, or as lumped parameter systems. A lumped parameter model is simpler, however it does not model high frequency oscillations that may be of importance.

Modal analysis can be employed to analyze the hydraulic lines as distributed parameter systems. Using the momentum equation for a fluid in two-dimensions, each mode for the system can be modeled and combined into a mode stack bond graph (Thoma and Richter, 1984). Combinations of R, C, and I 1-port elements are used to represent each mode of the system.

A lumped parameter analysis cuts the line into segments, which are assumed to act at a concentrated point. The desired frequency characteristics are based on the length of the line modeled and the characteristics of the line. The shorter the line length, the higher the frequency which can be analyzed. However, the size of the model increases as the number of segments are increased.

The lumped parameter method has sufficient accuracy if the wavelength of the highest frequency response is below the wavelength of the wave propagation in the fluid, which is a function of the speed of sound in the fluid. The required criteria is

$$l < \frac{C}{2f} \qquad [4.31]$$

where

l = line segment length (m),

C = speed of sound in fluid, and

f = desired system frequency response.

Since line lengths are relatively short on the harvester hydraulic system, and there is not a high frequency response desired from the simulation results, the lumped parameter method was used. For the longest line length, the highest frequency response is approximately 700 Hz. The highest frequency of interest occurs due to the pumping action of the axial piston pump. Each piston in

the piston pump causes a slight pressure and flow rise. Since there are nine pistons, the frequency of this occurrence is nine times the radial velocity of the pump. For the tested speeds, this frequency is approximately 300 Hz, which is well below the frequency response of the longest line.

In the bond graph model for a single line segment (Figure 18), the 0-junction on the left of the 1-junction represents the pressure at the inlet to the line segment, and the 0-junction to the right of the 1-junction represents pressure at the line segment outlet. Pressure loss in the line segment is modeled at the 1-junction.

Flow changes caused by fluid and line compliance are modeled by capacitors (C) at the 0-junctions. Capacitance for the entire line length was divided by two and used for each capacitor parameter. Capacitance is a function of the effective bulk modulus, and the volume of fluid in the line segment. Pressure losses are modeled by the resistors (R) and inertias (I) at the 1-junction. Fluid resistance is split into line losses based on pressure driven flow in a tube, and pressure losses which occur at 90° elbows in the hydraulic circuit. Fluid inertia is calculated based on force required to accelerate the fluid through the line. Equations used to find line loss parameters are discussed in Chapter 5.

4.2.6 Mechanical Drives

4.2.6.1 Accumulator Drive

The load coupled to the accumulator motor includes a 2-step chain drive, and the accumulator itself, a U-shaped frame which holds the stalks. An end view of the accumulator (Figure 19) shows the 2-step chain drive. Step 1 used No. 60 chain between the motor shaft and the dump jackshaft and step 2 used No. 100 chain between the the jackshaft and accumulator shaft. The sprocket ratio from the motor to the jackshaft was 8:1, and from the jackshaft to the accumulator shaft it was 3:1. Consequently, a motor speed of 96 RPM gave a 4 RPM accumulator rotation. The manually

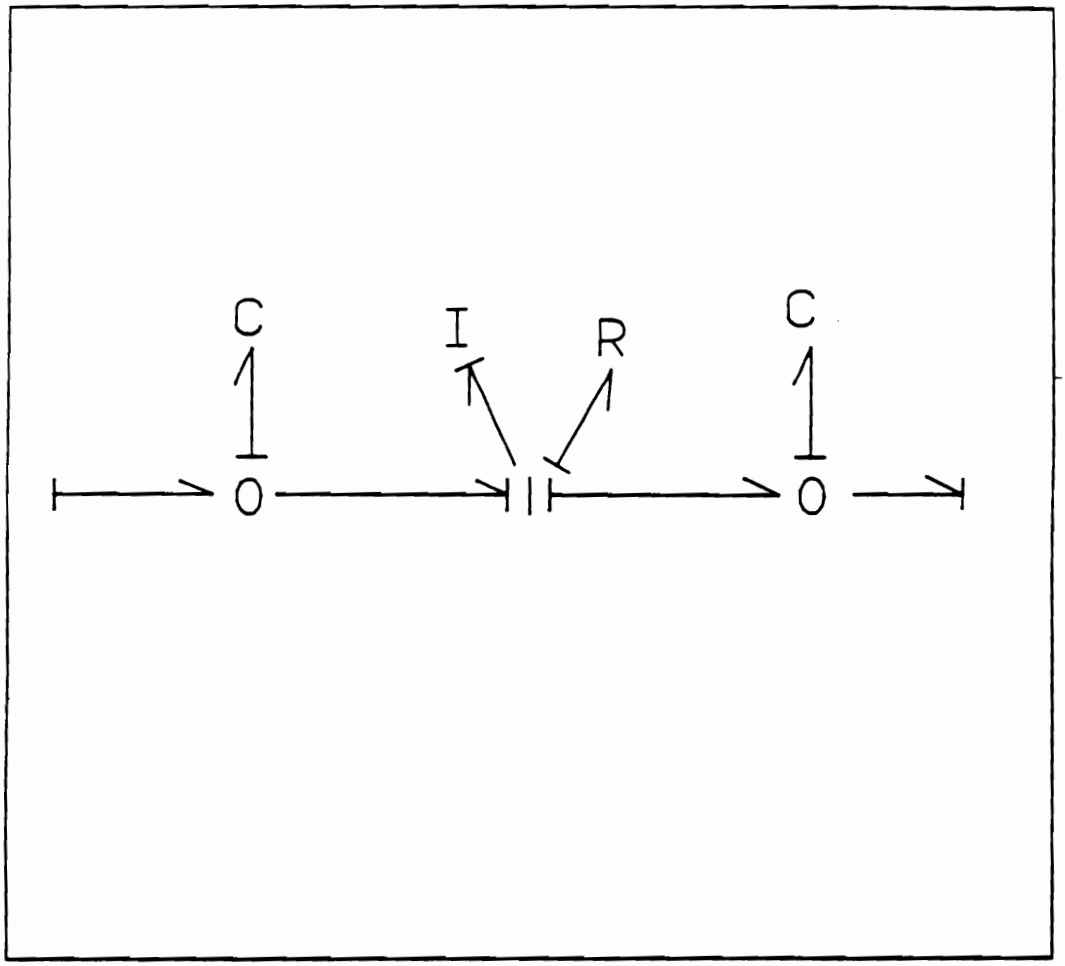

Figure 18. Bond graph model of line segment.

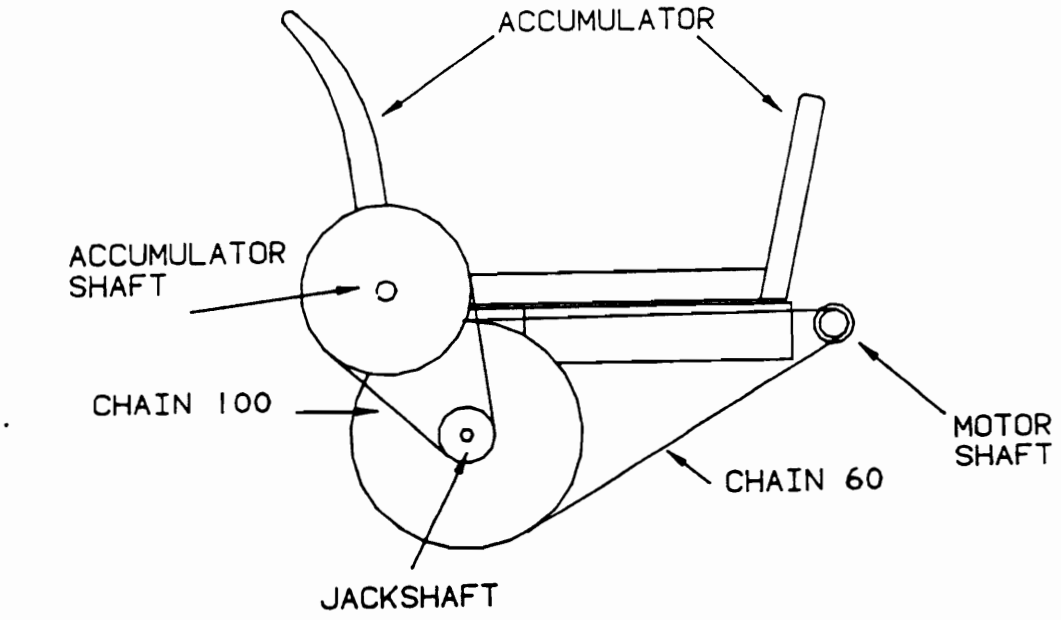

Figure 19. Rear view of accumulator drive.

operated DCV directed flow to the hydraulic motor, which rotated the accumulator to dump a load of stalks.

The mechanical load was modeled as shown in Figure 20. The 0-junctions represent points where the torque is constant, and angular velocity losses are bonded. The 1-junctions represent points where angular velocity is constant, and torque losses are bonded. The motor power output is bonded to the accumulator drive by 0-junction (14) . Chain compliance, C_{60}, is bonded to this 0-junction and models angular velocity loss due to chain stretching and torsional twisting in the shafts. A transformer, with modulus SR2, converts torque and speed in the motor sprocket to torque and speed on the jackshaft sprocket (Step 1). Inertia of the jackshaft sprocket and shaft (J_{sp}) and bearing losses (R_{b4}) are bonded to the transformer output at 1-junction (15) . The No. 100 chain drive is represented by a second transformer with a modulus (SR3) located between 0-junction (16) and 1-junction (17) (Step 2). Output of this transformer represents the torque and speed at the accumulator shaft. 1-junction (17) represents the angular velocity of the accumulator shaft, and has bonded to it the load torque (S_{el}), load inertia (J_{acc}), and torque to overcome journal bearing losses (R_{b5}).

Torque to turn the accumulator shaft is a function of the accumulator weight, stalk bundle weight, and angle of accumulator rotation. According to Rains and Cundiff (1991), torque on the accumulator shaft is given by

$$T_l = T_a \cos\theta + T_s \cos\theta \qquad [4.37]$$

where

T_l = torque required to rotate accumulator shaft (N-m),

T_a = torque due to accumulator frame (N-m),

T_s = torque due to stalks (N-m), and

θ = angle of accumulator rotation (rad).

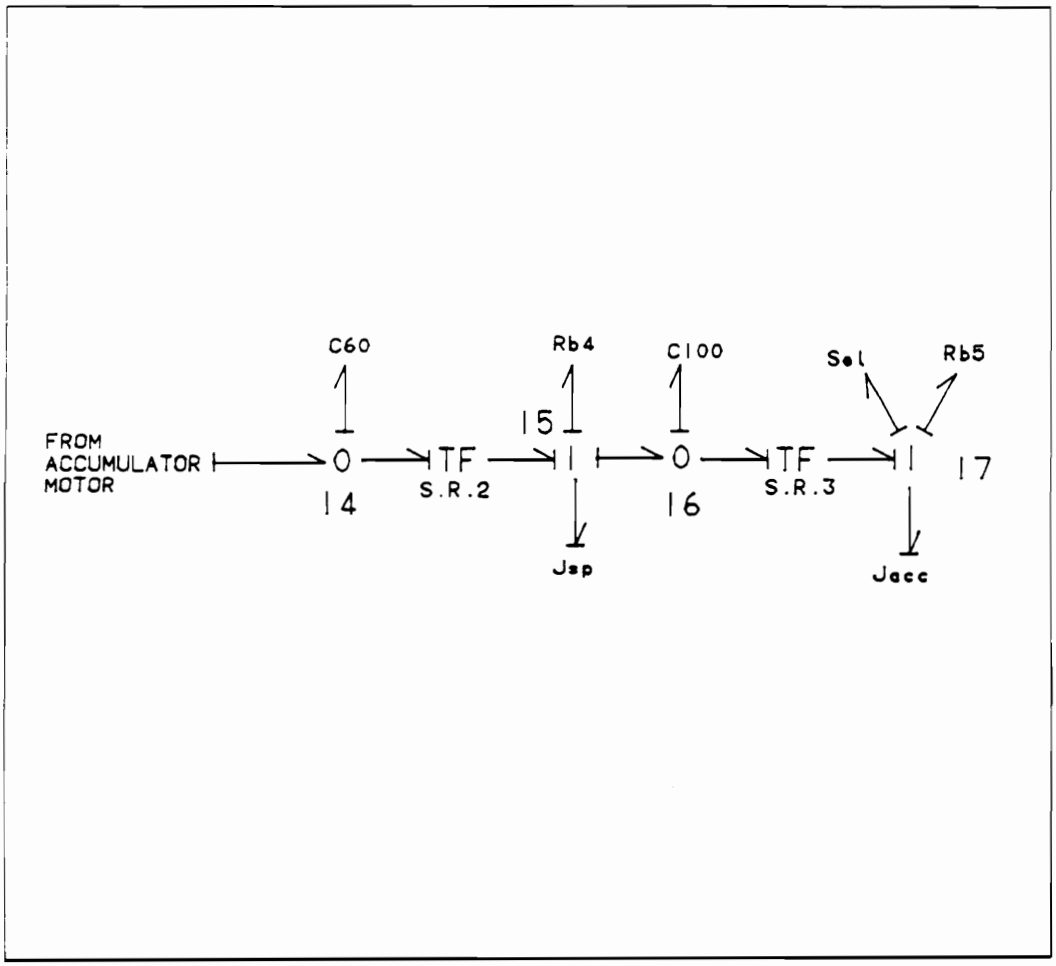

Figure 20. Bond graph model of accumulator load.

When the accumulator rotates 120°, the stalks begin sliding out, and the accumulator is completely empty after 150°. The changing center-of-gravity of the stalk bundle affects T_s, which is

$$T_s = Fr(\theta) \qquad [4.38]$$

where

T_s = torque due to stalks (N-m), and

F = weight of stalk bundle (N), and

r(θ) = distance from stalk bundle center-of-gravity to accumulator shaft (m).

r(θ) is a constant for $\theta \leq 120°$, and variable for $120° < \theta \leq 150°$. Initial distance of the stalk bundle center from the accumulator shaft is 25.4 cm. The function r(θ) between 120° and 150° can be written

$$r(\theta) = 25.4 + 29.1(\theta) \qquad [4.39]$$

r(θ) begins increasing until θ reaches 150°, at which point the stalk bundle slides completely off the accumulator, and a dump event is completed.

4.2.6.2 Cross-Conveyor Cylinder Load

When the two conveyor cylinders extend they increase the cross conveyor angle from α = 40° to 75° (Figure 21). The conveyor frame pivots on supports at the bottom. The centerline of the supports coincides with the centerline of the conveyor shaft. Sprockets to drive the conveyor chains were mounted on this shaft. As the conveyor frame rotated, the chains remained at the same tension.

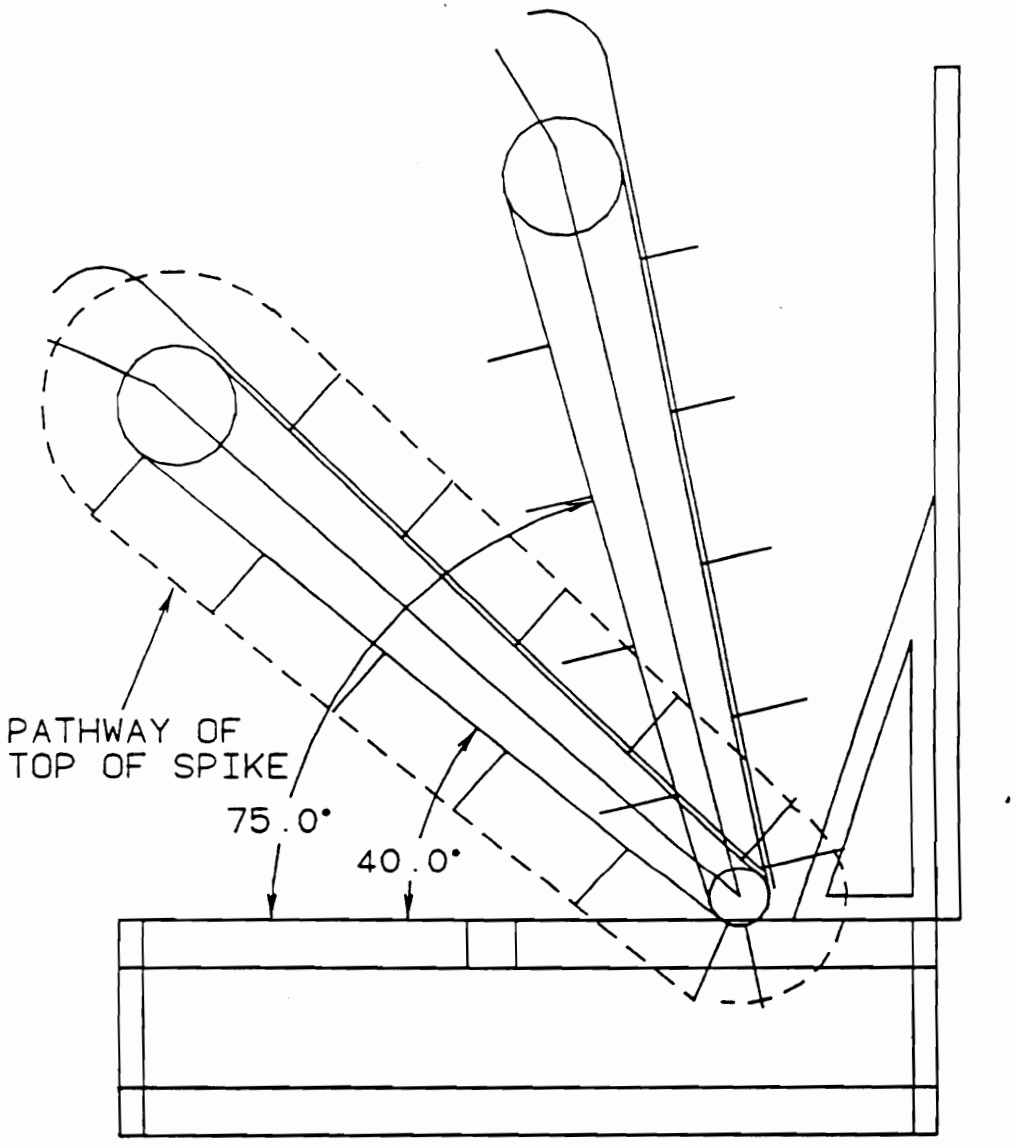

Figure 21. Rear view of cross conveyor at minimum and maximum angle.

The cylinders were connected to the cross conveyor in the orientation shown in Figure 22. The force on the cylinder rod changes as the conveyor angle changes. This force is calculated by summing the moments about the centerline of the conveyor shaft.

$$\Sigma M_B = W\bar{x}\cos\alpha - F_c x\cos\gamma \qquad [4.40]$$

where

W = weight of the conveyor (N),

α = angle of conveyor with horizontal plane (rad),

γ = angle of cylinder with plane perpendicular to conveyor (rad),

F_c = force on the cylinder rod (N),

$\bar{x}$ = distance from B to conveyor center-of-gravity (m), and

x = distance from B to cylinder connection (m).

At the point the conveyor just begins to rotate upward, $\Sigma M_B = 0$, and solving for F_c,

$$F_c = \frac{W\cos\alpha}{\cos\gamma}\left(\frac{\bar{x}}{x}\right) \qquad [4.41]$$

The bond graph model used to represent this load (Figure 23) shows that input comes from 1-junction (13) of the cylinder model (Section 4.2.3). A modulated transformer couples 1-junction (13) to 1-junction (14). Load force (F_L) is the weight of the conveyor (W). The modulus of the transformer (m) can be calculated from the causality and Eqn. (4.41),

$$F_L = mF_c$$

where

$$m = \left(\frac{x}{\bar{x}}\right)\frac{\cos\gamma}{\cos\alpha}$$

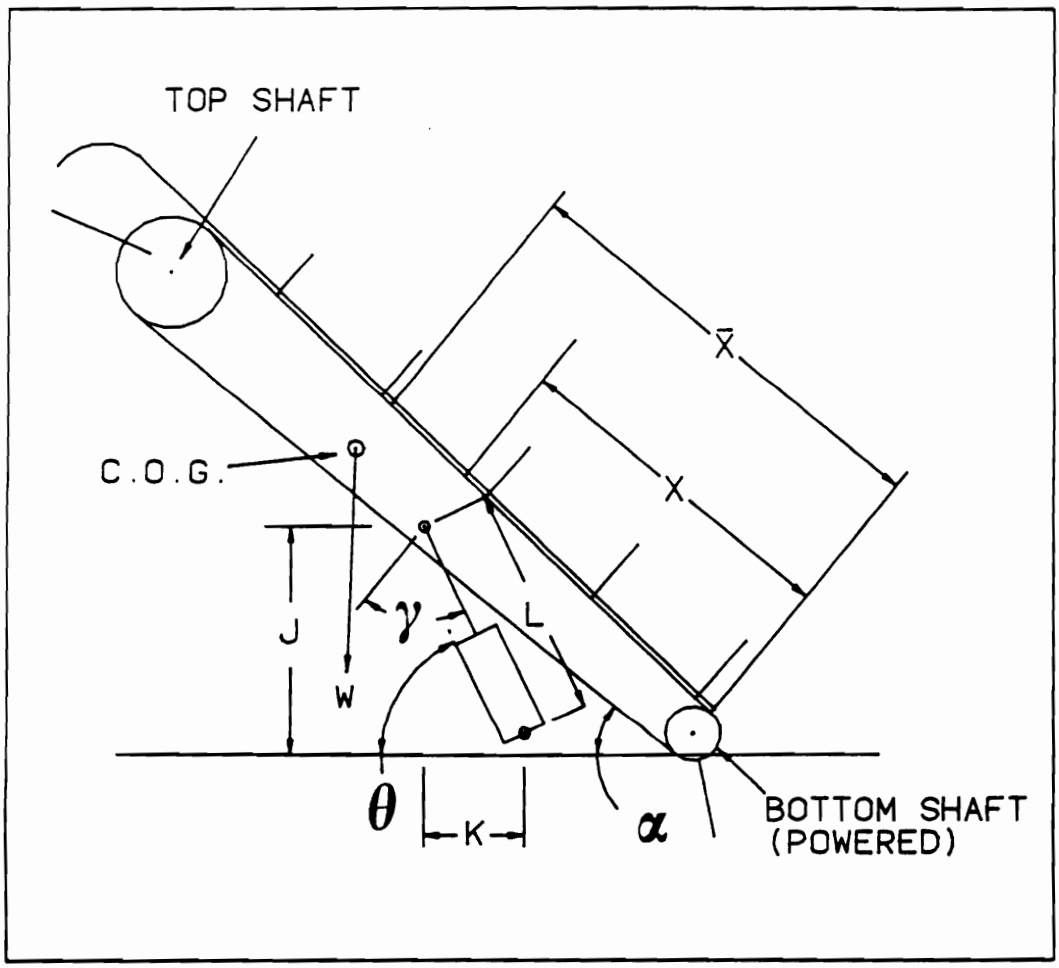

Figure 22. Rear view of cross conveyor and cylinder placement.

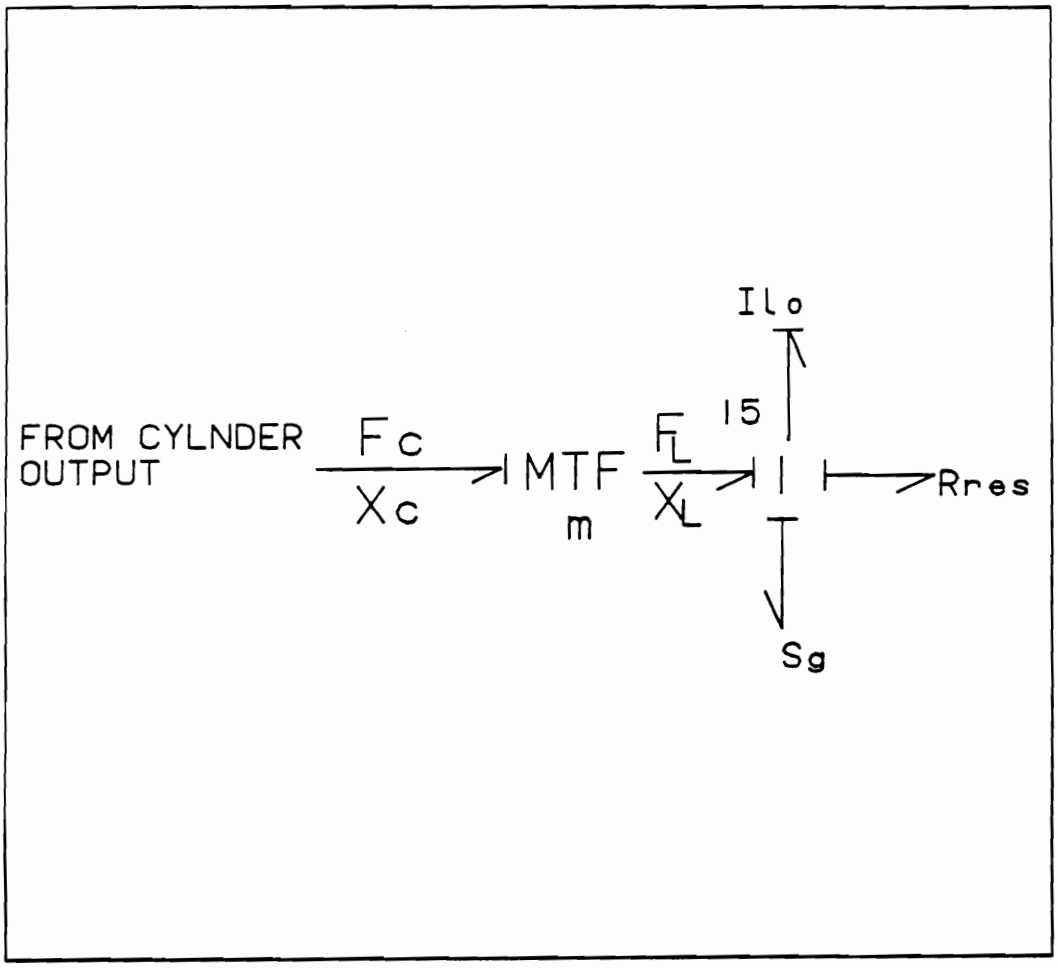

Figure 23. Bond graph model of the conveyor load on the cylinder.

The angles, α and γ, change as the cylinder extends and retracts. The exact length of the cylinder is determined by integrating the linear velocity of the cylinder, which is the common velocity at 1-junction (13) . Values of J and K (Figure 22) were determined at 5° increments of α using the relations,

$$J = x \sin \alpha$$

and

$$K = x \cos \alpha - 15.0$$

From the geometry of the mechanism,

$$\gamma = \alpha + 90° - \theta$$

Once these values were determined for 5° conveyor angle increments, a piecewise linear function was encoded into the computer simulation model. By integrating the rod velocity at 1-junction (13) , the length of the cylinder (L) was found and used to calculate α, γ, and subsequently, the modulus m.

4.2.6.3 Accumulator Cylinder Load

Two Cylinders connected in parallel are used to move the accumulator out from under the cross conveyor to the position where it is filled. Viewing the accumulator as shown in Figure 19, it can be moved left (out) and right (in). As stalks are harvested, moving the accumulator in and out helps to fill the accumulator evenly. In addition, the accumulator is retracted fully to reduce the width of the harvester to within eight feet, which is the legal width for highway travel.

The accumulator is supported by two I-beams which slide on brass plates at the support points. The I-beams are connected together by the accumulator frame. One cylinder is connected to each I-beam, thus the two cylinders are mechanically yoked together.

The accumulator cylinder load consists of the force to overcome friction over the brass plates and force to overcome inertia and accelerate the load. Figure 24 illustrates the additions to the cylinder model to include the accumulator load. The inertial and resistance terms are bonded directly to 1-junction ⑮ . The inertia (I_{acc}) is equivalent to the mass of the accumulator, including the I-beams. The resistor (R_{bp}) models the resistance from friction as the I-beams slide over the brass plates.

4.2.6.4 Gathering Chains Drive

Two counter-rotating chains mesh together to grip stalks as they enter the front of the harvester (Figure 25). Each chain consists of gripper pads made of a rubber material bolted to tabs on the chain. These pads deform around the stalk to hold it securely without crushing it. Two hydraulic motors connected in series power the two chains. Because the rubber loops are intermeshed, both motors turn at the same velocity.

Motor load includes the following terms:

1. torque to compress gripper pads,
2. torque to overcome friction,
3. torque to lift stalk weight, and
4. torque to accelerate stalks, if chain speed is faster than ground speed.

A force transducer was used to determine the force exerted by the grip pads on the stalks (Rains and Cundiff, 1990), and the value was found to be 40 N. This value was measured at the point where the intermeshing grip pads initially grasp the stalk. Tension in the chain resulting from the force to compress the pads is given by

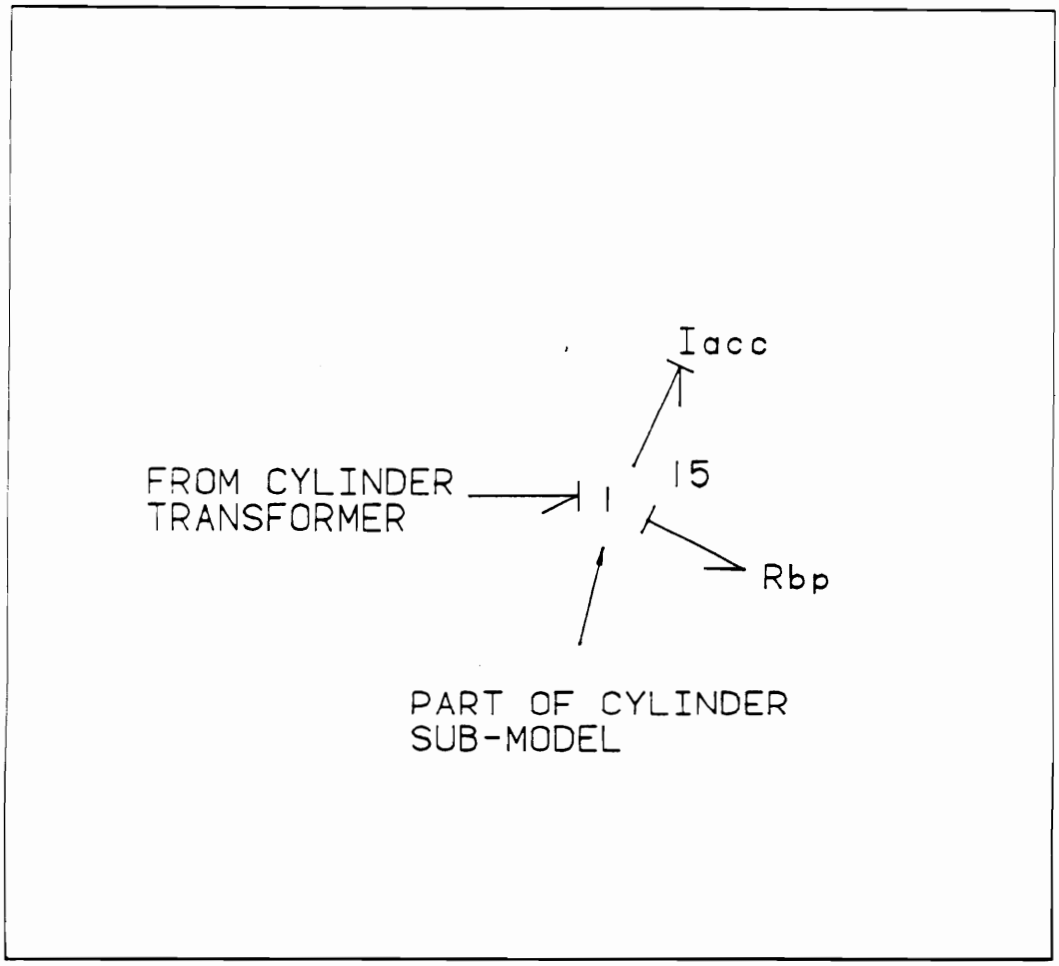

Figure 24. Bond graph model of the accumulator cylinder load.

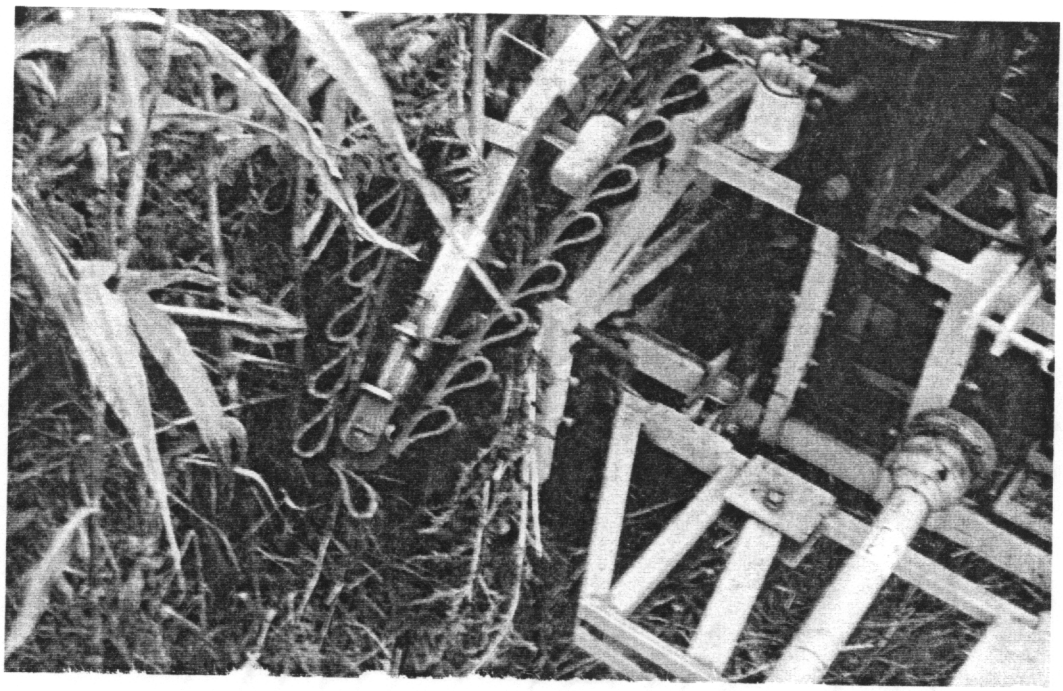

Figure 25. Photograph of stalk entry point on the gathering chains.

$$F_t = 40 \tan \zeta \qquad [4.42]$$

where

F_t = tension in chain (N), and

ζ = angle at which chains come together (rad) (Figure 26).

Bond graph representation of the two motors in series and their loads (Figure 27) includes two transformers to represent the conversion of hydraulic power to mechanical power, one for each motor. By bonding their output at 1-junction 23 , the two motors are forced to turn at the same angular velocity. Resistors and inertia bonded to this junction represents the characteristics of each motor described in Section 4.2.2.3. The output of 1-junction 23 represents the power output from both motors to move the gathering chains. It is coupled to 0-junction 24 through a transformer with a modulus equal to the sprocket radius on the motor shaft. The transformer converts torque and angular velocity in the motor shaft to force and linear velocity in the gathering chains. Force in the chain is represented by 0-junction 24 . A capacitor is bonded to this junction and represents the compliance of the chain and intermeshed gripper pads. 1-junction 25 is bonded directly to the output of 0-junction 24 . The chain velocity is common to this junction and bonded to it are resistors representing sliding friction and load resistance (R_{bs},R_L), inertia representing stalk mass (I_{gc}), and an effort source term representing the weight of the stalk (W_{st}). The load resistance accounts for the force to compress the gripper pads, and its value is obtained from Eqn. (4.42).

4.2.6.5 Stalk Flipper Load

One hydraulic motor is used to rotate two concave discs referred to as the flipper. The discs grasp the butt of the stalk as the top is released by the gathering chains, and rotates it 90° onto the cross conveyor. Total torque requirement includes torque to overcome resistance as the rubber surface is deformed when the discs come together, bearing friction, and torque to rotate the stalk mass.

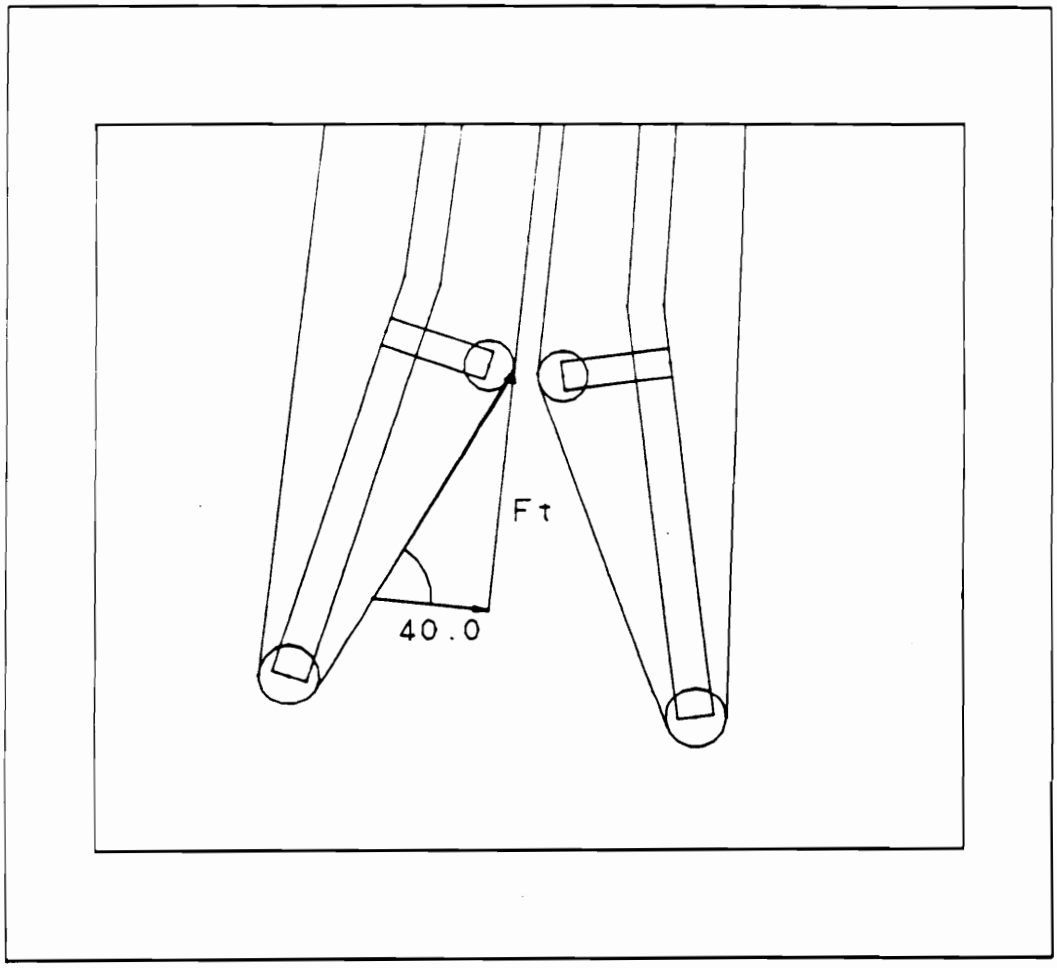

Figure 26. Diagram showing the chain tension resulting from the force required to compress the grip pads.

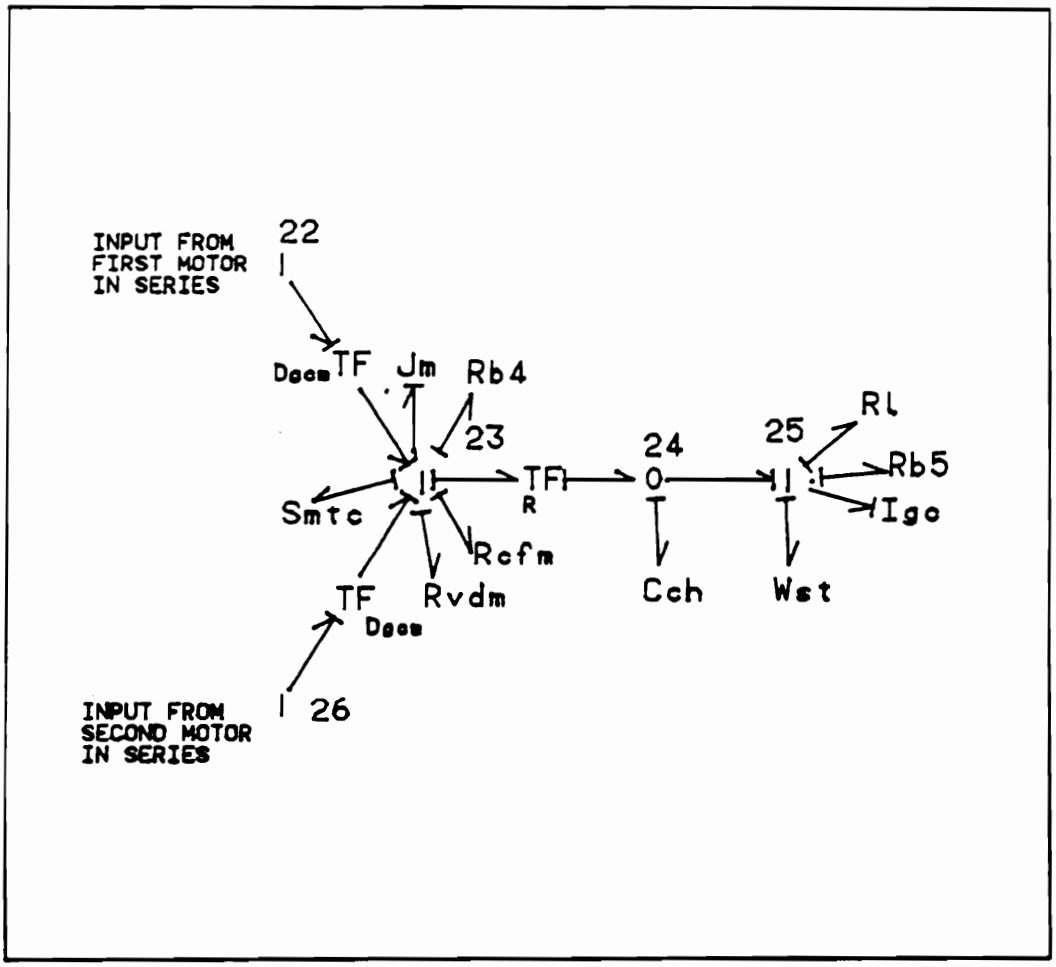

Figure 27. Bond graph model of the load on the two gathering chain motors.

Each disc rotates on a shaft supported by roller bearings. The flipper motor drives one disc, and friction between the discs drive the other disc.

To determine the torque to turn the shafts, the force existing between the two compressed discs must be determined. The same force transducer used for the gathering chains was used to measure gripping force between the discs. Maximum force was found to be 60 N. The resistive torque is a function of the angle between the two flipper disc shafts. The discs form angles in the horizontal and vertical planes as shown in Figure 28. The angles, α and γ, were measured on the actual machine. Torque required to rotate the flipper is

$$T_{sf} = 60(\sin\alpha - \sin\gamma)r \qquad [4.43]$$

where

T_{sf} = torque to rotate flipper (N-m),

r = radius of the flipper discs (m),

α = angle in horizontal plane (rad), and

γ = angle in vertical plane (rad).

The bond graph model of the flipper (Figure 29) includes inertia from the flipper discs and shafts (J_{sf}), a resistor (R_{b4}) to represent bearing resistance, and a resistor (R_{sf}) to represent torque required to compress the discs.

4.2.6.6 Cross-Conveyor Chain Drive

A hydraulic motor drives the cross conveyor via a chain drive (Figure 30). The cross-conveyor has three chains spaced 100 cm apart, giving the conveyor a total width of 200 cm. Each chain has 15-cm tall spikes bolted to tabs spaced 25 cm apart. The stalks are layered onto the cross-conveyor by the stalk flipper. Conveyor motor load was determined with and without a load of stalks on the conveyor.

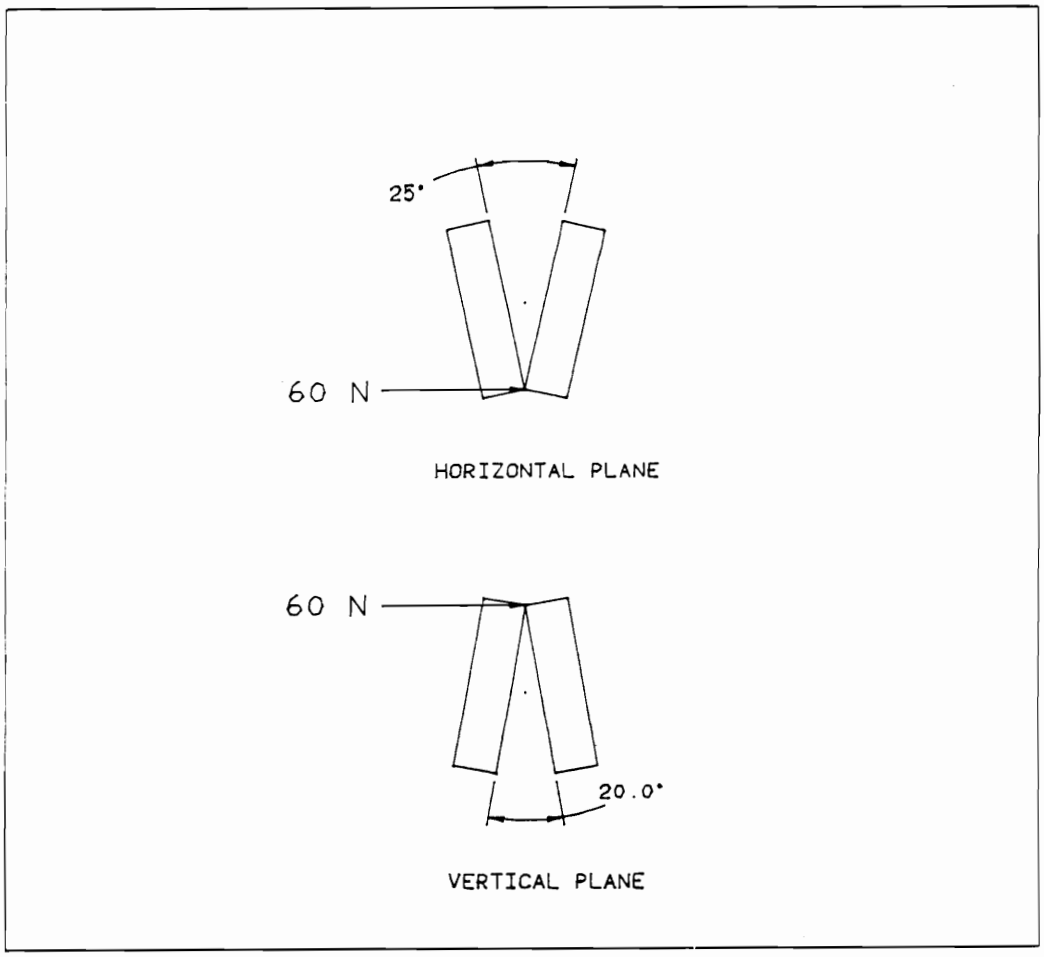

Figure 28. Angles between the flipper discs.

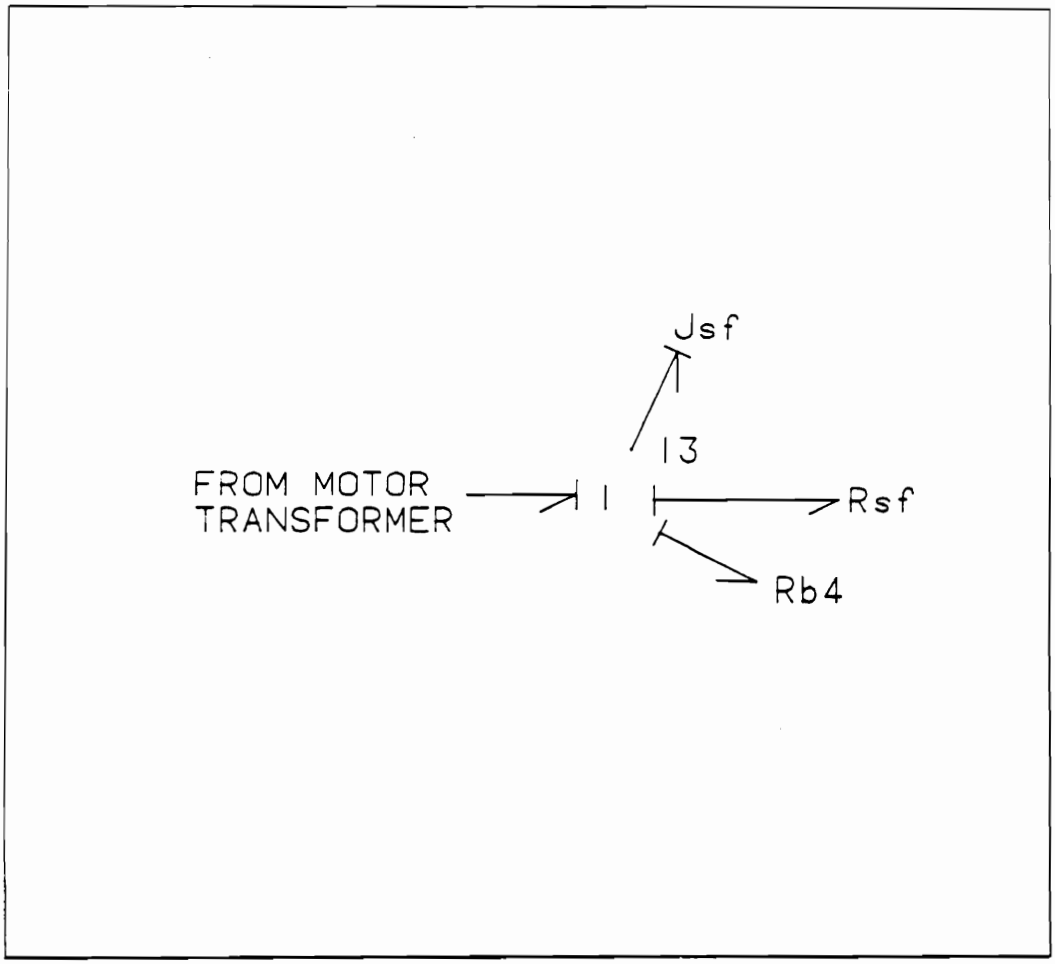

Figure 29. Bond graph model of the load on the stalk flipper motor.

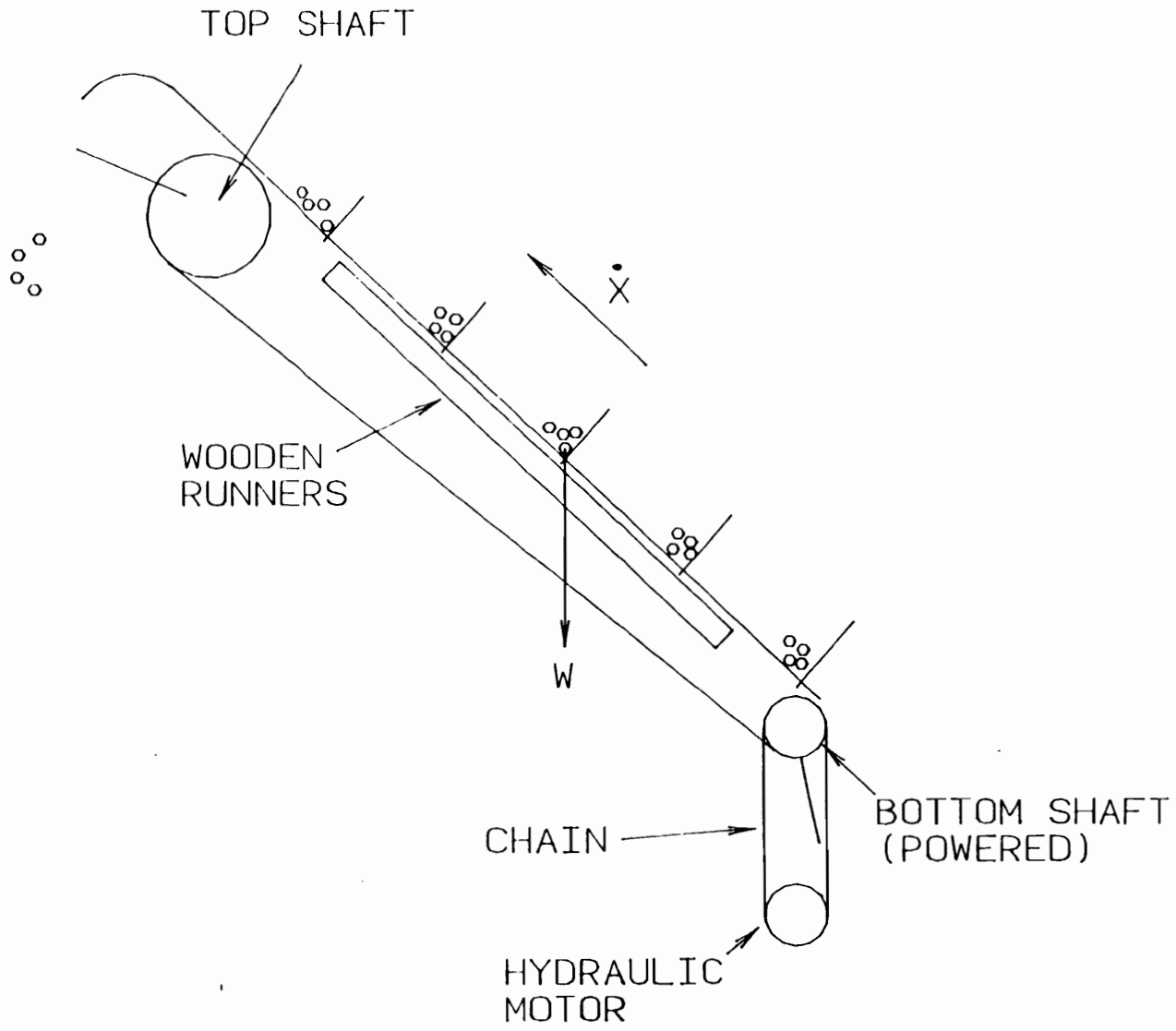

Figure 30. Rear view of cross-conveyor chain load.

The motor must supply torque to accomplish the following:

1. slide chain over wooden runners which support it,
2. lift stalk weight,
3. slide stalks over the galvanized sheet metal surface,
4. overcome bearing resistance, and
5. accelerate stalk mass (inertia) to conveyor speed after they land on conveyor.

Figure 31 is the bond graph representation of the conveyor motor load. The transformer coupling 1-junction (23) to 0-junction (24) converts angular velocity and torque to linear velocity and force in the conveyor chain. The transformer modulus (R_c) is the radius of the sprocket mounted on the conveyor driveshaft.

Force input to move the chain is modeled by 0-junction (24) . A capacitor (C_{ch}) is bonded to this junction to model the chain and conveyor shaft compliance. 1-junction (25) is bonded to the output of 0-junction (24) . Linear chain velocity is common to this junction, and the sum of forces is

$$F_{25} = F_{Wst} + F_{sm} + F_{ss} \qquad [4.44]$$

where

F_{25} = force input to the chain (N),

F_{Wst} = force to lift stalk weight (N),

F_{sm} = force to accelerate stalks (N), and

F_{ss} = force to move stalks over galvanized surface (N).

The weight of the stalks is not constant. Stalks are layered onto the conveyor and drop from the conveyor into the accumulator continuously. Consequently, the inertial term and effort source at 1-junction (25) are functions of time, and harvesting speed. The determination of these time functions and their parameters are discussed in Chapter 5.

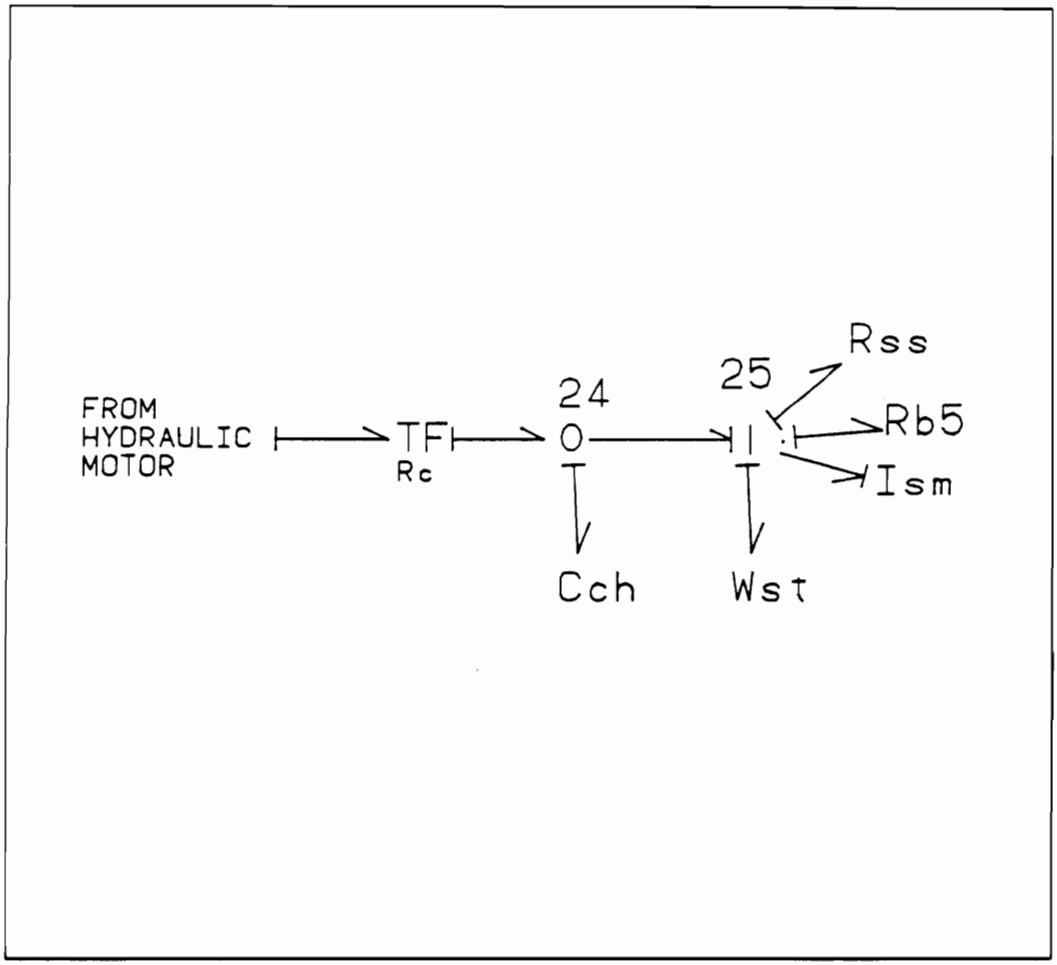

Figure 31. Bond graph model of the cross-conveyor motor load.

4.2.6.7 Disk-cutter Drive

The disk-cutter is a 30.5-cm diameter disk with six equally spaced blades projecting radially out from the disk periphery. The disk-cutter cuts the stalks approximately 10 cm above the ground as they are gripped by the gathering chains.

A hydraulic motor powers the disk-cutter through a V-belt drive. The load on the motor consists of torque to accelerate the disk, torque to cut stalks, and torque to overcome bearing losses. The bond graph model (Figure 32) shows a transformer between 1-junction (13) and 0-junction (14) . This transformer represents the power conversion through the V-belt drive. Angular velocity losses due to V-belt and shaft compliance (C_{14}), and V-belt slippage (R_{sl}) are bonded to this junction.

The torques which must be developed by the motor to turn the disk are bonded to 1-junction (15) . The inertial term is the disk moment of inertia. The resistors represent torque to overcome bearing friction (R_{bs}) and cut the stalk (R_{Disk}). Odouri and Gupta (1988) tested a similar basecutter for sugarcane harvesting, and reported power required to cut the stalk at various operating speeds. Their data was used to evaluate the load resistance (R_{Disk}) on the disk-cutter.

4.3 Computer Simulation

The computer software package TUTSIM was used to simulate the bond graph model because it had the capabilities to handle Non-linearities and bond graph/block diagram interaction. The package will operate on any IBM compatible computer and has a graphical output package to plot simulation results.

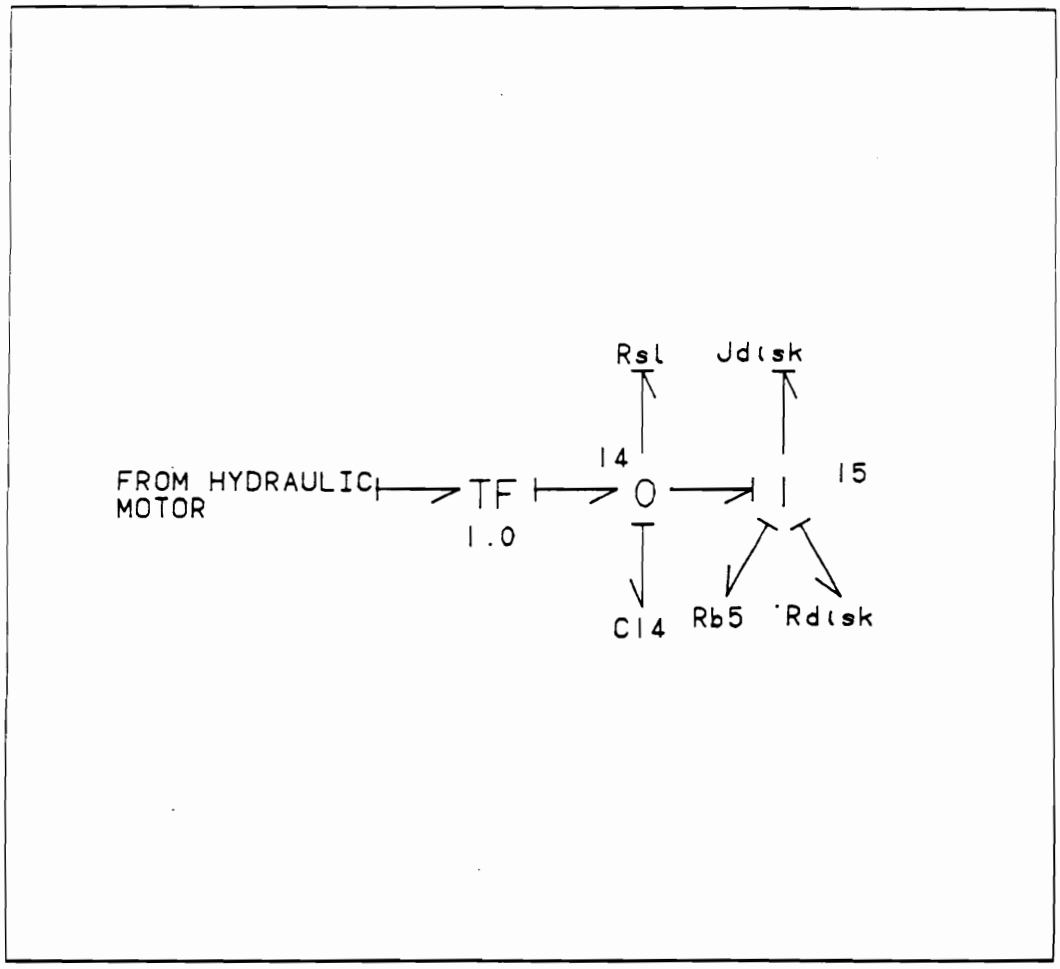

Figure 32. Bond graph model of the disk-cutter motor load.

TUTSIM was originally designed to solve systems constructed in block diagram form. Integrators, multipliers, summers, and other blocks were combined based on the equations defining the system to be analyzed. TUTSIM was later modified to incorporate bond graph representations of systems. Bond graph elements were created by combinations of blocks already in TUTSIM. As an example, a bond graph capacitor can be written as a combination of blocks:

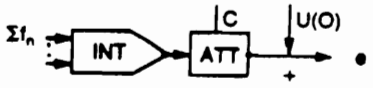

In equation form, the above blocks represent:

$$e = \frac{1}{C}\int(\Sigma f)dt$$

f is the generalized flow variable and e is the effort defined for the capacitor bond. In a hydraulic system, f is flow rate, and e is pressure.

Capacitors and inertias are 1-port energy storage elements (See Appendix A). They are modeled in the bond graph in integral form when possible. Computer round-off errors can occur when calculating derivatives. Causality on the element determines if it is in integral or derivative form. In TUTSIM, the energy storage elements may be defined in either form to accommodate all bond graph models. However, when using derivatives, the time step for the simulation must be reduced, and this increases computer run-time.

In TUTSIM code, storage elements are defined by: 1)block numbers which label the element output, 2) element symbol which identify the element to TUTSIM, 3) inputs to the integral or derivative, and 4) the parameter value used for the element. As an example, a line of TUTSIM code describing a capacitor constitutive equation in integral causality is

```
  0.200      100      C      101  -102  -103
Parameter  output   symbol     inputs
```

In integral form this is,

$$e_{100} = \frac{1}{0.200} \int (f_{101} - f_{102} - f_{103}) dt$$

The inputs inside the integral are the sum of the flow variables bonded to an 0-junction.

Resistors and transformers do not involve integration or differentiation. Their inputs are defined in terms of the output variable of the energy storage elements or flow and effort sources. As an example, an inertial term in integral causality determines the flow at a 1-junction to which it is bonded. A resistor also bonded to the 1-junction would be defined as

$$e = Rf_I$$

f_I is the flow determined by the inertia constitutive equation. Sources are not interactive and can be used to determine flow at a 1-junction and effort at an 0-junction.

TUTSIM will not solve algebraic loops. It is for this reason that resistors and transformers must be defined in terms of an 1-port energy storage element, or source.

Non-linear equations may be defined and encoded into TUTSIM. One example is the relief valve. Relief valves remain closed until the line pressure reaches the relief setting. At this point it opens and flow is relieved to a lower pressure line. The bond graph equation is

$$Q = \frac{1}{R} (\Delta P)$$

R is a resistor that must be a non-linear function of pressure. Function blocks (FNC) can define piecewise linear functions of one input variable. The input variable is pressure and the output is

flow rate through the relief valve. An example of the FNC block parameter list for a relief valve is

Pressure	Flow
0.0	0.0
0.1	0.0
1.0	0.0
4.0	50.0
5.0	500.0
10.0	10000.0

Pressure is in MPa and flow rate in cm^3/s. These units are used to reduce the stiffness associated with normal Pa and m^3/s units.

Non-linear 1-port energy storage elements can also be implemented into TUTSIM. The integration can be done by an integrator block (INT). The storage element (I,C) can be determined as a variable value using FNC, SIN (sine), and COS (cosine) blocks. After calculating the element parameter at that time step, it can be combined with an integration block to encode the bond graph constitutive equation.

A 2^{nd} order Adams Bashforth integration scheme is used by TUTSIM to solve integrals, and an Euler routine is available if desired. Step-size was determined by estimating the highest eigenvalue from the model. A step-size four times faster was the first guess, and step-size was increased until the model simulation changed or became unstable. Time step from the previous simulation was then used.

Each component model was put in a TUTSIM file. Components were put together interactively to create one of the actuating circuits on the harvester, which allowed motors, pumps, and loads to be interchanged for efficient analysis and design.

Chapter 5 Experimental Methods

5.1 Hydraulic Model Parameter Determination

Data was collected to define the parameters needed for the bond graphs. Values were determined from theoretical procedures, experimental measurements, and manufacturers data. The theoretical and experimental procedures used to determine the parameters are developed in this chapter.

5.1.1 Motor Characteristics

As previously stated, flow rate through a hydraulic motor is

$$Q = D_m\omega + \frac{C_{si}(\omega)D_m\Delta P_i}{\mu} + \frac{C_{se}(\omega)D_m\Delta P_e}{\mu} + Q_c \qquad [5.1]$$

and torque developed at the output shaft is

$$T_o = D_m\Delta P - C_f(\omega)D_m\Delta P - C_{vd}\mu\omega D_m - T_c - J\frac{d\omega}{dt} \qquad [5.2]$$

These equations were defined in Section 4.2.2 where a theoretical basis was given for the slip flow coefficient [$C_s(\omega)$] and coulomb friction coefficient [$C_f(\omega)$] as linear functions of the motor angular velocity. Table 1 gives the nomenclature for four test conditions used to determine motor loss coefficients. By measuring motor performance at a maximum and minimum pressure (ΔP_{max} and ΔP_{min}) for each speed (ω_{max} and ω_{min}), the loss coefficients were determined. Substituting test parameters A and B from Table 1 into Eqn. (5.2), and solving for the coulomb friction coefficient at the minimum speed, gives

$$C_f(\omega_{min}) = [\frac{T_a - T_b}{\Delta P_b - \Delta P_a}]\frac{1}{D_m} + 1.0 \qquad [5.3]$$

Substituting test parameters C and D from Table 1 into Eqn. (5.2), and solving for $C_f(\omega_{max})$ gives,

$$C_f(\omega_{max}) = [\frac{T_c - T_d}{\Delta P_d - \Delta P_c}]\frac{1}{D_m} + 1.0 \qquad [5.4]$$

These two equations are the same velocity dependent friction coefficients found by McCandlish (1984). If the two values of $C_f(\omega)$ are in close proximity to one another, the speed dependence may be neglected and a constant mean value used. As a matter of reference, this would reduce the friction term to that used in Eqn. (2.1) (Wilson's Equation). Using linear interpolation or extrapolation, $C_f(\omega)$ can be determined at any motor shaft velocity.

To determine the viscous drag coefficient, the $C_f(\omega)$ terms found at both speeds were substituted into Eqn. (5.2) and the equation solved for C_{vd}.

$$C_{vd} = \frac{T_c - T_a}{\omega_{max} - \omega_{min}}\frac{1.0}{\mu D} - \frac{\Delta P_a}{\mu}[\frac{C_f(\omega_{max}) - C_f(\omega_{min})}{\omega_{max} - \omega_{min}}] \qquad [5.5]$$

C_{vd} was assumed constant over all operating conditions. The equation used to describe flow has two coefficients which must be determined, the internal slip coefficient (C_{si}) and the external slip flow coefficient (C_{se}). Only the gathering chain motors have case drains and require determination of an external flow loss. The external flow rate was measured by collecting flow from the drain line

Table 1. Nomenclature for the four operating conditions to measure motor performance and measured values.

Test Condition	Motor Speed	ΔP across Ports	Inlet Flow	Case drain Flow	Torque
A	ω_{min}	ΔP_{min}	Q_a^1	Q_{exa}	T_a
B	ω_{min}	ΔP_{max}	Q_b	Q_{exb}	T_b
C	ω_{max}	ΔP_{min}	Q_c	Q_{exc}	T_c
D	ω_{max}	ΔP_{max}	Q_d	Q_{exd}	T_d

Q^1 = The subscripts (a,b,c,d) refer to data collected for tests A,B,C,D, respectively.

for a given time interval. The external flow coefficient at the maximum and minimum rotational velocity is given by

$$C_{se}(\omega_{\min}) = \frac{Q_{exa}\mu}{\Delta P_a D_m} \qquad [5.6]$$

$$C_{se}(\omega_{\max}) = \frac{Q_{exc}\mu}{\Delta P_c D_m}$$

where

Q_{exi} = measured external leakage for operating condition i (i = a,c),

ΔP_i = measured pressure drop across motor for operating condition i (MPa), and

D_m = motor displacement (cm^3/rad).

Once these values have been determined, linear interpolation and extrapolation may be used for values at other motor speeds. The internal slip flow coefficient (C_{si}) can also be found at $\omega_{\min}$ and $\omega_{\max}$. Substituting test conditions A and B into Eqn. (5.1) and solving for $C_{si}(\omega_{\min})$ gives

$$C_{si}(\omega_{\min}) = \frac{Q_a - Q_b}{\Delta P_b - \Delta P_a}\frac{\mu}{D_m} + \frac{\Delta P_b + \Delta P_a}{\Delta P_b - \Delta P_a} C_{se}(\omega_{\min}) \qquad [5.7]$$

By using test conditions C and D, the slip flow coefficient is

$$C_{si}(\omega_{\max}) = \frac{Q_c - Q_d}{\Delta P_d - \Delta P_c}\frac{\mu}{D_m} + \frac{\Delta P_d + \Delta P_c}{\Delta P_d - \Delta P_c} C_{se}(\omega_{\max}) \qquad [5.8]$$

5.1.1.1 Motor Test stand

A test stand was designed and built to measure the parameters shown in Table 1. The test stand hydraulic schematic is shown in Figure 33. Experimental methods suggested by ANSI standard B93.27/1973 were altered slightly to measure the desired motor parameters. A variable displace-

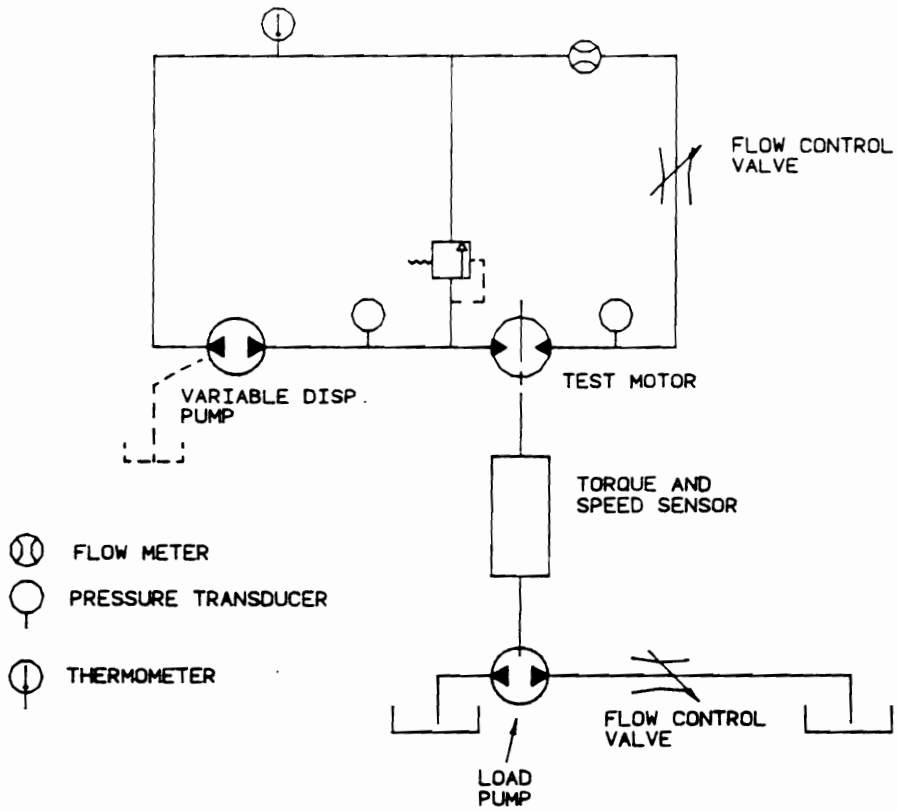

Figure 33. Motor test stand hydraulic schematic

ment pump was set to provide a given amount of flow to the test motor, subsequently controlling the motor shaft speed. A speed sensor on the shaft indicated when the desired shaft velocity had been achieved. To set the motor load, the motor shaft was coupled to the shaft of a fixed displacement pump, identified as the load pump. A flow control valve in the load pump output line was used to restrict flow, build pressure, and load the motor shaft. A pressure transducer at the motor port inlet indicated when the prescribed load was achieved. Once experimental operating parameters were set, the following data was collected: output torque, return line and case drain flow rate, motor speed, line pressure, and fluid temperature.

A data acquisition system was assembled to record fluid flow rate, line pressure, and torque output from the motor shaft on the test stand (Figure 34). A Turbo-Pascal program was written to call subroutines (supplied by the data acquisition board manufacturer) which took data from the board at 50 pts/s (See Appendix B for program listing.). Information was stored on disk and later retrieved to calculate mean values for the various parameters. Each motor was tested at conditions A,B,C, and D from Table 1.

Pressure measurements were made at the motor inlet port and outlet port using a strain gauge type pressure transducer (Dynisco Model PT310JA). Bridge excitation was supplied by a strain gauge amplifier (Validyne Model S671). Voltage output from the transducer was input back to the amplifier, and the amplifier gain set so that the resolution was 7v/27.5 MPa. The transducer was calibrated with a shunt resistor internal to the transducer which simulated a 27.5 MPa pressure. The amplified signal was input to channel 0 on the DAS-16 board and converted by a 12-bit A/D converter for storage on floppy disk.

Torque measurements were made at the motor output shaft by a slip ring strain gauge transducer (Lebow Model 1105-10K). A magnetic pulse pick-up, integral to the transducer, was used to measure motor shaft speed. A frequency counter (Phillips Model PM 6666) was used to read the frequency. The torque transducer signal went to the strain gauge amplifier for amplification, and

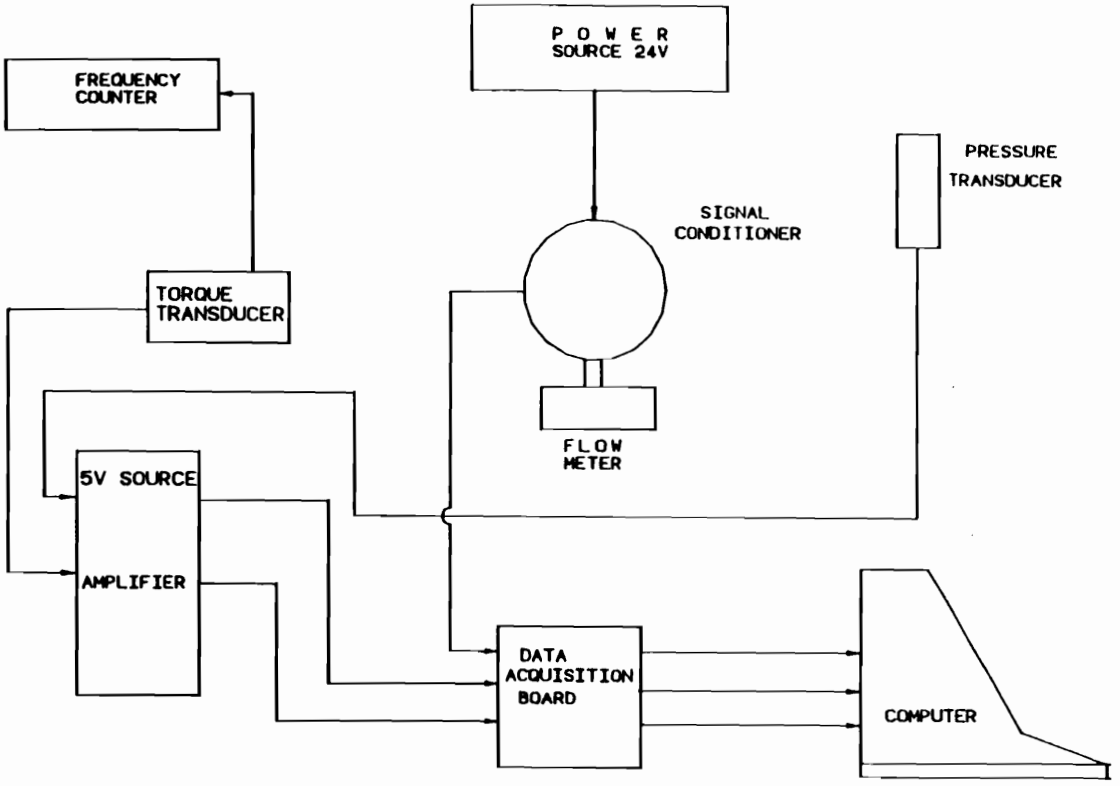

Figure 34. Motor test stand instrumentation.

the resulting voltage signal was connected to channel 1 on the DAS-16 board. Amplifier gain was set to 6.833v/772.0 N-m.

Flow rate measurement was taken in the return line of the motor by a turbine-type flow meter (Flow Technology Model FT-32) and output pulses were conditioned by a signal conditioner (CA03 Signal Conditioner) supplied with the flow meter. A 12v DC source was used to supply power to the signal conditioner. Flow meter output, a 10v square wave, was connected to the frequency counter input on the DAS-16 board. Pulses were counted every tenth of a second and frequency calculated. A 10-point calibration curve, supplied by the manufacturer for three fluid viscosities, was used to obtain flow as a function of pulse count and fluid viscosity (See Section 5.3.1).

Data collected with the test stand for the five motors on the harvester is given in Tables 2 through 6. Line pressure, flow rate, and torque data were recorded at each condition and averaged over a 10s interval to obtain the values shown in the tables. Ideal torque and flow rate are also shown. Mechanical and volumetric efficiency can be computed using the actual and ideal torque and flow rate measurements. Steady-state torque loss coefficients in Eqn. (5.2) were calculated by substituting the experimental data in Eqns. (5.3) through (5.8). The inertia term in Eqn. (5.2) includes the shaft, sheaves, and/or sprockets on the motor output shaft. Table 7 lists the resulting coefficients for the motor torque losses. These coefficients were implemented in the bond graph models as described in Chapter 4. Resulting slip flow coefficients are shown in Table 8. Internal leakage flow coefficients were determined for all motors, but external leakage flow coefficients were determined only for motors with case drains. Fluid compressibility is discussed in Section 5.1.4.

Table 2. Test stand experimental results for the accumulator dump motor.

Test Condition	ΔP (MPa)	ω (rad/s)	Ideal Torque(N-m)	Actual Torque(N-m)	Ideal Flow(cm^3/s)	Actual Flow(cm^3/s)
A	2.09	5.236	123.6	102.6	292.2	308.6
B	3.68	5.236	217.0	184.0	292.2	302.2
C	2.07	7.330	122.2	98.30	440.0	442.2
D	3.70	7.330	218.4	183.4	440.0	451.9

Table 3. Test stand experimental results for the gathering chain motor.

Test Condition	ΔP (MPa)	ω (rad/s)	Ideal Torque(N-m)	Actual Torque(N-m)	Ideal Flow(cm^3/s)	Actual Flow(cm^3/s)
A	3.77	5.236	146.6	127.4	203.5	216.3
B	5.53	5.236	215.2	186.9	203.5	213.5
C	3.71	8.378	144.5	122.5	325.5	351.1
D	5.55	8.378	215.9	188.6	325.5	345.8

Table 4. Test stand experimental results for the disk-cutter motor.

Test Condition	ΔP (MPa)	ω (rad/s)	Ideal Torque(N-m)	Actual Torque(N-m)	Ideal Flow(cm^3/s)	Actual Flow(cm^3/s)
A	4.43	10.47	32.4	21.0	81.9	84.2
B	5.44	10.47	39.8	26.4	81.9	85.6
C	4.47	18.33	32.7	20.7	143.4	140.3
D	5.56	18.33	40.7	26.6	143.3	141.2

Table 5. Test stand experimental results for the cross-conveyor motor.

Test Condition	ΔP (MPa)	ω (rad/s)	Ideal Torque(N-m)	Actual Torque(N-m)	Ideal Flow(cm^3/s)	Actual Flow(cm^3/s)
A	1.79	12.57	64.1	28.0	317.9	319.2
B	3.26	12.57	101.4	59.1	317.9	324.2
C	1.70	16.55	61.8	26.9	418.6	426.7
D	3.30	16.55	102.5	57.4	418.6	435.0

Table 6. Test stand experimental results for the flipper motor.

Test Condition	ΔP (MPa)	ω (rad/s)	Ideal Torque(N-m)	Actual Torque(N-m)	Ideal Flow(cm^3/s)	Actual Flow(cm^3/s)
A	2.19	4.190	102.5	78.6	195.6	237.8
B	3.86	4.190	179.5	140.3	195.6	251.1
C	2.25	5.760	105.3	73.0	268.8	272.5
D	3.30	16.55	102.5	57.4	268.8	287.1

Table 7. Motor torque loss coefficients.

Motor	C_{vd}	$C_f(\omega_{min})$	$C_f(\omega_{max})$	T_c (N-m)	D_m (cm^3/rad)
Disk-cutter	0.225	0.312	0.308	2.20	7.30
Flipper	5.9	0.20	0.074	12.46	46.68
Accumulator	2.30	0.219	0.115	18.00	58.94
Cross Conveyor	1.53	0.167	0.249	5.74	25.30
Gathering Chain	3.665	0.133	0.073	2.70	38.86

Table 8. Motor flow loss coefficients

Motor	$C_{si}(\omega_{min})$	$C_{si}(\omega_{max})$	$1/R_{exm}$[1]
Disk-cutter	.0053	.0031	
Flipper	.0052	.0063	
Accumulator	.0054	.0017	
Cross Conveyor	.0048	.0062	
Gathering Chain	.0012	.0022	1.70

[1]- External leakage bond graph resistor

5.1.2 Pump Characteristics

Pump characteristics were based on the same equations developed for a motor, except that pump inputs and outputs are reverse that of the motor. Flow rate output from the pump is

$$Q = D_p\omega - \frac{C_s(\omega)D_p\Delta P}{\mu} - Q_c \qquad [5.9]$$

and torque input at the pump driveshaft is

$$T_o = D_p\Delta P + C_f(\omega)D_p\Delta P + C_{vd}\mu\omega D_p + T_c + J\frac{d\omega}{dt} \qquad [5.10]$$

Resources were not available to build a pump test stand to measure pump characteristics experimentally. Therefore, to determine the torque and flow rate loss coefficients, pump characteristics were taken from the manufacturers volumetric and mechanical efficiency curves. Data was taken at four operating conditions, as was done for the motors, to determine the velocity dependent coulomb friction and flow slippage losses. The minimum (ω_{min}) and maximum (ω_{max}) speeds were chosen to encompass the speeds used when experimental data was collected on the harvester.

Torque and flow rate values for the four test conditions (A,B,C, and D) were taken from the manufacturer's efficiency curves. A combined performance curve was given by the manufacturer for the double pump assembly. The disk-cutter gear pump did not have performance data available. Assuming the three gear pumps were similar, one set of loss coefficients were determined and used for each one. Each variable displacement pump had loss coefficients determined separately, based on manufacturers data (Table 9 through 11).

Coulomb friction losses were calculated at ω_{min} by substituting data from test conditions A and B into Eqn. (5.10) to obtain

Table 9. Gear pump data taken from manufacturer's volumetric and mechanical efficiency curves.

Test Condition	ΔP (MPa)	ω (rad/s)	Ideal Torque(N-m)	Actual Torque(N-m)	Ideal Flow(cm^3/s)	Actual Flow(cm^3/s)
A	4.14	167.5	18.6	24.8	1005.0	879.5
B	20.70	167.5	113.0	124.2	1005.0	879.5
C	4.14	200.0	19.0	24.8	1193.5	1078.8
D	20.70	200.0	115.0	124.2	1193.5	1078.8

Table 10. Gathering chains variable displacement pump data taken from the manufacturer's volumetric and mechanical efficiency curves

Test Condition	ΔP (MPa)	ω (rad/s)	Ideal Torque(N-m)	Actual Torque(N-m)	Ideal Flow(cm^3/s)	Actual Flow(cm^3/s)
A	6.88	157.1	44.6	51.0	1015.7	975.4
B	20.65	157.1	133.8	145.8	1015.7	944.5
C	6.88	209.4	44.6	50.4	1354.5	1300.3
D	20.65	209.4	133.8	142.2	1354.5	1260.0

Table 11. Cross conveyor variable displacement pump data taken from the manufacturer's volumetric and mechanical efficiency curves.

Test Condition	ΔP (MPa)	ω (rad/s)	Ideal Torque(N-m)	Actual Torque(N-m)	Ideal Flow(cm^3/s)	Actual Flow(cm^3/s)
A	1.00	157.1	3.2	4.3	502.7	495.7
B	13.80	157.1	43.5	46.7	557.0	495.7
C	1.00	209.4	3.2	5.0	667.5	660.8
D	13.80	209.4	43.5	46.8	712.9	660.8

$$C_f(\omega_{\min}) = [\frac{T_a - T_b}{\Delta P_a - \Delta P_b}]\frac{1.0}{D_p} - 1.0 \qquad [5.11]$$

In like manner, data from test conditions C and D were used to calculate coulomb friction losses at ω_{max}.

$$C_f(\omega_{\max}) = [\frac{T_c - T_d}{\Delta P_c - \Delta P_d}]\frac{1.0}{D_p} - 1.0 \qquad [5.12]$$

Subsequently, as with the motors, these two coulomb friction coefficients were used to find the coefficient at any speed using linear interpolation and extrapolation. The viscous drag coefficient was calculated, using Eqn. (5.5), by substituting pump data instead of motor data.

The slip flow coefficient was not divided into external and internal losses when it was calculated. The volumetric efficiency data provided by the manufacturer did not discriminate between external and internal slippage flow. In addition, the three gear pumps did not have case drain lines, and therefore did not have external leakage flow. Slip flow at the minimum speed (condition A and B) was

$$C_s(\omega_{\min}) = \frac{Q_a - Q_b}{\Delta P_b - \Delta P_a}\frac{\mu}{D_p} \qquad [5.13]$$

By using test condition C and D, the slip flow loss coefficient was

$$C_s(\omega_{\max}) = \frac{Q_c - Q_d}{\Delta P_d - \Delta P_c}\frac{\mu}{D_p} \qquad [5.14]$$

Resulting torque and flow losses derived from Eqns. (5.11) through (5.14) are given in Table 12 and Table 13, respectively. For the variable displacement pumps, the slip flow coefficients were divided in half and used to represent the external and internal flow losses. The difference in the loss coefficients at ω_{min} and ω_{max} were small and, subsequently, average values were used for the simulation. The bond graph representation of the losses were discussed in Section 4.2.2.4. R_{slp} represented gear

Table 12. Torque loss coefficients for pumps derived from manufacturer's data.

Pump	C_{vd}	$C_f(\omega_{min})$	$C_f(\omega_{max})$	T_c (N-m)
Gathering Chains	0.132	0.050	0.034	1.20
Cross Conveyor	0.150	0.066	0.031	1.67
Gear Pumps	0.134	0.051	0.036	0.0

Table 13. Flow loss coefficients for pumps derived from manufacturer's data.

Pump	$C_{si}(\omega_{min})$	$C_{si}(\omega_{max})$
Gathering Chains	0.02	0.02
Cross Conveyor	0.0105	0.0137
Gear Pumps	0.0407	0.0340

pump slip, and R_{inp} and R_{exp} represented internal and external flow losses in the variable displacment pumps.

5.1.3 Cylinder Parameters

Cylinder performance including rod velocity (U_1), and force generated at the rod end (F_L), were described in Eqns. (4.32) and (4.33). These equations are repeated here.

$$U_1 A_c = Q_1 - Q_L \qquad [5.15]$$

$$F_L = P_1 A_c - K_{cfc} F_L - K_{vdc} U_1 - P_2 A_r \qquad [5.16]$$

Performance data was not found for the cylinders used. Resources to experimentally measure cylinder performance, as was done for the hydraulic motors, were not available. Henke (1983) gives a mechanical efficiency between 70 and 90 percent for cylinders at no load and rated load, respectively. Dransfield (1981) gave a value for the viscous drag coefficient to be K_{vdc} = 1.57 x 10^3 N-s/m. Lack of a better approximation led to the use of this value. The coulomb friction is derived from the rod and rod piston sliding against the cylinder. The coefficient of friction for steel sliding on steel (with a lubrication film) is 0.005. Putting the coulomb and viscous drag coefficients into Eqn. (5.16) gives

$$F_L = P_1 A_c - 0.005 F_L - 1.57x10^3 U_1 - P_2 A_r \qquad [5.17]$$

In the bond graph representation, the resistors take the value of the loss coefficients,

K_{cfc} = R_{cfc} = 0.005, and

K_{vdc} = R_{vdc} = 1.35 x 10^3.

These values were used for all the cylinders. Two cylinders acting in parallel were represented by one set of parameters representing the combined effects. Equivalent resistor coefficients (R_{eq}) were

$$\frac{1}{R_{eq}} = \frac{1}{R_1} + \frac{1}{R_2} \qquad [5.18]$$

where R_1 is resistance of one cylinder and R_2 is the resistance of the other. The equivalent resistance value for parallel cylinders is

R_{cfc} = 0.00025, and

R_{vdc} = 6.75 x 10^2.

Cylinder volumetric efficiency was estimated to be 95 percent. Flow loss develops from flow slippage around the cylinder piston, and is a function of the pressure differential between the cap and rod end. The relationship, given in Eqn (4.31), is repeated here,

$$Q_L = C_k\sqrt{\Delta P} \qquad [5.19]$$

The discharge coefficient, C_k, is equivalent to R_{cls} in the bond graph model representing a cylinder (Section 4.2.3). The resistor was calculated at one flow rate and pressure. Using Eqn. (5.15) and the volumetric efficiency, the resistor value was calculated at Q_1 = 500 cm^3/s and ΔP = 4.14 MPa, and found to be R_{slc} = 12.31. If the equation was linearized by using ΔP instead of $\sqrt{\Delta P}$, R_{slc} was 6.04. For the linearized equations, values of flow loss would be in error at flow rates and pressures other than 500 cm^3/s and 4.14 MPa. The linearization was justified by the fact that it reduced the stiffness and thus allowed the time step in the simulation to be increased. The error introduced, relative to the overall flow rate, was very small.

5.1.4 Line Segment Parameters

Three parameters were used to describe combined line conductor and fluid characteristics. The hydraulic lines were divided into segments and modeled by resistors, inertias, and capacitors. Justification for using a lumped parameter model to represent line segments was presented in Section 4.2.5.

Hydraulic line capacitance represents compressibility of the fluid and expandability of the hose or tubing. The capacitance value depends on the volume of fluid and effective bulk modulus of the fluid and conductor. The capacitor constitutive equation is

$$P = \frac{1}{C}\int \Sigma Q dt \qquad [5.20]$$

where

P = the pressure (MPa).

The integral of the sum of flow rates (ΣQ) is the change in volume (ΔV). Eqn. (5.20) can be rewritten as

$$P = \frac{\Delta V}{C} \qquad [5.21]$$

The bulk modulus (β) defines the compressibility of a fluid volume under pressure, and by definition is

$$\beta = V\frac{P}{\Delta V} \qquad [5.22]$$

Substituting ΔV from Eqn. (5.21) into Eqn. (5.22) and solving for P gives

$$P = \frac{\beta_e PC}{V} \qquad [5.23]$$

Solving for the capacitance,

$$C = \frac{V}{\beta_e} \qquad [5.24]$$

where V is the fluid volume and β_e is the equivalent bulk modulus of the fluid and conductor. Fluid bulk modulus is a function of fluid type, air entrainment, and fluid temperature. Merritt (1966) gave a value of 690 MPa for β_e, and this value gave satisfactory results in the system simulations.

Line resistance results in pressure losses, which are functions of the fluid velocity, viscosity, wall roughness, and line geometry. Resistance in a long thin tube is,

$$R_L = \frac{128\mu L}{\pi d^4} \qquad [5.25]$$

where

μ = fluid viscosity (N-s/m^2),

L = line segment length (m), and

d = line inside diameter (m).

Losses in hose bends were found by determining resistance for a 90° elbow and applying the result generally to other pressure losses due to change in direction of flow (e.g. tees). Miller (1970) did extensive testing of the fluid flow under specific conditions and found head loss (h_f) due to a 90° elbow was

$$h_f = \alpha_b K_b \frac{U^2}{2g} \qquad [5.26]$$

where

h_f = head loss (m),

α = correction factor for the Reynolds number (dimensionless),

K_b = loss coefficient at a Reynolds number of 10^6 (dimensionless), and

U = fluid velocity (m/s).

α_b is used to adjust the loss coefficient, K_b, for flow at Reynolds numbers other than 10^6, and is given by,

$$\alpha_b = \left(\frac{Re}{10^6}\right)^{-0.17} \qquad [5.27]$$

Eqn. (5.26) can be written in terms of flow rate and pressure by multiplying by the cross-sectional area of the conductor (A) and dividing by fluid density (ρ). The pressure loss (P_{loss}) is

$$P_{loss} = R_1 Q^2 \qquad [5.28]$$

where

$$R_1 = \frac{\alpha_b K_b}{\rho 2 g A^2} \qquad [5.29]$$

and ρ is the fluid density (kg/m^3). When the Q^2 term [Eqn. (5.28)] was implemented into TUTSIM, a very small time step had to be used to keep the model stable. The simulation time was increased beyond practical limits due to the instability. A small error in the pressure loss was incurred by linearizing Eqn. (5.28) and thus allowing an increase of the time step. Pressure loss was calculated from Eqn. (5.28) at a mean flow rate (Q_{mean}), determined by steady-state estimation of the flow. Eqn. (5.28) was re-written

$$P_{loss} = R_2 Q_{mean} \qquad [5.30]$$

and R_2 was evaluated from the calculated P_{loss} by

$$R_2 = \frac{R_1 Q_{mean}^2}{Q_{mean}} = R_1 Q_{mean} \qquad [5.31]$$

Consequently, R_2 was exact at a flow rate equal to Q_{mean}. As the actual flow rate, Q, deviated from Q_{mean}, the pressure loss was less accurate. Total pressure loss in a line segment is

$$P_{loss} = xR_2Q + R_LQ = (xR_2 + R_L)Q \qquad [5.32]$$

where x is the number of elbows, bends, and tees in the line segment. Resistance R_{Li} used in each model was

$$R_{Li} = (xR_2 + R_L) \qquad [5.33]$$

where i is the line segment number.

Fluid inertia represents the fluid mass in a conductor of a particular cross-sectional area (A) and length (L). It can be calculated from analysis of the force to move the fluid through the line. Newton's law states

$$F = M\frac{d\dot{x}}{dt} \qquad [5.34]$$

where

$\dot{x}$ = fluid velocity (m/s),

M = fluid mass (kg), and

F = force to move the flow (N).

Substituting M = ρLA, and Q = $\dot{x}$/A into Eqn. (5.34) gives,

$$F = \frac{\rho LA}{A}\frac{dQ}{dt} \qquad [5.35]$$

or

$$F = \rho L \frac{dQ}{dt} \qquad [5.36]$$

where

Q = flow rate (m^3/s),

ρ = fluid density (kg/m^3), and

F = force to accelerate fluid (N).

Developing Eqn. (5.36) in terms of pressure (P) gives

$$P = \frac{\rho L}{A} \frac{dQ}{dt} \qquad [5.37]$$

Using the constitutive equation for inertia (Appendix A), Q is derived from the equation,

$$Q = \frac{A}{\rho l} \int \Sigma P dt \qquad [5.38]$$

which gives the fluid inertia (I) as,

$$I_L = \frac{\rho L}{A} \qquad [5.39]$$

where A is the cross-sectional area of the fluid flow (m^2).

5.1.5 Valve Parameters

Relief valves, check valves, and a 3-section DCV were modeled. Each was represented by resistors, or combinations of resistors with non-linear characteristics. Non-linear parameters increase the model stiffness, reduce the required step-size, and increase the simulation run-time. Each valve and its parameters are discussed.

A pressure relief valve was used in each actuating circuit. Relief valve flow rate is a function of the pressure difference across the valve. The valve opens when the pressure differential reaches the relief setting. Although the valves were not tested, their characteristics were included to represent dampening effects on the system. It was found that the relief valve provided damping to reduce oscillations in the actual circuit. Relief valves begin opening and leak some flow below the relief setting. Pressure at which flow begins leaking is referred to as the "cracking pressure". The valves used were pilot-operated; therefore, the pressure difference between cracking and full-open pressure was much less than for a direct-acting relief valve. The relief valve setting was represented by a resistor with characteristics input with by a FNC block to account for non-linearities. Line pressure was input to the FNC block and output was flow rate through the valve. Figure 35 shows a typical flow rate (Q) vs. pressure (P) curve. By taking points along the curve, the FNC block inputs and outputs were determined.

Check valves are integral to variable displacement pumps. They allow flow into the main pump return line from the charge circuit. The charge circuit pressure is maintained at 1.0 MPa, and extra flow is relieved through the charge circuit relief valve. The check valve is a one-way flow valve which prevents main circuit flow from entering the charge circuit, but allows flow in the reverse direction (charge circuit to main circuit). A bond graph resistor was used in conjunction with a FNC block to model the non-linear characteristics. Flow as a function of pressure across the check valve is shown in Figure 36. Check valves in the charge circuit readily open to allow flow at a relatively small pressure differential, thus insuring that flow is available to keep the main circuit filled and prevent cavitation of the main pump.

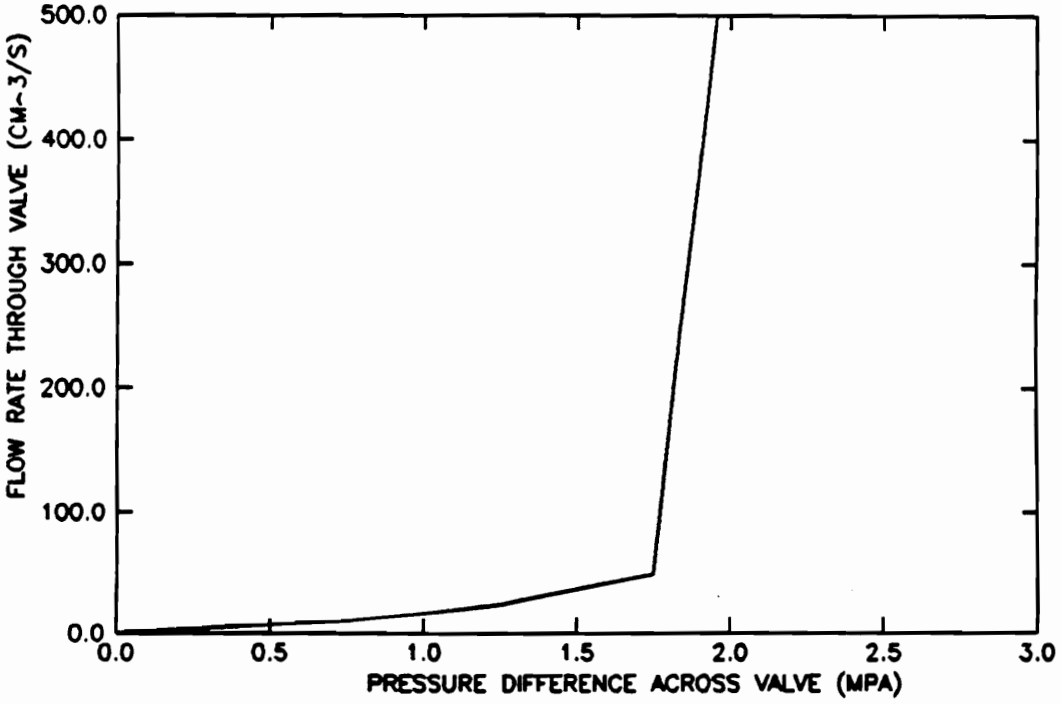

Figure 35. Flow rate (Q) vs. pressure (P) used for relief valve.

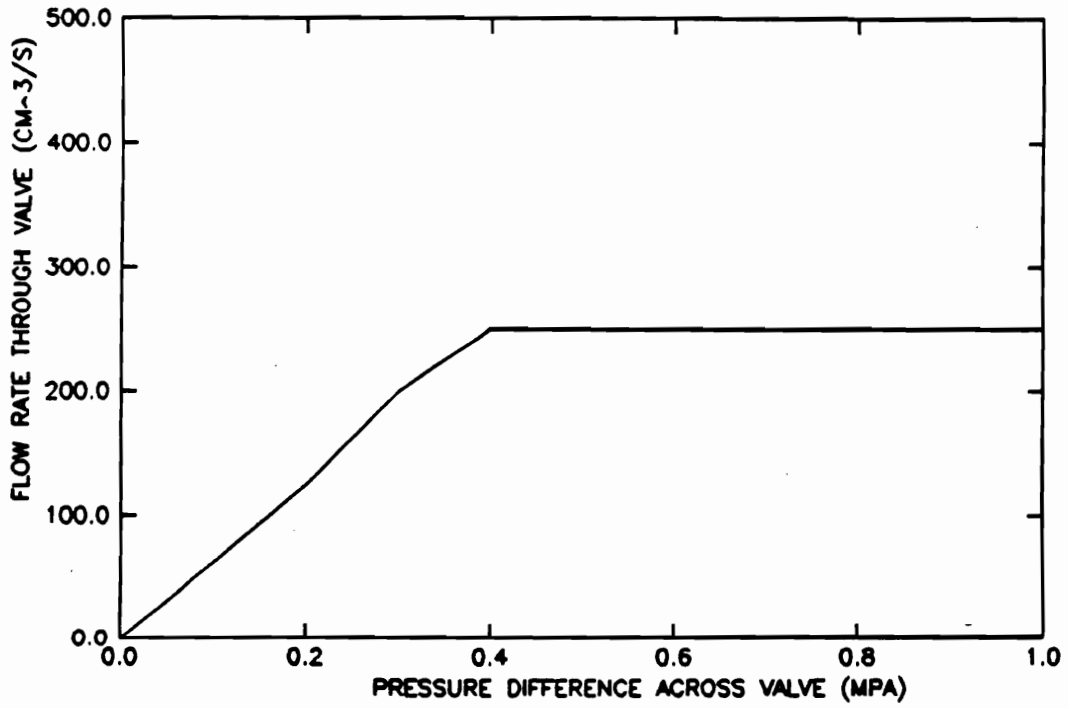

Figure 36. Flow rate (Q) vs. pressure (P) curve used for check valve.

5.2 Mechanical Model Parameters

5.2.1 Input Drive

Drive parameters were determined by examining the torque to drive the gathering chains when the tractor was positioned relative to the harvester at three different angles. Driveline angles were selected to duplicate driveline geometry when the harvester was being pulled around a turn in the field; therefore, the angles and torque measured were indicative of actual field conditions. The driveline angles were measured with the tractor pulling the harvester straight ahead (test condition one), and with the tractor pulling the harvester in a left turn at two angles; the maximum angle achievable (test condition three), and 1/2 the maximum turn angle (test condition two). The resulting driveline angles were measured at joint 1 and joint 2 (Figure 5) for each test condition (Table 14).

Experimental torque results for the three driveline conditions are shown in Figure 37. The torque amplitude increased as the joint angles in the driveline become larger. For test angle three, the torsional vibration showed significant peaks. A Fast Fourier Transform (FFT) analysis of each test condition (Figure 38) revealed the dominant excitation frequencies. Peaks were exhibited at 13 and 26 Hz for all three test conditions. The 26 Hz vibration corresponded to two cycles per revolution, which was the frequency of torsional vibration produced by Cardan joints operating at angles [See Eqn. (4.1)]. The 13 Hz frequency became more prominate as the driveline angle increased. In Figure 38 (a), the excitation was not well defined, however at test condition three, the 13 Hz peak was larger than the 26 Hz peak. In addition, higher harmonics of the driveline frequency (13,26,39,...etc.) were more defined as the joint angles increased.

A separate analysis was conducted to reduce the noise in the FFT of the experimental data. One cycle of the measured torque, including a major and minor peak, was used to create a 20 term

Table 14. Driveline joint angles for three test conditions

Test Condition	Joint 1 Angle (deg)	Joint 2 Angle (deg)
One (Straight Ahead)	5.5	8.5
Two (1/2 Maximum Left Turn)	11.5	8.0
Three (Maximum Left Turn)	20.0	6.5

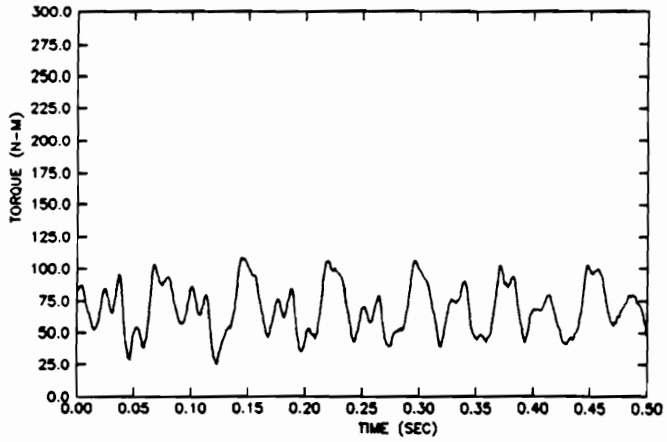

(a)

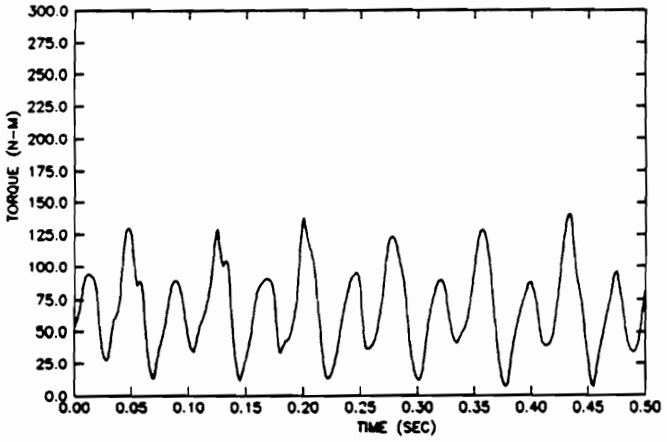

(b)

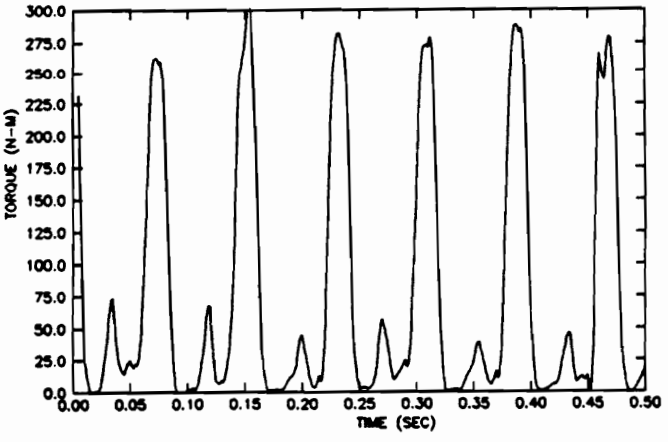

(c)

Figure 37. Torsional vibration measured for (a) test condition one, (b) test condition two, and (c) test condition three.

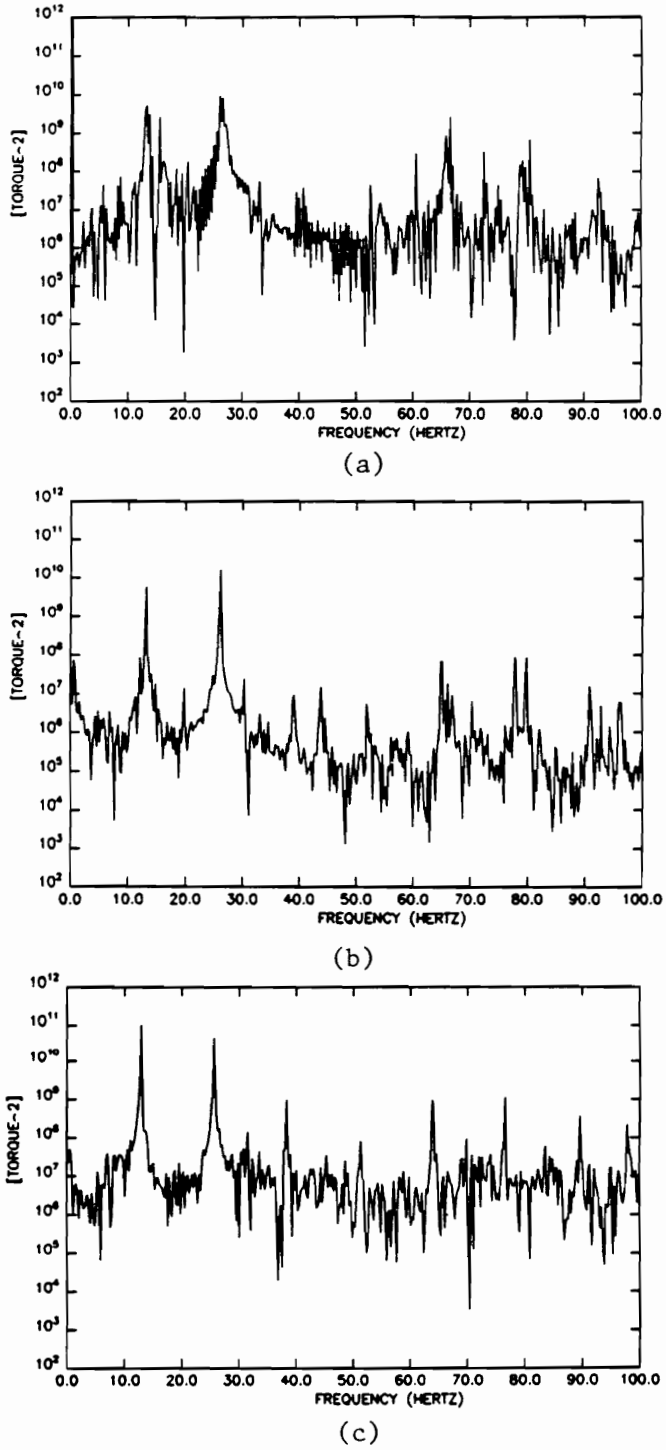

Figure 38. FFT of torsional vibration in (a) test condition one, (b) test condition two, and (c) test condition three.

Fourier series. The Fourier series was used to recreate 10 seconds of torque data, and an FFT of this data was run for test conditions one and three (Figure 39). 13 and 26 Hz peaks were found in both analyses, and the peaks were larger for test condition three. The higher order harmonics were also still apparent. The results were the same as the FFT of the experimental data, absent the noise, and showed that the experimental data could be re-created with a series of harmonic functions. The predominate frequencies of the Fourier series was the same as that found in the experimental data.

Standard driveline theory only discusses the velocity fluctuations caused by the kinematic relationship between the input and output shaft of a Cardan joint operating at an angle. It was proposed in Chapter 4 that the lateral deflection of the shaft caused by mass unbalance, and the secondary coupling associated with Cardan joints, created a varying inertia which affects the driveline torsional dynamics. Other effects are the backlash in the connecting couplings and gears in the tractor, and non-linear V-belt compliance. The torsional vibration at 26 Hz was expected. The 13 Hz vibration was not expected, and was determined to be a function of shaft whirl magnitude, whirl velocity, and non-linear V-belt compliance. The unknown quantities are U,V,$\dot{\gamma}$(Figure 7), and the V-belt stiffness.

The shaft whirl was visually observed when the driveline was operating at test condition three. U was chosen at approximately 1/2d for test condition three, where d was the shaft diameter. For test condition one and two, U was set to 1/8d, and 1/4d, respectively. After several simulations and comparisons of simulated and experimental results, it was determined that V should be chosen very small, on the order of 1×10^{-6}. This choice implies that the bearing supports were stiff in the vertical plane and relatively soft in the horizontal plane.

To force the inertia to cycle once per revolution, the whirl velocity was set at one-half the shaft angular velocity. This choice gave the inertia a one cycle per shaft revolution frequency, which was equal to the 13 Hz frequency seen in the FFT analysis.

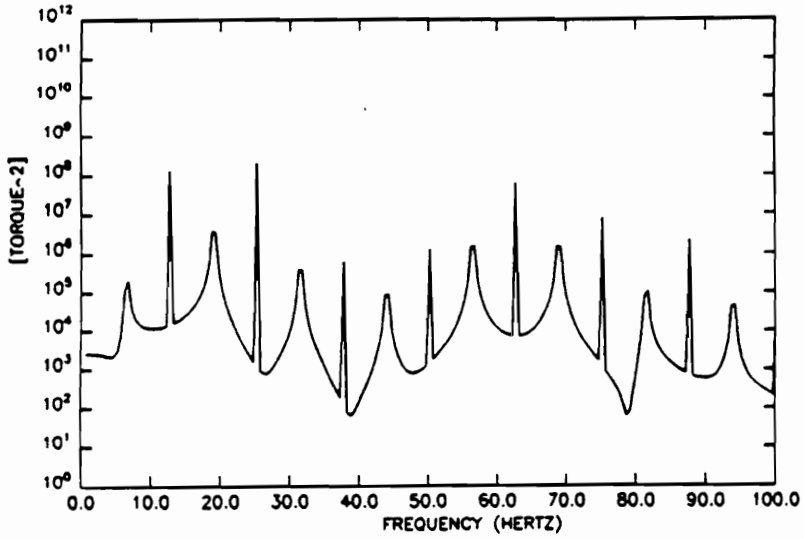

(a)

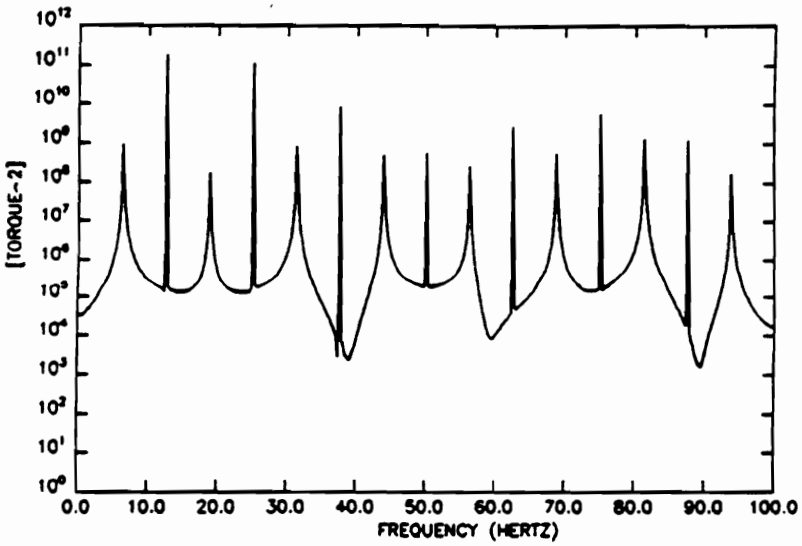

(b)

Figure 39. FFT of Fourier series representation using one pulse the experimental data for (a) test condition one, and (b) test condition three.

Backlash was added for the entire driveline, and the V-belt was modeled as a spring hardening component. A non-linear compliance, shown in Figure 40, was used for the driveline. The amount of backlash and spring-hardening were estimated. The inital V-belt compliance was taken from a report by Peeken and Fischer (1989).

5.2.2 Bearing Parameters

Self-aligning roller bearings and journal bearings were the only types of bearings used to support the various shafts. Torque was required to overcome friction in these bearings. The following illustrates the procedure used to determine bearing friction for each type.

Roller bearing friction torque was described by Eschmann et al. (1985) as

$$M = \frac{\mu F d}{2} \qquad [5.40]$$

where

M = friction torque (N-m),

μ = coefficient of friction (decimal),

F = bearing radial load (N), and

d = bearing bore diameter (m).

The value reported by Eschmann et al. (1985) for the coefficient of friction in a roller bearing was 0.002. The bearing load (F) was estimated from the tension in the V-belts and chains. The bond graph resistor used to represent bearing friction is

$$R_b = \frac{\mu F d}{2} \qquad [5.41]$$

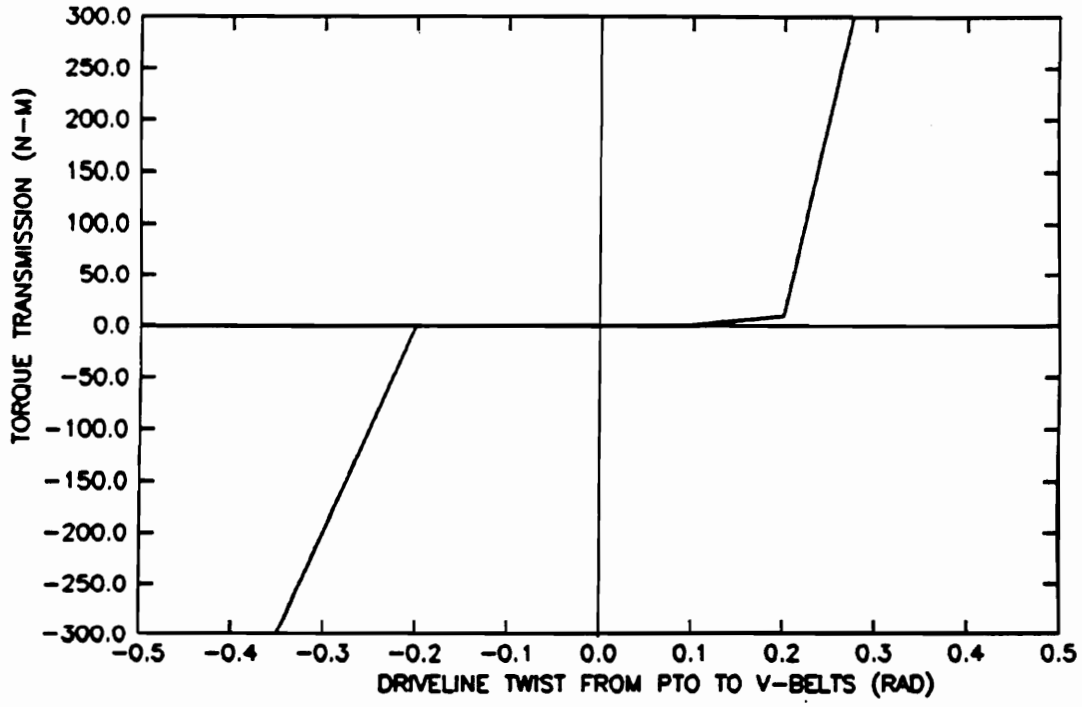

Figure 40. Torque vs. shaft twist used to represent backlash and non-linear V-belt compliance.

The journal bearings consisted of brass sleeves mounted inside the bearing bore. The shaft was slipped inside the brass sleeve. With a radial load, friction was caused by contact between the brass sleeve and the shaft. The coefficient of sliding friction for brass on steel is 0.4. The general force equation between two flat metal pieces sliding against each other is

$$F_L = \mu N = \frac{uFd}{2} \qquad [5.42]$$

where

N = normal force, or radial load (N),

μ = coefficient of friction, and

F_L = bearing force to overcome friction (N).

Estimating the radial load (N) and then determining F gave the force to overcome friction. Multiplying F by the radius of the bearing determined the friction torque.

5.2.3 Chain and Shaft Compliance

Chain and shaft compliance were included in the model primarily to prevent algebraic loops in the simulation. However, these parameters were calculated as close to the actual values as was possible, and were significant in some simulations.

Chain compliance was developed assuming that the weakest point on a chain occurred in the link plates. These plates were flat metal bars. The following steps led to the values for chain compliance (C). Chain stretching was estimated to be the change in length of the link plates,

$$\Delta L = \frac{F\Sigma L}{AE} \qquad [5.43]$$

where

ΔL = change in chain length (m),

F = chain tension (N),

A = cross-sectional area of link plates (m^2),

ΣL = sum of link plate lengths for entire chain (m), and

E = modulus of elasticity of steel (N/m^2).

Substitution of $r\Delta\theta = \Delta L$ into Eqn. (5.43), where r is the sprocket radius, gives the change in sprocket rotation ($\Delta\theta$) due to chain stretching. Torque on the sprocket is T = Fr. Substituting into Eqn. (5.43) and solving for T gives

$$T = \frac{r^2 \Delta\theta AE}{\Sigma L} \qquad [5.44]$$

Using the capacitor constitutive equation, the capacitors value for chain compliance (C) is

$$C = \frac{\Sigma L}{r^2 AE} \qquad [5.45]$$

When these C values were evaluated, they were very small and created a stiff model. It was then determined that the shaft compliance should be added to the chain compliance to help reduce model stiffness. Torsional twist of a shaft is defined by

$$\phi = \frac{TL}{JG} \qquad [5.46]$$

where

ϕ = angle of twist (rad),

L = length of shaft (m),

J = polar moment of inertia ($kg\text{-}m^2$),

G = modulus of rigidity (N/m^2), and

T = torque (N-m).

By equating Eqn. (5.46) to the constitutive equation for a capacitor, the value for the shaft compliance is

$$C = \frac{L}{JG} \qquad [5.47]$$

Since chain and shaft compliance act in series, they may be added directly to get an effective compliance (C_t), given by

$$C_t = \frac{L_{chain}}{r^2 AE} + \frac{L_{shaft}}{JG} \qquad [5.48]$$

5.2.4 Mass/Inertia and Load

Because of inertia, torque is required to accelerate or decelerate a load. The polar moment of inertia of shafts, sheaves, sprockets, loads, and pump/motor internal parts were included in the bond graph models. In some cases, the inertia made a significant contribution to the predicted response. Inertia and loads due to gravity are presented in this section.

5.2.4.1 Shaft, Sheave, and Sprocket Inertia

Sprocket and sheave inertias were obtained by contacting the manufacturers of the components. Shaft inertias were computed by

$$I_{xx} = 1/2mr^2 \qquad [5.49]$$

where

I_{xx} = shaft mass moment of inertia (kg-m^2),

m = mass of the shaft (kg), and

r = shaft radius (m).

5.2.4.2 Pump/Motor Inertia

Inertia of the gathering chains variable displacement pump was given by the manufacturer. Other pump and motor inertias were unavailable from manufacturers and were estimated. Compared to the load inertias, the pump and motor inertias were very small. Consequently, this estimation did not affect the model results significantly.

5.2.4.3 Accumulator Mass and Inertia

The inertia of the accumulator bin was calculated using the construction drawings. The accumulator was broken into simple geometric parts for which standard equations were already developed. Mass moment of inertia was calculated about the centroidal axis for each part. The parallel axis theorem was then used to calculate the mass moment of inertia about the accumulator shaft

$$I = \bar{I} + md^2 \qquad [5.50]$$

where

I = inertia about the accumulator shaft (kg-m^2),

$\bar{I}$ = inertia about the centroid of the part (kg-m^2),

m = mass of the part (kg), and

d = distance from the centroid of the part to the accumulator shaft centerline (m).

The total accumulator inertia about the shaft centerline was the sum of the individual part inertias.

Torque due to gravitational force was calculated by determining the centroid of the bin and assuming the total weight acted through the centroid. The changing angle and resultant movement of the stalk bundle were discussed in Section 4.2.6.1.

The accumulator cylinder moved the accumulator bin in and out in a horizontal direction; consequently, it did not have to lift the accumulator against the force of gravity. R_{acc} was calculated by multiplying total accumulator weight (frame plus support beams) by the sliding friction coefficient. The mass was input as I_{acc} in the accumulator cylinder drive model (Section 4.2.6.3).

5.2.4.4 Cross Conveyor

The actual mass of the cross conveyor was calculated by adding the mass of each individual piece used in its construction. This mass was used to determine the force required by the cylinder to change the conveyor angle. The center-of-gravity position was estimated and identified as $\bar{x}$ in Figure 22.

Mass of the conveyor chains were used to calculate inertial load on the conveyor motor. Mass of the stalks carried by the cross conveyor was added to chain mass in the calculation of the total inertia. A variable inertial and load term were used in the model to investigate the influence of changing stalk load. Section 4.3 discusses the non-linear capability of TUTSIM which were used for the inertial term. The inertia and load on the conveyor is a function of the rate at which stalks are flipped onto the cross conveyor and thrown off the conveyor into the accumulator. Force (F) on a moving flat conveyor with a changing mass is

$$F = \frac{dp}{dt} = V\frac{dm}{dt} \qquad [5.51]$$

where

p = conveyor momentum (N-s),

m = mass on the conveyor (kg), and

V = conveyor velocity (m/s).

By rearranging the terms and integrating,

$$(\int Fdt = mV) = (\frac{1}{m}\int Fdt = V) \qquad [5.52]$$

which is the constitutive equation for the mass bond graph element. The load created by stalks landing onto the conveyor can be incorporated, if the mass (m) is known as a function of time. Stalks are carried up the conveyor by the spikes attached to chain tabs spaced 33 cm apart. There are six spikes on the top side of the conveyor at any one time. As stalks are flipped onto the cross conveyor, they are picked up by the chain spikes, carried to the top of the conveyor, and thrown into the accumulator bin. The mass of stalks on the conveyor can be approximated as a sinusoid (Figure 41). The amplitude and average value are functions of conveyor speed and stalk density, assuming the flipper and gathering chains speed remain constant. For the speeds examined, two stalks and four stalks per spike were simulated. The force required to push the weight of stalks up the conveyor is

$$F_{sw} = Nmg\sin(\theta) \qquad [5.53]$$

where

F_{sw} = force to overcome gravity (N),

m = mass per stalk (kg),

g = gravitational constant (9.81 m/s^2),

θ = conveyor angle (rad), and

N = number of stalks on conveyor.

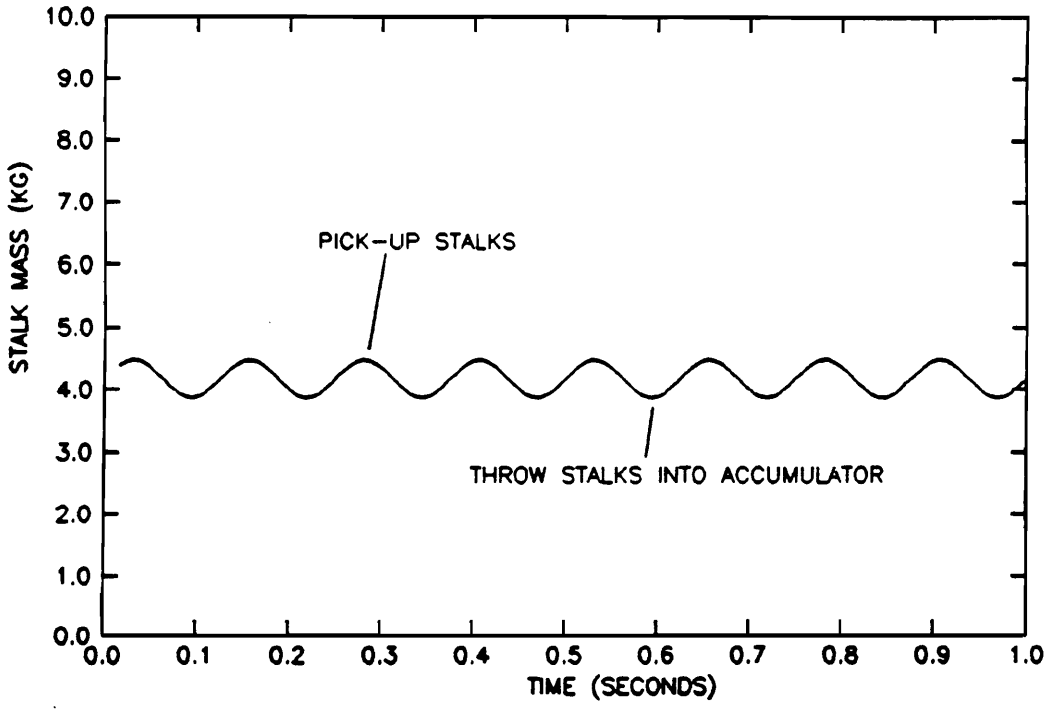

Figure 41. Stalk mass on cross-conveyor as a function of time.

The variable in this equation is the number of stalks on the cross conveyor. For two stalks per spike, the number of stalks varied from 12 to 14. Given a stalk mass function like that shown in Figure 41, a value of F_{sw} was determined.

5.2.4.5 Gathering Chains

The inertia of the gathering chains was added to the motor inertia, J_m. Stalk load on the gathering chains was equal to the weight of approximately 30 stalks, which would be the maximum carried while harvesting. The stalk weight was added to the effort source term, W_{st} in the gathering chains load model. Stalk mass would not signifiacntly affect the model if the gathering chain velocity is equal to ground speed.

5.2.4.6 Stalk Flipper

The stalk flipper mass (J_{sf}) includes the flipper discs and the mass of the stalks. The stalk mass was considered constant; i.e. as a stalk was released another stalk was grasped. Observation during field tests showed that the stalks were grasped approximately 10 cm above the butt. The mass moment of inertia of the stalk in the flipper was calculated by

$$I = (\frac{ml^2}{3})N \qquad [5.54]$$

where

I = inertia about the butt of the stalk (kg-m^2),

N = number of stalks in the flipper,

m = mass of each stalk (kg), and

l = length of the stalk (m).

Stalk mass and length was measured for stalks selected from the field. Mean stalk mass was 0.66 kg and mean stalk height was 325 cm. Flipper disc mass moment of inertia was calculated using Eqn. (5.49). The stalk and flipper disc inertias were added together to simulate performance during field operation.

5.2.4.7 Disk-cutter

The disk-cutter drive had a constant inertia which was calculated from the disk mass and geometry. The disk was circular and mass moment of inertia about the axis through its center was calculated using Eqn. (5.49).

5.3 Experimental Procedures for Circuit Performance

Experiments were conducted to validate the bond graph models of each harvester circuit. Line pressure and return line flow rate were measured in the circuit and, torque and driveline speed were measured at the harvester input shaft. Tests were conducted at 1400 and 1600 tractor engine rpm (680 and 780 driveline rpm). The same speeds were also used for the field tests with the harvester. Predicted and experimental results are compared.

5.3.1 Instrument Calibration

A data acquisition system was assembled as shown in Figure 34. Each transducer was calibrated to insure accurate readings.

The pressure transducer had strain gauges on a diaphragm. Fluid pressure deflected the diaphragm and changed the voltage across a wheatstone bridge. The transducer had a shunt resistor which could be switched into the circuit to simulate a 27.5 MPa pressure. The transducer was calibrated by switching in the shunt resistor, and setting the amplifier for an output of 7v/27.5 MPa.

The torque transducer also had a wheatstone bridge circuit to sense angular deflection in the transducer shaft. An external resistor, supplied by the manufacturer, was connected inside the calibration bridge of the amplifier. The 683 kΩ resistor represented a torque of 772 N-m, and the amplifier gain was set to 6.833v/772 N-m. The shunt resistor was used to calibrate the output from the strain gauge amplifier before each test.

The flow meter manufacturer supplied calibration curves for three viscosities. Flow rate at each viscosity was provided as a function of frequency. League and Cundiff (1984) developed the calibration equation for a 1.27-cm diameter flow meter, which was used on the stalk flipper circuit. However, all the other circuits had 1.9-cm hoses and required a 1.9-cm diameter flow meter. The calibration equation for the 1.9-cm diameter flow meter was calculated based on the procedure used by League and Cundiff. The equation is a function of fluid viscosity and frequency (As the turbine in the flow meter rotates, a square wave is produced). Six coefficients were determined for the following equation,

$$Q = (C_o + C_1\mu_k + C_2\mu_k^2) + (C_3 + C_4\mu_k + C_5\mu_k^2)f \qquad [5.55]$$

where

Q = flow rate (cm^3/s)

C_i = determined coefficients,

μ_k = kinematic viscosity (centistokes), and

f = pulse frequency from flow meter (Hz).

The viscosity was determined from the fluid temperature and input to a FORTRAN program to determine the flow rate.

5.3.2 Circuit Measurements

Schematics of the circuits on the harvester were given in Figures 3 and 4. The position of the pressure and flow measurements is labeled in each figure. Measurements were made on each circuit separately (separate test runs). When collecting data on the multiple-3 pump circuits, the V-belts to the multiple-2 pump were disconnected, and vice-versa. The relief valves on the circuits not being measured were opened so that the pumps were essentially pumping fluid back to the reservoir and required only a small amount of torque.

5.3.2.1 Gathering Chains

The variable displacement pump of the multiple-3 assembly provided flow to the gathering chains. Gathering chains performance was measured while evaluating the dynamics of the input drive (See Section 5.2.1). The pressure transducer was placed between the pump output and the cross-over relief valve, and the flow meter was placed between the pump return and cross-over relief valve. Flow was measured by reading voltage pulses at 5000 pt/s. This sampling rate was chosen in an attempt to record the flow rate fluctuations caused by the driveline.

FFT analysis of the torque and pressure data was conducted to determine the excitation frequencies related to the modeled dynamics.

5.3.2.2 Cross Conveyor Chains

The variable displacement pump on the multiple-2 assembly provided flow to the cross conveyor motor. Data was taken for the tractor pulling the harvester straight ahead only. Pressure transducer and flow meter placement was identical to that used for the gathering chains circuit. Pressure and torque measurements were measured at 50 pts/s.

5.3.2.3 Directional Control Valve

The pressure transducer was placed at the DCV inlet and the flow meter was placed in the DCV return line. Ten seconds of data at 200 pts/s was taken as an individual spool in the 3-section DCV was shifted. For the accumulator motor, the valve was shifted to dump the accumulator with a 60 kg bundle of sweet sorghum stalks. The cycle was complete once the stalk bundle had completely cleared the accumulator. The second section on the DCV raised and lowered the cross conveyor and data for this circuit was taken when raising the conveyor only. The third section activated cylinders to move the accumulator in and out. Data was taken for moving the accumulator out only.

5.3.2.4 Stalk Flipper

The second pump of the multiple-3 pump provided flow to the stalk flipper circuit. A pressure transducer was placed at the inlet of the hydraulic motor, and a 1.27-cm diameter flow meter was placed in the return line. Flow was regulated by a flow control valve upstream of the motor. The stalk flipper was set to the speed which gave successful field operation. Measurements were made for ten seconds at 50 pts/s.

Chapter 6 Model Equations

Equations from the bond graph model are developed in this section. They were developed from the constitutive equations for the 1-port energy storage elements of the model (capacitors and inertias). Parameter values used for the model were discussed in previous chapters, and specific values are given in Appendix C.

6.1 Input Drive

The input drive was the same for all the individual circuit models. Rather than discuss the input drive for each circuit, it will be discussed here to avoid repeating the same information. The input drive sub-model is given in Figure 8 and notation used refers back to this figure.

A constant flow source models the angular velocity being delivered by the PTO shaft of the tractor. A modulated transformer changes the angular velocity from the PTO based on the angles of joint 1 and joint 2, and the driveline angle of rotation (β). The driveline and V-belt stiffness are represented by C_{dl} at 0-junction (1). The capacitor is a non-linear function with backlash and spring

hardening effects incorporated (See Section 4.2.1). Using the capacitor constitutive equation, torque at 0-junction (1) is

$$T_1 = \frac{1}{C_{dl}} \int (\omega_{in} - \omega_2) dt \qquad [6.1]$$

ω_{in} is the input velocity from the driveline that has been transformed by the driveline joint angles. ω_2 is the angular velocity determined by the moment of of inertia constitutive equation. J_o is the moment of inertia for the driveline and harvester input shaft. This inertia is a non-linear function of the shaft whirl characteristics and was calculated in Eqn. (4.4). The angular velocity of the harvester input shaft is

$$\omega_2 = \frac{1}{J_o} \int (T_1 - T_{b2} - T_{HIS}) dt \qquad [6.2]$$

T_{HIS} is the torque required to turn the harvester input shaft, and T_{b2} is the torque to overcome bearing friction.

The sheave ratio which increases the u-joint driveline speed to the pump driveshaft speed is represented by the transformer coupling 1-junction (2) to 0-junction (3). The torque input to the pump driveshaft is determined at 0-junction (3). The integral equation is determined from the constitutive equation for the pump driveshaft compliance, C_v. Torque input is

$$T_3 = \frac{1}{C_v} \int (2.5\omega_2 - \omega_{slv} - \omega_4) dt \qquad [6.3]$$

where

$2.5\ \omega_2$ = ideal angular velocity input to the pump driveshaft,

$\omega_{slv} = 1/R_{slv}T_3$ = slippage of V-belts on sheaves, and

ω_4 = pump driveshaft angular velocity.

C_v is the torsional compliance of the pump driveshaft. Torque in Eqn. (6.2) can be related to the angular momentum (H_o) at the harvester input shaft. H_o is defined as

$$\Sigma H_o = \int \Sigma \omega dt \qquad [6.4]$$

or

$$\Sigma H_o = \int (T_1 - T_{b2} - T_{HIS}) dt$$

6.2 Gathering Chains/Cross Conveyor Model

The gathering chains and cross conveyor are each closed circuit systems, and their completed bond graphs are given in Figures 42 and 43. The models are identical up to the motor and load description. In the following discussion, models for the gathering chains and conveyor chains will be examined together from the pump driveshaft angular velocity (1-junction (4)) to the flow input to the motor (1-junction (17)). Each motor and load will then be examined separately.

The pump driveshaft angular velocity is represented by 1-junction (4). The causality dictates that the velocity at this junction is determined by the constitutive equation for the inertia, J_p. This inertia includes the mass moment of inertia of the pump shaft, V-belt sheaves, and pump internal rotating parts. The integral equation is

$$\omega_4 = \frac{1}{J_p} \int [T_3 - T_{b3} - T_{cfp} - T_{vdp} - P_{10} D_{cp} - (P_6 - P_8) D_{vp} - S_{ptc}] dt \qquad [6.5]$$

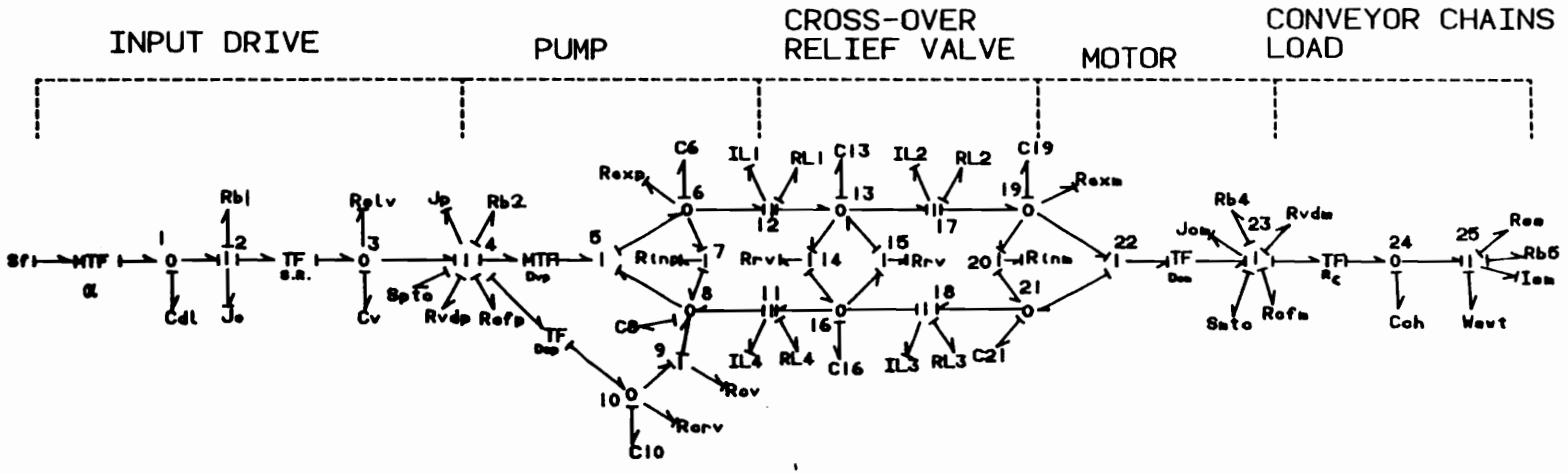

Figure 42. Bond graph model of cross-conveyor motor circuit.

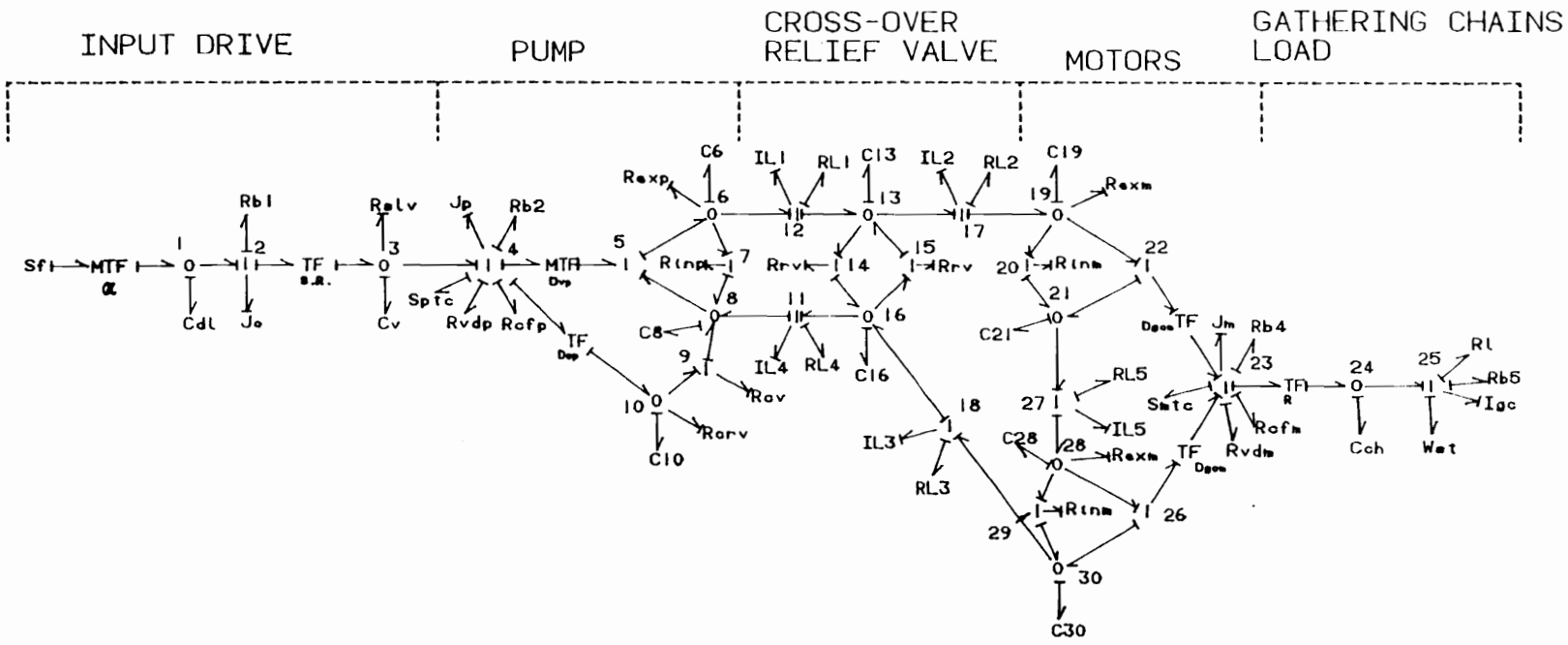

Figure 43. Bond graph model of gathering chains circuit.

where

T_3 = torque required to turn pump (N-m),

T_{cfp} and T_{vdp} = torque losses given by Eqn. (4.17) (N-m),

$T_{b3} = R_{b3}\omega_4$ = torque to overcome bearing friction (N-m),

$P_{10}D_{cp}$ = torque required to turn the charge pump (N-m),

$(P_6\text{-}P_8)D_{vp}$ = torque required to turn the main pump (N-m), and

S_{ptc} = pump torque constant (N-m).

The pump converts mechanical energy to hydraulic energy; consequently, it is appropriate to describe the input side as the mechanical side and the output side as the hydraulic side. P_{10}, P_6, and P_8 are pressures at their respective junctions on the hydraulic side of the pump. The pump torque constant (S_{ptc}) is the torque required to turn the gear pumps on the auxiliary mount.

The pump angular velocity in Eqn. (6.5) is defined by the integral of net torque divided by the pump inertia (J_p). Angular velocity of the pump driveshaft, ω_4, when multiplied times pump displacement, gives the ideal flow rate from the pump. D_{vp} is the pump displacement set by the swashplate angle and is represented by the modulus of the MTF.

Examining the hydraulic side of the pump, 0-junctions (6) and (8) represent the pressure at the outlet and inlet ports of the main pump, respectively. The pressure at 0-junction (6) is,

$$P_6 = \frac{1}{C_6}\int (Q_5 - Q_7 - Q_{\exp} - Q_{IL1})dt \qquad [6.6]$$

where

Q_5 = $D_{vp}\omega_4$, ideal flow rate (cm^3/s),

Q_7 = $(1/R_{inp})(P_6\text{-}P_8)$, internal leakage flow (cm^3/s),

Q_{exp} = $(1/R_{exp})(P_6 - 0)$, external leakage flow (cm^3/s),

Q_{IL1} = flow into the first line segment (cm^3/s), and

C_6 = hydraulic compliance in the pressure line (cm^3/s).

R_{inp} and R_{exp} are resistors which represent leakage flow characteristics of the pump.

Similarly, P_8 is determined by

$$P_8 = \frac{1}{C_8}\int(Q_7 + Q_{11} + Q_9 - Q_5)dt \qquad [6.7]$$

where

Q_{11} = return flow from the motor to the pump (cm^3/s),

Q_9 = $(1/R_{cv})(P_8\text{-}P_{10})$, check valve flow ($cm^3/s$), and

C_8 = hydraulic compliance in the return line of the pump ($cm^3/s\text{-}MPa$).

P_8 is pressure in the return line entering the pump. Pressure is being increased by flow injected at the check valve (Q_9), internal cross-port leakage (Q_7), and return flow from the motor (Q_{11}). The charge circuit keeps the return line pressure above a certain threshold (1.0 MPa). The check valve opens and increases flow until P_8 reaches the charge circuit pressure. Flow is a function of the pressure difference between the charge circuit and the main circuit.

Charge circuit pressure is determined at 0-junction (10) and is calculated from the constitutive equation for the hydraulic line compliance (C_{10}), which is

$$P_{10} = \frac{1}{C_{10}}\int(D_{cp}\omega_4 - Q_{crv} - Q_9)dt \qquad [6.8]$$

where

$D_{cp}\omega_4$ = flow developed by the charge pump (cm^3/s), and

Q_{crv} = $(1/R_{crv})(P_{10}\text{-}0)$, = charge relief flow ($cm^3/s$).

Eqn. (6.8) shows that charge circuit pressure is relieved by flow through the check valve (Q_9), and flow through the relief valve (Q_{crv}). If the return line pressure of the main circuit (P_8) is above charge circuit pressure, flow from the charge pump goes through the charge relief valve. The charge relief valve setting determines the maximum pressure which can be built in the charge circuit.

A line segment at the pump outlet represents the flow leaving the pump (1-junction (12)). Flow rate is determined by the constitutive equation for the fluid inertia (I_{IL1}) in the line segment,

$$Q_{12} = \frac{1}{I_{IL1}} \int (P_6 - P_{RL1} - P_{13}) dt \qquad [6.9]$$

where

I_{IL1} = fluid inertia (s-MPa/cm^3),

$P_{RL1} = R_{L1} Q_{12}$ = pressure loss due to line resistance (MPa), and

P_{13} = pressure in the hydraulic lines at the cross-over relief valve (MPa).

R_{L1} is the combined resistance term given by Eqn. (5.33). Flow rate (Q_{12}) is reduced by the pressure acting against the flow from the pump, which includes pressure from the next line segment (P_{13}), and losses from the line (P_{RL1}). Pressure in the next line segment is derived from the coupling of the load to the hydraulic motor.

The cross-over relief valve joins two line segments which model the flow between the pump and motor. The cross-over relief valve connects constant pressure 0-junctions in the pressure and return line (P_{13} and P_{16}). Flow resistors at the 1-junctions joining the two pressure junctions represent the relief valve flow characteristics. Forward pressure at the cross-over relief valve is represented at 0-junction (13) , and is calculated by

$$P_{13} = \frac{1}{C_{13}} \int (Q_{12} + Q_{15} - Q_{17} - Q_{14}) dt \qquad [6.10]$$

where

Q_{17} = flow entering the motor (cm^3/s),

$Q_{15} = (1/R_{15})(P_{16}\text{-}P_{13})$ (cm^3/s), and

$Q_{14} = (1/R_{14})(P_{13} - P_{16})$ (cm^3/s).

Q_{14} and Q_{15} are the relief valve flow rates. The flow rates are determined by non-linear resistors bonded to the junctions. Pressure is developed by flow from the pump and relief valve flow from the return line. Pressure is reduced by flow down the line (Q_{17}) and flow to the return line through the relief valve (Q_{15}).

The flow rate at the line segment exiting the cross-over relief valve is

$$Q_{17} = \frac{1}{I_{L2}} \int (P_{13} - P_{RL2} - P_{19}) dt \qquad [6.11]$$

Eqn. (6.11) is identical to Eqn. (6.9) in its form. P_{RL2} is the line resistance pressure loss from the cross-over relief valve to the hydraulic motor, and P_{19} is the pressure at the high pressure port of the motor.

The return line pressures and flows are based on the same nomenclature, so they will not be discussed.

At this point, the two models begin to differ; therefore the cross conveyor and gathering chains models will be discussed separately.

6.2.1 Cross-Conveyor Motor and Load

Pressure at the motor inlet is determined by the constitutive equation for the line segment compliance (C_{19}) at 0-junction (19) . 0-junction (19) couples the line segment entering the motor to the motor itself. Pressure at the motor port inlet is

$$P_{19} = \frac{1}{C_{19}} \int (Q_{17} - D_{cm}\omega_{23} - Q_{20})dt \qquad [6.12]$$

where

$D_{cm}\omega_{23}$ = motor flow (cm^3/s), and

Q_{20} = $(1/R_{inm})(P_{19} - P_{21})$, internal leakage flow (cm^3/s).

ω_{23} is the motor shaft angular velocity and D_{cm} (motor displacement) is the modulus of the transformer.

Pressure is a function of flow rate through the motor and leakage flow. Q_{21} is the internal cross-port leakage flow. The flow resistance (R_{inm}) and the pressure difference across the ports of the motor ($P_{19} - P_{21}$) determine the leakage flow rate.

0-junction (21) connects the motor return with the line segment. In the motor return line, the pressure is determined by the hydraulic capacitor (C_{21}) constitutive equation,

$$P_{21} = \frac{1}{C_{21}} \int (Q_{20} + D_{cm}\omega_{23} - Q_{18})dt \qquad [6.13]$$

Eqn. (6.13) for return line pressure is reversed from the inlet pressure, Eqn. (6.12). Leakage flow and return line flow tend to build pressure in the line. The flow rate into the line segment toward the pump reduces pressure.

Motor angular velocity is represented at 1-junction (23) . The causality of the bonds say that the inertial term determines the angular velocity at the junction. The constitutive equation for the inertial term is,

$$\omega_{23} = \frac{1}{J_{cm}} \int [D_{cm}(P_{19} - P_{22}) - T_{vdm} - T_{cfm} - T_{mtc} - T_{b4} - F_{24}R_c]dt \qquad [6.14]$$

where

J_{cm} = mass moment of inertia of three chains, sprocket, and motor (kg-m^2),

$D_{cm}(P_{19}\text{-}P_{21})$ = torque created by the motor (N-m),

T_{vdm} = $C_{vd}\mu D_{cm}\omega_{23}$ (N-m),

T_{cfm} = $C_f D_{cm}(P_{19} - P_{22})$ (N-m),

T_{mtc} = constant motor torque (N-m),

$F_{24}R_c$ = torque to turn the load (N-m), and

T_{b4} = $R_{b4}\omega_{23}$ = bearing friction load (N-m).

The integral in Eqn. (6.14) represents the net angular momentum for the hydraulic motor shaft. Torque output to the external load on the motor is $F_{24}R_c$. T_{cfm}, T_{vdm}, and T_{mtc}, are torques which are required to overcome internal losses of the motor. They reduce the net angular momentum of the motor driveshaft.

0-junction (24) is coupled to 1-junction (23) through a transformer which represents the force required to move the stalks on the conveyor. The load force is determined by the constitutive equation for the chain compliance

$$F_{24} = \frac{1}{C_{ch}} \int (\omega_{23}R_c - \dot{x}_{25})dt \qquad [6.15]$$

where

$\omega_{23}R_c$ = angular velocity of motor times the sprocket radius (R_c) (m/s),

$\dot{x}_{25}$ = linear velocity of chain (m/s), and

C_{ch} = chain compliance (m/N).

The output of 0-junction (24) is coupled to 1-junction (25) , which represents the conveyor chain linear velocity, and is given by

$$\dot{x}_{25} = \frac{1}{I_{sm}} \int (F_{24} - W_{st} - F_{ss}) dt \qquad [6.16]$$

where

W_{st} = weight of the stalks (N),

F_{ss} = $R_{ss}\dot{x}_{25}$ = force to slide the stalks over the galvanized steel conveyor covering (N), and

I_{sm} = stalk mass on the conveyor (kg).

Eqn. (6.16) is the net linear momentum of the stalk mass on the cross conveyor. Stalk mass and stalk weight are variable. Stalks falling onto the conveyor and being dumped into the accumulator create a varying momentum and affect the torque, and subsequently the pressure the pump must develop (See Section 5.2.4.4).

6.2.2 Gathering Chains Motor and Load

The gathering chains are powered by two motors in series. Each motor is modeled and shown in the bond graph (Figure 43).

The pressure at the inlet to the first of the two series-connected motors is determined by the constitutive equation for the hydraulic capacitor at 0-junction (19) . Motor inlet pressure is

$$P_{19} = \frac{1}{C_{19}} \int (Q_{17} - Q_{exm} - Q_{inm} - Q_{22}) dt \qquad [6.17]$$

where

Q_{17} = flow input to the motor from the previous line segment (cm^3/s),

$Q_{exm} = Q_{19} = (1/R_{exm})(P_{19})$, external flow leakage (cm^3/s),

$Q_{inm} = Q_{20} = (1/R_{inm})(P_{19}-P_{21})$, internal flow leakage (cm^3/s), and

$Q_{22} = D_{gcm}\omega_{23}$, useful flow to turn the motor (cm^3/s).

External flow leakage is included in this model because a drain line is connected to each motor casing, and flow into the casing drains directly back to the reservoir.

Return line pressure at the first motor outlet port is represented by 0-junction (21). The return line flow from the motor and leakage flow enter this junction and flow exits toward the line segment joining the two motors in series. The return line pressure at the outlet of the first motor is

$$P_{21} = \frac{1}{C_{21}} \int (Q_{20} + Q_{22} - Q_{27})dt \qquad [6.18]$$

Q_{27} is flow which enters the second motor in series. 1-junction (27) models the flow rate between the two motors. Flow rate in this line segment is

$$Q_{27} = \frac{1}{I_{L5}} \int (P_{21} - P_{RL5} - P_{28})dt \qquad [6.19]$$

Flow to the second motor is reduced by pressure at the second motor inlet (P_{28}), developed from the load, and pressure to overcome line resistance (P_{RL5}).

The pressure at the second motor inlet is represented at 0-junction (28), and is given by

$$P_{28} = \frac{1}{C_5} \int (Q_{27} - Q_{26} - Q_{exm} - Q_{inm})dt \qquad [6.20]$$

Pressure is built from flow coming out of the return line of the first motor (Q_{27}). Pressure is reduced by flow to the second motor (Q_{26}), external leakage flow (Q_{exm}), and internal leakage flow (Q_{inm}) to the return line.

Pressure in the return line of the second motor (P_{30}) is calculated by

$$P_{21} = \frac{1}{C_{30}} \int (Q_{26} + Q_{inm} - Q_{18}) dt \qquad [6.21]$$

where

C_{30} = hydraulic compliance in the return line at the motor (cm^3/s-MPa),

Q_{26} = useful motor flow rate (cm^3/s),

Q_{inm} = internal flow leakage (cm^3/s), and

Q_{18} = flow to motor return line (cm^3/s).

Two transformers represent the conversion of hydraulic power to mechanical power provided by two motors in series and these two transformers come together at 1-junction (23). The two motors must then both turn at the same angular velocity, because their chains they drive are intermeshed. The angular velocity of the motor shaft is determined by the constitutive equation of the motor and chain inertia (J_m),

$$\omega_{23} = \frac{1}{J_m} \int [D_{gcm}(P_{19} - P_{21}) + D_{gcm}(P_{28} - P_{30}) - T_{vdm} - T_{cfm} - T_{mtc} - T_{b4} - T_L] dt \qquad [6.22]$$

where

$D_{gcm}(P_{19} - P_{21})$, = torque provided by the first motor in series (N-m), and

$D_{gcm}(P_{28} - P_{30})$, = torque provided by the second motor in series (N-m).

Torque to move the load now comes from two motors, and the two torque outputs sum together in the integral. Load torque (T_L) includes torque to compress the gripper pads, accelerate the stalks

(if chain speed is greater than ground speed), and lift the stalks. T_L is equal to F_{24}R, where F_{24} is the load force defined by Eqn. (6.15), and R is the radius of the chain sprocket mounted on the hydraulic motor shaft. Chain compliance (C_{ch}) includes the compliance of the chain and the rubber gripper pads. The other terms are defined as in Eqn. (6.14).

0-junction (24) couples to 1-junction (25) which is the linear velocity of the gathering chains. The gathering chains linear velocity is

$$\dot{x}_{25} = \frac{1}{I_{gc}} \int (F_{24} - W_{st} - F_l - F_{b5}) dt \qquad [6.23]$$

The mass term, I_{gc}, is the mass of stalks carried by the gathering chains. Load resistance (F_l) comes from compressing the gripping pads together. F_{b5} represents friction to slide the chains over supports on the gathering chains frame. Stalk weight is modeled by the force source, W_{st}.

6.3 Open Circuit Models

Five of the harvester operations are powered via open circuit hydraulic systems. The appropriate bond graph model components described in Chapter 4 are coupled together to create each open circuit system. Equations were extracted from these models for input into the TUTSIM simulation package. The following sections describe the extracted equations for the open circuit models.

6.3.1 Accumulator Dump Circuit

The accumulator drive bond graph with each component labeled is shown in Figure 44. Description of the model begins at the pump driveshaft input.

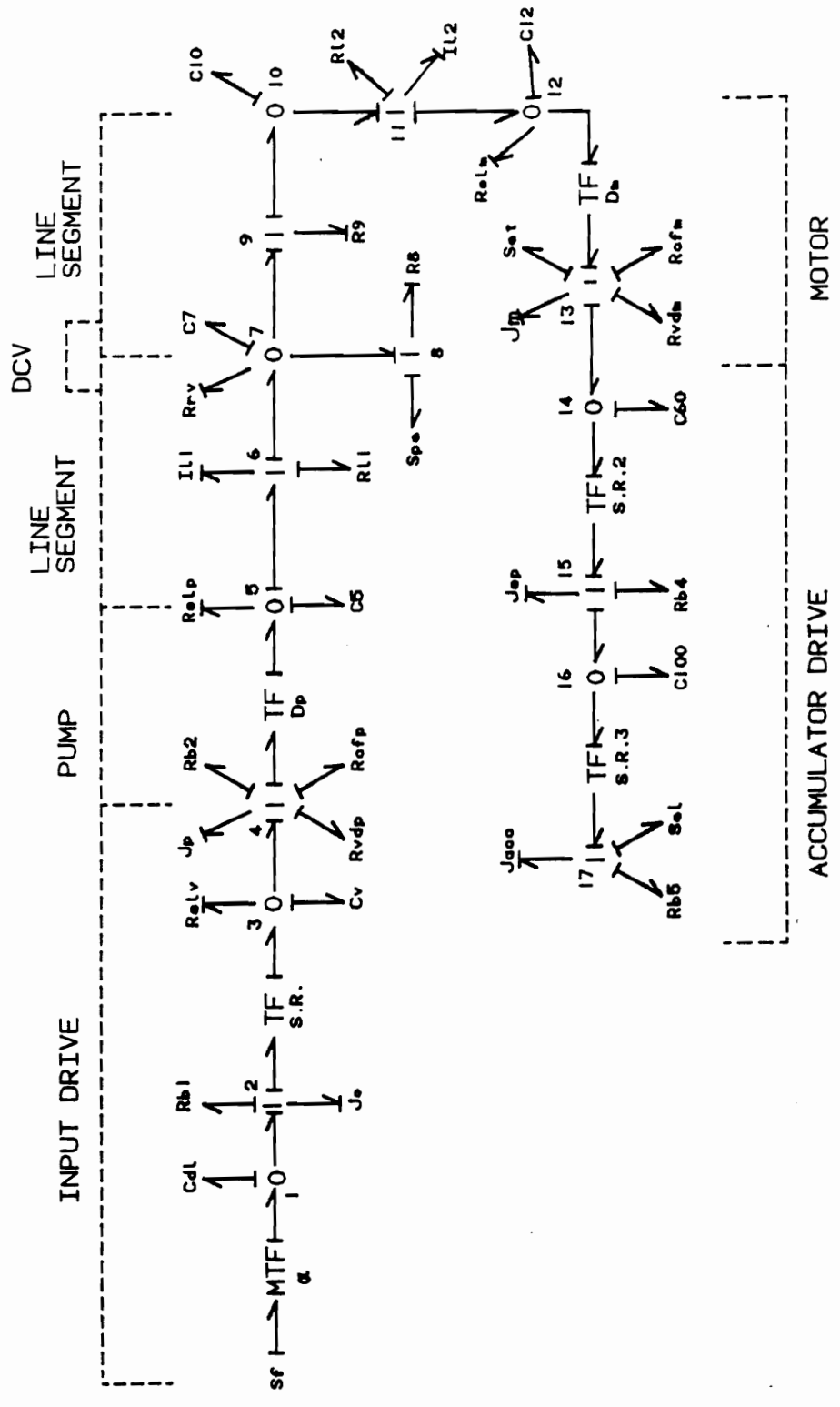

Figure 44. Accumulator dump drive bond graph model.

1-junction (4) represents the angular velocity of the gear pump driveshaft. The angular velocity of the gear pump is

$$\omega_4 = \frac{1}{J_p}\int (T_3 - T_{b2} - T_{vdp} - T_{cfp} - D_p P_5)dt \qquad [6.24]$$

The effect from the fluid at the pump port inlet was not included. This would have reduced the torque required to pump against the system pressure; but, this pressure component is small and does not significantly alter the results. Pumps used for the open circuit systems do not have charge circuits; subsequently, charge circuit effects are absent in Eqn. (6.24). The other torque terms are the same as described for the pump driveshaft angular velocity of the closed circuit variable displacement pump [Eqn. (6.15)].

A transformer couples 1-junction (4) to 0-junction (5). 0-junction (5) represents the pressure at the outlet port of the pump. As described before, pressure at the inlet port of the pump is negligible. The pressure at 0-junction (5) is

$$P_5 = \frac{1}{C_5}\int (D_p\omega_4 - Q_{slp} - Q_6)dt \qquad [6.25]$$

where

C_5 = line capacitance (cm^3/s-MPa),

$Q_{slp} = (1/R_{slp})(P_5)$ = slippage flow (cm^3/s), and

Q_6 = flow through the line segment (cm^3/s).

Slip flow is the internal leakage (cross-port) for the pump. External leakage does not exist, because a case drain was not connected to this pump. 0-junction (5) is coupled to 1-junction (6), which represents line segment flow. Flow losses due to line resistance are modeled by the resistor, R_{L1}. Line segment flow is

$$Q_6 = \frac{1}{I_{L1}} \int (P_5 - P_{RL1} - P_7) dt \qquad [6.26]$$

where

I_{L1} = fluid inertia (MPa-s/cm^3),

P_5 = pressure at pump port outlet (MPa),

P_7 = pressure at the DCV port inlet (MPa), and

P_{RL1} = pressure loss due to line resistance (MPa).

The line segment couples the pump to the DCV. Line pressure at the DCV port inlet is

$$P_7 = \frac{1}{C_7} \int (Q_6 - Q_{rv} - Q_8 - Q_9) dt \qquad [6.27]$$

where

C_7 = line capacitance (cm^3/s-MPa),

Q_{rv} = flow through the DCV relief valve (cm^3/s),

Q_8 = flow to the reservoir (cm^3/s), and

Q_9 = flow to the load (cm^3/s).

The resistance values at junctions (8) and (9) model the valve spool position. Flow to the load (Q_9) and flow to the reservoir (Q_8) are changed as the resistances are changed to simulate the shifting of the valve.

0-junction (10) represents line segment pressure between the DCV and hydraulic motor, which rotates the accumulator for dumping. The pressure at this junction is

$$P_{10} = \frac{1}{C_{10}} \int (Q_9 - Q_{11}) dt \qquad [6.28]$$

where

C_{10} = line capacitance (cm^3/s-MPa),

Q_9 = flow out of pressure port on the DCV (cm^3/s), and

Q_{11} = flow through the line segment (cm^3/s).

Flow through the line segment at 1-junction (11) is

$$Q_{11} = \frac{1}{I_{L2}} \int (P_{10} - P_{12} - P_{RL2}) dt \qquad [6.29]$$

I_{L2} is the fluid inertia and P_{RL2} is the pressure drop due to line resistance modeled by resistor R_{L2}. Pressure at the motor inlet (P_{12}) is represented by 0-junction (12) , and is calculated by

$$P_{12} = \frac{1}{C_{12}} \int (Q_{11} - Q_{slm} - D_m \omega_{13}) dt \qquad [6.30]$$

where

C_{12} = line capacitance (cm^3/s-MPa),

Q_{11} = line segment flow (cm^3/s),

Q_{slm} = pump flow slippage (cm^3/s), and

$D_m\omega_{13}$ = flow through the motor (cm^3/s).

A transformer between 1-junction (13) and 0-junction (12) converts hydraulic power to mechanical power at the hydraulic motor shaft. 1-junction (13) represents the angular velocity at the motor driveshaft. The inertial term (J_m) at this junction represents the internal rotating parts of the motor and the inertia of the No. 60 chain. The angular velocity at 1-junction (13) is

$$\omega_{13} = \frac{1}{J_m} \int (D_m P_{12} - T_{mtc} - T_{vdm} - T_{cfm} - T_{c60}) dt \qquad [6.31]$$

$D_m P_{12}$ is the torque produced by the motor. The definition of terms T_{mtc}, T_{vdm}, and T_{cfm}, can be found in Eqn. (6.14). T_{c60} is the torque transmitted to the load. A transformer is used to represent the sprocket ratio between the motor shaft and jackshaft (Figure 19). SR2 is the sprocket ratio and relates the speed and torque between the two shafts. 0-junction (14) is coupled to 1-junction (15) by the transformer. 0-junction (14) represents the torque from the hydraulic motor and 1-junction (15)represents the angular velocity of the jackshaft. Torque at 0-junction (14) is

$$T_{14} = \frac{1}{C_{60}} \int [\omega_{13} - \omega_{15}(SR2)]dt \qquad [6.32]$$

where

(SR2)ω_{15} = jackshaft angular velocity times the sprocket ratio (rad/s), and

ω_{13} = motor driveshaft angular velocity (rad/s).

Angular velocity at 1-junction (15) (velocity at jackshaft) is

$$\omega_{15} = \frac{1}{J_{sp}} \int (T_{14}SR2 - T_{b3} - T_{16})dt \qquad [6.33]$$

where

J_{sp} = mass moment of inertia for jackshaft sprocket and No. 100 chain (kg-m^2),

T_{14}(SR2) = torque developed by the hydraulic motor (N-m),

T_{b3} = torque required to overcome bearing friction (N-m), and

T_{16} = torque transmitted through the No. 100 chain to the accumulator shaft (N-m).

A second transformer (modulus SR3) represents the chain drive connection between the jackshaft and accumulator shaft. 1-junction (19) is the angular velocity of the accumulator shaft, which rotates the accumulator for dumping. The angular velocity is

$$\omega_{19} = \frac{1}{J_{acc}} \int (T_{16}SR3 - T_{sel} - T_{b4})dt \qquad [6.34]$$

where

J_{acc} = inertia of the accumulator and load (kg-m^2),

T_{16}(SR3) = torque delivered to the accumulator shaft (N-m), and

T_{sel} = torque required to overcome gravitational force (N-m).

T_{sel} varied as the accumulator rotated and the stalk bundle began sliding out of the bin (See Section 4.2.6.1).

6.3.2 Accumulator Cylinder Model

The 3-section DCV controls flow to two other circuits through the remaining two sections. Accumulator horizontal movement is controlled by one of these two circuits and its bond graph model (Figure 45) is described here. The model only represents cylinder extension and not retraction. The bond graph models for the DCV circuits are the same from the input drive to the actuators (0-junction (12)); therefore, Eqns. (6.24) through (6.29) also describe the model of the accumulator cylinder circuit from the pump (1-junction (4)) to the cylinder (0-junction (12)). Model equations will be described beginning at 0-junction (12) .

The pressure at the cap end of the cylinder is represented by 0-junction (12) and is determined by,

$$P_{12} = \frac{1}{C_{12}} \int (Q_{11} - Q_{slc} - A_c\dot{x})dt \qquad [6.35]$$

where

C_{12} = combined line and fluid capacitance inside the cylinder (cm^3/s-MPa),

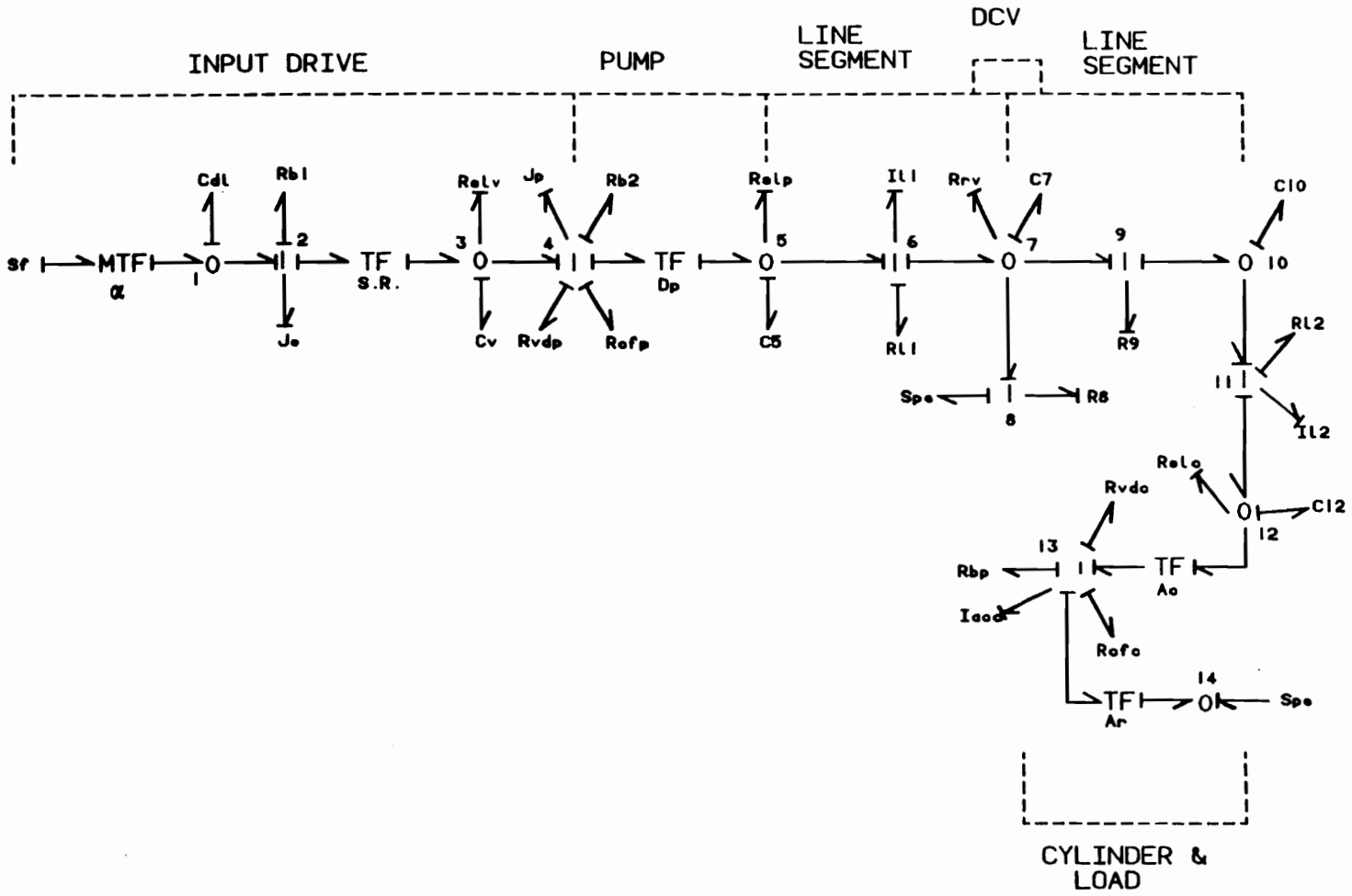

Figure 45. Bond graph model of accumulator cylinder circuit.

Q_{11} = flow input from the line segment (cm^3/s),

Q_{slc} = slippage flow around the cylinder cap (cm^3/s),

A_c = cap end area (mm^2), and

$\dot{x}$ = linear velocity of the cylinder rod (m/s).

A transformer couples 0-junction (12) to 1-junction (13). 1-junction (13) is the linear velocity of the cylinder rod. Force losses are bonded to it and output goes to another transformer representing the conversion back to hydraulic power in the rod end of the cylinder. The cylinder rod linear velocity is

$$\dot{x}_{13} = \frac{1}{I_{acc}} \int (P_{12}A_c - F_{vd} - F_{cf} - F_{bp} - P_{14}A_r)dt \qquad [6.36]$$

where

I_{acc} = mass of the accumulator and I-beams (kg),

$P_{12}A_c$ = force in the cap end of the cylinder (N),

F_{vd} = force to overcome viscous drag (N),

F_{cf} = force to overcome coulomb friction (N),

F_{bp} = force to slide the I-beams over the brass runners (N), and

$P_{14}A_r$ = back force (rod end) caused by back pressure (N).

Force available to move the load is reduced by internal losses, friction, and back pressure on the cylinder. This net force is integrated in Eqn. (6.36) to give the linear momentum of the accumulator and I-beams.

6.3.3 Cross-Conveyor Cylinder Model

The third circuit controlled by the DCV provides flow to the parallel mounted cylinders which raise and lower the cross conveyor. The bond graph model (Figure 46) is identical to the previous two DCV controlled circuits up to the actuator. As discussed in Section 6.3.2, Eqns. (6.24) through (6.29) represent the equations extracted from the model to describe energy flow from pump to actuator.

0-junction (12) represents the pressure input to the cylinders. Pressure is determined by the capacitor constitutive equation,

$$P_{12} = \frac{1}{C_{12}} \int (Q_{11} - Q_{slc} - A_c \dot{x}) dt \qquad [6.37]$$

Each term in Eqn. (6.37) is defined in Eqn. (6.35). The cylinders are different, therefore the magnitude of the values are different, but the concept is the same. 1-junction (13) is the linear velocity of the cylinder rod. The equation determining the linear velocity of the cylinder rod extension is,

$$\dot{x}_{13} = A_c(Q_{11} - Q_{slc} - Q_c) \qquad [6.38]$$

Linear velocity of the cylinder rod is the net flow rate (Q_{11}), minus slippage (Q_{slc}) minus compressible (Q_c) flow, times the cap end area. Integrating $\dot{x}_{13}$, gives the cylinder extension, which defines the length of the cylinder, L, and can then be used to determine the conveyor angle and subsequent load on the cylinder. These calculations are done in the transformer modulus m. The relationship of m to the cylinder rod force was given in Eqn. (4.41). 1-junction (14) represents the linear velocity of the load center-of-gravity, which can be found by the cross-conveyor mass (I_{lo}) constitutive equation,

$$\dot{x}_{14} = \frac{1}{I_{lo}} \int (F_c m - F_g - F_{res}) dt \qquad [6.39]$$

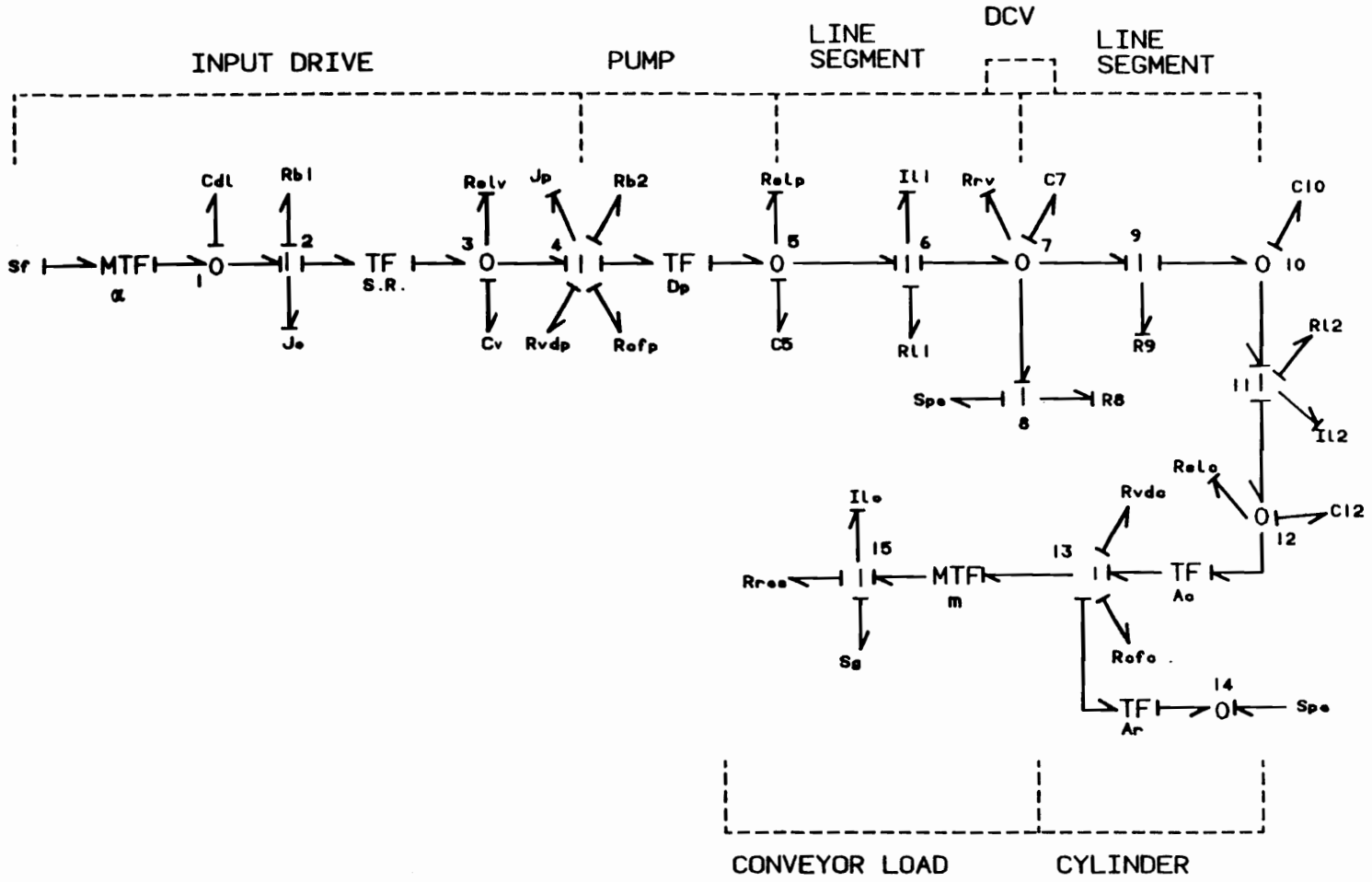

Figure 46. Bond graph model of conveyor cylinder circuit.

F_c is the force on the cylinder and F_cm is the load force at the conveyor center-of-gravity. F_g is the weight of the conveyor, and F_{res} is the frictional resistance.

6.3.4 Flipper Bond Graph

A separate pump provides flow to the flipper circuit. It is the first pump of a double pump (Vickers Model G5-20-16) bolted to the auxiliary mount of the variable displacement pump which provides flow to the gathering chains (Figure 3). A flow control valve was placed in the pressure line to control flow to the flipper motor. The bond graph model is given in Figure 47. The derived equations model the system from the pump input (1-junction ④) to the flipper mechanical load (1-junction ⑩). As has been shown in previous models, 1-junction ④ represents the angular velocity of the pump driveshaft,

$$\omega_4 = \frac{1}{J_p}\int (T_3 - T_{vdp} - T_{cfp} - T_{rb3} - P_5 D_p)dt \qquad [6.40]$$

The transformer converts the mechanical input to the pump into hydraulic power. Output of the transformer is bonded to 0-junction ⑤, which represents the pressure at the pump output. A resistor (R_{rv}) representing relief valve characteristics is bonded to this junction. The pressure is determined by the constitutive equation for the fluid and line capacitance (C_5),

$$P_5 = \frac{1}{C_5}\int (D_p\omega_4 - Q_{rv} - Q_{slp} - Q_6)dt \qquad [6.41]$$

where

C_5 = line and fluid capacitance (cm^3/s-MPa),

$D_p\omega_4$ = ideal flow developed by the pump (cm^3/s),

Q_{rv} = $(1/R_{rv})(P_5)$, = relief valve flow (cm^3/s),

Q_{slp} = pump flow slippage (cm^3/s), and

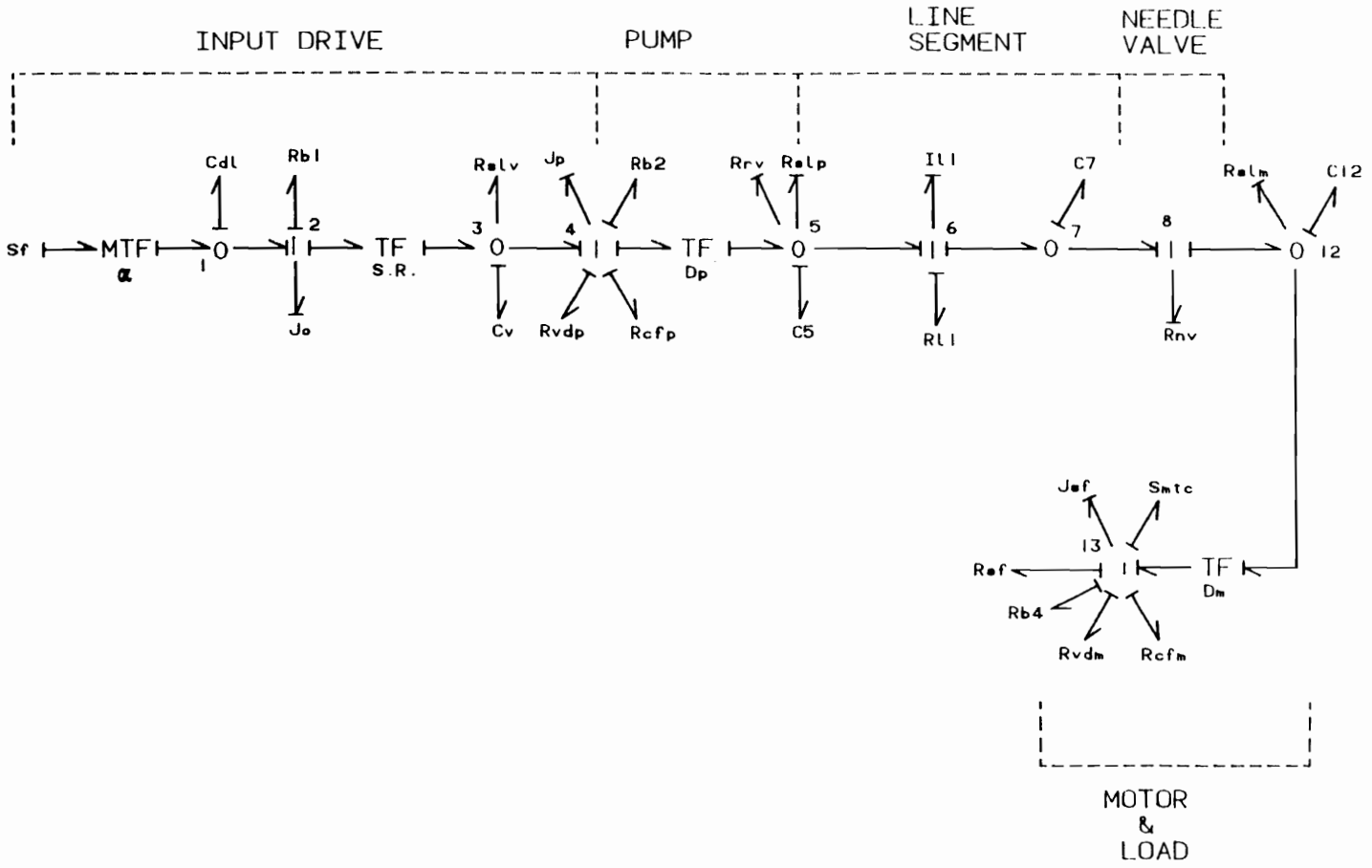

Figure 47. Bond graph model of stalk flipper circuit.

Q_6 = useful flow output from the pump (cm^3/s).

1-junction (6) represents flow through the line segment from the pump to the flow control valve modeled at 1-junction (8). Flow rate at 1-junction (6) is

$$Q_6 = \frac{1}{I_{L1}} \int (P_5 - P_{RL1} - P_7) dt \qquad [6.42]$$

where

I_{L1} = fluid inertia ($MPa\text{-}s/cm^3$),

P_5 = pressure at pump port outlet (MPa),

P_7 = pressure upstream of the flow control valve (MPa), and

P_{RL1} = pressure loss due to line resistance (MPa).

Pressure upstream of the flow control valve (0-junction (7)) is

$$P_7 = \frac{1}{C_7} \int (Q_6 - Q_8) dt \qquad [6.43]$$

where

C_7 = combined line and fluid capacitance ($cm^3/s\text{-}MPa$), and

Q_8 = flow through the flow control valve (cm^3/s).

1-junction (8) is flow through the flow control valve and is a function of the flow control valve setting, which is modeled by non-linear resistor, R_{nv}. Needle valve flow (Q_8) is

$$Q_8 = \frac{1}{R_{nv}} (P_{12} - P_7) \qquad [6.44]$$

where

P_{12} = pressure at motor port inlet (MPa),

P_7 = pressure at the inlet to the flow control valve (MPa), and

R_{nv} = flow control valve resistance (s-MPa/cm^3).

The needle valve (flow control valve) is not pressure compensated, so that flow is dependent on the load. The pressure at the input to the hydraulic motor is represented at 0-junction 12 .

$$P_{12} = \frac{1}{C_{12}} \int (Q_8 - D_m \omega_{13} - Q_{slm}) dt \qquad [6.46]$$

where

C_{12} = combined line and fluid capacitance (cm^3/s-MPa),

$D_m\omega_{13}$ = useful flow through the motor (cm^3/s), and

Q_{slp} = motor flow slippage (cm^3/s).

0-junction 12 is coupled to 1-junction 13 by a transformer which converts hydraulic power back to mechanical power to drive the flipper discs. 1-junction 13 represents the angular velocity of the flipper discs, and this velocity is given by

$$\omega_{13} = \frac{1}{J_{sf}} \int (D_m P_{12} - T_{vdm} - T_{cfm} - T_{mtc} - T_{sf} - T_{b4}) dt \qquad [6.45]$$

Internal hydraulic motor torque losses are T_{vdm}, T_{cfm}, and T_{mtc} [defined in Eqn. (4.17)]. T_{b4} is the torque to overcome bearing resistance which is a function of the resistor R_{b4}. Torque developed by the motor is D_mP_{12}. T_{sf} is the torque required to turn the flipper discs and is discussed in Chapter 5.

6.3.5 Disk-cutter Drive

As the harvester is presently designed, the disk-cutter is powered mechanically. A chain drive delivers power to a 90° gearbox with a 2:1 gear ratio and the disk-cutter is mounted on the output shaft of this gearbox. The placement of the gearbox interferes with passage of the stalks as they are transported rearward by the gathering chains. With the accumulation of grass and weeds in this congested area, the stalks are caught and pulled down below the normal grip point in the gathering chains. To solve this problem, the gearbox will be removed and the disk-cutter driven with a hydraulic motor mounted to the side of the stalk passageway. The motor will drive the disk-cutter via a V-belt drive. The proposed disk-cutter hydraulic and mechanical components are modeled in Figure 48. A gear pump bolted to the auxiliary mount of the conveyor chains variable displacement pump provides flow to the disk-cutter motor. The motor has a 7.304 cm^3/rad displacement motor and drives the disk-cutter via a V-belt drive with a 1:1 sheave ratio.

1-junction (4) is the junction representing angular velocity (ω_4) of the pump driveshaft. The angular velocity is

$$\omega_4 = \frac{1}{J_p}\int (T_3 - T_{b3} - T_{vdp} - T_{cfp} - D_p P_5)dt \qquad [6.47]$$

All terms are defined in Eqn. (6.24). 0-junction (5) is coupled to 1-junction (4) by a transformer having a modulus equal to pump displacement. 0-junction (5) represents the pressure at the pump output, and is defined by

$$P_5 = \frac{1}{C_5}\int (D_p\omega_4 - Q_{rv} - Q_{slp} - Q_6)dt \qquad [6.48]$$

where

C_5 = combined line and fluid capacitance (cm^3/s-MPa),

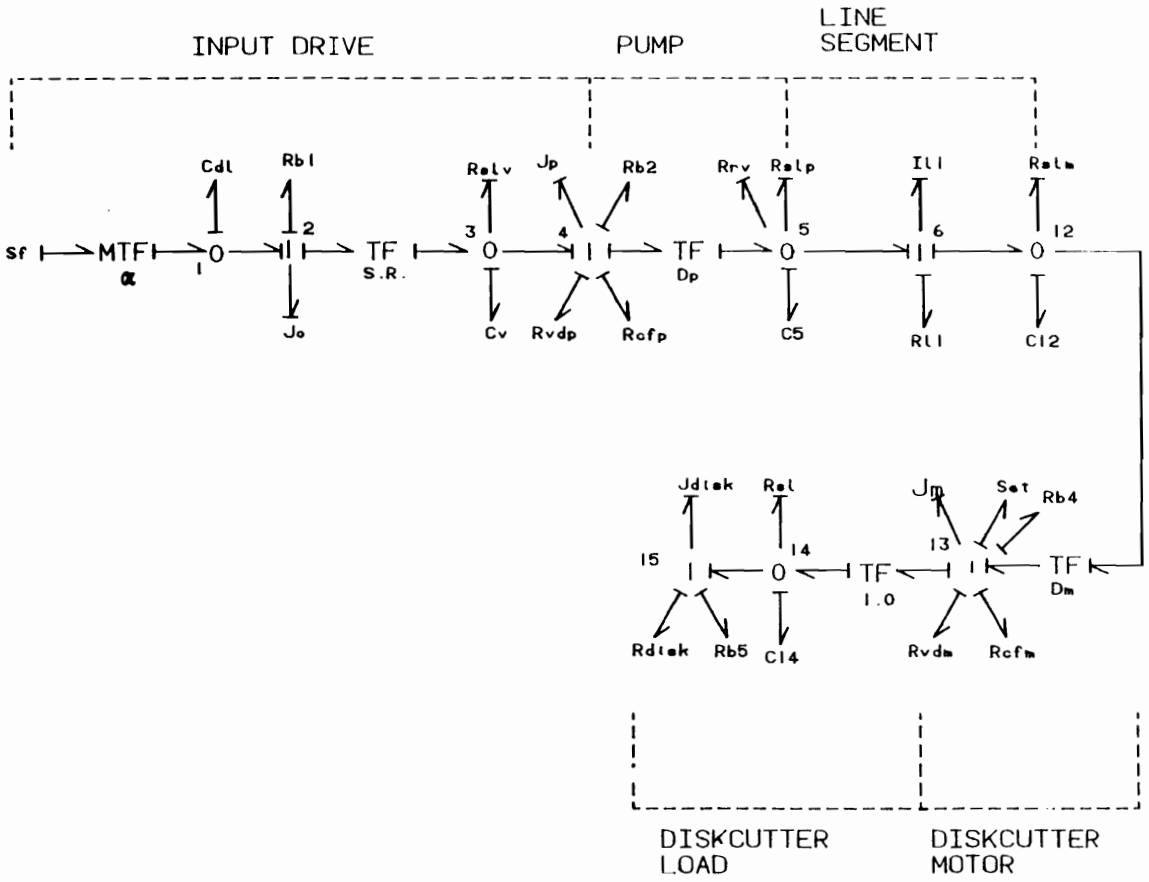

Figure 48. Bond graph model of proposed disk-cutter circuit.

$D_p\omega_4$ = ideal flow developed by the pump (cm^3/s),

Q_{rv} = $(1/R_{rv})(P_5)$, = relief valve flow (cm^3/s), and

Q_{slp} = pump slip (cm^3/s).

The pump is linked to the motor by a line segment. Line segment fluid flow is represented by 1-junction (6). Flow rate between the pump and motor is,

$$Q_6 = \frac{1}{I_{L1}} \int (P_5 - P_{RL1} - P_{12}) dt \qquad [6.49]$$

where

I_{L1} = fluid inertia ($MPa\text{-}s/cm^3$),

P_5 = pressure at pump port outlet (MPa),

P_{12} = pressure at the motor port inlet (MPa), and

P_{RL1} = pressure loss to line resistance (MPa).

Pressure at the motor port inlet is found from the capacitor constitutive equation,

$$P_{12} = \frac{1}{C_{12}} \int (Q_6 - D_m\omega_{13} - Q_{slm}) dt \qquad [6.50]$$

where

C_{12} = combined line and fluid capacitance ($cm^3/s\text{-}MPa$),

$D_m\omega_{13}$ = useful flow through the motor (cm^3/s), and

Q_{slp} = motor flow slippage (cm^3/s).

0-junction (12) is bonded to 1-junction (13) by a transformer with modulus equal to the motor displacement. 1-junction (13) represents motor shaft angular velocity, given by

$$\omega_{13} = \frac{1}{J_m}\int[D_m P_{12} - T_{vdm} - T_{cfm} - T_{b2} - T_{14}(SR1)]dt \qquad [6.51]$$

T_{14}(SR1) is the torque delivered to the disk-cutter driveshaft via a V-belt. The transformer at 1-junction (13) represented the torque and speed change due to the sheave ratio (SR1) between the motor and disk-cutter driveshaft. The transformer bonds to 0-junction (14) , which is the torque at the disk driveshaft required to turn the disk and cut stalks. Disk-cutter torque (T_{14}) is

$$T_{14} = \frac{1}{C_{14}}\int(\omega_{10} SR1 - \omega_{sl} - \omega_{15})dt \qquad [6.52]$$

where

(SR1)ω_{10} = motor driveshaft angular velocity times the sheave ratio (rad/s),

ω_{sl} = V-belt slippage (rad/s), and

ω_{15} = disk-cutter shaft angular velocity (rad/s).

Load torque and bearing torque losses are bonded to 1-junction (15) and the angular velocity is

$$\omega_{15} = \frac{1}{J_{disk}}\int(T_{14} - T_{disk} - T_{b5})dt \qquad [6.53]$$

where

T_{14} = torque required to turn disk-cutter (N-m),

J_{disk} = disk inertia (kg-m^2),

T_{disk} = load torque required to cut stalks (N-m), and

T_{b5} = torque required to overcome bearing friction (N-m).

Chapter 7 Results and Discussion

7.1 Gatherings Chains Circuit

7.1.1 Input Drive

The driveline torque for the three driveline conditions was described in Section 5.2.1 (Table 14) using the gathering chains model. Torque was extracted from the model at 0-junction (2) (Figure 43), which was the point where torque was measured with the torque transducer.

Test condition one represented the measurement of torque, pressure, and flow with the driveline cardan joints at small operating angles (straight ahead position); consequently, torque amplitude is relatively low (Figure 49). The experimental data varied from 30 to 120 N-m. Predicted torque had lower amplitude with values ranging from 50 to 90 N-m.

For test condition two, the joint angles were increased by turning the tractor to left approximately one-half the maximum achievable angle between the harvester and tractor. Model parameters were

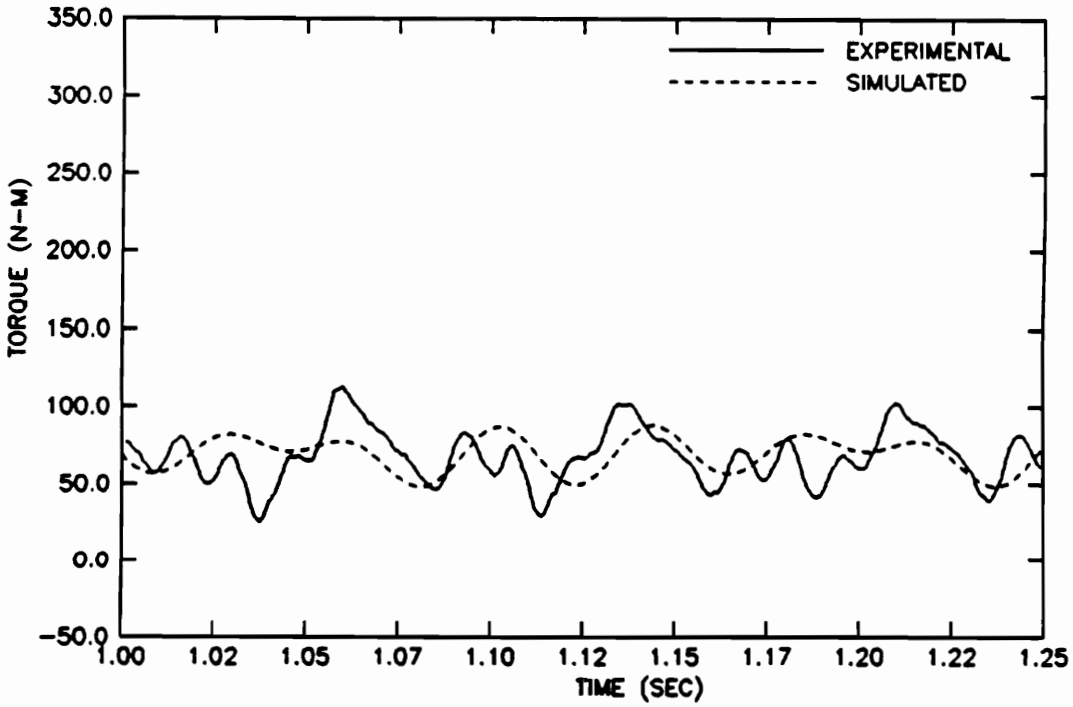

Figure 49. Experimental and simulated torque for test condition one.

adjusted for the effects of the increased joint angle and whirl amplitude. Predicted and experimental results are compared in Figure 50. Torsional amplitude varied from approximately 10 to 140 N-m in the experimental data, and 40 to 110 N-m in the simulation results. Again, the predicted results had a slightly smaller amplitude.

Test condition three was defined as the maximum angle achievable between the tractor and harvester. Any further angle would result in interference between the tractor tire and harvester hitch, therefore, this condition represented the highest possible joint angle in the driveline.

The resulting measured torsional vibration was very large (Figure 51). Torque peaked at approximately 280 N-m and and was clipped at zero. The predicted amplitude varied from approximately 200 N-m to zero N-m. The simulation results showed the small and large amplitudes which correspond to the 13 and 26 Hz excitation frequencies identified by the FFT analysis (Section 5.1.2). The modeled backlash produced clipping of the predicted torque at zero N-m, just as observed in the experimental data.

Difference in predicted and measured amplitudes is attributed to the estimation of parameters for whirl and non-linear driveline and V-belt stiffness. The shaft whirl amplitude was a function of shaft mass unbalance, and the secondary couple. Unbalance caused a centrifugal force which resulted in a lateral deflection in the shaft. The secondary couple caused a bending moment in the shaft which added to the lateral deflection.

When the shaft supports have non-uniform stiffness, the path of the whirl becomes elliptical, as the shaft rotates. The elliptical whirl created by the centrifugal force and the secondary couple causes a complex excitation in the driveline. The secondary couple is defined by

$$C = T \tan\theta \cos\beta \qquad [7.1]$$

where

C = secondary couple (N-m),

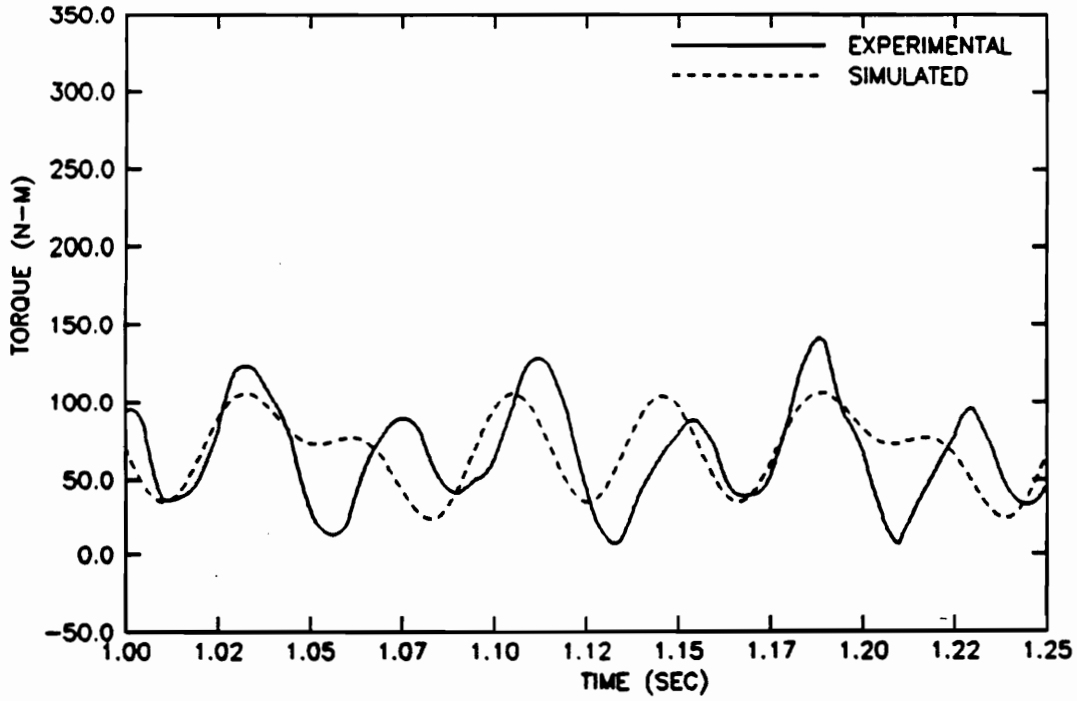

Figure 50. Experimental and simulated torque for test condition two.

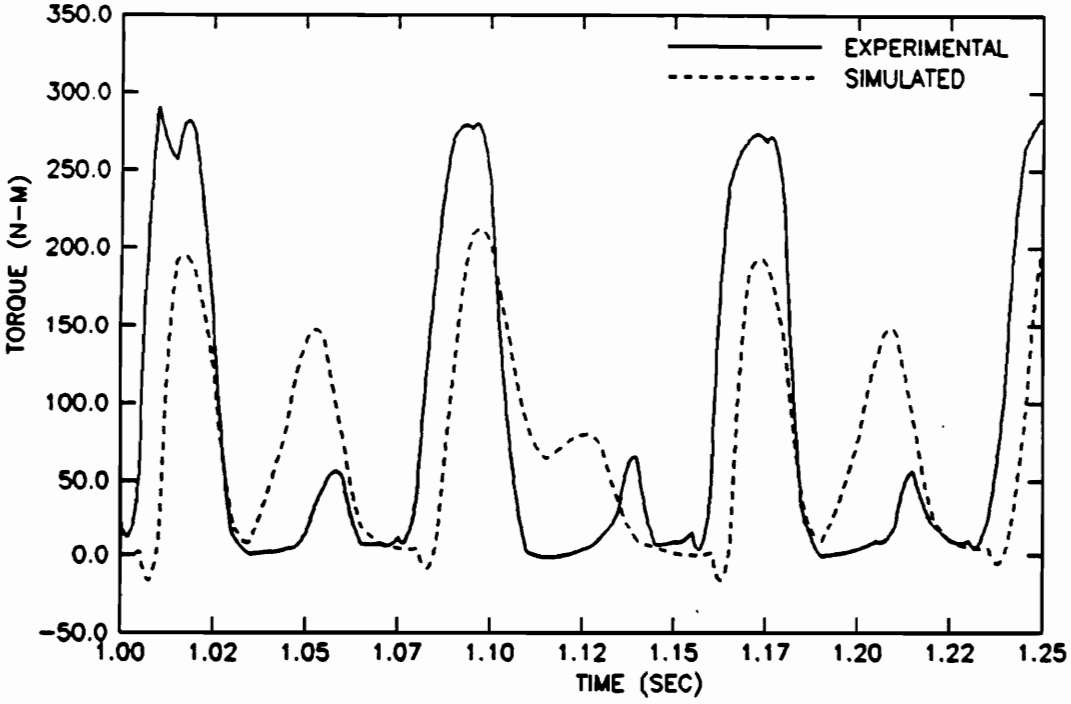

Figure 51. Experimental and simulated torque for test condition three.

T = transmitted torque (N-m),

θ = joint angle (rad), and

β = shaft rotation (rad).

The secondary couple (C) acts on the yokes of the cardan joints in the axial direction, causing a bending moment in the shaft and a resulting lateral deflection. The secondary couple increases (larger deflection) as the joint angle and transmitted torque increases [Eqn. (7.1)]. Consequently, as the joint angle increases, lateral deflection becomes larger and increases the amplitude of the fluctuating inertia. Based on these facts, the secondary couple was determined to be a major component of the increase in shaft whirl with increasing joint angle.

The lateral vibration and torsional vibration appear to be coupled to each other. Larger lateral deflection increases torsional vibration caused by the varying inertial term. When the torque fluctuates, it affects the secondary couple because the secondary couple is a direct function of the torque magnitude [Eqn. (7.1)]. The affected secondary couple, in turn, causes a change in the lateral vibration. The relationship between the transmitted torque and the secondary couple represents a dynamic coupling.

In the model created here, the coupling between transmitted torque and secondary couple is handled by increasing the whirl magnitude as the joint angles become larger. This simulates the increased lateral deflection for increased joint angles. The lateral deflection is then used to calculate the non-linear inertial term in Eqn. (4.4) which produces a fluctuating torque. The 13 Hz excitation frequency is simulated by choosing the shaft whirl velocity value equal to one-half the shaft angular velocity. The inertia then cycles once per revolution, a frequency of 13 Hz for 1600 tractor engine rpm (780 PTO rpm).

Driveline analysis contributes to the understanding of driveline dynamics for agricultural machines. Previously reported analyses have ignored the secondary couple and mass unbalance as an indirect

cause of torsional vibration. In this study, it is apparent that large torsional vibrations can result from large joint angles, even for modest transmitted torque.

7.1.2 Hydraulic Circuits

Pressure and flow rates were also measured for the three driveline operating conditions described earlier. The tractor engine speed was set to 1600 rpm and there was no stalk load on the gathering chains. Thus, model parameters defining the stalk load were set to zero during the simulation run. System pressure and flow were predicted at 0-junction (6) and at 1-junction (13), respectively. The experimental and predicted pressures are compared in Figure 52 for the three driveline operating conditions.

As the joint angle is increased, the input to the pump driveshaft fluctuates with increasing amplitude; but, these fluctuations do not produce significant pressure fluctuations. The fluctuations in the simulated pressure are in close agreement with experimental for test conditions one and two. Simulated pressure fluctuations in test condition three are much larger than experimental.

Mean predicted and experimental pressures are given in Table 15. The error ranges from 14 to 25 percent. One source of error was back pressure in the hydraulic return lines. Each test was run by first placing the tractor in the correct position with the harvester, and then setting the tractor engine to 1600 rpm. There was some variation in the set speed at each test, affecting the experimental results. Experimental pressure is nine percent less than experimental pressure in test condition three. The mean pressures should not be affected by changing joint angles; therefore the difference is attributed to a slight error in the setting of the tractor engine speed.

Charge pressure may be lower than was modeled, resulting in lower pressure in the return side of the hydrostatic drive. Return side pressures measured on the hydro-static circuit of the motor test stand were lower than the manufacturer's published setting. On the harvester, the charge relief

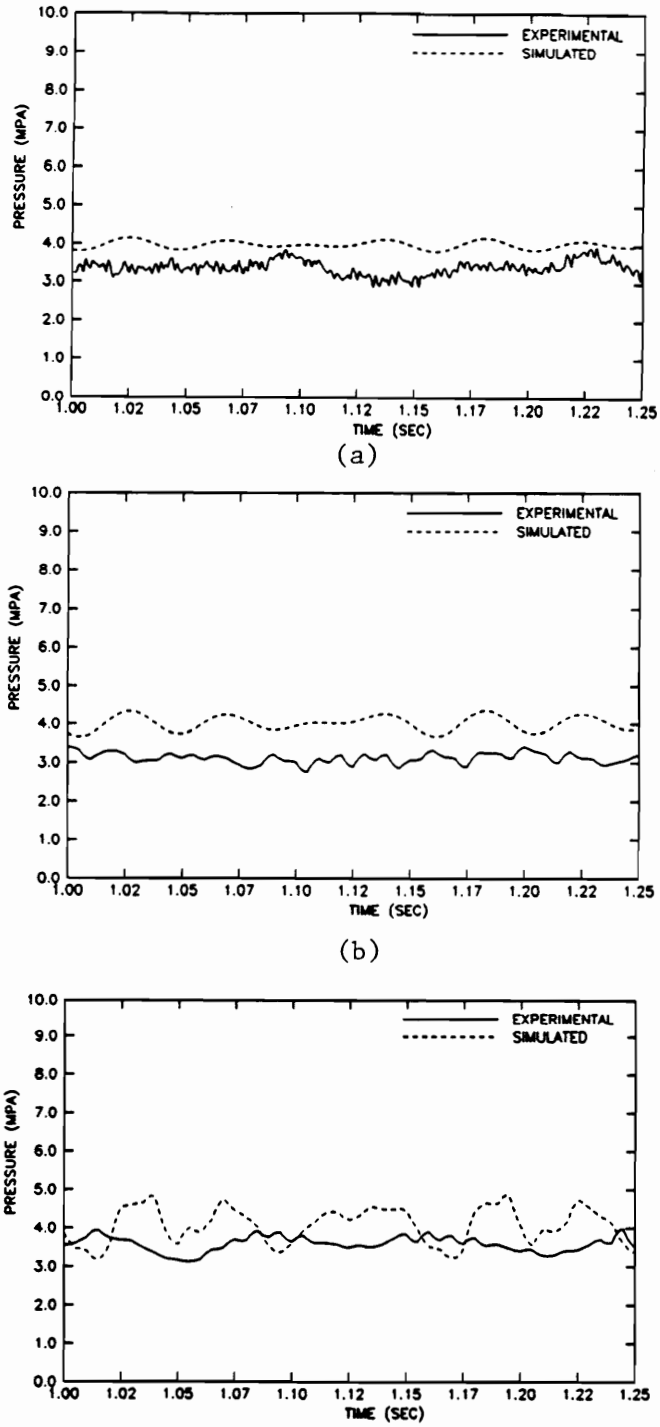

Figure 52. Experimental and simulated pressure in gathering chain circuit for test condition one (a), two (b),and three (c).

Table 15. Comparison of simulated and experimental mean pressure in gathering chain circuit for the three driveline test conditions

Test Condition		Pressure (MPa)
One	Simulated	4.01
	Experimental	3.36
	% Error	19.2
Two	Simulated	4.02
	Experimental	3.20
	% Error	25.0
Three	Simulated	4.01
	Experimental	3.52
	% Error	13.9

value was modeled at 1.0 MPa (manufacturer's data). If the setting is changed to 0.75 MPa, the resulting average pressures are 3.70, 3.71, and 3.70 for test conditions one, two, and three respectively, reducing the error between the predicted and measured results by 50 percent.

Hydraulic system response to the driveline fluctuations was important because of concern that actuator response would be affected. Pressure fluctuations were small considering the magnitude of the torsional vibration in the driveline. Large damping in the pump, lines, and motors reduced the amplitude. For this system, the fluctuations would not adversely affect operation in the field (i.e. gathering chain speed fluctuation is insignificant).

Flow rates were also measured for all three operating conditions. Pulses were recorded by reading 5000 pts/s on the data acquisition board. To get the frequency response desired, the sampling rate needed to be approximately 25000 pts/s. A hard disk was not available and data was taken at the best sampling rate available, (5000 pts/s) and averaged over a 0.02 second interval. The resulting flow rates for the experimental and simulated results are shown in Figure 53.

Error between simulated and experimental flow rates was 0.9, 12.6, and 7.0 percent, for test conditions one, two, and three, respectively. Flow rate from the pump could be varied by adjusting the swashplate angle. The swashplate setting was measured, but could not be determined with a high level of accuracy. Subsequently, the pump displacement was not known exactly, and there may have been a difference in actual displacement and the displacement used in the model. In addition, the small error in tractor engine speed directly affected flow rate output and was partly responsible for the 12.6 percent error in test condition two.

7.1.2.1 Motor Analysis

The gathering chains circuit had two hydraulic motors connected in series with case drain lines connected to the reservoir. Modeling of the external motor leakage was done with resistors (R_{exm}).

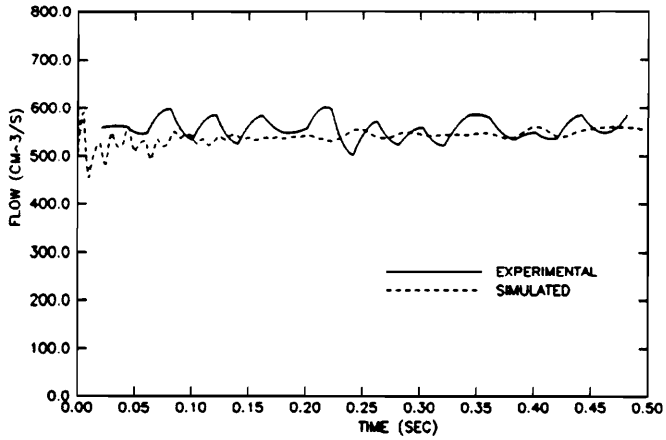

(a)

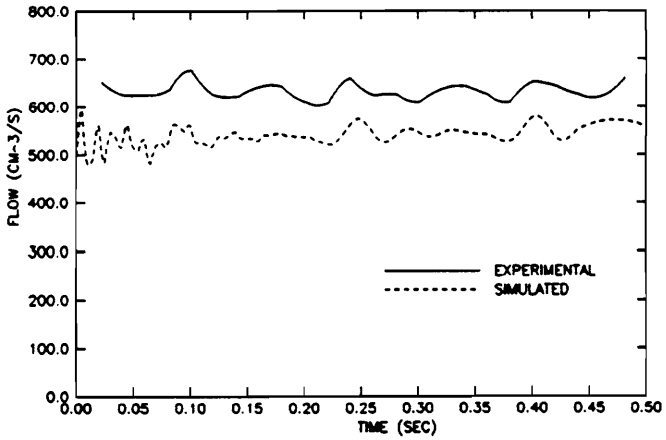

(b)

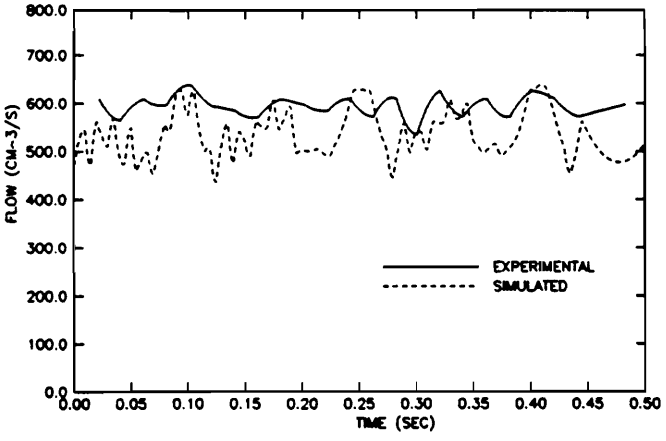

(c)

Figure 53. Experimental and simulated flow rate in gathering chain circuit for test condition one (a), two (b),and three (c).

The flow paths can be seen on the bond graph of the gathering chains (Figure 43). Interest in this design stems from the fact that both motors must turn at the same angular velocity because they are linked together by the gathering chains. When fluid enters the first motor some of the flow exits the external drain line. The second motor then receives less flow than the first motor, but must turn at the same angular velocity.

Analysis of the flow rates shows that flow to the first motor which produces shaft rotation is

$$Q_{22} = Q_{17} - Q_{exm1} - Q_{inm1} \qquad [7.2]$$

where

Q_{22} = useful flow for the first motor (cm^3/s),

Q_{17} = flow from the line segment input (cm^3/s),

Q_{exm1} = external flow loss (cm^3/s), and

Q_{inm1} = Q_{21} = internal flow loss (cm^3/s).

Flow that makes it to the return line of the first motor is the useful flow plus the internal line losses which pass from the high to low pressure port. The external flow loss returns to the reservoir. Useful flow for the second motor is then,

$$Q_{28} = Q_{27} - Q_{exm2} - Q_{inm2} \qquad [7.3]$$

where

Q_{28} = useful flow for the second motor (cm^3/s),

Q_{27} = flow from return line of the first motor (cm^3/s),

Q_{exm2} = external flow loss from second motor (cm^3/s), and

Q_{inm2} = Q_{21} = internal flow loss from second motor (cm^3/s).

Both motors turn at the same speed because of the meshing of the gripping pads from each chain. If their useful flow rates are equated ($Q_{28} = Q_{22}$), the relationship between the first and second motor is

$$Q_{inm1} = Q_{exm2} + Q_{inm2} \qquad [7.4]$$

This means that the total flow loss in the second motor must be less than the first to compensate for the smaller flow rate input. A simulation was run and the values extracted were

$Q_{inm1} = 24\ cm^3/s$
$Q_{exm2} = 5\ cm^3/s$
$Q_{inm2} = 19\ cm^3/s$

These values agree with Eqn. (7.4), thus the above explanation is believed to be correct. Assuming the two motors have identical parameters, the first motor is driving a large part of the load. Flow losses are functions of the pressure at the motor inlet port, and for losses in the second motor to be smaller, pressure drop across the motor must be smaller. When viewing the gathering chains, it can be seen that the first motor chain is pulling the second motor chain, causing the chains to be slightly uneven. Motors connected in parallel could alleviate this problem. Motor pressure would divide and drive both motors evenly. The fact that one chain pulls the other does not affect transport of stalks. It may be worthwhile to try to power the gathering chains with only one motor.

7.2 Cross-Conveyor Motor Circuit

A hydraulic motor drove the bottom shaft of the cross conveyor. Three sprockets spaced 1.2 m apart were placed on the shaft to drive the conveyor chains. The chains had spikes which pick up stalks as they were layered on the cross conveyor by the stalk flipper. Experimental data was collected with the motor driving the conveyor chains without a stalk load. The bond graph model was constructed to simulate the conveyor chains load with and without a stalk load. Pressure, torque, and flow rate were recorded at 0-junction (6), 0-junction (1), and 1-junction (11), re-

spectively (Figure 46). Measured and predicted results are compared for the u-joint driveline in the straight-ahead position (test condition one).

7.2.1 Experimental and Simulated Results

Tractor engine speed was set at 1400 rpm and data was collected for 10 seconds. A simulation was run using the same conditions. Comparison of the predicted and measured torque, pressure, and flow rate is shown in Figure 54, and tabular results of mean values is given in Table 16.

Predicted and measured torque were in close agreement qualitatively and quantitatively. The peak amplitude was very close except for two peaks in the experimental data. Frequency of the experimental torque was 22 Hz, which equals the twice per revolution excitation created by the cardan joints. The predicted torque also had a frequency of 22 Hz. Mean predicted and measured torque was 28.7 and 31.1 N-m, respectively (Table 16). Predicted torque was 7.7 percent lower than measured.

Predicted pressure did not exhibit the fluctuations seen in the experimental data [Figure 54 (b)]. Varying pressure is a result of a variable load on the hydraulic motor. The load of the conveyor chain was modeled as a constant resistive load; however, it is apparent that some other factor, or factors, produced a variable load.

Six steel plates supported the conveyor at the bottom pivot point. The bottom shaft operated in a tube that was supported on grooves machined in the steel plates. As the conveyor rotated up or down, the tube rotated in these grooves. The steel plates had holes cut in the center to allow the bottom shaft to pass through. Because of misalignment, the shaft did rub against one side of the hole or the other as it rotated causing the resistance to vary. An additional intermittent load resulted when the spikes brushed against the sides of the slotted opening in the conveyor covering as they made a turn at the top of the conveyor.

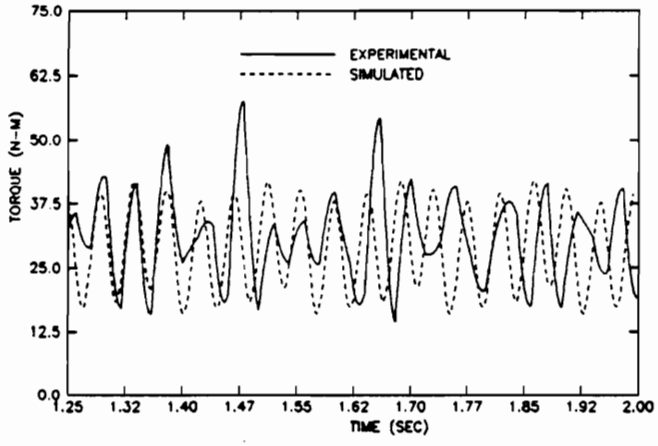

(a)

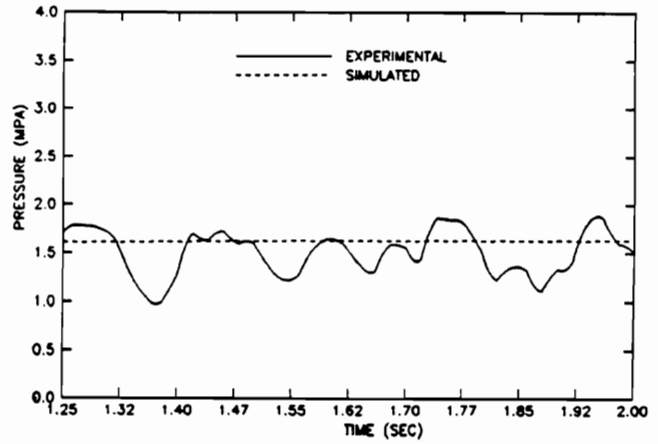

(b)

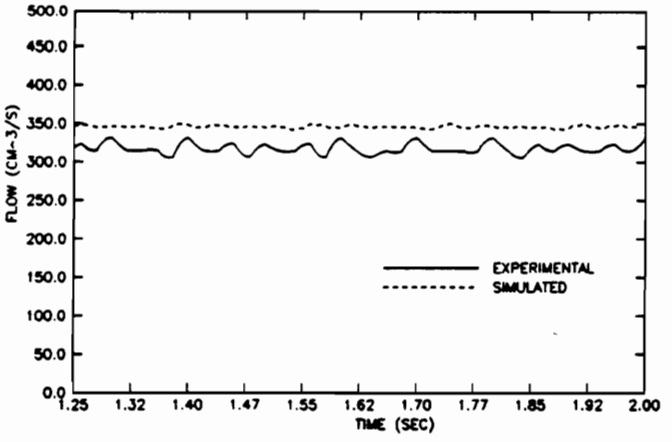

(c)

Figure 54. Measured and predicted torque (a), pressure (b), and flow rate (c) to power the cross-conveyor motor.

Table 16. Comparison of simulated and experimental mean pressure, flow, and torque to power the cross conveyor motor.

	Flow (cm^3/s)	Pressure (MPa)	Torque (N-m)
Simulated	346.1	1.62	28.7
Experimental	317.6	1.51	31.1
% Error	8.9	7.3	7.7

Predicted pressure was almost constant and was 7.3 percent larger than the measured pressure. The resistive load on the hydraulic motor was modeled as friction from bearings and sliding the chain over the wooden runners which supported its length on the top side of the conveyor. These modeled resistances were too large; however, the predicted and measured pressures were close (within 7.3 percent) and the model did give reasonable results for design purposes.

Experimental flow fluctuated more than simulated. The fluctuations are a result of injected flow from the charge circuit. Return line pressure fluctuated because the load fluctuated, which caused the charge circuit check valve to open and close. The simulation showed only a slight fluctuation due to check valve operation in the charge circuit. Check valve flow is defined from the bond graph model (Figure 42) as

$$Q_{cv} = \frac{1}{R_{cv}} (P_8 - P_{10}) \qquad [7.5]$$

where

Q_{cv} = check valve flow (cm^3/s),

R_{cv} = check valve flow resistance (non-linear),

P_8 = return line pressure (MPa), and

P_{10} = charge circuit pressure.

Charge circuit pressure (P_{10}) is kept relatively constant at 1.0 MPa by the charge relief valve. P_8 varies due to the variable load, and the check valve opens and closes thereby causing a variation in the return line flow at the point where flow rate was measured and extracted from the model. Check valve flow resistance was estimated, and the estimate does not accurately reflect the characteristics shown in the measured flow rate.

Mean predicted flow was 8.9 percent larger than measured. The swashplate setting on the pump could not be measured accurately, consequently, the actual displacement may have been different from the value used in the model.

7.2.2 Stalk Load Analysis

A load sub-model (Figure 31) was added to the bond graph to simulate the hydraulic circuit response to stalks falling onto, and being thrown off, the cross conveyor. A variable stalk mass, and force to raise the stalks against gravity, was incorporated as described in Section 5.2.4.4. The simulations were conducted at the same driveline angles and tractor engine speed used for the no-stalk load. Two conveyor chain speeds, full speed and one half full speed, and two stalk loadings, two stalks per spike and four stalks per spike, were examined. Table 17 gives predicted results for three stalk load conditions.

The full speed setting with two stalks per spike was the field operating condition. The appropriate load parameters were input into the model, and mean pressure and torque (Table 17) was 12.9 and 4.5 percent larger than values predicted with zero stalk load. Flow rate was slightly less due to the pressure dependent flow losses.

For the one half conveyor speed condition, four stalks are picked up per spike. The simulation predicted a pressure of 1.72 MPa, which is 6.2 percent more than the simulation with no stalk load.

Swashplate angle was reduced in the model to reduce the flow output, and consequently the conveyor chain velocity. Pump displacement was reduced by 50 percent and the pump required 8.3 percent less torque.

The third condition examined was for four stalks per spike at full conveyor speed. This situation will correspond to twice the normal plant population in a row (7.6 cm between plants instead of 15.2 cm). This condition showed an increase of 25 percent and 8 percent in pressure and torque, respectively, over the unloaded condition.

Quantitatively, increased load on the tractor for the different conditions is not significant. An 8 percent power increase resulted when the stalk load was doubled at full conveyor speed. At 30 N-m

Table 17. Predicted cross-conveyor circuit requirements for three stalk load conditions.

Test Condition	Flow (cm^3/s)	Pressure (MPa)	Torque (N-m)
Two Stalks per Spike, Full Speed	343.2	1.83	30.0
Four Stalks per Spike, Full Speed	342.5	2.02	31.0
Four Stalks per Spike, 1/2 Speed	171.5	1.72	26.3

driveline torque and 680 rpm driveline speed, the tractor PTO power requirement is 2.1 kW, which is relatively low.

Simulated pressure for the three stalk loading conditions (Figure 55) show varying levels of fluctuation. The four-stalks-per-spike at full chain speed loading had an amplitude of approximately 0.4 MPa. Since momentum is proportional to mass and velocity, the largest fluctuations is expected at the largest stalk density and conveyor speed combination. For the same number of stalks at half the full chain speed, pressure fluctuations were much smaller.

7.3 Accumulator Dump Circuit

Analysis of the accumulator dump circuit was done and corresponding experimental measurements made at 1400 and 1600 tractor engine rpm (680 and 780 driveline rpm). Ten seconds of data were taken while the DCV was shifted and a 60 kg bundle of stalks dumped from the accumulator bin. An accumulator dump event ended when the stalk bundle cleared the bin.

7.3.1 Torque, Pressure, and Flow Results

A comparison of measured and predicted fluid flow rate while dumping the accumulator is shown in Figure 56. Flow rate was taken from 1-junction (6) on the bond graph model of the accumulator dump circuit (Figure 44). There is a difference of approximately 100 cm^3/s between measurements made at 1400 and 1600 rpm. A slight drop in fluid flow rate can be seen in the experimental curves as the DCV is shifted at $t = 0.9s$. The simulated flow shows an oscillation as the DCV is shifted, which dampens out after approximately 0.25s.

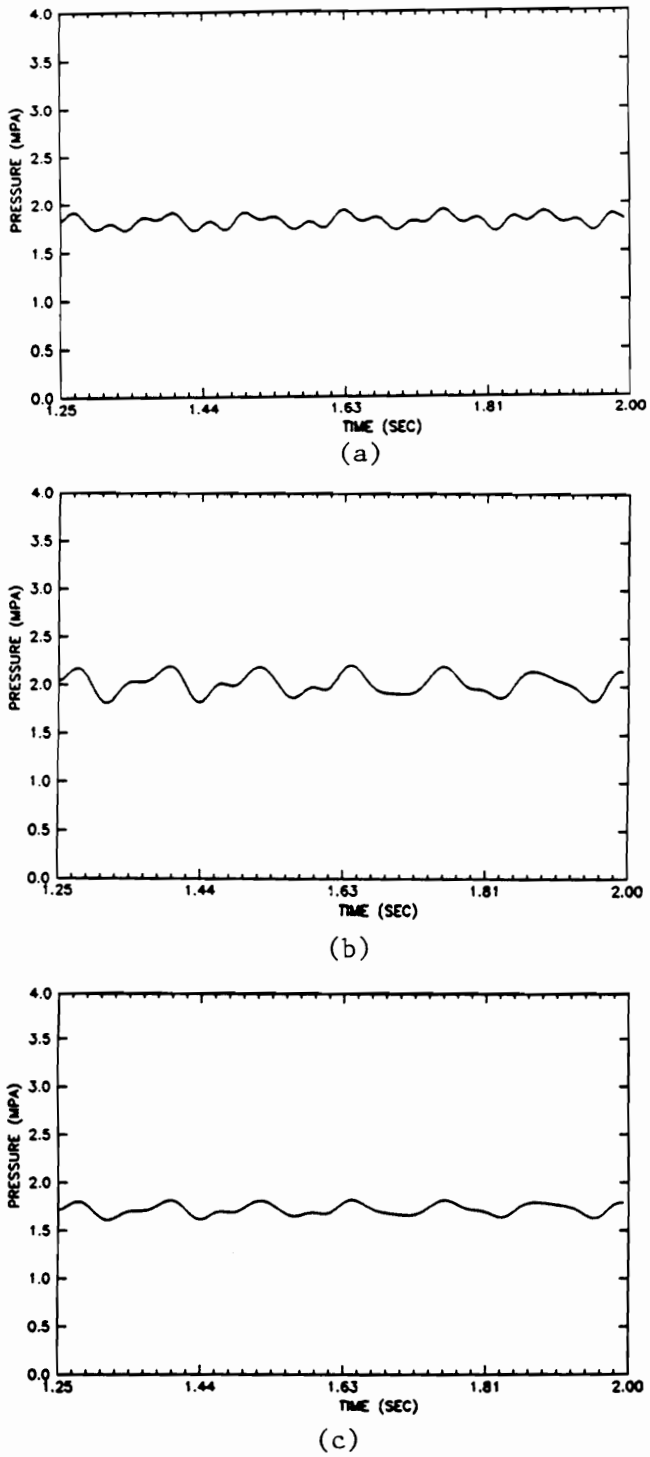

Figure 55. Predicted pressure for three stalk load conditions: (a) full speed, two stalks per spike, (b) four stalks per spike, and (c) one-half speed, four stalks per spike.

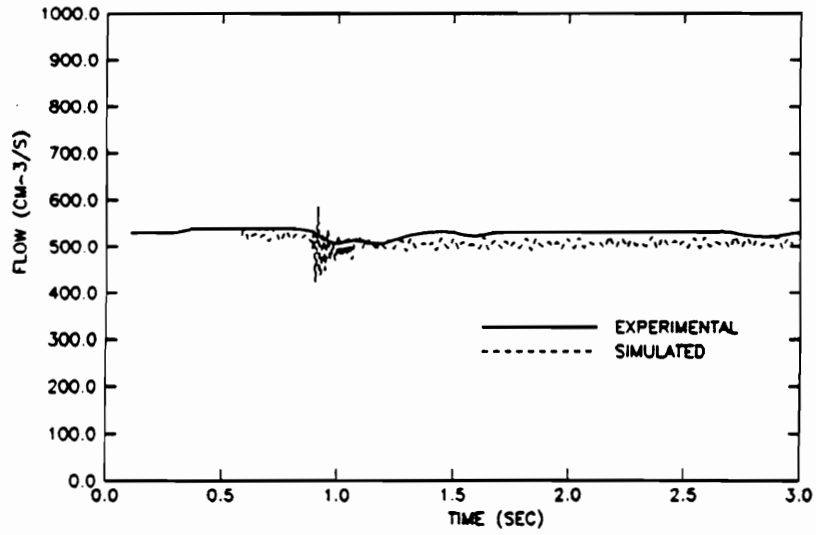

(a)

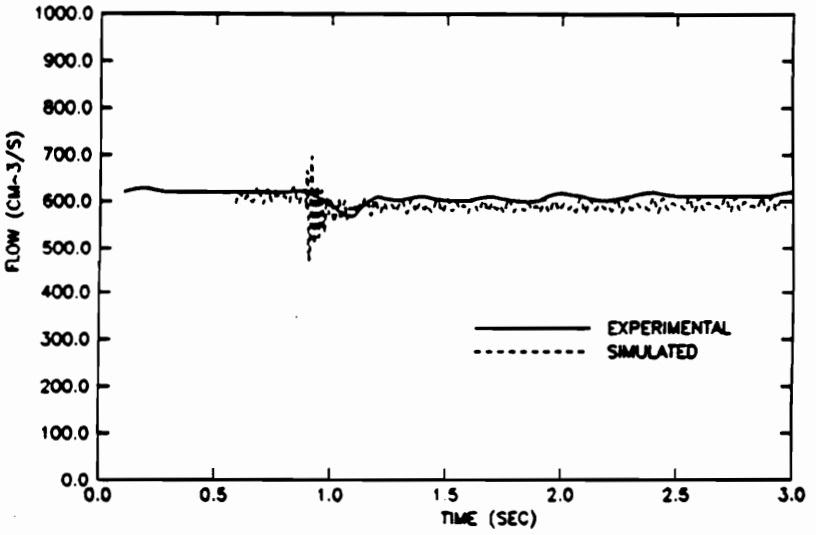

(b)

Figure 56. Experimental and simulated flow rate during an accumulator dump event for (a) 1400 rpm and (b) 1600 rpm tractor engine speed.

The small drop in flow is characteristic of a constant flow circuit. Flow rate was measured in the return line of the DCV. Since the DCV is open-center, flow is always present in the return line. When the DCV is shifted there is a slight drop in return line flow because pressure must build to move the load. Flow is reduced during this build-up period due to fluid compressibility, hose expansion, and pressure dependent flow losses, for example slip flow in the pump and motor.

Quantitative comparison between simulated and experimental flow was very close. Error between the experimental and simulated results was 4.2 and 3.0 percent for the 1400 and 1600 rpm experiments, respectively. Once the flow reached an equilibrium, it did not vary as the load changed. Pump efficiency at the relatively low operating pressure in the circuit was high enough that flow did not change as the load varied.

Due to changing load during a dump event, torque developed by the accumulator motor was not constant; consequently the load pressure is also not constant. Eqn. (4.37) gives the torque on the accumulator shaft as a function of the non-constant load. By incorporating the changing load in the model, a varying pressure was observed.

Pressure was taken from the model at 0-junction ⑤(Figure 44). Predicted and measured pressures were compared over an interval that brackets a dump event (Figure 57). The simulated and experimental results show a peak as the DCV is shifted at $t = 0.9s$. The measured pressure then oscillates and dampens out at approximately 2.8 seconds. The predicted pressure oscillates at a higher frequency and dampens out to follow the experimental results. After the oscillations are dampened, the predicted pressure closely follows the measured pressure.

The higher peak and oscillation in the simulated pressure may be attributed to the time period given to shift the valve. In the simulation, the valve was shifted from closed to fully open in 0.05 seconds. The actual time to shift the valve was dependent on how fast the operator reacted. A slower valve shift would reduce the shock on the circuit and the resulting pressure spike would be smaller and dampen out more quickly.

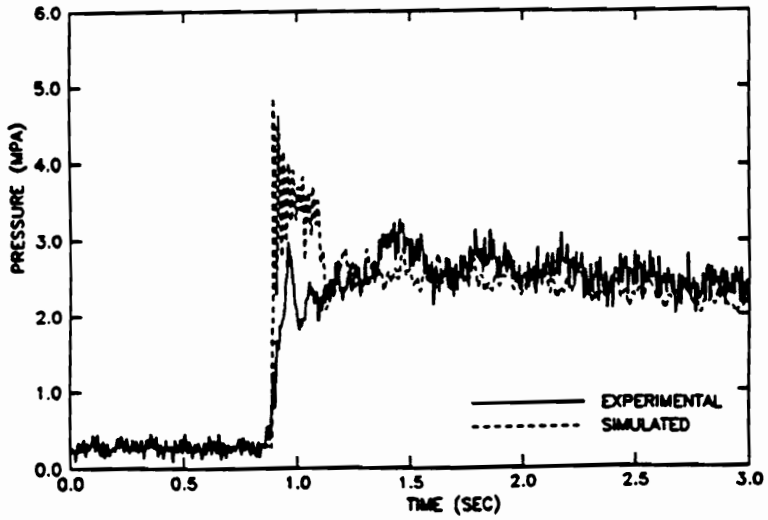

(a)

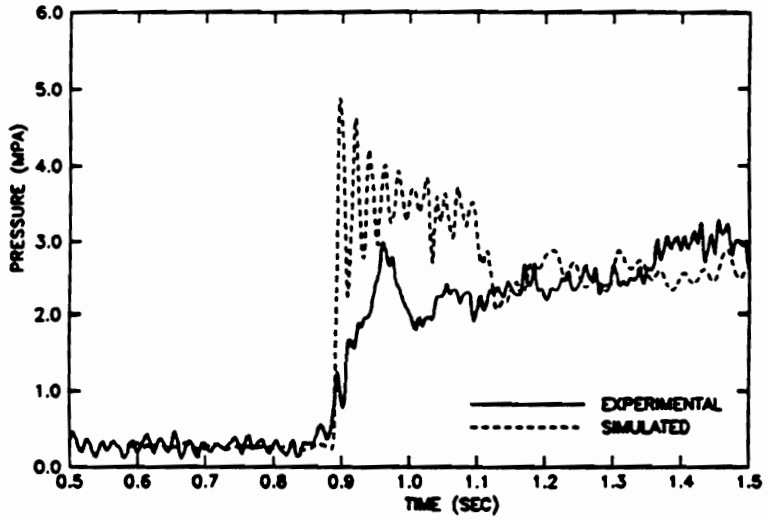

(b)

Figure 57. Experimental and simulated line pressure at DCV inlet during a dump event. Time scale (a) 0.0 to 3.0s and (b) 0.5 to 1.5s.

The pressure at six seconds (time required to fully rotate accumulator) was 1.5 MPa just before the bundle slides out of the accumulator bin. The reason the pressure increases and then decreases after an interval of time is because of the over-running nature of the load when the accumulator rotates far enough for the load center-of-gravity to shift to the left of the accumulator shaft. The load then begins to reduce the torque on the motor, since it is acting in the same direction.

Analysis of the bond graph model of the accumulator drive (Figure 44), and resulting mathematical equations gives a physical understanding to the over-running load. The constitutive equation at 1-junction (13) governs the rotational speed of the motor.

$$\omega_{13} = \frac{1.0}{J_m} \int \Sigma T dt + \omega_o \qquad [7.6]$$

where

ΣT = sum of torques at 1-junction (13),

ω_{13} = rotational speed of motor shaft (rad/s), and

ω_o = initial motor speed, t = 0 to t = 0.9 (rad/s).

When this equation is differentiated with respect to time, it represents the dynamic torque equation for the hydraulic motor,

$$J_m \frac{d\omega_{13}}{dt} = T_2 - T_4 - T_5 - T_6 - T_7 \qquad [7.7]$$

where

$J_m \frac{d\omega_3}{dt}$ = torque required to overcome inertia (N-m),

T_2 = total torque created by motor, $D_m P$ (N-m),

T_4 = torque constant, (T_c) (N-m),

T_5 = torque to overcome viscous drag (N-m),

T_6 = torque to overcome coulomb friction (N-m), and

T_7 = torque output to load (N-m).

By rearranging Eqn. (7.7), the total torque created by the motor (T_2) can be related to the torque required to move the load plus the torque to overcome motor losses,

$$T_2 = D_m P = J_m \frac{d\omega_{13}}{dt} + T_4 + T_5 + T_6 + T_7 \qquad [7.8]$$

If losses between the motor and accumulator shafts are neglected, $T_7 = T_i/24$, where T_i is given by Eqn. (4.37). As the angle of rotation of the accumulator (θ) increases, the load torque goes from positive to negative. If the magnitude of the load torque (T_7) is never numerically greater than the motor torque losses ($T_4 + T_5 + T_6$), motor torque and resulting line pressure is always positive. Motor torque losses are large for high-torque low-speed motors when they are operated at low pressures. These motors are designed to operate at high pressures.

Torque measurements were made for the tractor pulling the harvester straight ahead (test condition one) when the accumulator dump circuit was activated. Torque from the model was taken at 0-junction ②(Figure 44). Comparison of experimental and simulated results (Figure 58) show that frequency and amplitude were in close agreement.

7.3.2 Full-Load Analysis

A simulation was conducted to determine the pressure requirement to dump a 180 kg bundle of sorghum, equivalent to the mean bundle mass measured in field tests. Simulated results showed that, after the high frequency oscillation dampens out, the pressure is 3.1 MPa. At the point where the accumulator is fully rotated and the bundle is about to leave the bin, the pressure on the motor is 1.0 MPa. Because the lowest pressure is well above zero, the motor will not over-run during field operation. Subsequent simulations revealed that bundles up to 300 kg could be dumped without

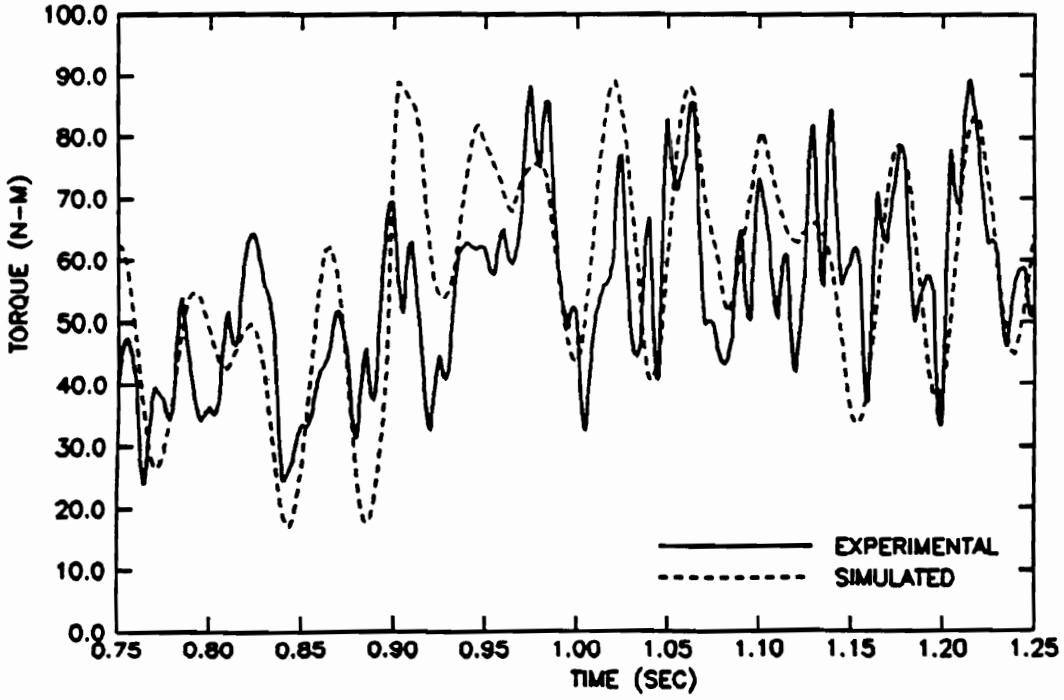

Figure 58. Experimental and simulated driveline torque during a dump event at 1600 rpm tractor engine speed.

the motor over-running. Bundles larger than 300 kg would over-run the motor, which may result in motor and/or pump cavitation. Cavitation is highly destructive and will damage a pump or motor very quickly.

7.4 Accumulator Cylinder Circuit

Two cylinders connected in parallel slide the accumulator in and out on I-beams. The accumulator cylinders were activated by the second section of the 3-section DCV.

Experimental and simulated pressure, flow, and torque are compared when the accumulator is fully extended (Figure 59). Model simulation results for pressure, flow, and torque were extracted from 0-junction ⑤, 1-junction ⑥, and 0-junction ①, respectively (Figure 45). The DCV was shifted to divert pump flow to the accumulator cylinders at 1.65 seconds.

When the DCV was shifted, simulated pressure peaked at 7.0 MPa before going into decaying oscillations. The steady-state pressure was relatively constant for the experimental and simulated results. The load on the cylinders is relatively constant as shown by the constant pressure after initial oscillations. Friction between the I-beams and brass runners (R_{bp}) was the modeled load resistance. Inertia was constant and only affected the dynamic response.

Measured and predicted flows were in close agreement after steady-state was reached [Figure 59 (b)]. Simulated flow was measured at the outlet of the cylinder and is zero until the valve is shifted. The flow meter was in the DCV return line, where flow was always present. As the valve was shifted, the experimental flow rate in the DCV return line dropped. This flow reduction was caused by the shift from full pump flow through the DCV to output flow from the rod end of the cylinder.

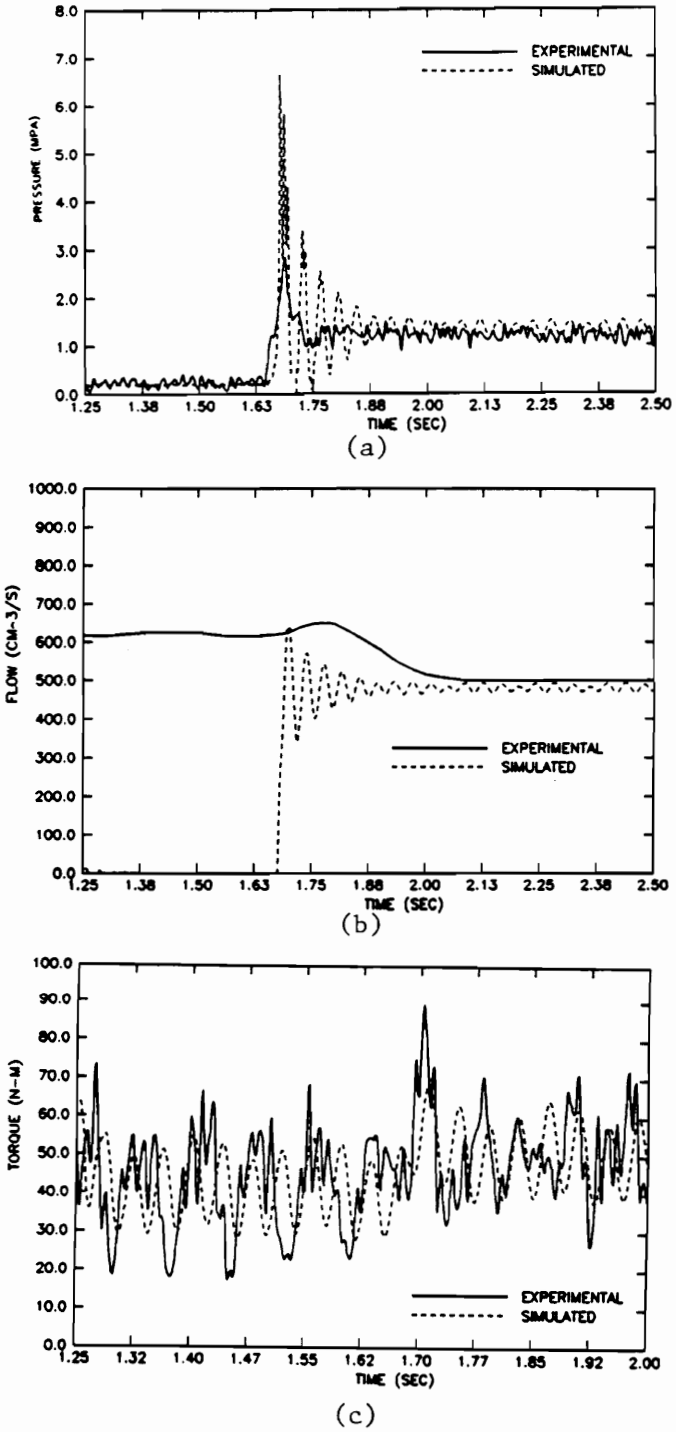

Figure 59. Experimental and simulated (a) pressure, (b) flow rate, and (c) torque to fully extend accumulator cylinders.

Because the fluid volume in the rod end is smaller than the cap end, flow rate into the cap end is higher than flow rate out of the rod end. Flow rate in the cap end of the cylinder is

$$Q_{ce} = \dot{x} A_c \qquad [7.9]$$

and flow rate out the rod end is

$$Q_{re} = \dot{x} A_r$$

The ratio between the flow rates is

$$\frac{Q_{re}}{Q_{ce}} = \frac{A_r}{A_c} \qquad [7.10]$$

or

$$Q_{re} = Q_{ce} \frac{A_r}{A_c}$$

A_r is 4064 mm^2 and A_c is 5026 mm^2, therefore flow rate out the rod end is 4064/5026 = 0.808 times that into the cap end.

Torque measurements were made in the driveline for straight ahead position (test condition one) during the accumulator extension. Figure 59 (c) shows the simulated and experimental torque. There is torsional vibration in the experimental curves not modeled by the simulation, though the simulation does show large variations with approximately the same amplitude. Frequency of the groups of peaks is 25 Hz which corresponds to driveline rotational velocity.

Steady-state comparisons were made and are shown in Table 18. The largest error was in predicted pressure (4.7 percent) and the smallest error was in predicted torque (1.2 percent).

Table 18. Comparison of simulated and experimental steady-state pressure, flow, and torque during accumulator extension.

	Flow (cm^3/s)	Pressure (MPa)	Torque (N-m)
Simulated	479.2	1.26	50.86
Experimental	498.7	1.20	50.26
% Error	3.9	4.7	1.2

7.5 Conveyor Cylinder Circuit

Two cylinders connected in parallel rotated the cross conveyor about its base, changing the angle of inclination. The conveyor was raised to allow the accumulator to retract in and reduce the width of the harvester to legal road width. It was also raised to allow room for the accumulator bin to rotate and dump a load of stalks. The conveyor cylinders were activated from the third section of the 3-section DCV.

The conveyor load was variable and calculated in the model as described in Section 4.2.6.2. The changing load was dependent on the kinematic relationship between the cylinder orientation and the conveyor position. As the cross-conveyor was lifted, the cylinder and conveyor position changed continuously. Load on the cylinder was calculated every 5° of rotation and input into the model using a FNC block. Predicted and measured pressure, flow, and torque are given in Figure 60.

Experimental and predicted pressure when raising the cross-conveyor are shown in Figure 60 (a). Pressure increases when the valve is shifted. As the cross-conveyor is lifted, the weight shifts from the cylinder to the conveyor base support, and pressure decreases as the cylinder continues to extend. Predicted pressure decreases faster and reaches a lower value at 3s. The function used to calculate the load on the cylinder begins to underestimate the actual load at approximately 1.9s. After 3s measured pressure is 2.8 MPa and predicted pressure is 1.4 MPa, a 50 percent difference. The model of the cross conveyor load (Section 4.2.6.2) was inadequate.

Predicted flow closely followed measured flow after steady state was reached. At the time the valve is shifted, the measured flow rate dropped to a lower value. This drop was due to the switch from DCV return port flow to rod end flow from the cylinders. Predicted flow rate took about 0.40 seconds to reach a steady output. The valve was shifted over a 0.25s time interval in the simulation

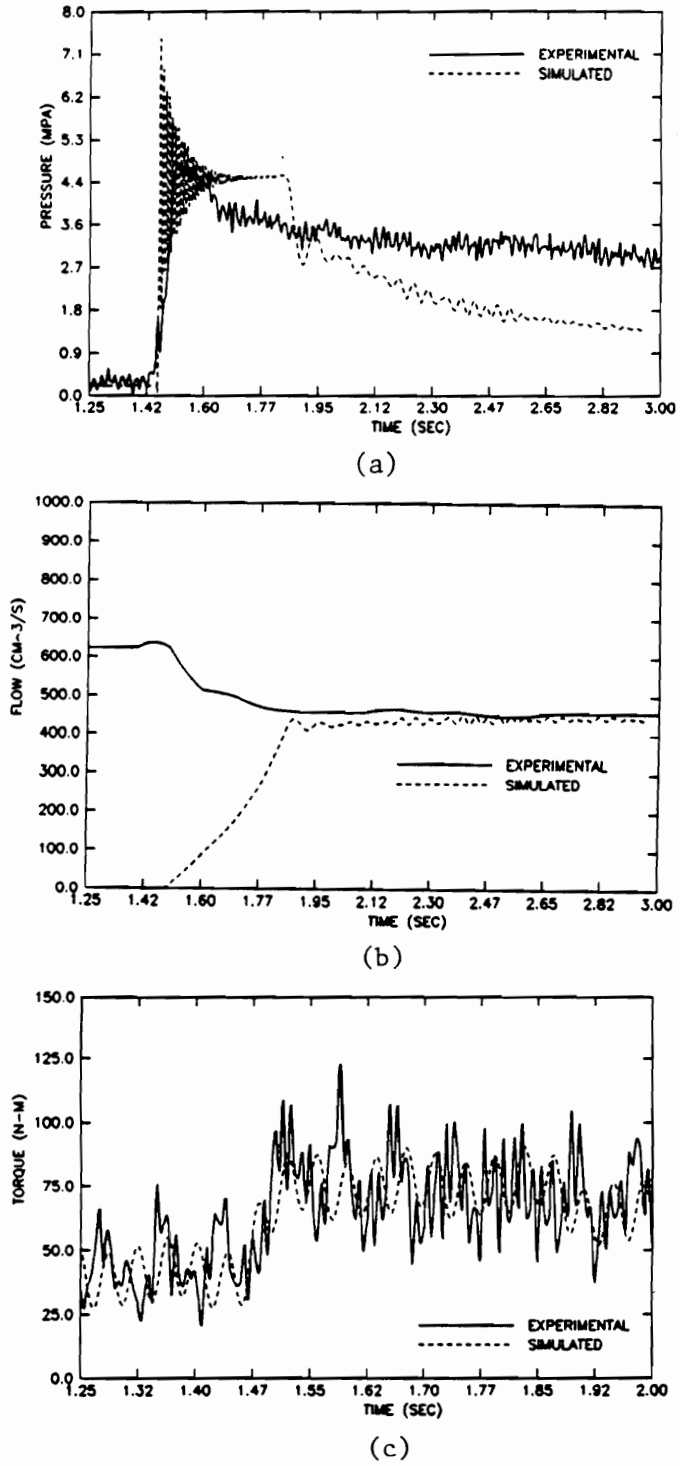

Figure 60. Experimental and simulated (a) pressure, (b) flow rate, and (c) torque to extend cross conveyor cylinders.

and during the time interval flow was divided between the DCV return and the cylinder until the end of the valve shift. The result was the slow flow rise in the predicted results.

Torque results were similar to the results for the accumulator cylinder. When the valve was shifted the measured and predicted torque both increased.

7.6 Stalk Flipper Circuit

The stalk flipper was driven by one hydraulic motor. Flipper speed was controlled by a flow control valve upstream of the motor inlet port. Pressure, torque, and flow measurements were made at a tractor engine speed of 1600 rpm with the driveline in the straight-ahead position (test condition one). Pressure, torque, and flow was extracted from the model at 0-junction (12), 0-junction (1), and 1-junction (6), respectively (Figure 47). The measurements were made when turning the flipper discs without a stalk load.

7.6.1 Experimental and Simulated Results

Predicted pressure over-estimated measured pressure by 93 percent (Table 19). Torque to turn the discs was a function of the force compressing the discs together. This force was measured with a force transducer. The force measurements were made before the flipper was set at its present position. With less air in the inner tubes used to produce a soft surface to grip the stalks, there was less resistance to turning the discs, and less resistance produced a lower measured pressure at the motor. Predicted pressure also did not show the fluctuations found in the measured data. [Figure 61 (a)]. These pressure fluctuations were caused by the irregular meshing as the discs rotated.

Table 19. Mean predicted and measured pressure, flow, and torque for the stalk flipper circuit.

	Flow (cm^3/s)	Pressure (MPa)	Torque (N-m)
Simulated	189.0	0.54	67.9
Experimental	210.2	0.28	86.1
% Error	10.0	93.0	21.1

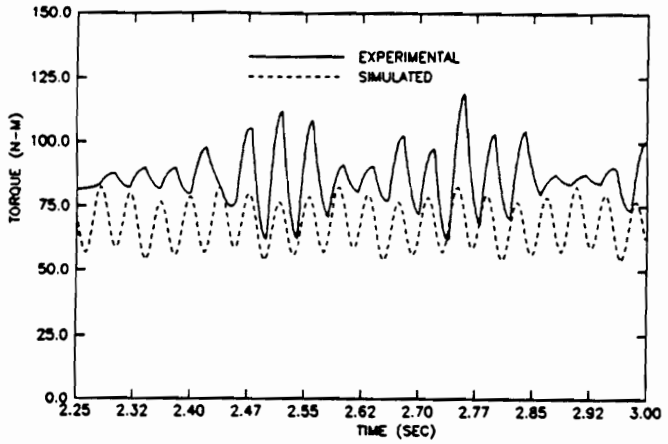

(a)

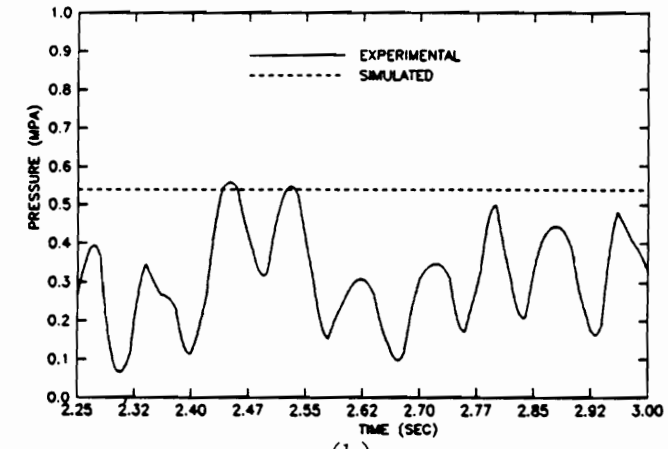

(b)

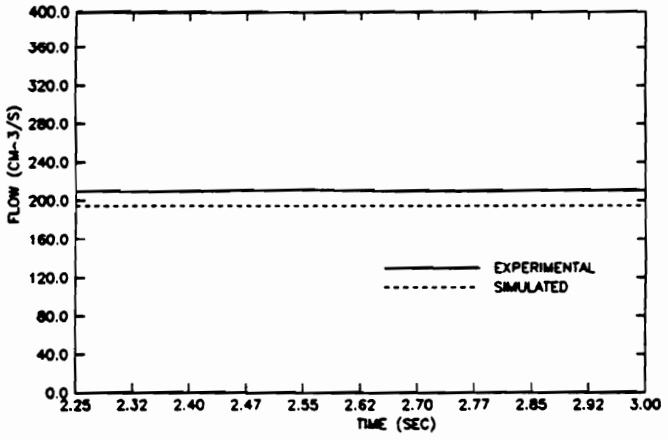

(c)

Figure 61. Measured and predicted torque (a), pressure (b), and flow rate (c) for the stalk flipper circuit.

Predicted torque was 21.1 percent less than measured torque. Torque to turn the pump driveshaft is a function of the pressure at the pump outlet port. Pressure measured at the motor inlet port by the pressure transducer was very low (less than 0.5 MPa); however, pressure upstream of the flow control valve was relatively high. When the flow control valve was closed to reduce flow to the motor, pressure increased and the pump had to deliver flow against this pressure. The upstream pressure was not measured on the actual circuit. The relief valve setting dictated the maximum pressure upstream of the flow control valve, and this setting was not known exactly. The upstream pressure in the simulation reached 3.8 MPa, which was the setting of the relief valve in the model.

Flow rate was measured in the motor return line. Flow at this point was equal to pump flow minus flow across the relief valve. The flow control valve was set by recursively checking the flipper disc rpm. The flow control valve setting was changed until the flipper disc speed equaled the measured value during field testing. Predicted flow was 10 percent less than the measured value. Flow was constant, because pump efficiency did not vary significantly as the pressure fluctuated.

7.7 Disk-cutter Circuit

The disk-cutter hydraulic circuit (Figure 4) was designed to use the existing gear pump (3.13 cm^3/rad) on the auxiliary pump mount of the multiple-2 pump assembly. The circuit is open and the hydraulic motor shaft is connected to the disk-cutter via a V-belt drive. The model was used to analyze four different design options. Two pumps having displacements of 3.13 cm^3/rad (identified as pump one) and 2.53 cm^3/rad (identified as pump two) were considered. Two motors having displacements of 7.3 cm^3/rad and 25.3 cm^3/rad were considered. The 7.3 cm^3/rad motor is identified as the disk-cutter motor, and the 25.3 cm^3/rad motor is identified as the cross conveyor motor. Required disk velocity, pressure in the circuit, and torque to cut stalks were examined.

The load was taken from torque to cut sugarcane stalk with a basecutter, described in Section 5.2.4.6.

7.7.1 Design Analysis

Circuit response at four junctions in the model were extracted and are given in Table 20 for the four motor and pump combinations. Both motors and pumps had loss coefficients determined and listed in Chapter 5. For pump one, disk rpm was 207 rpm using the cross conveyor motor and 722 rpm using the disk-cutter motor. For pump two, disk rpm was 157 and 570 rpm for the cross conveyor and disk-cutter motors, respectively.

A new disk-cutter disk was designed. The new disk had one-half the diameter of the existing disk. To keep the same blade tip velocity, the disk-cutter speed must be 1000 rpm. Only the pump one and disk-cutter motor combination comes close to this requirement. Blade tip velocity was 11.2 m/s for this combination. Predicted pressure was 3.18 MPa, and predicted torque to cut the stalks was 0.42 N-m.

Two other designs to increase disk speed with existing pumps and motors were examined. A 5:1 sheave ratio between the cross conveyor motor and pump one combination and a 2:1 sheave ratio between the disk-cutter motor and pump two were implemented into the bond graph model and a simulation run. Disk speed was increased to 1081 and 1040 rpm for the cross conveyor motor and disk cutter motor, respectively. Torque required to turn the disk and cut stalks was higher due to the higher ratio drive.

1. Option one is the disk-cutter motor, pump one, and a 1:1 sheave ratio between the motor shaft and disk-cutter shaft.

Table 20. Simulation-predicted parameters needed for design of disk-cutter circuit.

Motor and Pump Combination	Torque (N-m)	Pressure (MPa)	Flow (cm^3/s)	Speed (rpm)
7.3 (cm^3/rad) motor 2.53(cm^3/rad) pump	0.42	3.18	435.2	570
25.3 (cm^3/rad) motor 2.53(cm^3/rad) pump	0.39	1.77	457.6	172
7.3 (cm^3/rad) motor 3.13(cm^3/rad) pump	0.43	3.34	552.6	722
25.3 (cm^3/rad) motor 3.13(cm^3/rad) pump	0.39	1.99	575.7	217

2. Option two is the disk-cutter motor, pump two, and a 2:1 sheave ratio.

3. Option three is the cross conveyor motor, pump one, and a 5:1 sheave ratio.

Torque to turn the disk-cutter for the three design options is shown in Figure 62 and pressure in Figure 63. Pressure and torque peaks were caused by the disk-cutter cutting a stalk.

Three design options were then analyzed dynamically. The design options are as follows: Torque fluctuations for options one and two were very similar. These two options used the disk-cutter motor. The torque fluctuations for option three were much larger because the 5:1 sheave ratio amplified the stalk-cutting peaks. However, due to the large displacement of the cross conveyor motor, pressure fluctuations are very small in option three. Pressure fluctuations in option one were the largest, and the mean pressure was also the largest.

Option three is attractive since it has the lowest pressure fluctuations in the circuit, and lowest mean value. However, the large fluctuation in torque may cause the V-belt to slip when the stalk-cutting load is large. Option one has low torsional vibration, but the largest pressure variation. Option two has low pressure and low torsional vibration, consequently option two was picked based on this analysis.

There were several other options which could have been analyzed by inputing the loss coefficients for other motors and pumps. The analysis was done with components already modeled and showed the value of simulation in design, particularly for dynamic analysis.

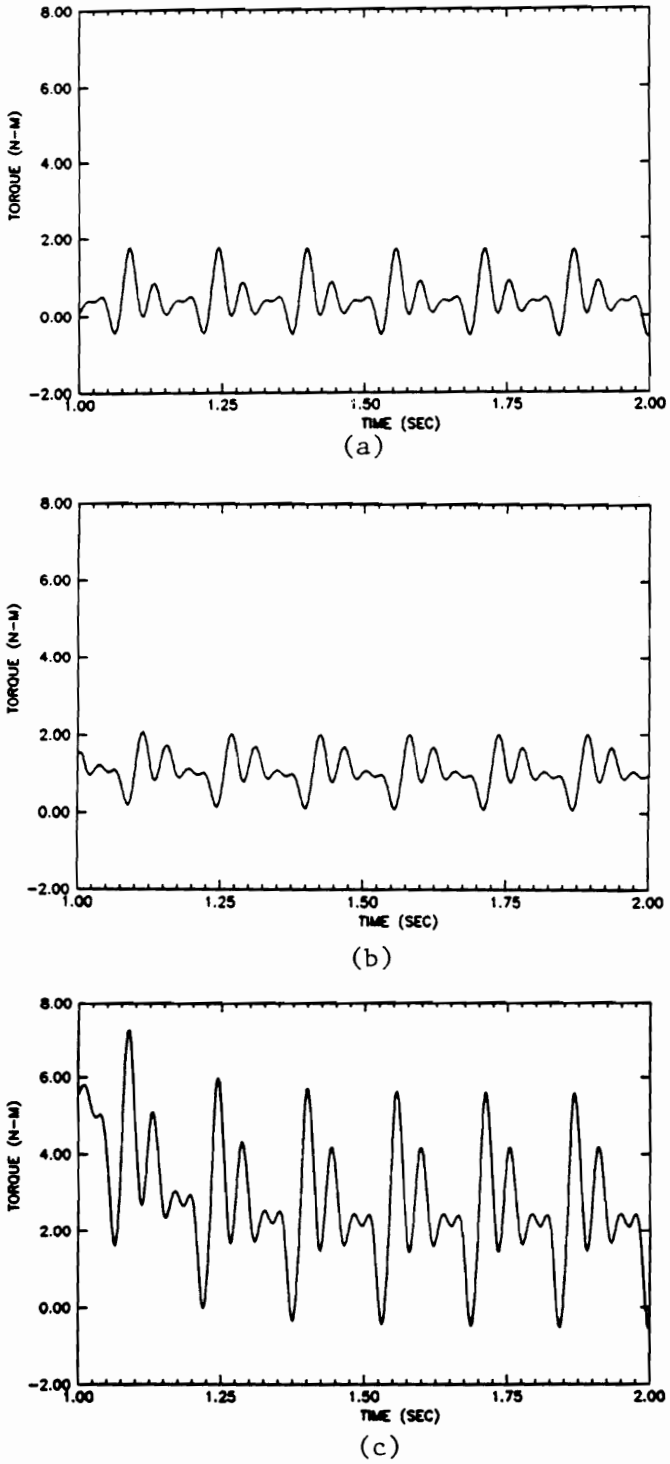

Figure 62. Torque requirement on disk-cutter motor for design option one (a), design option two (b), and design option three (c).

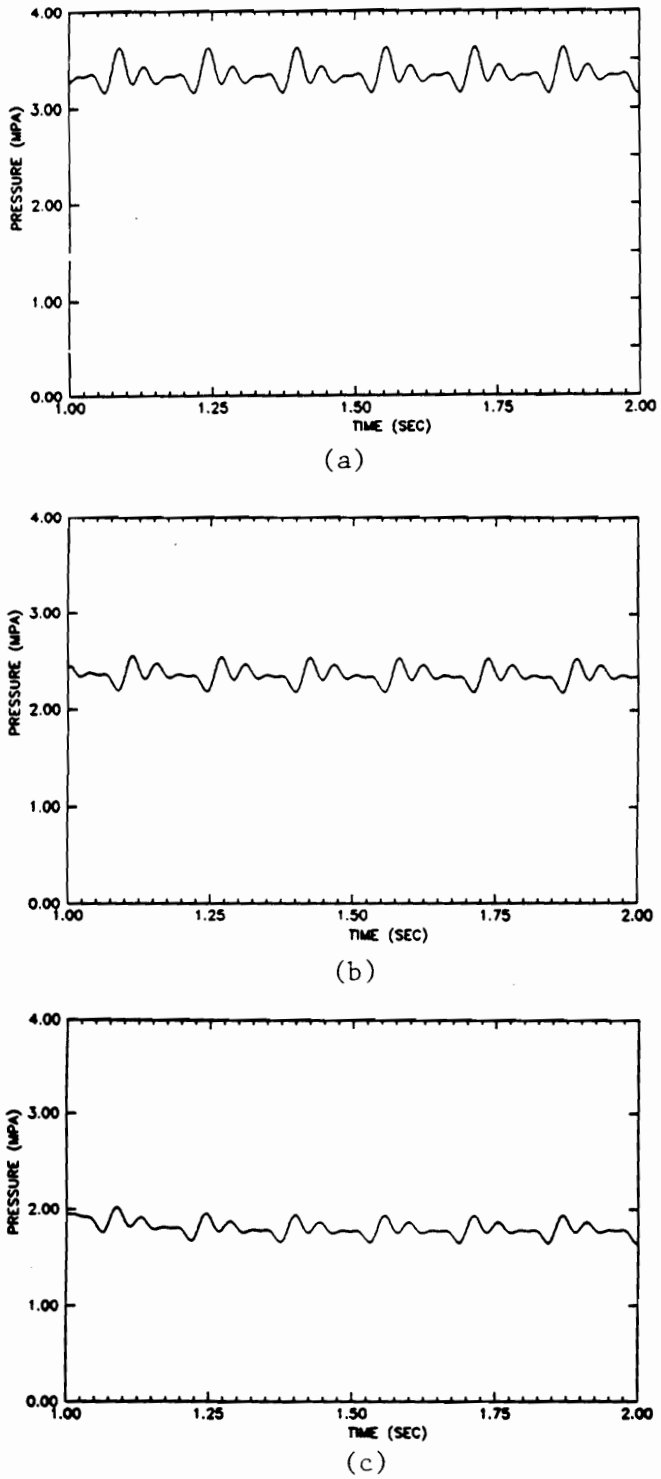

Figure 63. Required pressure at disk-cutter motor for design option one (a), design option two (b), and design option three (c).

7.8 Field Test

Approximately 0.5 hectare of sweet sorghum was planted to conduct performance tests on the whole-stalk harvester. Two varieties, Della and Dale, were planted with 76.2 cm row spacing in 183 m long rows. The harvester cut a single row and collected the stalks in the accumulator (Figure 64). The operator stopped the harvester and dumped the accumulator at the same point on each row, thus creating a windrow of aligned stalk bundles across the field. Bundle weight, tractor speed, and time for dumping was measured and used to calculate field capacity.

Preliminary tests were performed to position and adjust the sub-systems of the harvester. Prior to data collection, several meters were cut and the machine sub-systems adjusted based on subjective observations. Relative speeds between the gathering chains, flipper, and cross conveyor were critical for normal operation.

7.8.1 Field Test Results

Time to accumulate and dump a bundle was measured at three separate field speeds. Three repetitions at each speed were conducted and results are shown in Table 21. Time to accumulate and dump was reduced from 137 s to 81 s when the field speed was increased from 1.96 to 3.56 km/h. At 3.56 km/h, time to dump represented 22% of the time to harvest a bundle.

It was found that the harvester operated best at 3.56 km/h and 1600 rpm engine speed. This was the fastest speed tested and was 1.8 times the slowest speed of 1.96 km/hr. Twenty-one bundles were harvested and weighed to determine field capacity when operating at 3.56 km/h. Average weight per bundle was 161.5 kg and distance between each windrow of bundles was 62.5 m.

Figure 64. View of harvester harvesting a single-row of sweet sorghum for field tests.

Table 21. Time to accumulate a bundle of stalks for three different field speeds.

Field Speed (km/h)	Time to Accumulate (s)	Time to Dump (s)	Time to Accumulate and Dump (s)
1.96	116	21	137
2.95	76	18	94
3.56	63	18	81

Field capacity of the machine was determined from the average weights of harvested bundles, an assumed field efficiency, and a 10-hour work day. Published data for the field efficiency of a forage harvester was used for the whole-stalk harvester (Kepner et. al., 1985).

Field capacity at the three field speeds is given in Table 22. At 3.56 km/h, 1.56 ha/day can be harvested, while at 1.96 km/hr, only 0.92 ha/day could be harvested. Based on a 34.6 Mg/ha whole-stalk yield, 54.0 Mg/day could be harvested at 3.56 km/hr. Over a 30-day harvest season (30 operating days), 1620 Mg could be harvested.

Subjective observations were made under adverse harvesting conditions. Gusty winds and thick weeds growing in the stalk rows contributed to machine foul-ups. Wind blew the stalks out of position as they were released by the stalk flipper, preventing them from laying on the cross conveyor correctly. Misaligned stalks would clog under the flipper and the machine would have to be stopped periodically to clean out this area. In addition, weeds would tend to jam the machine at the point where the stalk guides funneled the stalks into the flipper. Although the machine cleaned itself approximately 85% of the time, eventually a large clump of weeds would jam between the guides and disrupt the flow of stalks. The machine would then have to be stopped and cleaned out.

At the front of the harvester, trash from the field clogged the area above the disk-cutter and the butt of the stalks would catch in this trash, causing them to be pulled down several cm as they were lifted by the gathering chains. Because the stalk was lower than normal in the gathering chains, the butt extended too far down between the flipper discs and improper flipping resulted. Redesign of the disk-cutter will alleviate this problem by clearing the obstruction that catches the "trash".

7.8.2 Sub-system performance

After preliminary adjustments, the harvester sub-systems were set at correct orientation and speeds relative to one another. Gathering chains, flipper, and conveyor speeds are shown in Table 23 for

Table 22. Field capacity data for different field speeds when harvesting a field with 183 m row length.

Time to harvest one bundle (s)	Harvesting Speed (km/h)	Capacity (10 h Day) ha/day	Mg/Day
137	1.96	0.92	31.9
94	2.95	1.34	46.4
81	3.56	1.56	54.0

Table 23. Velocity of gathering chains, flipper, and cross conveyor at 1400 and 1600 tractor engine speed.

Tractor RPM	Gathering Chain Speed (cm/s)	Flipper Speed (cm/s)	Conveyor Speed (cm/s)
1400	65.1	48.2	100.0
1600	78.8	49.3	109.0

two tractor speeds, 1400 and 1600 rpm. At 1600 rpm, gathering chain linear velocity was 1.6 times flipper tangential velocity. Angular velocity of the stalk at the flipper is 3.20 times the angular velocity of the stalk at the point it is released by the gathering chains. Field observations revealed that higher angular velocities at the flipper would cause the stalk to slip in the flipper, and not lay down properly on the conveyor.

The gathering chains linear velocity was 80% of ground speed. While it would have been ideal to have the gathering chains speed equal ground speed, observations showed that stalks were cut by the disk-cutter and grasped by the gathering chains very well at this condition. At higher plant populations (closer spacing in the row) it probably will be more important to have the gathering chains linear velocity as close to ground speed as possible.

Conveyor chain speed was 138% of the gathering chains speed. Stalks were thrown off the conveyor into the accumulator with such velocity that they sometimes were not well aligned. A slower conveyor speed should be investigated in further tests. Selection of a slower conveyor speed only requires adjustment of the swashplate position on the variable displacement pump that supplies flow to the conveyor motor.

Chapter 8 Summary and Conclusions

8.1 Model Development

A whole-stalk sweet sorghum harvester was developed as part of a sweet-sorghum-for-ethanol production system. The harvester has four sub-systems: 1)gathering chains, 2) stalk flipper, 3) conveyor, and 4) accumulator. Sorghum is harvested as follows: The harvester passes over a single-row of sorghum stalks. A disk-cutter cuts the stalks at approximately 10 cm from the ground as the gathering chains simultaneously grasp the stalk 100 cm above the butt. The stalks are carried rearward and upwards until they reach the top of the gathering chains. As the gathering chains release the stalks, they are grasped 10 cm from the bottom by the stalk flipper, which rotates the stalks 90° and layers them onto the cross conveyor. The cross-conveyor chain then picks up the stalks and carries them into the accumulator bin. Once the accumulator has filled, the harvester is stopped, the accumulator is moved out, and the stalks are dumped into a continuous windrow.

All the systems on the harvester were powered hydraulically. Five pumps supplied flow to seven actuator circuits. A V-belt drive delivered power to a muliple-3 pump mounted on the right side

of the harvester input shaft and a multiple-2 pump mounted on the left side. The harvester input shaft was connected to the tractor PTO via a universal joint driveline.

Bond graphs were used to model the seven hydraulic circuits. The models were developed with lumped-parameter elements. High frequency responses were not of interest, therefore a distributed element model was not needed. The bond graph parameters represented physical characteristics which lended itself to interpretation of the model for analysis and design. Once the bond graph was finished, the model equations were extracted in integral form for simulation.

Models of each component were constructed and then concatenated to create each circuit. Model components included pumps, motors, valves, line segments, load functions, and the input drive. Pump and motor models were constructed based on loss coefficients developed by Wilson (1949) and modified by McCandlish (1984). Solving the torque and flow loss equations at four operating conditions determined the coulomb friction and flow slippage loss coefficients at two speeds. Linear interpolation was used to determine the loss coefficients at other speeds.

The most challenging part of the model development was parameter determination. Parameters were determined from theoretical procedures, experimental measurements, and manufacturer's data. Motor losses were measured with a motor test stand designed and built to apply a given load at a given speed. The test stand was successfully used to test all five motors on the harvester and loss coefficients were determined.

Loss coefficients for the pumps were determined from manufacturer's data, not actual testing. Loads on the actuators were determined by solution of the equations of motion and measurements made with a force transducer. Stalk loads were determined from field measurements of average stalk mass and size.

Computer implementation of the models was accomplished using a simulation package called TUTSIM. TUTSIM allowed input in bond graph or block diagram form, plotted results during

simulation, was PC based, and required 256k of RAM. Each component model was input into TUTSIM in separate files (motors, pumps, line segments, DCV, and mechanical loads), and a simulation was run by concatenating the desired components into a complete circuit. TUTSIM proved to be a useful tool in the simulation of non-linear bond graph models.

To validate the model, driveline torque, line pressure, and return line flow rate were measured. Measurements were made at two tractor engine speeds(1400 and 1600 rpm), for the six circuits on the harvester. The measured data was collected with a computer data acquisition system and stored on disk. Simulated and measured data was compared to determine the accuracy in predictions.

8.2 Experimental and Simulated Results

When the measured torque was analyzed, it became apparent that the torsional vibration was more complex than could be explained by excitation from Cardan joint characteristics only. Torsional vibration in the driveline increased significantly as joint angle increased. Cardan joints produce a sinusoidal velocity output at two cycles per revolution which increases in amplitude with the joint angle. Analysis of the data showed that there was also a one cycle per revolution frequency which increased as the joint angle increased. It was determined that this phenomenon was a result of mass unbalance and a secondary couple. The mass unbalance caused shaft whirling which created a time-varying moment of inertia. The secondary couple added to the shaft deflection and contributed to shaft whirling, particularly at larger joint angles. The mass unbalance, and the secondary couple were implemented into the bond graph model by creating a variable inertia term, which increased in magnitude as joint angle increased.

One other phenomenon was cut-off, or clipping, of the measured torque at zero. Due to the couplings in the driveline, backlash was inherent to the system. After adding backlash, mass unbalance,

and secondary couple effects, predicted torque followed the measured torque very well. Differences in the predicted and measured torque was attributed to poor definition of the interaction between the mass unbalance and secondary couple in the model. When the parameters in the model can be defined with higher accuracy, and this interaction is better understood, predicted torque will better emulate measured torque. Even with current understanding, the simulation results were quite acceptable. Mean values of predicted torque were within 0.9 to 8.2 percent of measured mean torques.

Torsional vibration reduces the life of the driveline. The author has not found any reports of mass unbalance and secondary couple effects on torque transmission in a driveline. Further research should be conducted since this phenomenon could result in driveline fatigue and significantly decrease the operating life.

Although the torsional vibration in the driveline had a large amplitude, the resulting pressure measured at the pump outlet did not fluctuate significantly. The hydraulic system will operate satisfactorily for the highest driveline joint angles during field operation. Predicted pressure fluctuations were higher than the measured fluctuations indicating some damping inherent to the hydraulics was not modeled.

Predicted mean pressure did not compare well with measured for the closed circuit systems. The pressure setting of the charge relief valve was not what was reported by the manufacturer, which caused an error in the predicted pressure. By reducing the relief valve setting, error between predicted and measured pressure was reduced by 50 percent.

The two motors in the gathering chains circuit had case drain lines and were connected in series. If the first motor lost fluid through its drain line, the second received less fluid. However, since the motors were linked together by the intermeshing of the gathering chains, they had to turn at the same angular velocity. Input flow to each motor was different, but analysis of the simulation revealed that the second motor was forced to have less drain line and internal cross-port leakage flow.

Subsequently, because the leakage was pressure dependent, a majority of the load was being driven by the first motor. Observing the gathering chains in operation, it was apparent that the first chain was pulling the second. Based on simulation results, it is recommended that one motor be used to drive the two gathering chains.

The cross-conveyor circuit model was the same as the gathering chains up to the motor and loads. The cross conveyor had one motor with no external drain line. Predicted flow was within 8.9 percent, predicted pressure was within 7.3 percent, and predicted torque was within 7.7 percent of measured values.

A load component was added to the model to predict pressure and torque when harvesting in the field. Stalk loads were created on the cross conveyor by stalks falling onto the conveyor and being captured by spikes attached to the chain tabs. Three different stalk loading conditions were analyzed: 1) two stalks captured per spike at full conveyor speed, 2) four stalks captured per spike at one-half conveyor speed, and 3) four stalks captured per spike at full conveyor speed. The load was incorporated as a sinusoidal varying mass to represent stalks being captured at the bottom of the conveyor and thrown off at the top. Full conveyor speed was defined as normal operating speed used in the field (100 cm/s). The stalk load conditions were compared and pressure was 12.9 percent larger and torque was 4.5 percent larger (compared to the no-stalk simulation) when the conveyor was operated at full speed. When the conveyor chain was slowed to one-half full speed (doubling the number of stalks per spike), the pressure only rose 6.2 percent. The largest pressure fluctuations occurred where the stalk load is doubled and the chain is moving at full speed, a condition which would result when the normal plant spacing in the row is doubled. Power increase was only 8 percent, consequently stalk loading on the cross conveyor will not significantly affect the tractor PTO power requirement.

The accumulator was dumped with a hydraulic motor, controlled with one section of a 3-section DCV. When the accumulator rotated far enough for the load center-of-gravity to be at the left of the accumulator shaft (when viewing from the rear), the load reaction was in the same direction as

the motor rotation. An analysis was conducted to determine if the load would become over-running, and cavitate the motor and pump.

Measurements on the circuit were made while dumping a 60 kg bundle of sorghum. Comparison of flow and pressure predictions to measured flow and pressure showed good agreement. When dumping the 60 kg bundle, pressure was well above zero MPa, indicating that the over-running load did not produce a condition that would cause cavitation. With the model validated for one set of conditions, a simulation was run to determine if the load would become over-running for a typical bundle size, 160 kg. When this size bundle was dumped, minimum pressure was 1.0 MPa. Further runs revealed that the circuit would not over-run until a bundle of 320 kg was dumped, and the accumulator frame will not hold a bundle of this size. The circuit was safe for field operation and a design modification was not necessary.

The accumulator cylinder circuit was controlled by the first section of the DCV. When the valve was shifted, the accumulator was extended horizontally. Data was taken when sliding the accumulator out with a 60 kg bundle of stalks in the bin. Predicted mean pressure was 3.9 percent higher than the measured pressure, and mean predicted torque was 1.2 percent larger than measured.

The cross-conveyor cylinder circuit was controlled by the second section of the DCV. Load on the cylinders was a function of the changing angle of inclination of the cross conveyor as the cylinder extended. The conveyor angle was increased from 40° to 75° during a full extension of the cylinder (20 cm). Pressure in the circuit rose to 4.5 MPa, and then began going down as the load on the cylinder began to shift to the pivot point at the base of the conveyor. Predicted pressure underestimated measured, which indicated that the load model needed improvement.

The stalk flipper circuit was powered by the second section of the multiple-3 pump. Flipper rotational velocity was controlled by a flow control valve upstream of the flipper motor. The flow control valve was used to build pressure and open the relief valve so that some flow was diverted

to tank and the flipper speed was reduced. The flipper load was measured before the discs were set in their present configuration; consequently, the actual force between the flipper discs was different than what was measured with the transducer. The measured pressure also fluctuated due to the imperfect alignment between the discs. Mean measured torque was 86.1 N-m and mean predicted torque was 67.9 N-m. The large torque requirement was the result of the high upstream pressure produced by the flow control valve.

The disk-cutter circuit was not yet implemented on the harvester. The bond graph model was developed and simulations run to examine several pump, motor, and sheave ratio combinations. The design option chosen was a 7.3 cm^3/rad motor, the existing pump on the harvester, and a 2:1 sheave ratio between the motor shaft and disk-cutter shaft. This choice was selected because it produced the required 1000 rpm disk speed with the smallest amplitude pressure and torque fluctuations. Torsional vibration was created by the simulated load for cutting the stalks. This analysis proved very useful in designing the circuit, since the torsional vibration may be important to the life of the circuit and the V-belt drive.

8.3 Field Tests

Field tests were conducted with the harvester to measure field performance subjectively, and determine field operating capacity. Optimum field speed was 3.56 km/h with the tractor engine speed set at 1600 rpm. Tractor engine speed determined the speed of operation of all the harvester circuits.

Field capacity was based on a 10-h work day and the field efficiency equal to that of a forage harvester. For a 34 Mg/ha sorghum yield, 54 Mg per day could be harvested. The field results

showed that the harvester can be used to harvest whole-stalk sorghum much like a single-row forage chopper is used to harvest silage.

When the mechanical disk-cutter is replaced with a hydraulic drive, this will eliminate a problem with weeds and grass collecting in an area over the disk-cutter and creating an obstruction. This problem causes the stalks to be out of position at the flipper, and subsequently they are not correctly layered onto the cross conveyor. With this design modification the harvester can be expected to satisfactorily harvest and windrow whole-stalk sorghum.

8.4 Design Modifications

Bond graph models and subsequent simulations were a useful analysis and design tool. Specific design modifications were derived from simulation and field test results. These modifications would reduce the cost of the harvester, and improve efficiency in the use of hydraulic power.

1. The variable displacement pumps were used to change the speed of the gathering chain and cross-conveyor motors. Once the speed of the motors are set for correct field operation, they do not need to be changed; therefore, constant displacement gear pumps would be adequate. Gear pumps are much cheaper and their use will reduce the cost of manufacturing the harvester. In the model, the variable pump displacement was set to attain a motor speed equal to that measured in the field. A gear pump with this displacement would be satisfactory.

2. Predicted and experimental results showed that pressure in the accumulator cylinder lines were relatively low (2 MPa). In addition, the cylinder extension was too slow, which reduced the the field capacity of the machine by increasing the time required to dump a bundle of stalks. A smaller cylinder bore would increase the required pressure, but also increase the cylinder

extension speed as needed. If cylinder bore is cut in-half, pressure and speed doubles. The smaller cylinder is less costly, and the time to move the accumulator out and dump a bundle is reduced, increasing field capacity.

3. Analysis of the gathering chains motor models showed that the load was driven primarily by the first motor. The pressure across the second motor was much lower. In examining the actual operation in the field, it was noticed that the first motor was indeed pulling the second, and that the stalks were carried satisfactorily. By using only one motor to drive both chains, the harvester would have one less hydraulic motor and less hydraulic hose used, thus reducing cost.

Bibliography

Advances in Engineering Series No. 7. 1979. Universal Joint and Driveshaft Design Manual. The Society of Automotive Engineers, Inc., 400 Commonwealth Drive, Warrendale, PA 15096.

Ayers, P. D. and K. Venugopal Varma. 1986. Personal computer aided design of electro-hydraulic control systems. ASAE paper no. 86-5036, American Society of Agricultural Engineers, St. Joseph MI, 49085.

Barnard, B. W. and P. Dransfield. 1977. Predicting response of a proposed hydraulic control system using bond graphs. Trans. of the ASME- Journal of Dynamic Systems, Measurement, and Control, :1-8.

Blackburn, J.F., G. Reethoff, and J. L. Shearer. 1960. Fluid Power Control , John Wiley & Sons, New York NY.

Bond, W. A. and H. R. Martin, 1980. Computer-Aided design of a hydrostatic transmission using bond graphs. Proceedings of the 36th National Fluid Power Conference, October 1980.

Clark, R.L. 1973. Computer design of a hydraulic system. Trans. of the ASAE 16(2):193-194.

Crolla, D.A. 1978. Torsional vibration of tractor and machine PTO drivelines. Journal of Agricultural Engineering Research Vol. 23:259-272.

Cundiff, J.S. and D.J. Parrish. 1984. Drying and storage of whole-stalk sweet sorghum. Final Report, USDA Grant No. 82-CRSR-2-1096. Washington, D.C.

Cundiff, J.S. 1990. Potential of sugar cane/sweet sorghum as a feedstock for energy systems. USDA Broad Form Agreement 90-CSA-XA1-155 Washington D.C.

Cundiff, J.S. and Glen Rains. 1991. 1990 annual sweet sorghum project report. Unpublished research summary, Agricultural Engineering Dept. VPI&SU, Blacksburg VA.

Eschmann, P., L. Hasbargen, and R. Weigand. 1985. Ball and Roller Bearings Theory, Design, and Application. John Wiley & Sons NY NY.

Ge, J. and P. D. Ayers 1989. Design of controllers for nonlinear electro-hydraulic systems with transport lag. ASAE paper no. 89-1568, American Society of Agricultural Engineers, St. Joseph MI, 49085.

Gordon, Greg P. 1989. Computer software for hydraulic circuit design. ASAE paper No. 89-1569, St. Joseph MI, 49085.

Granda, J. J. 1985. Computer generation of physical system differential equations using bond graphs. Journal of the Franklin Institute, Vol. 319, No. 1/2, :243-254.

Henke, Russell L. 1983. Fluid power systems and circuits. Penton Publishing Co. Cleveland OH.

Hibi, A. and T. Ichikawa. 1975. Torque performance of hydraulic motor and its mathematical model. 4th International Fluid Power Symposium. Sheffield, UK, paper B3.

Kepner, R.A., Roy Bainer, and E.L. Barger. Principles of Farm Machinery. Third Edition. AVI Publishing Co. Inc. Westport Conn.

League, Richard B. and J. S. Cundiff. 1988. Bond graph model of a hydrostatic drive test stand. Trans. of the ASAE, Vol. 31, No. 1 :28-36.

Lebrun, M. 1985. The use of modal analysis concepts in the simulation of pipeline transients. Journal of the Franklin Institute, Vol. 319 No. 1/2, :137-155.

Lipinsky, E.S. and S. Kresovich. 1980. Sorghums as energy crops. Proceedings Bio-energy '80 World Congress and Exposition, April 21, 1980, Atlanta GA.

McCandlish, D. and R. Dorey. 1981. Steady state losses in hydrostatic pumps and motors. 6th International Fluid Power Symposium, Cambridge, UK, paper C3 131-144.

Martin, Hugh R. and Jean U. Thoma. 1984. TUTSIM- a fluid power design tool. National Conference on Fluid Power. :89-97.

McCandlish, D. and R. Dorey. 1984. The mathematical modeling of hydrostatic pumps and motors. Proc. IMechE., 198B, No. 10.

Merritt, Herbert E. 1967. Hydraulic Control Systems. John Wiley & Sons, New York New York.

Miller, Donald S. 1971. Internal Flow - A guide to losses in pipe and duct systems. The British Hydromechanics Research Association, Bedford, England.

Mithchell and Gauthier. 1981. "Advanced Continuous Simulation Language (ACSL) User Guide/Reference Manual". Mitchell and Gauthier, Assoc. Inc., Concord, MA.

Nakashima, Yusei, and Tomio Baba. 1989. OCHS: hydraulic circuit design assistant, a knowledge-based system for Kayaba Industry Co., LTD. Proceedings of the 1989 Conference on Innovative Applications of artificial intelligence.

Peeken, H. and F. Fischer. 1989. Experimental investigation of power loss and operating conditions of statically loaded belt drives. Proceedings of the 1989 International Power Transmission and Gearing Conference, Chicago, Ill. April 25-28. 1:15-17.

Rains, G.C. and J.S. Cundiff. 1990. Transducer for measuring force exerted on plant stem. Applied Engineering in Agriculture. 6(3):342-344.

Rains, G.C., J.S. Cundiff, and D.H. Vaughan. 1990. Developement of a whole-stalk sweet sorghum harvester. Trans of the ASAE Vol. 33(1):56-62.

Schlosser, W. M. J. 1961. A mathematical model for displacement type pumps and motors. Oelhydraulik und pneumatik, 1961.

Speckhart, F.H., and W.L. Green. 1976. A guide to using CSMP. Englewood Cliffs, NJ. Prentice-Hall, Inc. 1976.

Technalysis Inc. 1990. Flowmaster-Fluid flow analysis & pipe network design. 7120 Waldemar dr. Indianapolis IN, 46268.

Thoma, J. U. and H. R. Martin, 1983. Simulation for fluid-structure interactions from bond graphs. Fluidics Quarterly, Vol. 14 Issue 1, :67-74.

Thoma, Jean U. and Doris B. Richter. 1987. Simulation of fluid pipes in hydrostatic circuits using modal and segmented methods. Trans. of the Society for Computer Simulation, Vol. 3 No.4 :337-349.

Thoma, J. U., 1989. Link up with bond graphs for HST design. Hydraulics and Pneumatics, April:77-79.

Watton, J. 1989. Fluid Power Systems - Modeling, Simulation, analog, and Microcomputer Control. Prentice Hall Intnl. Ltd., (UK).

Wilson, W. E. 1949. Performance criteria for positive displacement pumps and fluid motors. Trans. of ASME.

Worley, John W. 1990. A systems analysis of sweet sorghum harvest for a piedmont ethanol industry. Phd. Dissertation, VPI&SU, Blacksburg, Va.

Zarotti, G. L. and N. Nervegna. 1981. Pump efficiencies approximation and modeling. 6th International Fluid power Symposium, Cambridge, UK, paper C4, 145-164.

Appendix A - Bond Graph Tutorial

A.1 Introduction

Bond graphs are a unified approach to modeling systems in different energy domains. For example, an electro-mechanical system would require a combination of a mechanical schematic, electrical circuit, and possibly block diagrams. Bond graphs can represent the complete system in a uniform manner which is simpler to understand and more structured in its configuration.

Structured modeling of systems is made possible because bond graphs represent power flow between elements, in any energy domain. Two variables in each bond of the model can be multiplied together to determine power flow. These variables are generically called effort(e) and flow(f). Half-arrows at the end of the bond stroke reveals the direction of the power flow. Power may flow to or from 1-port elements, 2-port elements, or 0 and 1 junctions. In addition, causality determines the cause and effect of the power flow. Each of these elements to bond graph modeling will be discussed to get a full understanding to what gives a model structure.

A.2 Passive 1-port Elements

There are three passive 1-port elements analogous to the mechanical system elements, dashpot, spring, and mass. 1-ports represent power flow through one bond only, and they are passive because the power through them must be derived from some other source.

The R-element is an energy dissipation bond graph. Power to an R-element is dissipated in the energy domain that it represents, and this energy cannot be recovered. The bond graph symbol and constitutive equations associated with an R-element are:

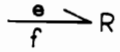

$$Rf = e$$

$$f = 1/Re$$

The variables e and f, together with the resistance element symbol R, represent a linear constitutive equation. R may be a function which creates a non-linear relationship. A resistance element may be used in bond graph models to represent any loss mechanism. As examples, it may represent coulomb friction, viscous drag, and electrical resistance.

The capacitance element is an energy storage bond. Power may be stored and released in this element. The symbol and constitutive equations are:

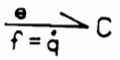

$$e = \frac{1}{C}\int \dot{q}\,dt$$

$$q = \frac{de}{dt}\,C$$

The generalized displacement, q, is a state variable of the system. A spring in the mechanical system is an example of a capacitor element. The element relates effort to the generalized displacement.

It could also be written as a non-linear function. Examples of capacitive elements in different energy domains are mechanical springs, electrical capacitors, and hydraulic accumulators.

Inertia elements are also energy storage elements. However, in the inertia element, a generalized momentum, P, is the state variable for the system. The symbol and constitutive equations are:

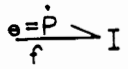

$$f = \frac{1}{I}\int \dot{P}dt$$

$$e = I\frac{df}{dt}$$

As with the other passive 1-ports this representation is a linear case; however, I can be a non-linear function. Some examples of inertia elements are mechanical mass, fluid inertia, and electrical inductance.

P and q are the bond graph state variables derived from the energy storage elements I and C, respectively. They help set-up first order equations which can be written directly from the bond graph model. They can then be assimilated to create a system matrix that may be solved for other variables.

A.3 Active 1-Ports

There are two active 1-ports. They are active because they generate a flow or effort and nothing can affect their generated output. The effort source is represented as:

e is set by the user as the output from the effort source and cannot be changed by effects from the system. The ideal flow source is symbolized by:

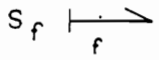

The flow is set and cannot be changed by effects from the system. Effort and flow sources are used as system inputs. Examples include an electrical battery(voltage source), fluid reservoir (flow or pressure source), and the weight of an object (gravity source).

A.4 2-Port Elements

2-port elements are ideal elements which conserve power through the two ports of the element. A modulus is used to produce a proportional relationship between the input and output efforts and flows at each port. There are two types of 2-port elements, the transformer and the gyrator.

The effort at one port of the transformer is proportional to the effort at the other port. The transformer symbol and constitutive equations are:

$$e_1 = Me_2$$

$$f_2 = Mf_1$$

M is the modulus and may be constant or variable; in which case, the transformer is called a modulated transformer (MTF). As an example, a motor produces a torque and a pressure is the result across the motor. If torque is e_1 and pressure is e_2, the modulus is the motor displacement. Shaft speed and fluid flow are similarly related.

The second 2-port element is the gyrator. The gyrator is similar to the transformer in syntax, however, the major difference is how the modulus relates the two ports. Instead of relating the two efforts or flows to one another, the gyrator relates the effort at one port to the flow at the other port. The symbol is:

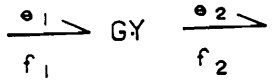

$$e_1 = rf_2$$

$$rf_1 = e_2$$

The symbol r is the modulus for the gyrator. As before, the modulus may be variable creating a modulated gyrator (MGY). An example of a gyrator is an electric dc motor. The torque (e_1) output from the motor is proportional to the current (f_2) input. The modulus r represents a function of flux density, conductor length, and armature radius.

A.5 0 and 1 Junctions

Junctions are the points in bond graphs where power is divided into various directions. There are two junction types used in connecting the elements, described in previous sections, into useful models.

The 0-junction has two characteristics which control their usage. The bonds connected to the junctions all have equivalent efforts, and their flows sum to zero. The following demonstrates these traits for a 3-port junction.

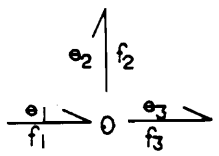

$$e_1 = e_2 = e_3$$

$$f_1 - f_2 - f_3 = 0$$

The 1-junction is the complement to the 0-junction. Flows are equal, and efforts sum to zero for all ports connected to that junction. An example of a 3-port junction is:

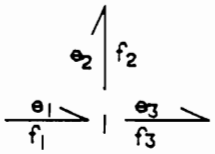

$$f_1 = f_2 = f_3$$

$$e_1 - e_2 - e_3 = 0$$

In analogy to electrical and mechanical systems, 0-junctions represent elements in parallel, and 1-junctions represent elements in series.

A.6 Causality

Causality is shown by a bar perpendicular to the bond stroke. Causality is essential to the equation generation from the model. As the name implies, the causal stroke determines the inputs and outputs for the equations. In physical terms, it reveals the cause and effect relationship between the power variables, effort and flow. A causal stroke placed on the end of the bond stroke away from the half arrow means that the flow through that bond is causing a effort to be imposed on the system. The following illustrates this:

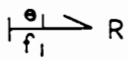

$$e_1 = f_1 \frac{1}{R}$$

Several causal relationships are possible (Table A1). Integral causality is preferred over derivative because of instability which may occur when calculating derivatives on digital computer. Source elements have only one possible causality since their cause and effect relationship is set.

0-junctions are common effort points and have one causal stroke at the junction, as shown in Table A1. Since all efforts are the same, only one causal bar is required at the junction to determine the effort there. The characteristics of 1-junctions are similar. Since 1-junctions have a common flow at that point all bond strokes except one has the causal stroke at the junction; thus, the one that does not, determines the flow at that junction.

Table A1. Element causality relationships and resulting constitutive equations.

Causality Relationships	Constitutive Equations
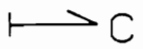	$e = 1/C \int \dot{q}\, dt$
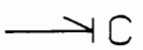	$\dot{q} = C\frac{de}{dt}$
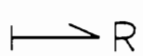	$e = R\, f$
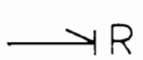	$f = R\, e$
	$f = \frac{1}{I} \int \dot{P}\, dt$
	$\dot{P} = I\frac{df}{dt}$
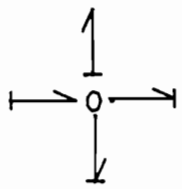	
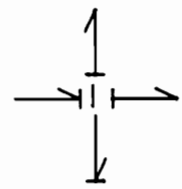	
	
	

Appendix B - Turbo-Pascal Data Acquisition Program

```
program counter_DA_converter;

  uses crt,dos,tp4d16;
  const torque_constant = 4.8852;
  const pressure_constant = 2.791;
  const max = 100;

  var
    board_num, err_code, int_level, dma_level, i, base_adr: integer;
    cntr_data, hour, minute, second, sec100: word;
    raw_data, channel_data: array [0..$fa0] of integer;
    raw_flow: array [1..$c8] of integer;
    elapsed_time,time1,time2,c,interval,rate,time,tim,ti: real;
    total1,total2,total3,avg1,avg2,avg3: real;
    hour1, minute1, second1, sec1001: word;
    out_data: array[0..$7d0] of real;
    flow_data: array[1..$c8] of real;
    add1,add2,chnlo,chnhi,cnt_num,mode,trigger,cycle,j: integer;
    outpress,outflow,outtorq: text;
    DMAPointer : pointer;
    datavector : integer;
```

```
  begin
  clrscr;

{***************
        free DMA buffer memory
                        ********************************}

      GetDMABuffer(8000,DMAPointer,err_code);

      if err_code < > 0 then
          writeln('Get DMA buffer error number',err_code:4);

      datavector := DMAPointer;


{********
      initialize the acquisition board
                                ***************}

      board_num := 0;      {Board number 0}
      int_level := 7;      {interupt level 7}
      dma_level := 1;      {DMA level 1 (for PC-XT with no hard disk}
      base_adr := $300;    {board address is 300 hex}


      d16_init(board_num,base_adr,int_level,dma_level,err_code);

       if err_code < > 0 then
          writeln('initialization error number',err_code:4);

      d16_set_cntr0_config(board_num,0,err_code);

            if err_code < > 0 then
          writeln('initialization counter error number',err_code:4);
{***********
      give values to be used in the D/A routine d16_ainm
                                ***************}


      rate := 100.0;               {50 points per second}
      cnt_num := 1000;               {collect 1000 points}
      mode := 2;                   {DMA mode 2}
      trigger := 1;                {collects data till reaches 4000}
      chnlo := 0;    chnhi  := 1;  {read channels 0 and 1}
      cycle := 0;

{***********
      assign files for output to disk in drive b
                                ***************}

     assign(outpress, 'b: pressure.dat');
     assign(outflow, 'b: flow.dat');
     assign(outtorq, 'b: torque.dat');
```

```
{************
   begin data acquistion from channel 0 to get pressure values
   board is set for bi-polar at +/- 10.0 volts
                                 *************}

     writeln('data acquistion has begun');

     d16_ainsc(board_num,chnlo,chnhi, mode,cycle,trigger,cnt_num, rate,
     datavector, err_code);



{*******
   This loop calculates the number of pulses after approximately
   10 ms and stores the number in raw_data array
                                          ********}

 {*******
   First, initialize the clock time
                                      **********}

  gettime(hour1,minute1,second1,sec1001);

{*******
    now do loop to calculate the number of counts during a period
    and store in array raw_data
                                      ************}

   for i := 1 to max do
   begin

   d16_cset0(board_num, $ffff,err_code);

   delay(98);
   d16_cins0(board_num,1,cntr_data,err_code);
   raw_flow[i] := 65535 - cntr_data;
   end;

   gettime(hour,minute,second,sec100);

{**********
   This marks the end of the data acquistion
                                  *************}

   writeln('This marks the end of data acquistion');

   time1 := 3600.0*hour1 + 60.0*minute1 + second1 + (sec1001/100.0);
   time2 := 3600.0*hour + 60.0*minute + second + (sec100/100.0);

   elapsed_time := (time2 - time1) ;
   interval := elapsed_time/max;

   writeln('time elapsed during loop is',elapsed_time);

   {****************
          begin transforming converted data to useable
```

```
        values and writing to file.
        pressure(psi) = raw_data(odd)*1.953
        torque(in-lbs) = raw_data(even)*6.5
        flow_data = raw_flow/time interval
                              **********}

    rewrite(outpress);
    rewrite(outflow);
    rewrite(outtorq);

        d16_convert_data(2048,1000,datavector,raw_data[0],
                    channel_data[0],0,err_code);

    writeln('Now writing data to disk in psi,in-lbs, and freq.');


        add1 := 0;
        time := 0.0;
        tim  := 0.0;
        add2 := 0;
        total1 := 0.0;
        total2 := 0.0;
        total3 := 0.0;



    for i := 0 to 1000 do
        begin


        if odd(i) then
    begin
        out_data[add1] := (raw_data[i])*pressure_constant;
        time := time + 0.02;
        writeln(outpress,time:10:3,out_data[add1]:12:4);
        total1 := out_data[add1] + total1;
        add1 := add1 + 1;

    end
          else begin
        out_data[add2] := (raw_data[i])*torque_constant;
        tim := tim + 0.02;
        writeln(outtorq,tim:10:3,out_data[add2]:12:4);
        total2 := out_data[add2] + total2;
        add2 := add2 + 1 ;
    end;

    end;
{**********
      now begin data transmission to the files asssigned in
      the B drive.
                              **********}

    ti := 0.0;

    for i := 1 to max do
```

```
begin
flow_data[i] := raw_flow[i]/interval;
ti := ti + 0.10;
writeln(outflow,ti:10:3,flow_data[i]:12:4);
end;

for i := 51 to max do
begin
total3 := flow_data[i] + total3;
end;




close(outflow);
close(outpress);
close(outtorq);

{*********
    Average data and print to screen
                              **********}


 avg1 := total1/500.0;
 avg2 := total2/500.0;
 avg3 := total3/50.0;

 writeln('average pressure is ',avg1:12:4);
 writeln('average torque is ',avg2:12:4);
 writeln('average flow frequency is ',avg3:12:4);


FreeDMABuffer(8000,DMAPointer,err_code);

end.
```

Appendix C Model Parameters

Table C.1 Gathering Chain Circuit

Symbol	Definition	Units	Value
S_f	tractor PTO output	rad/s	81.68 71.51
α	Cardan joint kinematic relationship	-	C.1.1
C_{dl}	driveline stiffness	s/N-m	C.1.2
J_o	shaft inertia	kg-m^2	C.1.3
R_{b1}	bearing friction resistor	N/s	0.04
R_{slv}	V-belt slip resistor	1/N-m-s	13.33
C_v	pump shaft compliance	rad/N-m	0.0015
J_p	pump, shaft, sheave, inertia	kg-m^2	0.00553
R_{b2}	bearing friction resistor	N-m-s/rad	0.02
S_{ptc}	pump torque constant including torque to turn the double pump	N-m	7.5
R_{vdp}	pump viscous drag resistor	N-m-s/rad	0.0125
R_{cfp}	pump coulomb friction resistor	N-m-s/rad	C.1.4
D_{vp}	pump displacement	cm^3/rad	3.0

D_{cp}	charge pump displacement	cm^3/rad	2.712
R_{exp}	pump external leakage resistor	$s\text{-}MPa/cm^3$	0.5
R_{inp}	pump internal leakage resistor	$s\text{-}MPa/cm^3$	0.5
R_{crv}	charge relief valve resistor	$s\text{-}MPa/cm^3$	C.1.5
R_{cv}	check valve resistor	$s\text{-}MPa/cm^3$	C.1.6
C_6	line compliance at pump outlet port	cm^3/MPa	0.192
C_8	line compliance at pump return port	cm^3/MPa	0.192
C_{10}	fluid compliance in charge pump	cm^3/MPa	0.01
I_{L1}	fluid inertia	$MPa\text{-}s/cm^3$	5.55×10^{-6}
R_{L1}	line resistance	$MPa\text{-}s/cm^3$	29.4×10^{-6}
R_{rv}	cross-port relief valve resistor	$MPa\text{-}s/cm^3$	C.1.7
C_{13}	line compliance at cross-over relief valve	cm^3/MPa	0.5343
I_{L2}	fluid inertia	$MPa\text{-}s/cm^3$	17.9×10^{-6}
R_{L2}	line resistance	$MPa\text{-}s/cm^3$	86.7×10^{-6}
C_{16}	line compliance at cross-over relief return line port	cm^3/MPa	0.379
C_{19}	fluid compliance at motor inlet port	cm^3/MPa	0.7892
R_{exm}	motor external leakage resistor	$s\text{-}MPa/cm^3$	1.27
R_{inm}	motor internal leakage resistor	$s\text{-}MPa/cm^3$	7.25
C_{21}	fluid compliance at motor return port	cm^3/MPa	0.4290
D_{gcm}	gathering chain motor displacement	cm^3/rad	38.86
J_m	motor and chain inertia	$kg\text{-}m^2$	0.12525
R_{b4}	bearing friction resistor	N-m-s/rad	0.04

S_{mtc}	motor torque constant	N-m	2.7
R_{vdm}	motor viscous drag resistor	N-m-s/rad	4.37
R_{cfm}	motor coulomb friction resistor	N-m-s/rad	C.1.8
R_c	sprocket radius used for transformer modulus	m	0.056
C_{ch}	chain and gripper pad compliance	rad/N-m	50.0×10^{-5}
R_l	load resistance on gathering chains	N	1.335
R_{bs}	bearing friction resistor	N-m-s/rad	1.522
J_l	stalk load mass	kg-m^2	(no stalk load)
W_{st}	stalk load weight	N	(no stalk load)
I_{L3}	fluid inertia	MPa-s/cm^3	11.1×10^{-6}
R_{L3}	line resistance	MPa-s/cm^3	51.3×10^{-6}
I_{L4}	fluid inertia	MPa-s/cm^3	5.55×10^{-6}
R_{L4}	line resistance	MPa-s/cm^3	29.4×10^{-6}
I_{L5}	fluid inertia	MPa-s/cm^3	5.017×10^{-6}
R_{L5}	line resistance	MPa-s/cm^3	122×10^{-6}
C_{21}	line compliance at motor return port	cm^3/MPa	1.0476
C_{28}	line compliance motor inlet port	cm^3/MPa	1.0476
C_{30}	line compliance at motor return port	cm^3/MPa	0.4290

C.1.1 Modulus of Joint Effects

$$\alpha = \frac{\omega_{his}}{\omega_{PTO}} = \frac{\cos\theta_1 \cos\theta_2}{(1 - \sin^2\beta_1 \sin^2\theta_1)(1 - \sin^2\beta_2 \sin^2\theta_2)}$$

where

ω_{his} = harvester input shaft velocity (rad/s),
θ_1 = joint angle in joint 1 (rad),
θ_2 = joint angle in joint 2 (rad),
β_1 = rotational position of front shaft driving yoke measured from the plane perpendicular to joint angle (rad)
β_2 = rotational position of connecting shaft driving yoke measured from the plane perpendicular to joint angle (rad), and
ω_{in} = input velocity from tractor PTO (rad/s).

C.1.2 Driveline Backlash and Non-linear V-belt Function

Torque	$\Delta\theta$
-200.0	-0.300
0.0	-0.200
0.0	0.095
10.0	0.200
200.0	0.250
300.0	0.300

C.1.3 Shaft Inertia Function

$$J_o = \bar{J} + m[r(t)]^2$$

where
J_o = mass moment of inertia (kg-m^2),
$\bar{J}$ = mass moment of inertia about mass center (kg-m^2),
m = mass of shaft (kg), and
r(t) = distance between axis of rotation to mass center (m).

C.1.4 Pump Coulomb Friction Resistor Function

C_f	ω
0.0900	0.00
0.0700	100.00
0.0502	167.50
0.0338	200.00
0.0338	400.00

$$T_{cfp} = C_f(P_6 - P_8)D_{vp}$$

C.1.5 Charge Relief Valve Resistor Function

Q_{crv}	P_{10}
0.0	-200.0

0.0	0.0
25.0	1.5
50.0	2.5
100.0	3.5
100.0	4.5

C.1.6 Check Valve Resistor Function

Q_9	$(P_{10} - P_8)$
0.0	-10.0
0.0	0.0
200.0	1.0
400.0	1.5
700.0	1.6
700.0	1.7

C.1.7 Cross-Port Relief Valve Resistor Function

Q_{14}	$(P_{13} - P_{16})$
0.0	0.0
0.0	2.0
5.0	4.0
10.0	6.5
1000.0	7.0
1000.0	8.0

C.1.8 Motor Coulomb Friction Resistor Function

C_f	ω
0.000	0.300
0.133	5.236
0.073	8.380
0.025	31.416
0.025	50.000

$$T_{cfm} = C_f(P_{19} - P_{21})D_{gcm}$$

Table C.2 Cross-Conveyor Motor Circuit

Symbol	Definition	Units	Value
S_f	tractor PTO output	rad/s	81.68 71.51
α	Cardan joint kinematic relationship	-	C.2.1
C_{dl}	driveline stiffness	s/N-m	C.2.2
J_o	shaft inertia	kg-m^2	C.2.3
R_{b1}	bearing friction resistor	N/s	0.04
R_{slv}	V-belt slip resistor	1/N-m-s	13.33
C_v	pump shaft compliance	rad/N-m	0.0015
J_p	pump, shaft, sheave, inertia	kg-m^2	0.00553
R_{b2}	bearing friction resistor	N-m-s/rad	0.02
S_{ptc}	pump torque constant including torque to turn the gear pump	N-m	3.725
R_{vdp}	pump viscous drag resistor	N-m-s/rad	0.0125
R_{cfp}	pump coulomb friction resistor	N-m-s/rad	C.2.4
D_{vp}	pump displacement	cm^3/rad	3.13
D_{cp}	charge pump displacement	cm^3/rad	1.88
R_{exp}	pump external leakage resistor	s-MPa/cm^3	0.5
R_{inp}	pump internal leakage resistor	s-MPa/cm^3	0.5
R_{crv}	charge relief valve resistor	s-MPa/cm^3	C.2.5
R_{cv}	check valve resistor	s-MPa/cm^3	C.2.6
C_6	line compliance at pump outlet port	cm^3/MPa	0.192

C_8	line compliance at pump return port	cm^3/MPa	0.192
C_{10}	fluid compliance in charge pump	cm^3/MPa	0.01
I_{L1}	fluid inertia	$MPa\text{-}s/cm^3$	4.05×10^{-6}
R_{L1}	line resistance	$MPa\text{-}s/cm^3$	20.6×10^{-6}
R_{rv}	cross-port relief valve resistor	$MPa\text{-}s/cm^3$	C.2.7
C_{13}	line compliance at cross-over relief valve	cm^3/MPa	0.5343
I_{L2}	fluid inertia	$MPa\text{-}s/cm^3$	2.14×10^{-6}
R_{L2}	line resistance	$MPa\text{-}s/cm^3$	15.4×10^{-6}
C_{16}	line compliance at cross-over relief return line port	cm^3/MPa	0.379
C_{19}	fluid compliance at motor inlet port	cm^3/MPa	0.7892
R_{inm}	motor internal leakage resistor	$s\text{-}MPa/cm^3$	4.59
C_{21}	fluid compliance at motor return port	cm^3/MPa	0.1100
D_{cm}	cross conveyor motor displacement	cm^3/rad	25.30
J_m	motor and chain inertia	$kg\text{-}m^2$	0.035
R_{b4}	bearing friction resistor	N-m-s/rad	0.02
S_{mtc}	motor torque constant	N-m	5.7
R_{vdm}	motor viscous drag resistor	N-m-s/rad	1.17
R_{cfm}	motor coulomb friction resistor	N-m-s/rad	C.2.8
R_c	sprocket radius used for transformer modulus	m	0.056
C_{ch}	chain compliance	rad/N-m	50.0×10^{-5}
R_{ss}	sliding resistance of stalks over conveyor covering	N	1.335

W_{sw}	stalk weight	N-m-s/rad	C.2.9
I_{sm}	stalk load mass	kg-m^2	C.2.10
I_{L3}	fluid inertia	MPa-s/cm^3	2.57 x 10^{-6}
R_{L3}	line resistance	MPa-s/cm^3	15.6 x 10^{-6}
I_{L4}	fluid inertia	MPa-s/cm^3	5.65 x 10^{-6}
R_{L4}	line resistance	MPa-s/cm^3	29.4 x 10^{-6}
C_{21}	line compliance at motor return port	cm^3/MPa	0.1100

C.2.1 Modulus of Joint Effects

$$\alpha = \frac{\omega_{hls}}{\omega_{PTO}} = \frac{\cos\theta_1 \cos\theta_2}{(1 - \sin^2\beta_1 \sin^2\theta_1)(1 - \sin^2\beta_2 \sin^2\theta_2)}$$

where

ω_{hls} = harvester input shaft velocity (rad/s),
θ_1 = joint angle in joint 1 (rad),
θ_2 = joint angle in joint 2 (rad),
β_1 = rotational position of front shaft driving yoke measured from the plane perpendicular to joint angle (rad),
β_2 = rotational position of connecting shaft driving yoke measured from the plane perpendicular to joint angle (rad), and
ω_{in} = input velocity from tractor PTO (rad/s).

C.2.2 Driveline Backlash and Non-linear V-belt Function

Torque	$\Delta\theta$
-200.0	-0.300
0.0	-0.200
0.0	0.095
10.0	0.200
200.0	0.250
300.0	0.300

C.2.3 Shaft Inertia Function

$$J_o = \bar{J} + m[r(t)]^2$$

where
J_o = mass moment of inertia (kg-m^2),
$\bar{J}$ = mass moment of inertia about mass center (kg-m^2),
m = mass of shaft (kg), and
r(t) = distance between axis of rotation to mass center (m).

C.2.4 Pump Coulomb Friction Resistor Function

C_f	ω
0.0900	0.00
0.0700	100.00
0.0502	167.50
0.0338	200.00
0.0338	400.00

$$T_{cfp} = C_f(P_6 - P_8)D_{vp}$$

C.2.5 Charge Relief Valve Resistor Function

Q_{crv}	P_{10}
0.0	-200.0
0.0	0.0
25.0	1.5
50.0	2.5
100.0	3.5
100.0	4.5

C.2.6 Check Valve Resistor Function

Q_9	$(P_{10} - P_8)$
0.0	-10.0
0.0	0.0
200.0	1.0
400.0	1.5
700.0	1.6
700.0	1.7

C.2.7 Cross-Port Relief Valve Resistor Function

Q_{14}	$(P_{13} - P_{16})$

0.0	0.0
0.0	2.0
5.0	4.0
10.0	6.5
1000.0	7.0
1000.0	8.0

C.2.8 Motor Coulomb Friction Resistor Function

C_f	ω
0.300	0.300
0.167	12.570
0.249	16.550
0.050	31.000
0.050	50.000

C.2.9 Variable stalk weight (2 stalks per spike)

$$W_{sw} = (A \sin 2\pi t + W_o)(\sin \theta)$$

where

A = amplitude of stalk variation (12.75 N)
W_o = average weight of stalks on conveyor (90 N), and
θ = angle of conveyor (40°)

C.2.10 Variable stalk mass (2 stalks per spike)

$$I_{sw} = (A \sin 2\pi t + I_o)(\sin \theta)$$

where
A = amplitude of stalk variation (1.3 kg)
I_o = average mass of stalks on conveyor (9.1 N), and
θ = angle of conveyor (40°)

Table C.3 Accumulator Motor Circuit

Symbol	Definition	Units	Value
S_f	tractor PTO output	rad/s	81.68 71.51
α	Cardan joint kinematic relationship	-	C.3.1
C_{dl}	driveline stiffness	s/N-m	C.3.2
J_o	shaft inertia	kg-m^2	C.3.3
R_{b1}	bearing friction resistor	N/s	0.04
R_{slv}	V-belt slip resistor	1/N-m-s	13.33
C_v	pump shaft compliance	rad/N-m	0.0015
J_p	pump, shaft, sheave, inertia	kg-m^2	0.050
R_{b2}	bearing friction resistor	N-m-s/rad	0.02
S_{ptc}	pump torque constant including torque to turn the gear pump and variable displacement pump	N-m	7.5
R_{vdp}	pump viscous drag resistor	N-m-s/rad	0.01282
R_{cfp}	pump coulomb friction resistor	N-m-s/rad	0.04
D_{vp}	pump displacement	cm^3/rad	3.1558
R_{slp}	pump internal leakage resistor	s-MPa/cm^3	4.239
C_5	line compliance from pump to DCV	cm^3/MPa	0.1285
C_7	line compliance at DCV	cm^3/MPa	0.112
C_{10}	line compliance from DCV to motor	cm^3/MPa	0.112
I_{L1}	fluid inertia	MPa-s/cm^3	46.6 x 10^{-6}

R_{L1}	line resistance	MPa-s/cm^3	337.4 x 10^{-6}
R_8	valve shift resistor	MPa-s/cm^3	C.3.4
R_9	valve shift resistor	MPa-s/cm^3	C.3.5
R_{rv}	relief valve resistor	MPa-s/cm^3	C.3.6
I_{L2}	fluid inertia	MPa-s/cm^3	16.0 x 10^{-6}
R_{L2}	line resistance	MPa-s/cm^3	115.8 x 10^{-6}
C_{12}	line compliance at motor port inlet	cm^3/MPa	0.4715
R_{slm}	motor internal leakage resistor	s-MPa/cm^3	0.4715
C_{21}	fluid compliance at motor return port	cm^3/MPa	0.1100
D_m	accumulator motor displacement	cm^3/rad	58.94
J_m	motor and chain inertia	kg-m^2	1.00
R_{b4}	bearing friction resistor	N-m-s/rad	0.02
S_{mtc}	motor torque constant	N-m	18.00
R_{vdm}	motor viscous drag resistor	N-m-s/rad	2.665
R_{cfm}	motor coulomb friction resistor	N-m-s/rad	0.172
C_{60}	chain compliance	rad/N-m	22.0 x 10^{-6}
SR2	sprocket ratio	-	8:1
J_{sp}	sprocket inertia	kg-m^2	2.72
R_{b4}	bearing friction resistor	N-m-s/rad	0.500
C_{100}	chain compliance	rad/N-m	2.20 x 10^{-6}
SR3	Sprocket ratio	-	3:1
R_{b5}	journal bearing resistance	N	3.60

S_{el}	accumulator and stalk weight	N-m-s/rad	C.3.7
J_{acc}	accumulator and stalk load mass	kg-m^2	108.2

C.3.1 Modulus of Joint Effects

$$\alpha = \frac{\omega_{his}}{\omega_{PTO}} = \frac{\cos\theta_1 \cos\theta_2}{(1 - \sin^2\beta_1 \sin^2\theta_1)(1 - \sin^2\beta_2 \sin^2\theta_2)}$$

where

ω_{his} = harvester input shaft velocity (rad/s),
θ_1 = joint angle in joint 1 (rad),
θ_2 = joint angle in joint 2 (rad),
β_1 = rotational position of front shaft driving yoke measured from the plane perpendicular to joint angle (rad),
β_2 = rotational position of connecting shaft driving yoke measured from the plane perpendicular to joint angle (rad), and
ω_{in} = input velocity from tractor PTO (rad/s).

C.3.2 Driveline Backlash and Non-linear V-belt Function

Torque	$\Delta\theta$
-200.0	-0.300
0.0	-0.200
0.0	0.095
10.0	0.200
200.0	0.250
300.0	0.300

C.3.3 Shaft Inertia Function

$$J_o = \bar{J} + m[r(t)]^2$$

where
J_o = mass moment of inertia (kg-m^2),
$\bar{J}$ = mass moment of inertia about mass center (kg-m^2),
m = mass of shaft (kg), and
r(t) = distance between axis of rotation to mass center (m).

C.3.4 Valve Shift Resistor (R_8)

R_8	time (s)
0.01	0.0
0.01	0.50
3250.0	0.505
3250.0	10.000

C.3.5 Valve Shift Resistor (R_9)

R_9	time (s)
3250.0	0.0
3250.0	0.50
0.01	0.505
0.01	10.000

C.3.6 Relief Valve Resistor Function

Q_7	P_7
0.0	0.000
12.0	3.400
25.0	3.500
300.0	3.502
600.0	3.504
900.0	3.506

C.3.7 Accumulator and Stalk Mass Function

$$S_{el} = T_a \cos\theta + T_s \cos\theta$$

where

S_{el} = torque required to rotate accumulator shaft (N-m),
T_a = torque due to accumulator frame (N-m),
T_s = torque due to stalks (N-m), and
θ = angle of accumulator rotation (rad).

Table C.4 Accumulator Cylinder Circuit

Symbol	Definition	Units	Value
S_f	tractor PTO output	rad/s	81.68 71.51
α	Cardan joint kinematic relationship	-	C.4.1
C_{dl}	driveline stiffness	s/N-m	C.4.2
J_o	shaft inertia	kg-m^2	C.4.3
R_{b1}	bearing friction resistor	N/s	0.04
R_{slv}	V-belt slip resistor	1/N-m-s	13.33
C_v	pump shaft compliance	rad/N-m	0.0015
J_p	pump, shaft, sheave, inertia	kg-m^2	0.050
R_{b2}	bearing friction resistor	N-m-s/rad	0.02
S_{ptc}	pump torque constant including torque to turn the gear pump and variable displacement pump	N-m	7.5
R_{vdp}	pump viscous drag resistor	N-m-s/rad	0.01282
R_{cfp}	pump coulomb friction resistor	N-m-s/rad	0.04
D_{vp}	pump displacement	cm^3/rad	3.1558
R_{slp}	pump internal leakage resistor	s-MPa/cm^3	4.239
C_5	line compliance from pump to DCV	cm^3/MPa	0.1285
C_7	line compliance at DCV	cm^3/MPa	0.112
C_{10}	line compliance from DCV to motor	cm^3/MPa	0.112
R_8	valve shift resistor	MPa-s/cm^3	C.4.4

I_{L1}	fluid inertia	MPa-s/cm^3	16.0 x 10^{-6}
R_{L1}	line resistance	MPa-s/cm^3	115.8 x 10^{-6}
R_9	valve shift resistor	MPa-s/cm^3	C.4.5
R_{rv}	relief valve resistor	MPa-s/cm^3	C.4.6
I_{L2}	fluid inertia	MPa-s/cm^3	16.0 x 10^{-6}
R_{L2}	line resistance	MPa-s/cm^3	286.7 x 10^{-6}
C_{12}	line compliance at motor port inlet	cm^3/MPa	0.200
R_{slc}	cylinder leakage resistor	s-MPa/cm^3	6.04
A_c	cylinder cap end area	mm^2	10053.0
A_r	cylinder rod end area	mm^2	8128.0
I_{acc}	accumulator and I-beam mass	kg	400.0
R_{bp}	sliding friction resistor	N-s/m	0.45
R_{vdc}	cylinder viscous drag resistor	N-s/m	675.0
R_{cfc}	cylinder coulomb friction	N-s/m	0.00025

C.4.1 Modulus of Joint Effects

$$\alpha = \frac{\omega_{his}}{\omega_{PTO}} = \frac{\cos\theta_1 \cos\theta_2}{(1 - \sin^2\beta_1 \sin^2\theta_1)(1 - \sin^2\beta_2 \sin^2\theta_2)}$$

where

ω_{his} = harvester input shaft velocity (rad/s),
θ_1 = joint angle in joint 1 (rad),
θ_2 = joint angle in joint 2 (rad),
β_1 = rotational position of front shaft driving yoke measured from the plane perpendicular to joint angle (rad),
β_2 = rotational position of connecting shaft driving yoke measured from the plane perpendicular to joint angle (rad), and
ω_{in} = input velocity from tractor PTO (rad/s).

C.4.2 Driveline Backlash and Non-linear V-belt Function

Torque	$\Delta\theta$
-200.0	-0.300
0.0	-0.200
0.0	0.095
10.0	0.200
200.0	0.250
300.0	0.300

C.4.3 Shaft Inertia Function

$$J_o = \bar{J} + m[r(t)]^2$$

where

J_o = mass moment of inertia (kg-m^2),
$\bar{J}$ = mass moment of inertia about mass center (kg-m^2),

m = mass of shaft (kg), and
r(t) = distance between axis of rotation to mass center (m).

C.4.4 Valve Shift Resistor (R_8)

R_8	time (s)
0.01	0.0
0.01	0.50
3250.0	0.505
3250.0	10.000

C.4.5 Valve Shift Resistor (R_9)

R_9	time (s)
3250.0	0.0
3250.0	0.50
0.01	0.505
0.01	10.000

C.4.6 Relief Valve Resistor Function

Q_7	P_7
0.0	0.000
12.0	3.400

25.0	3.500
300.0	3.502
600.0	3.504
900.0	3.506

Table C.5 Cross-Conveyor Cylinder Circuit

Symbol	Definition	Units	Value
S_f	tractor PTO output	rad/s	81.68 71.51
α	Cardan joint kinematic relationship	-	C.5.1
C_{dl}	driveline stiffness	s/N-m	C.5.2
J_o	shaft inertia	kg-m^2	C.5.3
R_{b1}	bearing friction resistor	N/s	0.04
R_{slv}	V-belt slip resistor	1/N-m-s	13.33
C_v	pump shaft compliance	rad/N-m	0.0015
J_p	pump, shaft, sheave, inertia	kg-m^2	0.050
R_{b2}	bearing friction resistor	N-m-s/rad	0.02
S_{ptc}	pump torque constant including torque to turn the gear pump and variable displacement pump	N-m	7.5
R_{vdp}	pump viscous drag resistor	N-m-s/rad	0.01282
R_{cfp}	pump coulomb friction resistor	N-m-s/rad	0.04
D_{vp}	pump displacement	cm^3/rad	3.1558
R_{slp}	pump internal leakage resistor	s-MPa/cm^3	4.239
C_5	line compliance from pump to DCV	cm^3/MPa	0.1285
C_7	line compliance at DCV	cm^3/MPa	0.112
C_{10}	line compliance from DCV to motor	cm^3/MPa	0.112
R_8	valve shift resistor	MPa-s/cm^3	C.5.4

R_9	valve shift resistor	MPa-s/cm^3	C.5.5
R_{rv}	relief valve resistor	MPa-s/cm^3	C.5.6
I_{L1}	fluid inertia	MPa-s/cm^3	16.0 x 10^{-6}
R_{L1}	line resistance	MPa-s/cm^3	115.8 x 10^{-6}
I_{L2}	fluid inertia	MPa-s/cm^3	16.0 x 10^{-6}
R_{L2}	line resistance	MPa-s/cm^3	169.7 x 10^{-6}
R_{slc}	cylinder leakage resistor	s-MPa/cm^3	6.04
A_c	cylinder cap end area	mm^2	5654.0
A_r	cylinder rod end area	mm^2	4241.0
m	modulus representing the kinematic relationship between load and conveyor angle	-	C.5.7
I_{lo}	cross conveyor mass	kg	350.0
S_g	cross conveyor weight	N	3425.0
R_{res}	load friction resistor	N-s/m	0.05
R_{vdc}	cylinder viscous drag resistor	N-s/m	672.0
R_{cfc}	cylinder coulomb friction	N-s/m	0.00025

C.5.1 Modulus of Joint Effects

$$\alpha = \frac{\omega_{his}}{\omega_{PTO}} = \frac{\cos\theta_1 \cos\theta_2}{(1 - \sin^2\beta_1 \sin^2\theta_1)(1 - \sin^2\beta_2 \sin^2\theta_2)}$$

where
ω_{his} = harvester input shaft velocity (rad/s),
θ_1 = joint angle in joint 1 (rad),
θ_2 = joint angle in joint 2 (rad),
β_1 = rotational position of front shaft driving yoke measured from the plane perpendicular to joint angle (rad),
β_2 = rotational position of connecting shaft driving yoke measured from the plane perpendicular to joint angle (rad), and
ω_{in} = input velocity from tractor PTO (rad/s).

C.5.2 Driveline Backlash and Non-linear V-belt Function

Torque	$\Delta\theta$
-200.0	-0.300
0.0	-0.200
0.0	0.095
10.0	0.200
200.0	0.250
300.0	0.300

C.5.3 Shaft Inertia Function

$$J_o = \bar{J} + m[r(t)]^2$$

where
J_o = mass moment of inertia (kg-m^2),
$\bar{J}$ = mass moment of inertia about mass center (kg-m^2),

m = mass of shaft (kg), and
r(t) = distance between axis of rotation to mass center (m).

C.5.4 Valve Shift Resistor (R_8)

R_8	time (s)
0.01	0.0
0.01	0.50
3250.0	0.505
3250.0	10.000

C.5.5 Valve Shift Resistor (R_9)

R_9	time (s)
3250.0	0.0
3250.0	0.50
0.01	0.505
0.01	10.000

C.5.6 Relief Valve Resistor Function

Q_7	P_7
0.0	0.000
12.0	3.400

25.0	3.500
300.0	3.502
600.0	3.504
900.0	3.506

C.5.6 Load modulus (m)

$$m = \left(\frac{x}{\bar{x}}\right) \frac{\cos \gamma}{\cos \alpha}$$

where

α = angle of conveyor with horizontal plane (rad),
γ = angle of cylinder with plane perpendicular to conveyor (rad),
$\bar{x}$ = distance from base of cylinder to conveyor center of gravity (m), and
x = distance from base of cylinder to cylinder connection (m).

Table C.6 Stalk Flipper Circuit

Symbol	Definition	Units	Value
S_f	tractor PTO output	rad/s	81.68 71.51
α	Cardan joint kinematic relationship	-	C.6.1
C_{dl}	driveline stiffness	s/N-m	C.6.2
J_o	shaft inertia	kg-m^2	C.6.3
R_{b1}	bearing friction resistor	N/s	0.04
R_{slv}	V-belt slip resistor	1/N-m-s	13.33
C_v	pump shaft compliance	rad/N-m	0.0015
J_p	pump, shaft, sheave, inertia	kg-m^2	0.00553
R_{b2}	bearing friction resistor	N-m-s/rad	0.02
S_{ptc}	pump torque constant including torque to turn the double pump	N-m	7.5
R_{vdp}	pump viscous drag resistor	N-m-s/rad	0.01282
R_{cfp}	pump coulomb friction resistor	N-m-s/rad	0.04
D_p	pump displacement	cm^3/rad	2.53
R_{slp}	pump internal leakage resistor	s-MPa/cm^3	4.239
R_{rv}	relief valve resistor	MPa-s/cm^3	C.6.4
C_5	line compliance at pump outlet port	cm^3/MPa	0.117
I_{L1}	fluid inertia	MPa-s/cm^3	261 x 10^{-9}
R_{L1}	line resistance	MPa-s/cm^3	304 x 10^{-6}
R_{nv}	flow control valve resistor	s-MPa/cm^3	C.6.5

C_7	line compliance at flow control valve	cm^3/MPa	0.106
C_{12}	line compliance at motor inlet port	cm^3/MPa	0.319
R_{slm}	motor internal leakage resistor	s-MPa/cm^3	8.79
D_m	flipper motor displacement	cm^3/rad	46.68
J_{sf}	motor and flipper disc inertia	kg-m^2	7.615
R_{b4}	bearing friction resistor	N-m-s/rad	0.04
S_{mtc}	motor torque constant	N-m	12.46
R_{vdm}	motor viscous drag resistor	N-m-s/rad	4.79
R_{cfm}	motor coulomb friction resistor	N-m-s/rad	C.6.6
R_{sf}	load resistance on flipper discs	N	132 x 10^{-6}

C.6.1 Modulus of Joint Effects

$$\alpha = \frac{\omega_{his}}{\omega_{PTO}} = \frac{\cos\theta_1 \cos\theta_2}{(1 - \sin^2\beta_1 \sin^2\theta_1)(1 - \sin^2\beta_2 \sin^2\theta_2)}$$

where

ω_{his} = harvester input shaft velocity (rad/s),
θ_1 = joint angle in joint 1 (rad),
θ_2 = joint angle in joint 2 (rad),
β_1 = rotational position of front shaft driving yoke measured from the plane perpendicular to joint angle (rad)
β_2 = rotational position of connecting shaft driving yoke measured from the

plane perpendicular to joint angle (rad), and
ω_{in} = input velocity from tractor PTO (rad/s).

C.6.2 Driveline Backlash and Non-linear V-belt Function

Torque	$\Delta\theta$
-200.0	-0.300
0.0	-0.200
0.0	0.095
10.0	0.200
200.0	0.250
300.0	0.300

C.6.3 Shaft Inertia Function

$$J_o = \bar{J} + m[r(t)]^2$$

where
J_o = mass moment of inertia (kg-m^2),
$\bar{J}$ = mass moment of inertia about mass center (kg-m^2),
m = mass of shaft (kg), and
r(t) = distance between axis of rotation to mass center (m).

C.6.4 Relief Valve Resistor Function

Q_{rv}	P_s

0.0	0.0
10.0	4.0
25.0	4.25
365.0	4.50
10000.0	6.25

C.6.5 Flow Control Valve Resistor Function

$$R_{nv} = 6.04\sqrt{P_{12} - P_7}$$

C.6.6 Motor Coulomb Friction Resistor Function

C_f	ω
0.896	0.000
0.200	4.189
0.074	6.283
0.074	10.000

$$T_{cfm} = C_f P_{12}$$

Table C.7 Disk-cutter Circuit

Symbol	Definition	Units	Value
S_f	tractor PTO output	rad/s	81.68 71.51
α	Cardan joint kinematic relationship	-	C.7.1
C_{dl}	driveline stiffness	s/N-m	C.7.2
J_o	shaft inertia	kg-m^2	C.7.3
R_{b1}	bearing friction resistor	N/s	0.04
R_{slv}	V-belt slip resistor	1/N-m-s	13.33
C_v	pump shaft compliance	rad/N-m	0.0015
J_p	pump, shaft, sheave, inertia	kg-m^2	0.00553
R_{b2}	bearing friction resistor	N-m-s/rad	0.02
S_{ptc}	pump torque constant including torque to turn the double pump	N-m	3.75
R_{vdp}	pump viscous drag resistor	N-m-s/rad	0.01282
R_{cfp}	pump coulomb friction resistor	N-m-s/rad	0.04
D_p	pump displacement	cm^3/rad	3.167
R_{slp}	pump internal leakage resistor	s-MPa/cm^3	4.239
R_{rv}	relief valve resistor	MPa-s/cm^3	C.7.4
C_5	line compliance at pump outlet port	cm^3/MPa	0.117
I_{L1}	fluid inertia	MPa-s/cm^3	12.2 x 10^{-6}
R_{L1}	line Resistance	MPa-s/cm^3	137 x 10^{-6}
C_{12}	line compliance at motor inlet port	cm^3/MPa	0.0738

R_{slm}	motor internal leakage resistor	s-MPa/cm^3	8.79
D_m	flipper motor displacement	cm^3/rad	7.304
J_m	motor and sheave inertia	kg-m^2	0.050
R_{b4}	bearing friction resistor	N-m-s/rad	0.04
S_{mtc}	motor torque constant	N-m	2.2
R_{vdm}	motor viscous drag resistor	N-m-s/rad	0.0498
R_{cfm}	motor coulomb friction resistor	N-m-s/rad	C.7.5
SR	V-belt sheave ratio	-	1:1
C_{14}	V-belt compliance	N-m/rad	0.001
R_{disk}	load resistance from cutting stalks	N	C.7.6
R_{b5}	bearing friction resistor	N-m-s/rad	0.04
J_{disk}	disk inertia	kg-m^2	0.07

C.7.1 Modulus of Joint Effects

$$\alpha = \frac{\omega_{hls}}{\omega_{PTO}} = \frac{\cos\theta_1 \cos\theta_2}{(1 - \sin^2\beta_1 \sin^2\theta_1)(1 - \sin^2\beta_2 \sin^2\theta_2)}$$

where

ω_{hls} = harvester input shaft velocity (rad/s),
θ_1 = joint angle in joint 1 (rad),
θ_2 = joint angle in joint 2 (rad),
β_1 = rotational position of front shaft driving yoke measured from the plane perpendicular to joint angle (rad)
β_2 = rotational position of connecting shaft driving yoke measured from the plane perpendicular to joint angle (rad), and
ω_{in} = input velocity from tractor PTO (rad/s).

C.7.2 Driveline Backlash and Non-linear V-belt Function

Torque	$\Delta\theta$
-200.0	-0.300
0.0	-0.200
0.0	0.095
10.0	0.200
200.0	0.250
300.0	0.300

C.7.3 Shaft Inertia Function

$$J_o = \bar{J} + m[r(t)]^2$$

where
J_o = mass moment of inertia (kg-m^2),
$\bar{J}$ = mass moment of inertia about mass center (kg-m^2),
m = mass of shaft (kg), and
r(t) = distance between axis of rotation to mass center (m).

C.7.4 Relief Valve Resistor Function

Q_r	P_s
0.0	0.0
10.0	0.68

25.0	1.37
50.0	2.75
400.0	5.16

C.7.5 Motor Coulomb Friction Resistor Function

C_f	ω
0.600	0.000
0.312	10.470
0.308	18.330
0.308	20.000

$$T_{cfm} = C_f P_{12}$$

C.7.6 Stalk Cutting Load Function

$$R_{dlsk} = A \mid \sin(2\pi ft) \mid$$

where

A = amplitude of torque to sut stalk (0.586),
f = frequency of cut (Hz) (3.25).

Vita

Glen Christpher Rains was born in Columbus Georgia on July 16, 1965, and most of his youth was spent on a cattle farm in Woodland Georgia. He graduated from Manchester High School in 1983 and received a bachelors degree in Agricultural Engineering at the University of Georgia in 1987. Upon finishing his degree at Georgia, Glen spent one summer on a research internship at the Georgia Experiment Station in Griffin. He began a Masters program in the fall of 1987 at Virginia Tech. Upon completion of his Masters degree in May of 1989, Glen immediately began a PhD program. Glen received his PhD degree in May 1992 and has accepted a position at the National Highway Traffic Safety Administration (NHTSA) in Washington D.C.